Structure and Dynamics in Two-Dimensional Glass-Forming Alloys

Asaph Widmer-Cooper

A thesis submitted in fulfilment
of the requirements for the degree of
Doctor of Philosophy

Physical and Theoretical Chemistry
University of Sydney
May 2006

Abstract

The glass-transition traverses continuously from liquid to solid behaviour, yet the role of structure in this large and gradual dynamic transition is poorly understood. This thesis presents a theoretical study of the relationship between structure and dynamics in two-dimensional glass-forming alloys, and provides new tools and real-space insight into the relationship at a microscopic level.

The work is divided into two parts. Part I is concerned with the role of structure in the appearance of spatially heterogeneous dynamics in a supercooled glass-forming liquid. The isoconfigurational ensemble method is introduced as a general tool for analysing the effect that a configuration has on the subsequent particle motion, and the dynamic propensity is presented as the aspect of structural relaxation that can be directly related to microscopic variations in the structure. As the temperature is reduced, the spatial distribution of dynamic propensity becomes increasingly heterogeneous. This provides the first direct evidence that the development of spatially heterogeneous dynamics in a fragile glass-former is related to spatial variations in the structure. The individual particle motion also changes from Gaussian to non-Gaussian as the temperature is reduced, i.e. the configuration expresses its character more and more intermittently.

The ability of several common measures of structure and a measure of structural 'looseness' to predict the spatial distribution of dynamic propensity are then tested. While the local coordination environment, local potential energy, and local free volume show some correlation with propensity, they are unable to predict its spatial variation. Simple coarse-graining does not help either. These results cast doubt on the microscopic basis of theories of the glass transition that are based purely on concepts of free volume or local potential energy. In sharp contrast, a dynamic measure of structural 'looseness' - an isoconfigurational single-particle Debye-Waller (DW) factor - is able to predict the spatial distribution of propensity in the supercooled liquid. This provides the first microscopic evidence for previous correlations found between short- and long-time dynamics in supercooled liquids. The spatial distribution of the DW factor changes rapidly in the supercooled liquid and suggests a picture of structural relaxation that is inconsistent with simple defect diffusion. Overall, the work presented in Part I provides a *real-space* description of the transition from structure-independent to structure-dependent dynamics, that is complementary to the configuration-space description provided by the energy landscape picture of the glass transition.

In Part II, an investigation is presented into the effect of varying the interparticle potential on the phase behaviour of the binary soft-disc model. This represents a different approach to studying the role of structure in glass-formation, and suggests many interesting directions for future work. The structural and dynamic properties of six different systems are characterised, and some comparisons are made between them. A wide range of alloy-like structures are formed, including substitutionally ordered crystals, amorphous solids, and multiphase materials. Approximate phase diagrams show that glass-formation generally occurs between competing higher symmetry structures. This work identifies two new glass-forming systems with effective chemical ordering and substantially different short- and medium-range structure compared to the glass-former studied in Part I. These represent ideal candidates for extending the study presented in Part I. There also appears to be a close connection between quasicrystal- and glass-formation in 2D via random-tiling like structures. This may help explain the experimental observation that quasicrystals sometimes vitrify on heating. The alignment of asymmetric unit cells is found to be the rate-limiting step in the crystal nucleation and growth of a substitutionally ordered crystal, and another system shows amorphous-crystal coexistence and appears highly stable to complete phase separation.

The generality of these results and their implications for theoretical descriptions of the glass transition are also discussed.

Acknowledgements

Peter Harrowell provided the inspiration that got the project started and the humour and enthusiasm to keep me going when frustration set in and my interests waned. This work would have been much the leaner without his ongoing help, encouragement and entertaining conversation, for all of which I am very grateful.

During the course of the Ph.D. I was fortunate enough to attend several local and international conferences and meet some of the people whose work is cited here. I wish to thank everyone who took the time to discuss my research for the stimulating discussions that are the real joy of science. Unfortunately there is not enough space to mention everyone here.

I also wish to thank the entire Harrowell group - Julian, Adam, Robert, Janka, Toby, David, Scott, and Jimmy - for much advice and good humour over the last four years. Special thanks go to Toby Hudson, for providing the conjugate gradient code used to generate inherent structures in Part I, and to Sai Ho Lee, who - as a summer research student - investigated the time evolution of the DW factor and thus contributed to the research presented in Section 3.3.2 and Chapter 8.

My postgraduate degree has been funded by an Australian Postgraduate Award. The University of Sydney chipped in with a supplementary Gritton scholarship in 2003, and Peter Harrowell generously provided assistance when the scholarship funds ran out. I am also grateful for support from the Postgraduate Research Support Scheme for funds to attend a conference in Japan and to assist with the purchase of a computer and research texts.

Finally, a huge thank you to my parents for all their love and support over the years, and to Danielle for topping that by also proof-reading the entire thesis and providing me with the most amazing birthday/thesis writing present anyone could ever hope for.

Publications

Most of the work presented in Part I of this thesis has been published or submitted for publication, and it is anticipated that much of the work presented in Part II will also be published. The chapters and corresponding publications are as follows:

Chapter 2:

- "How Reproducible is the Structure of Dynamic Heterogeneities in Glass-Forming Liquids?", Widmer-Cooper, A., Harrowell, P., *AIP Conference Proceedings* **708**, 711 (2004).
- "How Reproducible are Dynamic Heterogeneities in a Supercooled Liquid?", Widmer-Cooper, A., Harrowell, P., Fyneweaver, H., *Phys. Rev. Lett.* **93**, 135701 (2004).
- "On the Study of Collective Dynamics in Supercooled Liquids through the Statistics of the Iso-Configurational Ensemble", Widmer-Cooper, A., Harrowell, P., *submitted for publication* (2006).

Chapter 3:

- "On the Relationship Between Structure and Dynamics in a Supercooled Liquid", Widmer-Cooper, A., Harrowell, P., *J. Phys. Condens. Matter*, **17** S4025 (2005).
- "Free Volume cannot Explain the Spatial Distribution of Debye-Waller Factors in a Glass-Forming Binary Alloy", Widmer-Cooper, A., Harrowell, P., *J. Non-Cryst. Solids*, **352**, 5098 (2006).
- "Predicting the Long-Time Dynamic Heterogeneity in a Supercooled Liquid on the Basis of Short-Time Heterogeneities", Widmer-Cooper, A., Harrowell, P., *Phys. Rev. Lett.*, **96**, 185701 (2006).

We shall not cease from exploration
And the end of all our exploring
Will be to arrive where we started
And know the place for the first time.

From ‘Little Gidding’, by T. S. Eliot (1888–1965)

Contents

Chapter 1

Introduction

We introduce the study of amorphous solids and glass-formation and emphasise the importance of a structural underpinning for any complete description of this transition. The aim of the thesis is also established in relation to recent experimental work on glass-formers and amorphous alloys.

1.1 What is the Role of Structure in the Glass Transition?

Glasses and the glass transition represent, in the much quoted estimate of a Nobel laureate,"perhaps the deepest and most interesting unsolved problem in condensed matter physics" [1]. Glass-forming materials have also become an integral part of our lives, from plastics to building facades, food storage, health science and the rewritable CD; and the recent discovery of bulk metallic glasses looks set to greatly increase the range of applications. However, a detailed understanding of the connection between structure and dynamics in these materials, and in glass-formers in general, is lacking. We believe that this knowledge is necessary for any complete theoretical description of the glass transition, and will likely aid in the engineering of such materials for specific applications. As Cahn [2] has argued, it is generally the ability to make a strong link between microscopic structure and physical properties that essentially defines an established field of material science.

It has been known for centuries that if a liquid is quenched sufficiently fast, it can be cooled below its melting/freezing point T_m without crystallising. Below T_m, the fluid is called a supercooled liquid. With continued cooling its viscosity increases rapidly until eventually viscous flow ceases on the timescale of a typical experiment. At lower temperatures the structural relaxation time can be years or longer. The glassy state is a true solid, as the shattering of a mirror demonstrates. However, despite its rigidity, mechanical strength and elastic properties, the microscopic structure of a glass lacks any form of long-range order, thus distinguishing it from crystalline solids. For this reason, the term *amorphous solid* is often used synonymously with glass. The glassy state is sometimes incorrectly assumed to have the same structure as a liquid. While there is no development of long-range order, there are some changes in local and medium range ordering which, as we demonstrate in this thesis, become significant as the glass-forming liquid is supercooled.

The continuous transition from the liquid to solid state associated with the glass transition presents a number of puzzles with respect to the role of structure: (i) how does structure change to cause a continuous transition from fluid liquid to rigid solid? (ii) what is responsible for the rigidity of the glassy state? and (iii) how do preferred higher-symmetry structures influence the properties of the glass-former and its stability to crystallisation? While the precise structural details will vary from material to material, the broad phenomenology common to all glass-formers suggests that some aspects of the relationship between structure and dynamics are universal.

Experimental probes of structure in the supercooled liquid and glassy states generally return information on the average structure about particles in the form of the structure factor - from X-ray and neutron scattering - and the pair distribution function that can be derived from it. As these show only small changes, most experimental work on glasses has focused on studying the large changes in dynamic properties and unusual dynamic behaviour associated with the glass transition, and on finding correlations between various dynamic properties of glass-forming liquids. It has been largely left to theoreticians to address the role of structure in glass-formation, often involving the study of simple model systems. In this thesis we use molecular dynamics to investigate the relationship between dynamics and structure in a family of binary soft-disc mixtures that form 2D analogues of many of the structures observed in alloys. We discuss our choice of model further in Section 1.4. Interestingly, the latest generation of experiments using modern neutron and synchrotron X-ray sources, together with a number of new theoretical methods, hold promise for bridging the gap between experimental and theoretical studies of structure in disordered materials. For example, new radiation sources have improved the resolution of experimental data, and techniques such as reverse Monte Carlo [3, 4], empirical potential structure refinement [5] and experimentally constrained molecular relaxation [6], are now able to provide a pool of candidate structures consistent with the data. While none of these structures can ever be proven to be ‘correct’, they can help our understanding of the structure itself, and of the relationships between local structure and other physical properties. See, for example Sheng et al. [7], for a recent application of reverse Monte Carlo to the study of structure in metallic glasses.

In the next section we review some aspects of the phenomenology of supercooled liquids and glasses that will be important for later discussion. In particular, we emphasise the discovery of spatially heterogeneous dynamics which, as we demonstrate in Part I, offers insight into the microscopic relationship between structure and dynamics. More extensive reviews and discussion of other aspects of supercooled liquids and glasses can be found in references [1, 8–15]. Various theoretical models of the glass transition are discussed in other chapters.

1.2 Phenomenology of Supercooled Liquids and Glasses

Far from being unusual, glasses are ubiquitous in the world around us and can be found in many structural and technological applications that exploit both the solid-like and fluid-like nature of glasses, as well as their optical, electrical and magnetic properties. These applications include building materials, household utensils, objects of art, photoconductors, optical fibres, computer memory elements, the rewritable CD and solar cells. Rawson [8] and Zallen [9] provide many more examples. Metallic glasses have greatly increased the range of possible applications due to their exceptional mechanical strength, magnetism in ferromagnetic alloys, atomic smoothness, and ability to be easily molded into complex shapes. Their properties and applications are discussed in more detail in Chapter 4. Many insects, micro-organisms and seeds also protect themselves against harsh environmental conditions by loading their cells with a glass-forming liquid or encasing themselves in a glassy coat of sugars. Research is also being carried out to investigate the glassy properties of carbohydrates for the preservation of food and protein-derived drugs [17, 18]. In addition to metal alloys, glass-formers include oxide glasses (e.g. SiO_2), polymeric glasses (e.g. polystyrene), simple molecular organic glasses (e.g. glycerol), hydrogen-bonded fluids (e.g. water)

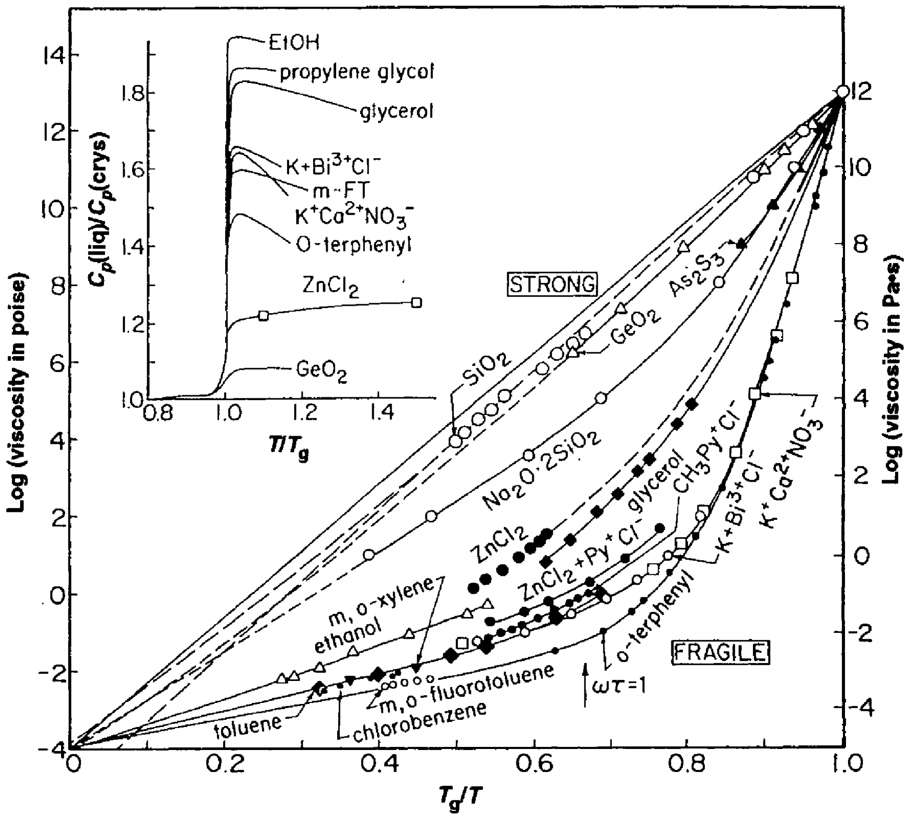

Figure 1.1: Arrhenius plots of viscosities scaled by T_g, the temperature at which the viscosity $\eta = 10^{13}$ P, showing strong and fragile extremes of supercooled liquid behaviour. The inset shows that, in general, strong liquids have small heat capacity jumps at T_g, whereas fragile liquids have larger steps. Hydrogen bonding enhances the drop in the heat capacity at T_g. Reproduced from Angell [16].

and ionic glasses (e.g. $ZnCl_2$). Of these, alloys are among the structurally simplest. Despite their variety, glass-formers all share much common phenomenology.

All glass-formers reach the solid state via a continuous transition from the liquid, with an accompanying large increase in their viscosity η, sometimes over a relatively narrow temperature range. In Figure 1.1 the increase in viscosity as the glass transition temperature T_g is approached has been compared for a variety of different glass-formers. Here T_g is defined as the temperature at which the viscosity reaches 10^{13} Poise. For some glass-formers, for example covalent network glasses, the increase follows an Arrhenius law as indicated by the straight line. These are generally referred to as strong liquids. However, for many glass-formers, the increase in viscosity near T_g shows a strongly non-Arrhenius behaviour as indicated by the non-linear increase in viscosity. These are commonly referred to as fragile liquids. The deviation from

Arrhenius behaviour is often quantified by a 'fragility' parameter, that is large for fragile glass-formers and small for strong glass-formers.

The transition into the glassy state is accompanied by a rapid change in thermodynamic derivatives such as the isobaric heat capacity $C_p = (\delta H/\delta T)_P$, where H is the enthalpy. This change occurs over a small temperature interval, resulting in a well-defined step in C_p on cooling at constant pressure, as shown in the inset to Figure 1.1. These rounded discontinuities are the most apparent and commonly used signatures of the glass transition in the laboratory. The drop in C_p - to within a few percent of the heat capacity of the crystal - on cooling through the glass transition is due to the loss of some configurational degrees of freedom on the experimental timescale. Simple molecular and ionic liquids, which have short range structures that are quite sensitive to temperature changes, exhibit large C_p jumps at the glass transition. In contrast, network glass-formers, which form tetrahedrally coordinated three-dimensional networks that undergo very little structural change around T_g, have very small C_p changes. These differences are also visible in the inset of Figure 1.1.

One consequence of this dynamic transition is that the density of the final amorphous state depends upon the quench rate. Figure 1.2 shows the specific volume (volume per unit mass) V as a function of temperature T for a typical liquid. Upon cooling from a high temperature, the liquid may crystallize at the melting/freezing temperature T_m. This is a first order transition which results in an abrupt discontinuity in V. A liquid that manages to pass T_m without crystallising, typically by cooling at a faster rate, is called a supercooled liquid. Although this is strictly a metastable state, supercooled liquids may be stable for years and in the absence of crystal nuclei can be regarded as equilibrium states since their thermodynamic properties are reproducible and independent of thermal history.

As the supercooled liquid is cooled to lower temperatures, its viscosity and density rapidly increase, and the molecules that comprise it slow down. Eventually, the time required for relaxation to the equilibrium configuration becomes comparable to or exceeds the experimental timescale, i.e. the inverse of the cooling rate. At this stage, the liquid falls out of metastable equilibrium and, at a temperature not much lower than this, behaves like a rigid solid (the glassy state). This change from fluid-like to solid-like properties occurs continuously over a temperature interval called the *glass transition* region. The glass transition temperature T_g lies somewhere in this region and can be defined operationally in a number of ways, one common definition being

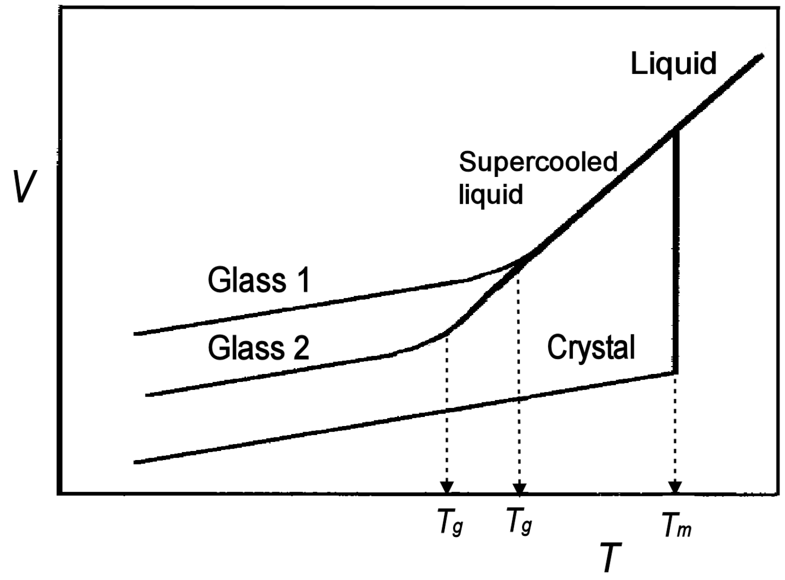

Figure 1.2: A schematic representation of the specific volume V as a function of temperature T on cooling for a typical glass-forming liquid. If the quench rate is sufficiently high, the liquid can be supercooled below the freezing point into a glassy state which depends on the cooling rate. Glass 1 is prepared at a faster cooling rate than Glass 2. The glass-transition temperature T_g decreases as the cooling rate decreases.

the temperature at which the average relaxation time reaches 10^2 s. Both T_g and the width of the transition region depend on the cooling rate. Smaller cooling rates allow the liquid to stay in metastable equilibrium until lower temperatures, and higher quench rates cause the transition region to widen. This is particularly prominent in computer simulations of glasses where the cooling rate is typically greater than 10^{10} K s^{-1}. The glass transition, at least as observed in the laboratory, is not a thermodynamic phase transition, but rather a kinetic event.

Besides the thermodynamic signatures of the glass transition and the rapidly increasing relaxation times as T_g is approached, there are dramatic changes in the *manner* in which supercooled glass-forming liquids relax towards equilibrium following a perturbation such as a change in temperature, pressure or applied external field. In the following discussion we consider only small perturbations such that the response of the system is independent of the sign and magnitude of the perturbation, i.e. linear relaxation.

The return of an observable, such as the dielectric modulus, to its average value following a perturbation can be monitored by a relaxation function X. At temperatures above and just below T_m, X often displays simple exponential behaviour ($X = exp[-t/\tau]$), characteristic of processes dominated by a single activation energy. However, as T_g is approached many supercooled liquids exhibit departures from this simple exponential decay. Such non-exponential relaxation can be reasonably well described by a stretched exponential function of the form $X = Aexp[-(t/\tau)^{\gamma}]$, where $0 < \gamma < 1$, indicating a distribution of relaxation times in the system. There is a rough correlation between the value of the exponent γ and the degree of departure from Arrhenius temperature dependence of relaxation times, i.e. the degree of fragility. Strong liquids typically have γ values close to 1, while fragile liquids tend to have exponents in the range 0.3–0.5. An extensive compilation of γ values and degrees of fragility for about 70 glass-forming systems is provided by Böhmer et al. [19].

The above discussion has focused on the main relaxation process which gives rise to viscous flow in supercooled liquids. This is generally referred to in the literature as the primary or α relaxation. A number of faster relaxation processes have also been identified. The only one that we will refer to in the present work is the *fast* β process. A variety of experiments - neutron scattering [20–22], depolarised light scattering [23–25] and nuclear magnetic resonance [26] - as well as molecular dynamics simulations [27, 28], have now clearly shown that for several diverse glass-forming liquids there exists a fast relaxation process on the *picosecond* timescale. In contrast to the α process, the fast β relaxation has an Arrhenius temperature dependence. Figure 1.3 shows the decay of the incoherent scattering function for *ortho*-terphenyl as measured by neutron scattering. The relaxation curves broaden with decreasing temperature until first a shoulder and then a plateau appears at intermediate times. Both the width and height of the plateau increase with decreasing temperature. The initial decay to the plateau is associated with the fast β process and the second decay from the plateau is associated with the α process.

Measurements of incoherent scattering functions by dynamic light scattering [29, 30], inelastic neutron scattering [31] and neutron spin-echo [32] experiments are often carried out at wavevectors at, or close to, the main peak of the static structure factor. This is because the most intense peak in the structure factor k_{max} provides a measure of the lengthscale for the dominant short-range ordering in the system. The decay of density correlation functions, such as the incoherent scattering function, at wavevectors k close to k_{max} therefore provides information on the main structural

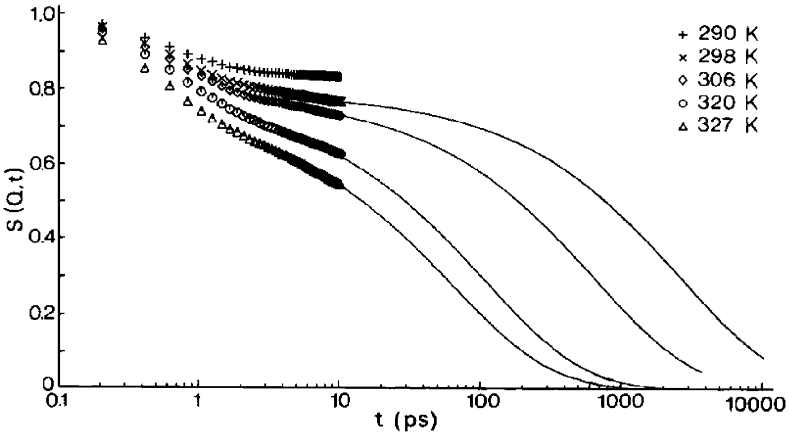

Figure 1.3: Temperature dependence of the intermediate scattering function for *ortho*-terphenyl as observed by incoherent neutron scattering. Note the appearance of a two-step relaxation function with the first decay occuring on the picosecond timescale. Figure reproduced from Kiebel et al. [22].

relaxation process in the system.

Crystallisation is a serious problem for a supercooled liquid on its way to the glassy state. In order to avoid crystallisation, the cooling rate must exceed the maximum rate of crystal nucleation and growth, R_c. This rate has a maximum because below T_m there are two competing effects. Initially, the increasing thermodynamic driving force towards crystal nucleation, due to the growing free energy difference between the supercooled liquid and the crystal, causes the rate to increase. At lower temperatures, however, the increase in viscosity causes diffusional processes to slow down and the rate to decrease. Below T_g, the rate of structural relaxation is so small that crystal nucleation and growth are not a problem. It is therefore only in the intermediate temperature region below and near T_m that the risk of crystallisation is high. Theories of the rates of crystal nucleation and growth and their implications for glass-formation are provided by Turnbull et al. [33–35] and Uhlmann [36]. These studies show that if T_g lies closer to T_m, then the maximum in R_c also moves towards T_m with a decrease in both the height and width of this peak. Thus, crystallisation can be avoided with a lower cooling rate. This change is due to the narrower temperature interval over which the viscosity increases, and the fact that the viscosity near T_m is often greater if T_g is close to T_m. Good glass-formers like *ortho*-terphenyl and SiO_2, which require only slow cooling rates (< 0.1 K s^{-1}) to be quenched into the glassy state, generally have a ratio of $T_g/T_m \approx 0.7$; the latter also has a high viscosity on the order of 10^6 P at T_m [37,38]. In addition, mixtures usually have a greater glass-forming ability than the individual pure components because of the depression in T_m. For example, metal alloys are easier to quench into the glassy state than elemental metals. For alloys, the glass-forming ability is greatest near the eutectic composition where the gap between T_m and T_g is smallest.

An intriguing aspect of the glass transition is that the slowing down, and associated increase in the complexity of the dynamic behaviour, occurs without an obvious structural cause. X-ray and neutron scattering studies of supercooled liquids generally show only subtle changes in local packing associated with a viscosity change of 12 orders of magnitude [39, 40]. In the next section we introduce a recent discovery that may help to address this question.

1.2.1 Spatially Heterogeneous Dynamics

Liquids do not become glasses homogeneously. Tammann [41] suggested as much as far back as 1933, and with the accumulation of data from experiments and simulations of dynamic heterogeneities in supercooled liquids [11,14,42,43], we can now state the situation more explicitly. The transition to rigidity involves the appearance of slowly relaxing domains whose dimensions and lifetimes increase with supercooling. In this section we briefly review some of the evidence from simulations and experiments for the existence of spatially heterogeneous dynamics.

An example of spatially heterogeneous dynamics in a supercooled soft-disc liquid is shown in Figure 1.4. The particle displacement vectors have been plotted over a timescale that is an order of magnitude *longer* than the timescale for α-relaxation. For the 2D mixture that these displacements are taken from, this corresponds to a time five orders of magnitude longer than the average time between particle collisions. The particle displacements are shown as arrows connecting the initial and final positions of each particle. It is clear that some of the particles have moved long distances, while there are large domains of particles that have hardly moved at all. If this was a normal liquid the displacements over this timescale would be similar for all the particles.

Simulations of many different model systems have found direct evidence for such spatially heterogeneous dynamics on intermediate timescales. Foley and Harrowell [45] studied the two-dimensional facilitated kinetic Ising model and found that the relaxation rates were spatially correlated, i.e. that slow spins tend to form 'islands'

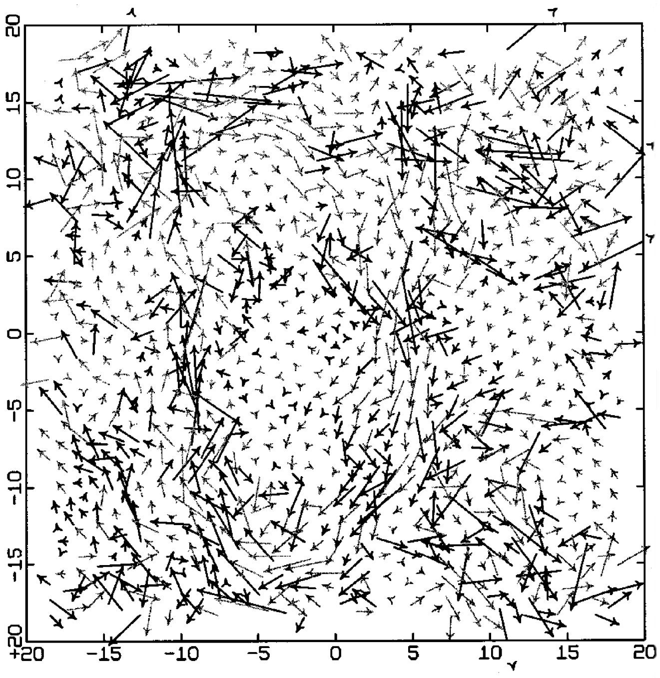

Figure 1.4: The particle displacements, indicated as vectors joining the initial to final particle positions, for particles in a binary soft-disc mixture over a timescale that is an order of magnitude longer than that characteristic of the main α-relaxation. Reproduced from Perera and Harrowell [44].

on the background formed by fast spins; and Kob et al. [46] found that 'mobile' particles in a supercooled 3D Lennard-Jones liquid tend to form clusters whose sizes grow with decreasing temperature. The purely repulsive 2D model, for which the particle displacements are plotted in Figure 1.4, has also been found to have spatially heterogeneous dynamics [44], and similar dynamics has been observed in a number of other 2D [47, 48] and 3D [49, 50] models. Perera and Harrowell [51] have also shown that the assumption of dynamic heterogeneity in a diffusing defect model naturally leads to many of the dynamic properties associated with supercooled liquids, including strong and fragile behavior, two-step relaxation processes, nonlinear relaxation following temperature jumps, spatially correlated kinetics, and non-Gaussian behavior of incoherent processes.

While experiments on supercooled liquids cannot, in general, directly access such structural information, there are now a wide range of experiments that support the existence of heterogeneous dynamics in fragile glass-formers. These include such diverse techniques as NMR [52], solvation dynamics [53], and optical [54] and dielectric dynamic hole burning [55]. A number of other experimental results have been attributed to the existence of *spatially* heterogeneous dynamics. These include the breakdown of scaling between translational and rotational diffusion at low temperature [56], the appearance of non-Fickian or dispersive transport [57], and the dependence of T_g on film thickness in free-standing polymer films [58].

The first experimental technique to actually measure a dynamic correlation length - and thus provide strong experimental evidence for spatially heterogeneous dynamics as opposed to purely heterogeneous dynamics - was a 4D NMR spin diffusion technique introduced by Tracht et al. [59] in 1998. It uses a specially developed technique to selectively magnetise domains of slow particles. This magnetisation then spreads quickly from particle to particle via proton spin diffusion on a timescale that is fast with respect to the particle motion until eventually the magnetisation is spread evenly among slow and fast domains. By selectively measuring how long it takes for the magnetisation in the slow domains to decay and knowing how fast the magnetisation travels, it is possible to calculate a lengthscale for the slow domains. Lengthscales for a range of materials including glycerol, ortho-terphenyl and poly(vinyl acetate) have been measured using this technique. Typical lengthscales obtained are of the order of 1.0–3.7 nm [60].

With these and many other experiments and simulations carried out over the past ten years, there is now indisputable evidence that spatially heterogenous dynamics is a general feature of fragile supercooled liquids. In a sense, this inhomogenous slowing down answers the question of how the transition from liquid to solid can be continuous, and provides an explanation for many of the unusual dynamic properties of supercooled liquids. However, this phenomenological account of the glass transition neatly sidesteps an important question, namely what is responsible for the slow domains? It is an intriguing notion that it could be due to some property of the structure. While experiments are only able to detect subtle changes in the average structure on cooling, the large spatial variation in dynamics appears to contain much information about what aspects of structure are important for dynamics. This is discussed further in Part I.

In the next section we contrast the picture of dynamics in supercooled liquids with that of normal liquids and crystalline solids. We emphasise the transition from mean-field to fluctuation-dominated behaviour during glass-formation and the challenges this poses for any complete theoretical description of glass-formation.

1.3 On the Applicability of Mean-Field Theories near the Glass Transition

Self diffusion in a simple liquid above its melting point is generally well described by mean-field theory, whether one looks at the problem via kinetic theory or a generalised Langevin with memory [61] (the latter including the mode coupling treatments of the memory function [62]). These theories are mean-field in the sense that the dynamics are determined by the average structure of the liquid. In contrast, diffusion in solids is dominated by rare fluctuations in the structure - point defects, dislocations and grain boundaries. As happens whenever kinetics are subject to rare events (nucleation phenomena or fracture, for example), the associated theory treats the relevant fluctuations explicitly rather than trust to the dubious accuracy of the wings of distributions. This is certainly the case in the extensive theoretical literature concerning the defect and grain-boundary mediated transport in solids [63].

The continuous transition from fluid to solid associated with the glass transition traverses between these two extremes. This imposes serious challenges for any complete theoretical description of the glass transition. Can a single theory describe a range of behaviour that at one extreme is well predicted by averages and at the other extreme depends upon rare events? The conceptual transition from mean-field to fluctuation-dominated is perhaps not immediately evident from the literature. The major theoretical treatment of the glass transition - the mode coupling theory (MCT) [62] - incorporates the average liquid structure through vertex functions. This qualifies the MCT as a mean-field theory. The term ‘mean-field’, however, does require some qualification. A hierarchy of generalised Langevin theories can be imagined in which the neglect of fluctuations (the ‘mean-field’ approximation) occurs at increasingly higher orders of correlations. Szamel [64] has recently presented a mode coupling theory of relaxation in a simple lattice model of a glass in which the factorisation is applied to one order higher in correlation to that of the standard approximation. This theory captures scaling laws previously thought to be obtainable only from an explicit treatment of the rare fluctuations responsible for dynamics [65].

In spite of its mean-field character, the evidence that the mode coupling theory can provide a quantitative treatment of diffusion and structural relaxation leading up to the glass transition is impressive [62]. The more recent success of mode coupling theory in providing a unified treatment of colloidal glasses and associating gels is quite remarkable [66]. The problem is that the transition itself - the ideal glass transition - is an artifact of the mathematical structure of the self-consistency introduced by the factorisation approximation. From one point of view, this is an attractive feature of the model - the fact that arrest enters naturally without having to burden the treatment with all the physical correlations that actually stabilise the solid. On the question of the actual physical origins of rigidity of the glass, however, the mode coupling theory is silent. It is necessary to look elsewhere to understand the relationship between structure and dynamics in the liquid as this rigid state is approached.

1.4 This Work

We study the relationship between structure and dynamics in 2D glass-forming alloys by approaching the problem from two directions: (i) by directly examining the spatial distribution of structure and structure-determined dynamics in a binary soft-disc mixture; and (ii), by varying one of the interaction parameters in the model and studying what effect this has on the structure, dynamics and phase behaviour of the system. In Part I we take the former approach, developing new techniques to explore the structural origin of the spatially heterogeneous dynamics that has been widely observed in supercooled liquids. In particular, we consider a binary soft-disc mixture whose glass-forming ability has previously been studied in detail [44, 67]. Then, in Part II, we explore the parameter space of the binary soft-disc model. We study the effect of varying both the interparticle potential and the composition, and show that this simple model is able to form a wide variety of phases, including substitutionally ordered crystals, a range of structurally different glasses, and several phase separated systems. Each has interesting properties (some of which we explore further) and some comparisons are made between the different systems. Finally, in Chapter 8, we discuss how further insight may come from comparing the relationship between structure and dynamics in the initial model with the glass-formers discovered in Part II.

We choose to study the binary soft-disc model for several reasons. The purely repulsive potentials make it one of the simplest models in which real particle dynamics can be studied, and the 2D nature of the model allows for direct visual analysis and comparison of the spatial distribution of both structural and dynamic properties. As already mentioned, the system that we study in Part I - which also forms the starting point of the exploration of parameter space in Part II - has previously been studied in detail and found to reproduce the full range of phenomenology of glass-formation. While there are some differences between the structure and dynamics of 2D and 3D systems, we note that there are also very large variations among different 3D glass-formers. Ultimately, there is insight to be gained from a complete description of any glass-former. If this is not achievable in relatively simple 2D systems then one must ask what hope is there for understanding more complex glass-formers. We therefore expect that the physical insight gained from studying binary soft-disc mixtures will be useful for improving our understanding of real 3D alloys and glass-formers.

Part I

The Relationship Between Structure and Dynamics in a Supercooled Liquid

Introduction to Part I

As explained in Section 1.2.1, the transition to rigidity in glass-forming liquids involves the appearance of spatially heterogeneous dynamics. Using this as a handle, we examine the relationship between structure and dynamics in a supercooled glass-forming liquid. In particular, we address the following two questions: (i) Is there something in the structure that is responsible for dynamics that can vary by orders of magnitude from one region of the sample to another at T_g? and (ii) Can the mobile regions, as identified by anharmonic excitations or higher propensities, be associated with particular types of local structure, and if so what is the structural signature of these 'soft' spots?

There are at least two ways to analyse the spatial distribution of particle dynamics. The approach that we take is to consider the correlation between the initial particle configuration and the subsequent dynamics. The second, which has received considerable attention, is to consider the correlation between the mobile particles themselves. For completeness sake, and to provide further motivation for the work presented in this part, we provide a brief review of the latter approach.

Particle motion in dense liquids is, to a large extent, entrained so that particles follow along in each other's path. In 1998, Donati et al. [68] showed that displacements in a supercooled liquid exhibited a strong tendency to locally align. The dynamics associated with such correlations are generally quite complex. To appreciate this, consider, first, the *simple* scenario of a diffusing vacancy. The linear character of this pattern of displacements reflects a rough local conservation of free volume, that is, the volume left free by the motion of a particle is more likely to be filled by a single particle rather than the collective rearrangement of a number of particles. There is also a correspondence between spatial structure and temporal sequence so that one end of the resulting string of displacements represents the first step while the other end represents the last step. Ritort and Sollich [65] have recently reviewed the predictions of a number of diffusing defect models.

The diffusing defect picture, presented above, ignores the possibility that the propensity for motion lies distributed in a configuration and that relaxation is not a simple consequence of the transport of a rare fluctuation (even one more complex than a simple vacancy) but rather a sequence of unlocking events which add up, over the observation interval, to a linear path. Vogel et al. [69] have presented simulation evidence of just this latter process. Delaye and Limoge [70], in an interesting study, considered the different fates of vacancies created in a model glass. The resulting behaviour was divided into three groups: those defects that remained stable and stationary, those that relaxed by propagation (the diffusing defects) and a third group that relaxed by being, essentially, 'absorbed' back into the surrounding disordered medium through a local collective rearrangement. The presence of this last process distinguishes the amorphous material from the crystalline.

In terms of a simple model that can capture this more complex collective behaviour, the class of facilitated spin flip models introduced by Fredrickson and Andersen [71] and extended by Jäckle [72] is particularly useful. The term 'facilitated' refers to the idea that the local state of a system can influence the kinetics of adjacent regions. To date, models of facilitated dynamics have all relied on the introduction of explicit kinetic constraints. Recently, Garraghan and Chandler [73] have proposed that this idea of 'facilitation' represents a general aspect of dense amorphous phases. The interesting unanswered question here is whether the implied general mapping from systems of interacting particles to systems governed by kinetic constraints exists. Central to this question is the need to understand the degree to which a particle configuration determines the propensity of particles to subsequently move. This is precisely the subject of Chapter 2.

The analysis of the correlation between particle displacements sketched here provides (i) a compact summary of the information presented by dynamic heterogeneities, (ii) an explanation of some observed features of relaxation functions and transport behaviour in terms of microscopic dynamics, and (iii) the prospect of identifying kinetic rules that govern relaxation in disordered systems. This approach, however, does not explain what it is about a configuration that permits motion in one region but not in another, nor how this distribution varies with temperature, composition, particle interactions, etc. One could imagine, for example, studying transport in crystalline solids via this description, amassing a considerable amount of phenomenological information about the dynamic heterogeneities and yet never arriving at a clear structural (and, hence, predictive) picture of vacancies and interstitials. For this reason, we would like to directly address the question of the relationship between structure and dynamics, which we investigate in detail in Chapter 3.

Chapter 2

Dynamic Propensity

In this chapter we tackle the question of the degree to which a given configuration determines the subsequent particle dynamics. We begin by demonstrating that not all of the dynamics in the supercooled liquid can be related to structure. Through the introduction of the isoconfigurational ensemble method and the dynamic propensity, we are able to provide explicit proof that something in the structure is *responsible for the development of spatially heterogeneous dynamics in this system. In particular, we find that as the liquid is cooled, the structure-determined propensity for particle motion becomes increasingly heterogeneous, both in magnitude and in spatial extent. We characterise the variation of the propensity distribution with temperature and configuration, study its convergence properties, and demonstrate that additional insight into glass-formation can be obtained via the analysis of other correlations within the isoconfigurational ensemble.*

2.1 Introduction

Over the last ten years, dynamic heterogeneity has become recognised as a general phenomenological feature of glass formation [11]. The existence of these long-lived kinetic fluctuations has been useful in rationalising some puzzling aspects of kinetics in supercooled liquids. These include non-Fickian diffusion [74, 75], deviations from classical nucleation theory [76], and the breakdown of the scaling between translational diffusion, on the one hand; and, on the other, rotational diffusion [77], shear viscosity [57], and structural relaxation [78]. Helpful as these developments are, they do not address the fundamental question of the relationship between structure and kinetics in the supercooled liquid.

The *spatial* distribution of particle mobilities, however, does appear to offer a considerable amount of information on this very point. A number of papers have considered the local connection between dynamics and structure, the latter being characterised using topology [44], potential energy [69, 79], and free volume [80]. While most have reported some correlation, none have established a correlation of sufficient strength to indicate a causal link, i.e. that the local kinetics was determined by the selected aspect of the local structure. In a recent review [11], Ediger observed, "At present, it is an article of faith that something in the structure is responsible for dynamics that can vary by orders of magnitude from one region of the sample to another at T_g."

Instead of trying to directly address the question 'What aspect of the structure gives rise to the observed dynamic heterogeneity?', we will answer the related question, 'What aspect of the dynamic heterogeneity actually arises from the structure?' It is logically necessary to answer this question before attempting the first. As we show, it is also possible to answer the latter question without having to first identify the correct measure of the particle structure relevant to determining the subsequent dynamics.

The degree to which the liquid dynamics reflects a persistent influence of a configuration is related to the idea, introduced in Section 1.3, of the crossover between liquid-like and solid-like behaviour on cooling. One measure of this transition from the liquid to solid-like descriptions is the crossover temperature proposed by Goldstein in 1969 [81]. The crossover temperature marks the transition from the high-temperature liquid - where momentum transfer (as binary collisions and, collectively, in hydrodynamic modes) plays a dominant role - to the low-temperature liquid in which dynamics is said [82] to become 'landscape dominated', the landscape referring to the potential energy surface over the configuration space. The configuration space, in other words, has begun to break up into kinetically isolated domains.

We answer the question - 'what aspect of particle dynamics in a liquid is determined by the initial configuration?' - with the construction of a new measure of structure-related dynamics, which we term the *dynamic propensity.* The isoconfigurational method used to calculate the dynamic propensity, and the analysis of the resulting ensemble of runs, are the subject of this chapter.

The rest of this chapter is structured as follows. In Section 2.2 we describe the model glass-former and algorithms used in this work and introduce the general isoconfigurational ensemble method. We begin, in Section 2.3, by testing the reproducibility of the dynamics, and demonstrate that not all of it can have a structural origin. Then we introduce the dynamic propensity as a measure of structure-dependent particle dynamics, and show that this new dynamic quantity is also spatially heterogeneous. The effect of varying configuration and temperature is examined, and the convergence properties of the propensity are also discussed. In Section 2.4 we show that the variance in individual particle motion from run to run represents a new piece of dynamic information, and discuss the consequences of this 'intermittent' particle motion. And in Section 2.5 we demonstrate how the isoconfigurational ensemble method can be used to obtain insight into the process of relaxation by looking at correlations between particle motion within the same run and within different runs of the isoconfigurational ensemble. Finally, we summarise the key results of this work in Section 2.6, discuss their implications, and suggest some areas for further study.

2.2 Model and Algorithms

We consider a two-dimensional (2D) glass-forming liquid consisting of an equimolar binary mixture of particles interacting via purely repulsive potentials of the form

$$u_{ab}(r) = \epsilon \left[\frac{\sigma_{ab}}{r}\right]^{12} \tag{2.1}$$

where $\sigma_{12} = 1.0 \times \sigma_{11}$ and $\sigma_{22} = 1.4 \times \sigma_{11}$. All units quoted will be reduced so that $\sigma_{11} = \epsilon = m = 1.0$ where m is the mass of both types of particle. Specifically, the reduced unit of time is given by $\tau = \sigma_{11}\sqrt{m/\epsilon}$.

A total of $N = 1024$ particles were enclosed in a square box with periodic boundary conditions. The molecular dynamics simulations were carried out at constant number of particles, pressure and temperature using the Nosé-Poincaré-Andersen (NPA) algorithm developed by Laird et al. [83, 84]. See Appendix A for further details of this method. The use of constant NPT constaints allows one to compare systems with different composition and particle interactions, as we do in Part II. The pressure ($P = 13.5$), was chosen so that our results would be directly comparable to those of Weeks et al. [85] for the single-component soft-disk system. The 'masses' of the Anderson piston and Nosé thermostat were $Q_v = 0.0002$ and $Q_s = 1000$, respectively, for all temperatures. The equations of motion were integrated using a generalised

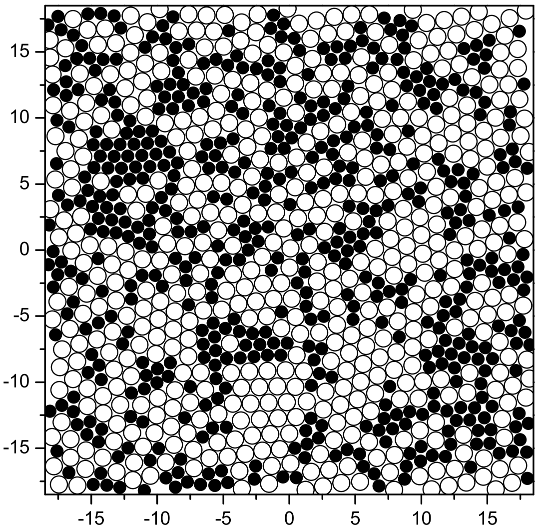

Figure 2.1: An equilibrated particle configuration at $T = 0.4$. The large and small particles are indicated by filled and open circles, respectively.

leapfrog algorithm [84], and are provided for 2D simulations in Appendix A. The time step employed was 0.05τ for $T > 1$, and 0.01τ for $T \leq 1$. For argon units of $\eta = 120k_B$, $m = 6.6 \times 10^{-23}g$ and $\sigma_{11} = 3.4\mathring{A}$, these time steps correspond to approximately 10 and 20 femtoseconds respectively.

The structural, dynamic and thermodynamic properties of this model glass-forming liquid have been characterised by Perera and Harrowell [44, 67]. For reference, the onset of the plateau region in the mean-squared displacement, and in the incoherent scattering functions, occurs near $T = 0.5$. The structural relaxation time and diffusion constants also have non-Arrhenius temperature dependence below $T = 0.55$. Together, these dynamic changes suggest the presence of at least two relaxation processes for $T \leq 0.5$.

All configurations investigated were equilibrated configurations taken from the study in ref. [67] and re-equilibrated with the NPA Hamiltonian. They represent amorphous stationary states in the sense that these states are stable over time scales at least an order of magnitude longer than the structural relaxation time and show no development of long-range correlations associated with established ordered phases. While the supercooled liquid state is strictly metastable, we will refer to such configurations as 'equilibrated'.

In this work we analyse correlations among the set of N-particle trajectories that pass through a given configuration. To generate this *isoconfigurational ensemble* of runs at a given temperature T, we start with a configuration that has been equilibrated at T and for each run randomly assign the initial particle momenta from the appropriate Maxwell-Boltzmann distribution. A representative configuration at $T = 0.4$ is shown in Figure 2.1.

2.3 The Spatial Distribution of Dynamic Propensity

We examine the reproducibility of the dynamic heterogeneities in the supercooled liquid. Figure 2.2 shows the particle displacement vectors following three different runs starting from the same configuration - plotted in Figure 2.1 - of an equilibrated liquid. The three runs differ only in the random assignment of particle momenta from the Maxwell-Boltzmann distribution at the appropriate temperature. Each run was carried out at a pressure $P = 13.5$ and a temperature $T = 0.4$, which is below the onset-temperature of two-step relaxation.

Each plot in Figure 2.2 exhibits the now familiar features of dynamics in deeply supercooled liquids: large variations in the particle displacements, clear clustering of the 'slow' particles, and aggregation of the more mobile particles, sometimes in 'string-like' features. What is striking is that the spatial arrangement of particle

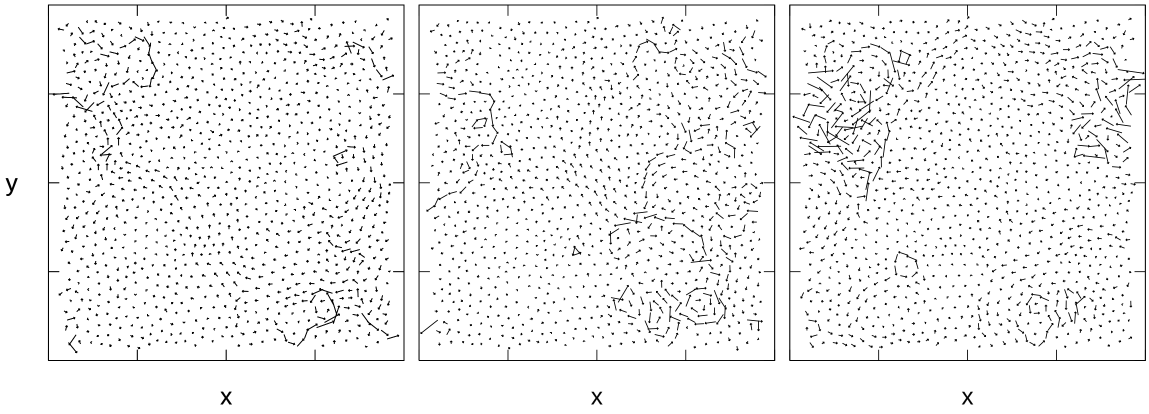

Figure 2.2: The particle displacements, indicated as vectors joining the initial to final particle positions, resulting from three MD runs of 1000τ at $T = 0.4$. All runs made use of the same initial configuration and differed only in the assignment of initial momenta to particles.

displacements differs markedly from plot to plot. While some particles exhibit a mobility that is reproducible from run to run, the dynamics of other particles varies substantially. We conclude that not all the dynamics can be determined by the initial configuration.

The variation in an individual particle's motion from run to run provides additional insight into the relationship between structure and dynamics. We explore this further in Section 2.4.

Now consider the possibility that there is no correlation at all between an initial configuration and the subsequent particle dynamics. In this case, each particle's squared displacement, averaged over many trajectories with the same initial configuration, would be the same as that of every other particle of the same species. This conclusion arises from the fact that the only point of connection between the different trajectories is the common initial configuration. It follows, therefore, that the magnitude of variation between the trajectory-averaged squared displacements of different particles of the same species is sufficient to establish the degree to which the initial configuration determines the dynamics.

To this end, we introduce the *isoconfigurational ensemble* consisting of N_{runs} separate simulation runs over a fixed time interval, all starting from the same particle configuration but with momenta randomly assigned from the Maxwell-Boltzmann distribution at the appropriate temperature. (Note that Doliwa and Heuer [86] have used multiple trajectories from a single configuration at *different* temperatures to establish the Arrhenius character of transitions between metabasins.) Let $f_i(\Delta r)$ be the ensemble distribution of the displacement of particle i over the fixed time interval. These distributions represent the ensemble characterisation of each particle's capacity for movement from a specific initial configuration. They are also invariant to time reversal. We shall refer to the second moment of $f_i(\Delta r)$, i.e. the ensemble mean of the squared displacement of particle i, $< \Delta r_i^2 >_{ic}$, as the *dynamic propensity* of particle i in the given initial configuration. The expression $< \cdots >_{ic}$ indicates an average over the isoconfigurational ensemble. We stress that 'propensity' as defined here should not be associated with the actual equilibrium distribution of trajectories that pass through a point in configuration space, since in constructing the propensity we have not taken into account the correlation between a particle's momentum and either the potential energy of that particle or the force acting on that particle.

To compare propensities from different temperatures T, we set the run time for a

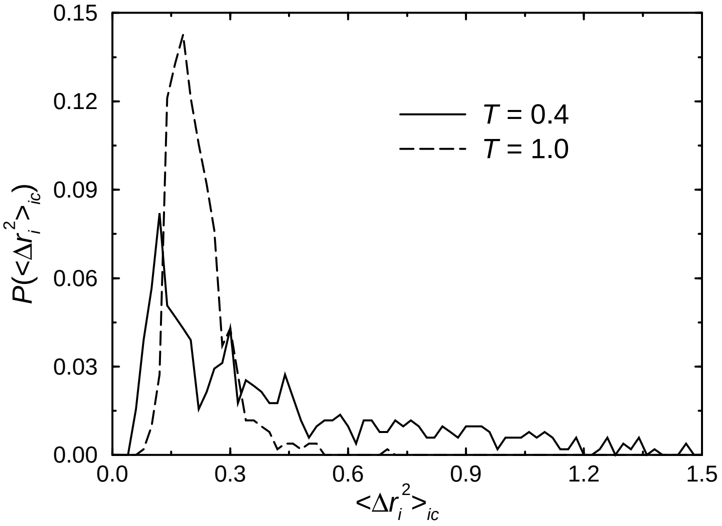

Figure 2.3: The distribution of small-particle propensities calculated using 1000 runs for single configurations at $T = 0.4$ and 1.0. Note the increase in width with increasing supercooling.

given trajectory to be 1.5 times the structural relaxation time τ_e (τ_e is defined in terms of the intermediate incoherent scattering function $F(k,t)$ such that $F(k_{max}, \tau_e) = 1/e$, where k_{max} is the wavevector of the Bragg peak and $e = 2.7183$, the base of the natural logarithm). This run interval was chosen to maximise the observed dynamic heterogeneities. If one was to choose run times much shorter or longer the dynamic heterogeneities would be unobservable - since they represent only a transient phenomenon - and all discussion of their relationship to structure would be obsolete.

Figure 2.3 shows the distribution of propensities for the small particles for configurations at $T = 1.0$ and 0.4, averaging over 1000 runs at each temperature. The width of the distribution increases substantially on cooling. As argued above, this increase in the range of the propensity distribution on cooling can only be the result of the increasing degree to which particle configurations determine the subsequent dynamics. With this result we can now replace the 'act of faith' of ref. [11] with the explicit demonstration of the heterogeneity of particle *propensities*, a feature that is completely determined by the initial configuration.

To visualise the spatial distribution of the propensity, it is useful to first remove the additional complexity of the configuration and use contour plots that contain no information about the location of individual particles. Any suitable graphing program can be used to generate a contour plot from regularly spaced data. In our case the

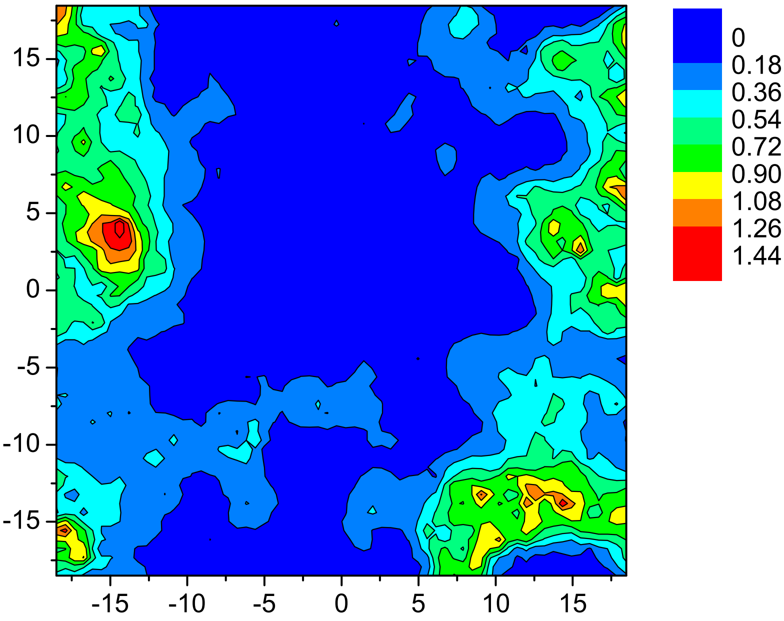

Figure 2.4: The spatial distribution of propensities at $T = 0.4$, calculated using 100 runs.

data points are generally located at irregularly spaced coordinates, namely the particle coordinates, so it is necessary to interpolate them. We found the modified version of Shepard's method [87] that is built into Origin [88] a useful algorithm for obtaining good fits to the data without introducing erroneous peaks and valleys. Interpolation parameters of 6 and 6 worked well. The occasional inconsistencies introduced by the interpolation near the periodic boundaries could be removed by fitting to a set of coordinates containing additional periodic images.

The spatial distribution of dynamic propensity for the same $T = 0.4$ configuration used in Figure 2.2 is mapped in Figure 2.4. Note the substantial spatial heterogeneity. There is a large sea of low propensity populated by islands of high propensity. On comparison of the propensity map with the individual trajectory maps, we find that the domains of high propensity are generally more compact than the often 'string-like' clusters of large displacements observed in individual trajectories. This suggests that the occasional string-like motion that is observed does not generally have a structural origin but rather must be the result of how mobility is transferred through the system. The comparison between particle trajectories and the propensity map also demonstrates that, as expected, motion occurs predominantly in regions of high propensity. We therefore conclude that the development of spatially heterogeneous dynamics in this glass-former is due to the increasing influence of microscopic variations in structure on the motion of particles in the supercooled liquid.

An interesting question that arises is whether or not the local peaks in propensity represent 'defects'. We stress that the peaks indicate those particles with the highest average mobility over the runs examined, and may therefore not be the initiators of motion but rather some essential path through which relaxation is propagated. The propensity can provide only limited insight into the actual process of relaxation since it is the overlap of the individual relaxation processes. Other analyses of the isoconfigurational ensemble, however, can provide some insight into relaxation, e.g. the analysis of correlations between particle motion within the same run and within different runs. This is discussed further in Section 2.5.

2.3.1 The Increasing Heterogeneity upon Cooling

Because we are effectively probing single configurations, there will be variation in the spatial structure and degree of heterogeneity from run to run. We therefore study the effect of varying both the configuration and the temperature on the shape and spatial variation of the resulting propensity distribution. We generated ten configurations each at $T = 0.4$, 0.46, 0.5, 0.55, 0.6, 0.8 and 1 and calculated the propensities. The propensities were averaged over 100 runs, and the configurations were separated by $75\tau_e$ to ensure that they were significantly different from each other. The run time was kept constant at $1.5\tau_e$ for all temperatures. As a result, the run time ranged from 1000τ at $T = 0.4$ to 1.155τ at $T = 1$.

Table 2.1: Characteristic times for the 2D glass-former. τ_e is the structural relaxation time and t^* is the time at which the non-Gaussian parameter $A(t)$ (see text) reaches a maximum. The run times used to calculate the propensity have also been listed.

T	τ_e	run time	t^*
0.4	673	1000	200
0.46	51.7	76.8	65
0.5	13.6	20.2	32
0.55	4.31	6.4	16
0.6	2.91	4.32	8.5
0.8	1.19	1.77	3.5
1	0.775	1.155	1.4

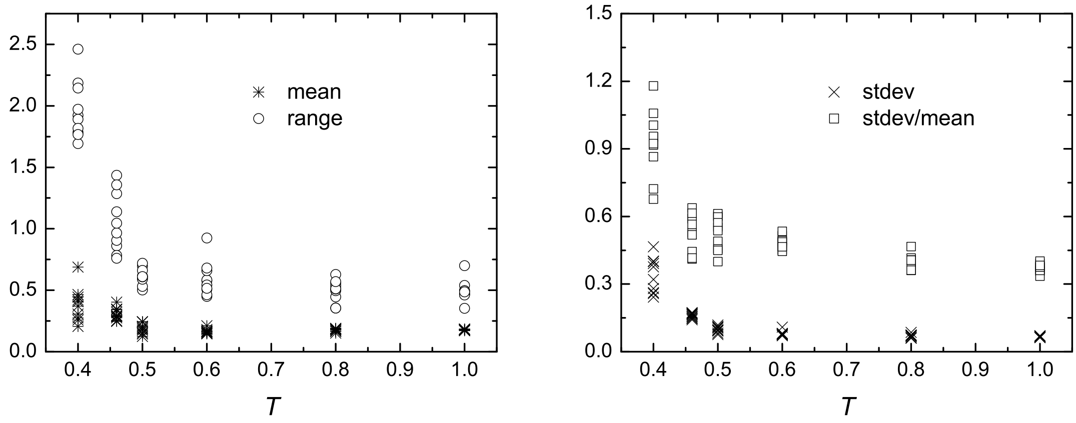

Figure 2.5: The mean, range, standard deviation (stdev) and the ratio stdev/mean for the propensity distributions calculated for ten configurations each at $T = 0.4$, 0.46, 0.5, 0.6, 0.8, and 1. At each temperature, the configurations were separated by $75\tau_e$ from each other, and the propensities were averaged over 100 runs of $1.5\tau_e$. Note the different y-axis scales.

We note that any choice of time scaling as a function of temperature is somewhat arbitrary given that different characteristic times can be chosen that scale differently with temperature. Another characteristic time that has previously been used [46] to study dynamic heterogeneities is the time t^* at which the non-Gaussian parameter $A(t)$ reaches a maximum (see Section 5.3.3 for the definition of $A(t)$). In Table 2.1 we list t^*, τ_e and the run time used to define the propensity as a function of temperature for our model glass-former, i.e. $1.5\tau_e$. The values of τ_e were taken from ref. [44] and t^* was calculated from data in ref. [89]. Note that t^* and τ_e scale quite differently. From a similar value at $T = 1$, t^* initially increases more rapidly with cooling. Later, τ_e increases more rapidly, until at $T = 0.4$ $\tau_e > 3t^*$. We note that at $T = 0.4$ the run time of 1000τ is several times longer than t^*; therefore the maximum heterogeneity in the propensity at $T = 0.4$ may well be larger than what we calculate here.

In Figure 2.5, we compare the mean, range, standard deviation (stdev) and the ratio stdev/mean for the propensity distribution calculated for each configuration. The most obvious change is a rapid increase in the range and standard deviation below $T = 0.5$, with the mean showing a smaller increase at low temperature. These changes are accompanied by an increase in the variation between different isothermal configurations, however a clear trend with change in temperature can still be distinguished. We conclude that below $T = 0.5$, there is a strong increase in the effect that

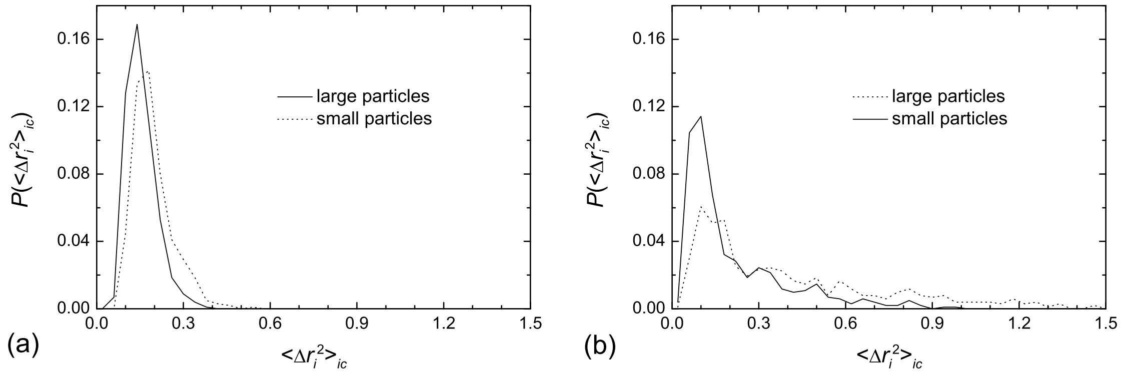

Figure 2.6: The propensity distributions over small and large particles for selected configurations at (a) $T = 1$ and (b) $T = 0.4$. The propensities were averaged over 100 runs of $1.5\tau_e$.

the structure has on the dynamics, and also in the effect that *fluctuations* in structure, both within and between different configurations, have on dynamics. In other words, the particle motion becomes increasingly sensitive to differences in structure.

In Figure 2.6 we plot the propensity distributions separately for small and large particles for individual configurations at $T = 0.4$ and 1. At $T = 1$ the distributions are very narrow and quite similar for both particle species, but as the temperature decreases the distributions become more spread out and the small and large particle distributions become less similar. The distributions still overlap, but on average the small particles have higher propensity than the large ones. This association between species type and propensity is discussed further in Section 3.2.1.

A change in temperature or configuration also affects the spatial variation of propensity. The propensity maps for four configurations at $T = 0.4$ are shown in Figure 2.7. As expected, the distribution of high and low propensity regions varies significantly from plot to plot. Particles that have low propensity in one configuration have high propensity in the next and vice versa, suggesting that sufficient change in structure has taken place to affect large changes in the spatial distribution of propensity. In Section 3.18 we present further analysis and discussion of the timescale over which structural changes affect the spatial distribution of mobility. Also note that although the mean propensity varies between configurations, i.e. some configurations are more mobile than others, their propensity distributions all have a high degree of spatial heterogeneity.

For comparison, Figure 2.8 shows the spatial distribution of propensity for selected

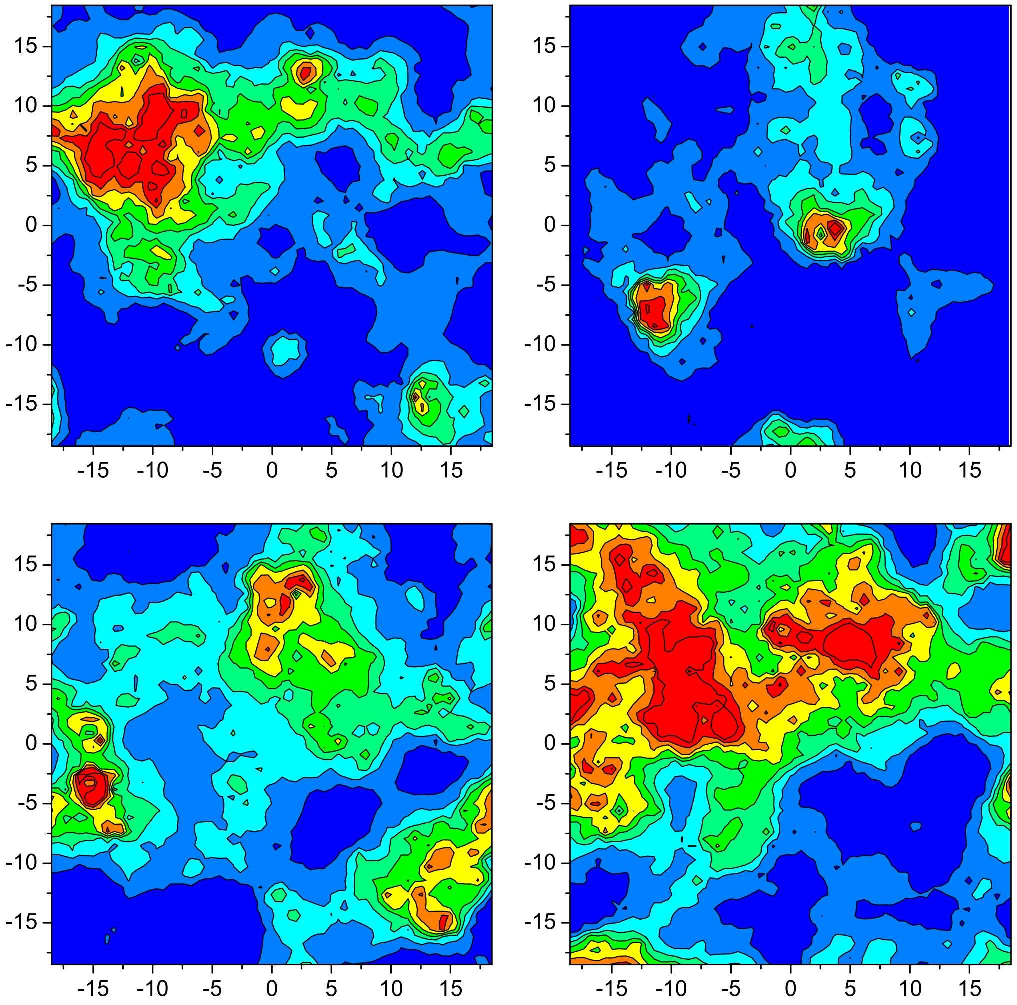

Figure 2.7: The spatial distribution of propensities at $T = 0.4$ for four configurations separated by $75\tau_e$. The propensities were averaged over 100 runs, and the scale is the same as in Figure 2.4.

configurations at $T = 0.46$, 0.5, 0.6 and 1. In order to observe the spatial variation at these higher temperatures, we have used different propensity scales than in Figures 2.4 and 2.7. Although the propensity range is similar for $T = 0.5$–1, there is a clear increase in spatial variation as the temperature is reduced (mainly due to an increase in the population of the extremes of the distribution), with further large increases at $T = 0.46$ and again at $T = 0.4$ (both of these mainly due to an increase in the width of the distribution).

There also appears to be an increase in the clustering of particles with similar mobility below $T = 1$. To better quantify this, we consider the aggregation of high

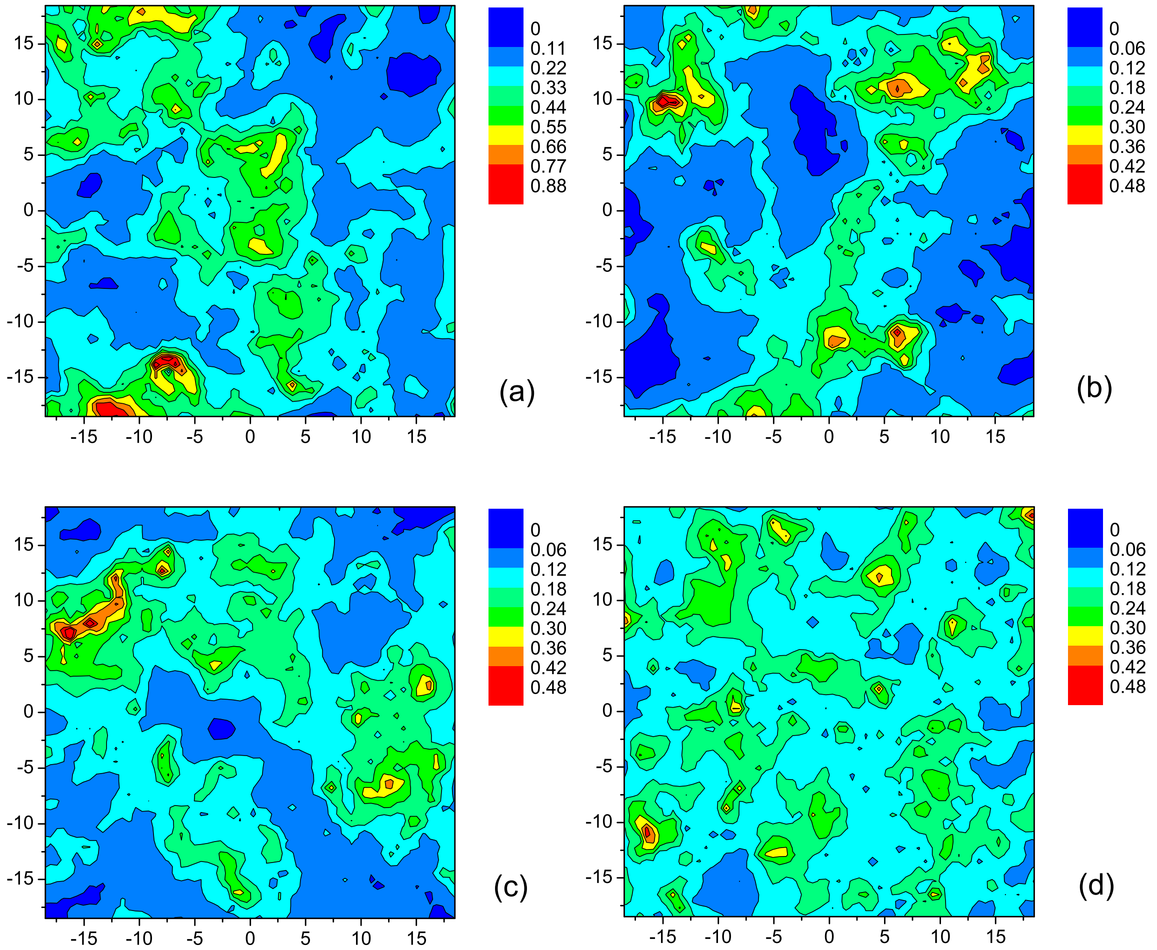

Figure 2.8: The spatial distribution of propensity for selected configurations at (a) $T = 0.46$, (b) $T = 0.5$, (c) $T = 0.6$, and (d) $T = 1$; where the propensities were averaged over 100 runs. Note the different propensity scales.

propensity particles using a cluster analysis that is described in general terms in Section 3.2.2. Basically, for each configuration we select the 10% of particles with the highest propensities and assign them to clusters depending on whether they are a nearest neighbour to another particle already in a cluster. When all particles have been assigned to clusters, we count the total number of clusters and the variance in cluster size, and use these two quantities to characterise the degree of spatial clustering. Figure 2.9 shows the results of the cluster analysis for ten configurations each at $T = 0.4$, 0.5, 0.6, 0.8 and 1. While there is considerable variation in the clustering of high propensity particles between different isothermal configurations and overlap between data points from different temperatures, it is clear that, on average, particles with high propensity cluster together more as the temperature is reduced.

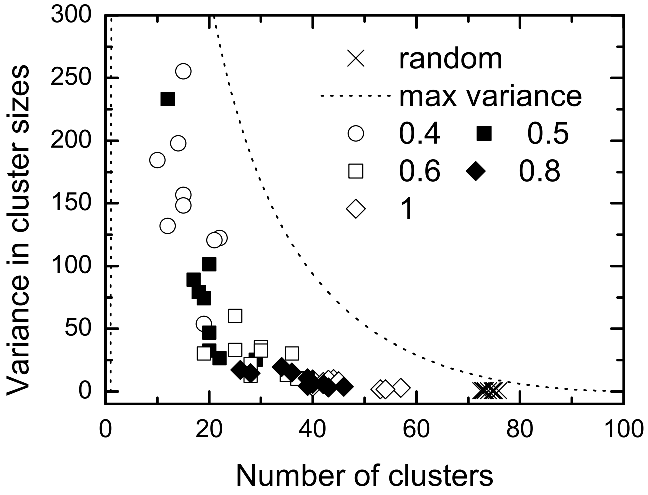

Figure 2.9: Cluster measures of spatial heterogeneity for particles with propensities in the top 10%. Data points are shown individually for ten configurations each at $T = 0.4$, 0.5, 0.6, 0.8 and 1. Statistics obtained using random values are shown for comparison. The dotted line represents the maximum variance possible for a given number of clusters (see text for more details).

In summary, we have established three ways in which the spatial heterogeneity of propensity increases upon cooling: (i) through a gradual increase in the clustering of particles with similar propensity, (ii) through an increase in the population of the extremes of the propensity distribution, and (iii) through a rapid increase in the range of the propensity distribution below $T = 0.5$. We also observed increasing variation between different isothermal configurations as the temperature was reduced. We therefore conclude that as the binary soft-disc liquid is cooled, variations in structure become increasingly important for the dynamic properties of the glass-former.

2.3.2 Statistical Convergence and Reliability

The need for the propensity as a measure of structure-related dynamics is directly due to the large difference in particle displacements from run to run, as discussed above. Given this high variability in particle motion, it is sensible to consider how the size of the isoconfigurational ensemble affects the propensity distribution and the comparisons that can meaningfully be made. In this section we investigate the uncertainty in the propensity distribution as a function of the number of runs, and discuss the practical consequences of our results.

The uncertainty in the propensity (mean squared displacement) of particle i is

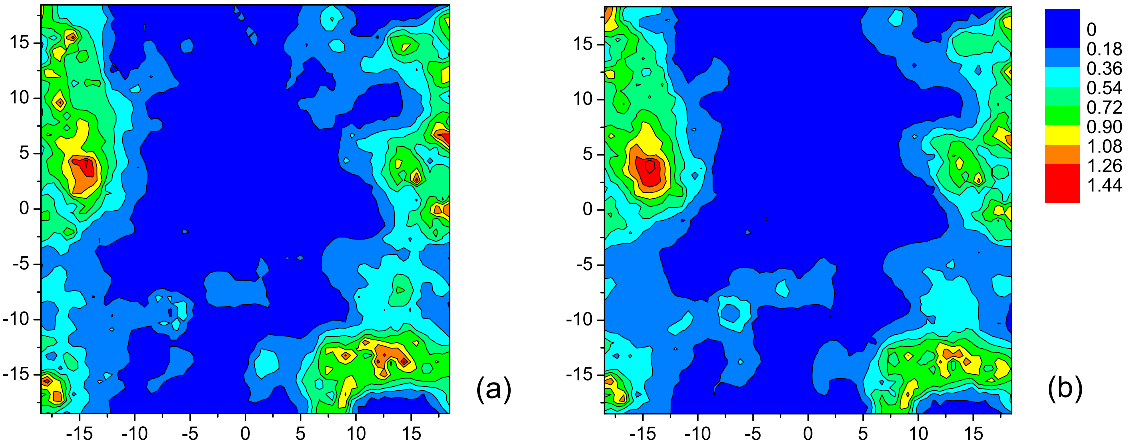

Figure 2.10: Convergence of the spatial distribution of propensity as a function of the number of runs for a configuration at $T = 0.4$. The propensities were calculated using (a) 50 runs and (b) 1000 runs. Note that there is little difference in the coarse grained spatial variation between the two plots.

measured by the standard error $\sigma_i/\sqrt{N_{runs}}$, where N_{runs} is the total number of runs and $\sigma_i = \sqrt{< \Delta r_i{}^4 >_{ic} -(< \Delta r_i{}^2 >_{ic})^2}$ is the standard deviation in the squared displacement distribution for particle i. Hence, the standard error decreases as a function of $1/\sqrt{N_{runs}}$, and the number of runs needed to further reduce the uncertainty increases rapidly. While this means that it takes many runs to reduce the uncertainty in a single propensity - for example after 200 runs some particles at $T = 0.4$ still have relative uncertainties of 60% - we find that both the shape of the total propensity distribution and its coarse-grained spatial variation converge far more rapidly.

In Figure 2.10 we compare the spatial distribution of propensity averaged over ensembles of 50 and 1000 runs for the same configuration at $T = 0.4$. Although there are minor differences between the two plots, it is clear that the coarse grained spatial variation has already converged by 50 runs, i.e. it is possible to distinguish all the regions of high, low and intermediate propensity after only 50 runs. We also find that it takes only 100 runs, at both $T = 0.4$ and $T = 1$, for the standard deviation of the total propensity distribution to converge to within 2% of the extrapolated limit at infinite number of runs. We therefore conclude that ensembles of 100 runs are large enough to determine the spatial distribution of propensity with a high degree of confidence.

To investigate the convergence of the individual propensities in more detail, we define the relative uncertainty in the propensity at the 95% confidence level and

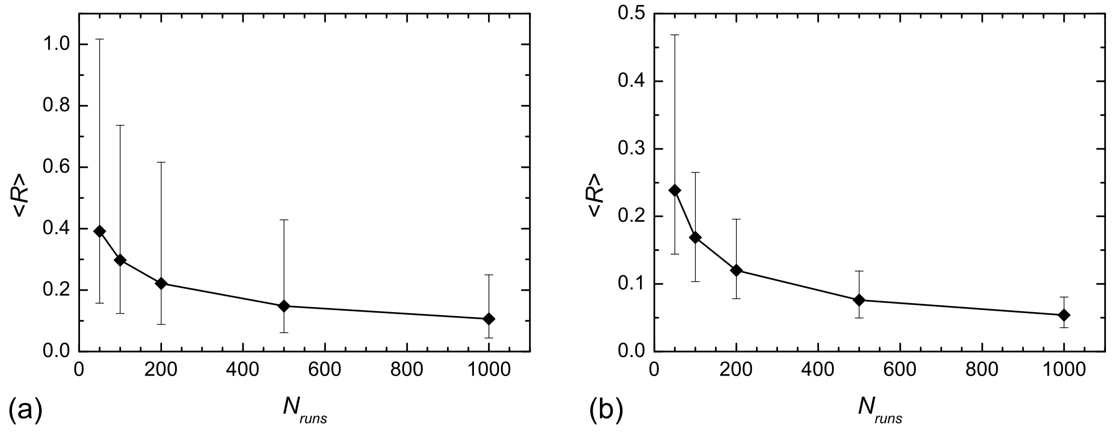

Figure 2.11: Convergence of the relative uncertainty in the propensity R (see Eq. 2.2) as a function of the total number of runs N_{runs} for configurations at (a) $T = 0.4$ and (b) $T = 1$. The error bars indicate the range of R values at a given number of runs, and the curve joins the mean values of R, where the average is taken over particles.

study its convergence as the number of runs increases. The $P\%$ confidence interval is defined as the interval in which there is a $P\%$ chance of finding the true population mean. To calculate the confidence interval for the propensity one should strictly use the two-sided Student's t-distribution [90] since the population mean and variance are unknown. However, in practice we find that the sample size, i.e. the number of runs, is sufficiently large that we can use the normal distribution instead (note that Student's t-distribution converges to the normal distribution as the sample size increases). The relative uncertainty R_i in the propensity of a particle i at the 95% confidence level as a function of the number of runs is therefore given by

$$R_i(N_{runs}) = 1.649\frac{\sigma_i}{\sqrt{N_{runs}}} / < \Delta {r_i}^2 >_{ic} \tag{2.2}$$

where $< \Delta {r_i}^2 >_{ic}$ is the propensity of particle i and N_{runs} is the number of runs used to calculate the propensity. The normal and t-distributions can also be used to test whether the difference in propensity between two particles is significant or not.

In Figure 2.11, we plot the mean uncertainty $< R >$ (averaged over particles) as a function of the total number of runs for configurations at $T = 0.4$ and $T = 1$. The error bars indicate the range of R_i values at a given N_{runs}. At $T = 0.4$ [plot (a)], we find that while $< R >$ has decreased to about 0.2 (i.e. 20%) after 200 runs, the maximum value decreases much slower, e.g. there are still some particles with $R_i = 0.6$. By 1000 runs $< R >$ has decreased to 0.1, but the largest relative uncertainties are still around 25%. In comparison, the uncertainty decreases much faster at $T = 1$ [plot (b)]. After 200 runs $< R >= 0.12$ and the maximum uncertainty is about 20%, and by 1000 runs $< R >= 0.06$ and the maximum is around 8%.

We therefore conclude that it is difficult to compare propensities that are similar in magnitude. How similar depends on how many runs one is willing to wait for, e.g. at $T = 0.4$ it will be rather impractical to compare propensities that are within 25% of each other. The reason why the *spatial* distribution of propensity converges far more rapidly is that the difference between high and low propensities, i.e. the range of the propensity distribution, is generally much larger than the mean. In fact, as shown in Figure 2.5(a), the range increases rapidly relative to the mean below $T = 0.5$. If this rate is faster than the rate at which the uncertainty in the propensity increases, which it appears to be, then the spatial distribution of propensity should converge even more rapidly at lower temperatures. It is an attractive idea that this may make propensity calculations practical at deeper supercoolings than we have studied here.

2.4 The Increasing Variance of the Individual Particle Motion

The variation in an individual particle's mobility between runs not only affects the convergence properties of the propensity, but represents another area where analysis of the isoconfigurational ensemble can provide new insight, this time into the *manner* in which the configuration influences the dynamics. To illustrate what we mean by this it is useful to consider that the same spatial distribution of propensity could be produced in many different ways. For example, a particle could move the same amount in every run, or its mobility could vary strongly from run to run, without necessarily changing its mean-squared displacement, i.e. its propensity. The shape of the displacement distribution therefore contains additional information about how the structure affects dynamics.

The increasing variation in particle mobility between runs, which we investigate here, indicates that there is considerable randomness or noise in the manner in which the configuration influences the dynamics at low temperature. We argue that this could be interpreted in terms of stick-release events. While there is a higher probability of a release event occurring in a high propensity region, both high and low propensity regions are capable of sticking the particles, i.e. not allowing them to move in a given run. In other words, the configuration expresses its character intermittently.

The results in this section provide: (i) the reason why the propensity is needed to characterise the effect of structure on dynamics; (ii) physical information on the process by which the configuration influences the dynamics; and (iii) a view of dynamics that is consistent with recent experiments describing the intermittency of relaxation events in colloidal clays.

2.4.1 Variance versus Propensity

We quantify the variation in the ith particle's mobility between different runs using the standard deviation, σ_i, of the propensity, where $\sigma_i = \sqrt{< \Delta {r_i}^4 >_{ic} -(< \Delta {r_i}^2 >_{ic})^2}$. As shown in Figure 2.12, σ_i at $T = 0.4$ is significantly larger relative to the propensity $< \Delta {r_i}^2 >_{ic}$ than one would have expected from a continuum random walk in 2D. The inset shows the same results at $T = 1$.

To understand the significance of this finding we provide some background information. Freely diffusing particles in a liquid can be modelled as a continuum random

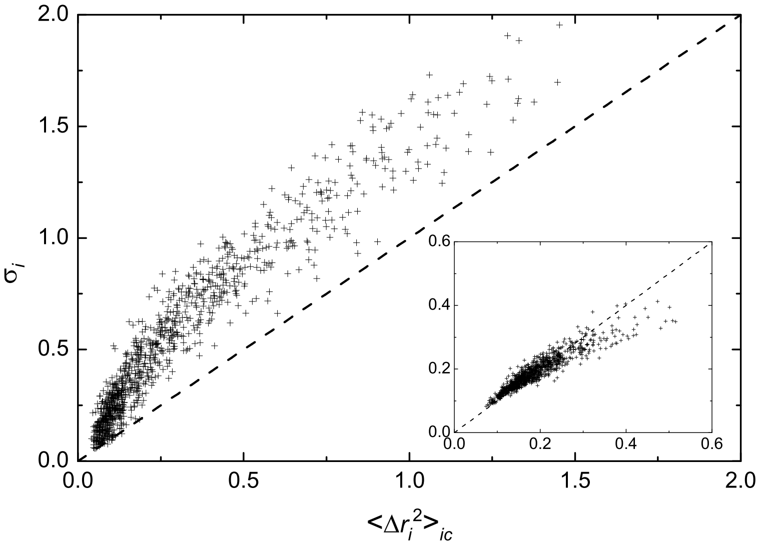

Figure 2.12: A scatter plot of the standard deviation σ_i (calculated over 1000 runs at $T = 0.4$) of the squared displacement of each particle plotted against its propensity. The inset shows the same data obtained for a configuration at $T = 1$. Note the difference in scale. The dashed line is the expected relation for a 2D random walk where each point along the line can be interpreted as arising from a different value of the diffusion constant.

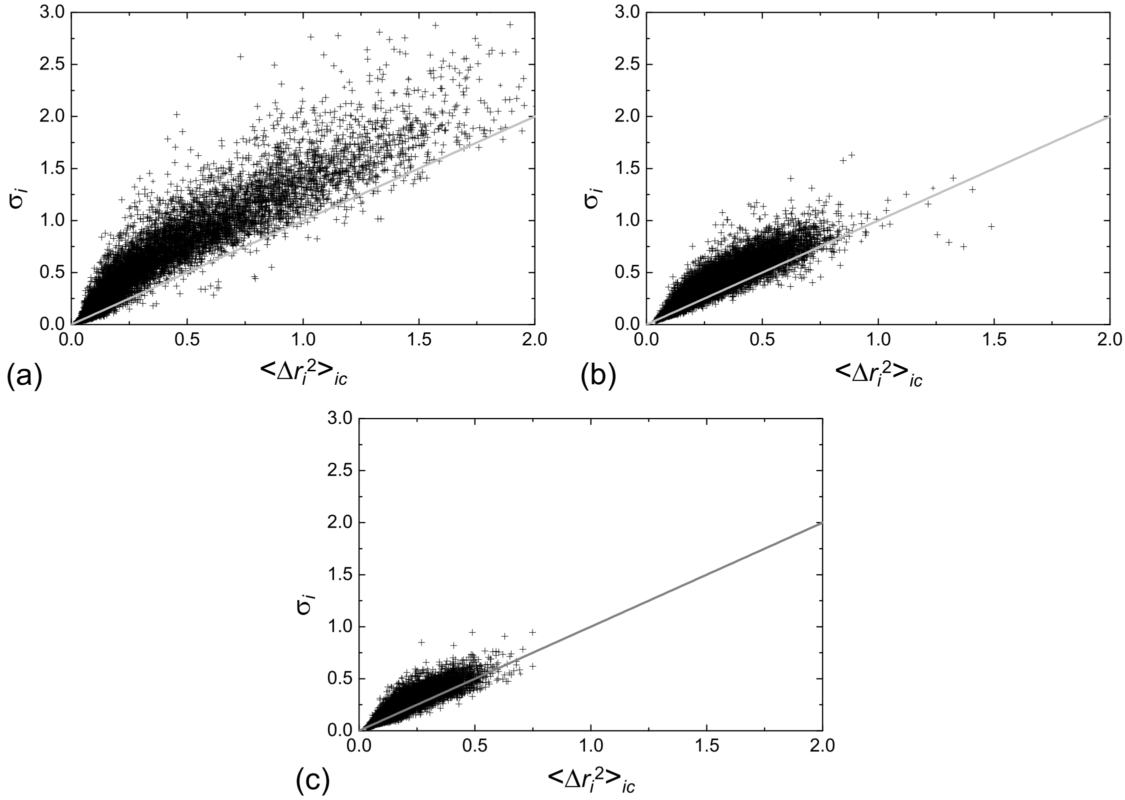

Figure 2.13: A scatter plot of the standard deviation σ_i of the squared displacement of each particle plotted against its propensity for ten configurations each at (a) $T = 0.4$, (b) $T = 0.46$, and $T = 0.5$. All quantities have been calculated using ensembles of 100 runs, and the solid grey line is the expected relation for a 2D random walk where each point along the line can be interpreted as arising from a different value of the diffusion constant.

walk. After a large number of independent steps in the random walk, i.e. after a time that is long compared to the mean collision time in the liquid, the particle's position will be given by a probability distribution that is equal to a normal distribution [91]. The isoconfigurational distribution of particle displacements for each particle in the 2D binary mixture should therefore be given by a normal distribution if the particle motion can be described by simple diffusion. In 2D the standard deviation and mean of a normal distribution are equal. Therefore each point along the line of slope equal to one in Figure 2.12 can be interpreted as arising from a different value of the diffusion constant. Hence, our results indicate that at low temperature the heterogeneity in the propensity cannot be described simply by a scenario in which particles are undergoing simple diffusion, but with different diffusion constants.

We investigate the relationship between the variability in particle motion, as measured by σ_i, and the propensity as a function of temperature and configuration. Figure 2.13 shows the relationship between σ_i and the particle propensity for ten configurations each at $T = 0.4$, $T = 0.46$ and $T = 0.5$. All quantities were calculated using ensembles of 100 runs. The data points at $T = 0.4$ show greater scatter compared to the results in Figure 2.12, partly due to the greater convergence of the variance and propensity in Figure 2.12 where these quantities were calculated over 1000 runs, and partly due to some variation from configuration to configuration. There is, however, a clear increase in variability below $T = 0.5$. At $T = 0.5$ the majority of data points are still clustered around the expected relation for a 2D random walk. The change in the variability of particle motion is therefore a strong characteristic of the change in dynamics as the liquid is supercooled.

We conclude that the increasingly large variation, upon supercooling, in an individual particle's movement from run to run represents an important piece of kinetic information, distinct from the propensities and their spatial distribution.

2.4.2 The Single Particle Non-Gaussian Parameter

The large variances of the individual particles are typically associated with highly asymmetric $f_i(\Delta r)$ distributions, with a peak at a low value of Δr and a long tail extending to large displacements, as shown in Figure 2.14 for a representative particle at $T = 0.4$.

This asymmetry can be quantified as a deviation from a Gaussian form through the use of a non-Gaussian parameter α_i for particle i given by

$$\alpha_i = \frac{< \Delta {r_i}^4 >_{ic}}{2(< \Delta {r_i}^2 >_{ic})^2} - 1 \tag{2.3}$$

The quantity α_i equals zero for a Gaussian distribution. The α_i distributions for configurations at $T = 1.0$ and 0.4 are plotted in Figure 2.15. While all the individual $f_i(\Delta r)$ distributions are close to Gaussian at high temperature, the supercooled sample exhibits a broad distribution of α_i values with most particles exhibiting a significantly non-Gaussian distribution of displacements.

Note that this non-Gaussian parameter is quite distinct from that discussed previously in the context of supercooled liquids [74, 92]. The α_i introduced here refers to the variety of displacements achieved by a *single* particle over the ensemble of

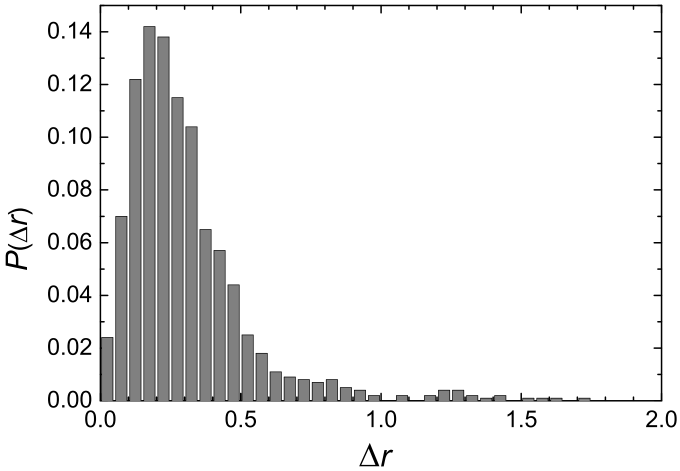

Figure 2.14: The distribution of particle displacements, $f_i(\Delta r)$, over an isoconfigurational ensemble of 100 runs for a single particle at $T = 0.4$. Note the highly asymmetric and non-Gaussian shape of the distribution.

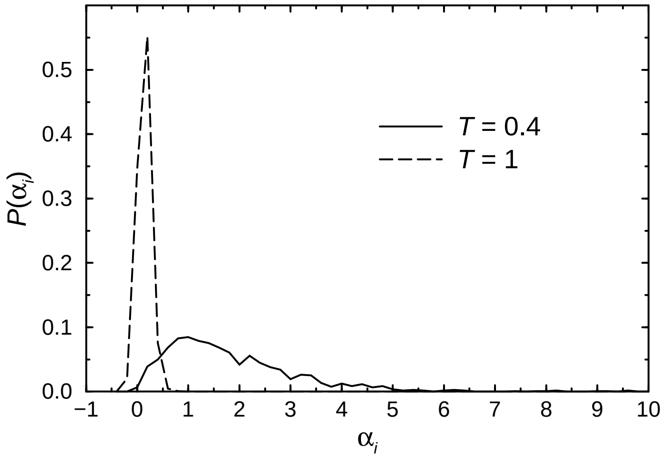

Figure 2.15: The distribution of single particle non-Gaussian parameters α_i (see Eq. 2.3) for configurations at $T = 0.4$ and 1.0, calculated using ensembles of 1000 runs.

trajectories, as opposed to the variety of displacements achieved by *different particles* in a single trajectory. In the language of the jump model of particle motion [93], the propensity characterises the average waiting time and jump length, while the non-Gaussian character of the $f_i(\Delta r)$ distributions is a result of either displacement correlations between successive jumps and/or non-Poisson statistics for the number of jumps within the observation time. We explore this question further in the next section.

2.4.3 The Jump Model of Particle Motion

We investigate the origin of the non-Gaussian character of the $f_i(\Delta r)$ distributions in terms of the jump model of particle motion [93]. In particular, we define a jump, compare the propensity to the average waiting time, and investigate whether the number of jumps per run can be described by a Poisson distribution. This analysis is incomplete as we do not study temperatures below $T = 0.5$, where the variability in particle dynamics changes most dramatically. Instead, it serves as a useful introduction to some conceptual views of dynamics in supercooled liquids and the methods by which they can be investigated.

The dynamics in supercooled alloys is often discussed in terms of ‘caging’ and the ‘escape’ from the cage. In this picture the plateau that develops in the intermediate scattering function upon supercooling (see Section 1.2) is ascribed to particles being trapped in the cage formed by their neighbours. The scattering function only starts to decay again once particles begin to escape from this cage. It is this picture of diffusive motion via large discrete jumps, between which the atoms oscillate as in a solid, that has inspired the jump model and large number of similar models and simulations (see, for example, refs. [94,95]). The common assumption is that jumping is the main process that explains the dynamics. Starting, generally, from a random walk, the anomalous diffusion is then incorporated via a distribution of waiting times or jump lengths.

Now imagine the simple scenario in which the waiting time, for a given particle, is the same for every jump. Then the resulting distribution of jumps per run should be given by a Poisson distribution (see Eq. 2.4 on page 41). Conversely, if the distribution of jumps per run is not Poisson distributed, then the waiting time cannot be the same for every jump. In this conceptual framework, the non-Gaussian character of the $f_i(\Delta r)$ distributions must be due to either displacement correlations between successive jumps or a tendency for mobile particles to continue being mobile, i.e. waiting times that are smaller for successive jumps. For this reason, we investigate whether the number of jumps per run can be described by a Poisson distribution.

To study the particle dynamics in this context, we first need to define a jump length. Ideally this jump length will maximise the amount of non-vibrational motion that is captured while minimising the amount of vibrational motion that is measured. One possibility is to define each jump individually using a relative criterion, where for each particle a jump is defined as motion that is of large amplitude relative to short-time (vibrational) fluctuations in position. This method has been used to study motion in a Lennard-Jones (LJ) glass-former below T_g [95]. However, it appears unlikely that this method will be suitable for the present system. We are interested in motion that occurs above the glass transition, and it is not obvious that there will be a clear distinction between vibrational and non-vibrational motion. Even for the LJ glass studied in ref. [95], near T_g the amplitude of short-time fluctuations (0.14–$0.16u$) is not much smaller than the smallest (reversible) jumps ($0.2u$). A different jump criterion that has been used involves defining a minimum hopping distance [96, 97]. This criterion should provide us with sufficient dynamic information for the present question. Provided that we choose a distance that means that the local environment of the particle must have changed, this should be large enough that successive jumps or moves are statistically independent in time and direction for a normal liquid.

In this work we define a 'move' as occurring when a particle has moved a distance of R_{move} from its previous position. We choose $R_{move} = 1$ for all particles. Perera and Harrowell found that this distance maximised the degree of spatial segregation of the dynamics in the present glass-former when it was used to define a local relaxation time [44]. Values of 0.5 and 0.7 were also investigated, but appear to capture much vibrational motion. Single configurations at $T = 0.5$ and $T = 1$ were investigated using 1000 runs of $1.5\tau_e$ and 100 runs of 100τ at each temperature. We note that additional analysis below $T = 0.5$ would be interesting since the variability of particle motion increases rapidly below this temperature.

We consider the number of moves per run k for each particle, and define p as the probability of 'moving' into a new position in a given time interval. By increasing the number of time intervals N per run we can make p arbitrarily small. If p is the same for every move, then the distribution of moves per run $P(k)$ should be given by a Poisson distribution, i.e. we expect

$$P(k) = \frac{a^k}{k!} e^{-a} \tag{2.4}$$

where k is the number of moves per run, and $a = Np$ is the mean value of k

We define $f_i(k)$ as the distribution of the number of moves per run for particle i. To quantify how far this distribution deviates from Poisson we define a non-Poisson parameter as $nonP = u_2/u_1 - 1$, where $u_n = \sum_i (k_i - <k>)^n$ is the n-th central moment of the the $f_i(k)$ distribution. For a Poisson distribution $nonP$ will equal

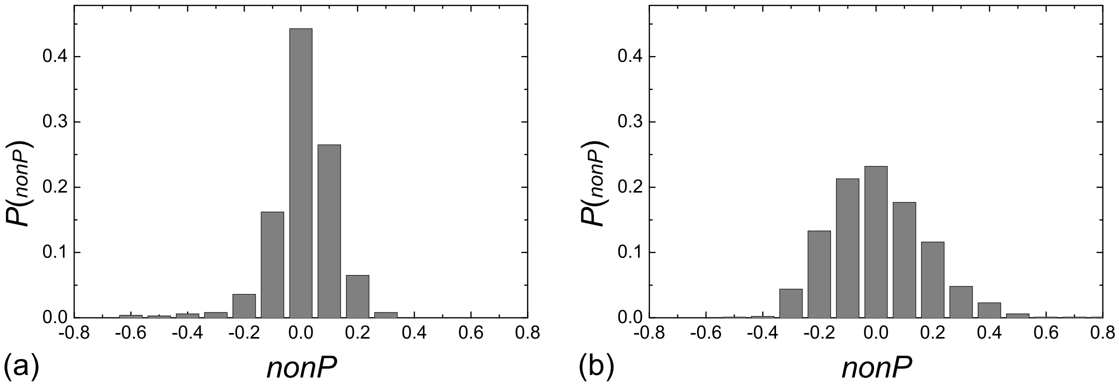

Figure 2.16: The distribution of non-Poisson parameters $nonP$ (see text) for particles in a configuration at $T = 0.5$. The distributions were calculated using (a) 1000 runs of duration $1.5\tau_e = 20.2\tau$, and (b) 100 runs of duration 100τ each.

zero, since $u_1 = u_2 = a$. To calculate an unbiased estimator for $nonP$ we use k-statistics [98], i.e. we calculate

$$nonP = \frac{k_2}{k_1} = \frac{\frac{n_{runs}}{n_{runs}-1} m_2}{\mu} \tag{2.5}$$

where k_n is the n-th k-statistic, n_{runs} is the total number of runs (i.e. the sample size), $m_2 = \frac{1}{n_{runs}} \sum_{i=1}^{n_{runs}} (k_i - \mu)^2$ is the sample variance, and $\mu = u_1$ is the sample mean.

The results are plotted in Figures 2.16 and 2.17. At $T = 0.5$, most individual particles have $P(k)$ distributions that are approximately Poisson distributed ($-0.4 \leq nonP \leq 0.4$ for most particles) for both choices of run length. At $T = 1$ we obtain similar results, although the longer 100τ runs have $nonP$ values that range from -0.6 to -0.2 rather than being centered about 0. The fact that we get Poisson statistics for the number of moves per run tells us that P, the probability of 'moving' into a new position, is roughly the same for every move. This suggests that there is little tendency for moving particles to continue moving above $T = 0.5$. The higher $nonP$ values obtained for the longer $100\tau = 86.6\tau_e$ runs at $T = 1$ are probably due to the fact that particles are able to sample both fast and slow regions over this very long timescale and thus have P values that change significantly over the course of the run.

We conclude that the waiting time per particle is roughly the same for every move above $T = 0.5$, at least over times that are of the same order of magnitude as the structural relaxation time. Similar analysis at $T = 0.4$ would help to address whether

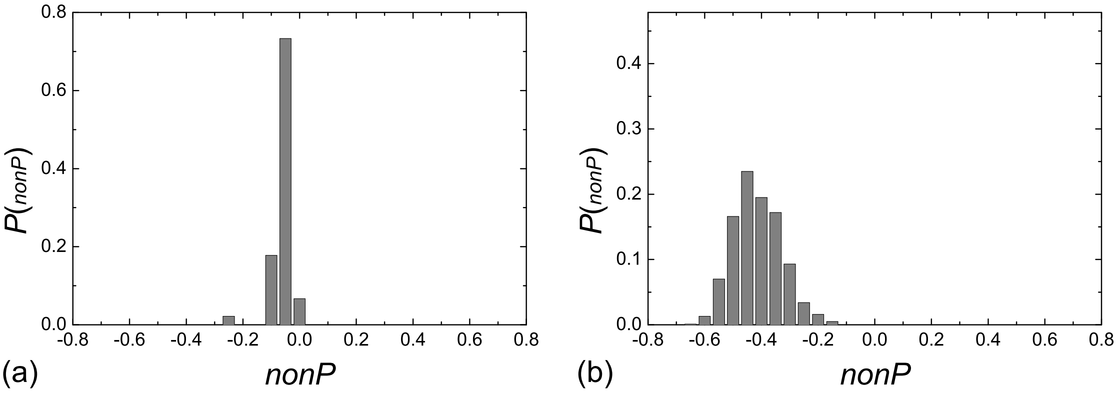

Figure 2.17: The distribution of non-Poisson parameters $nonP$ for particles in a configuration at $T = 1$. The distributions were calculated using (a) 1000 runs of duration $1.5\tau_e = 1.155\tau$, and (b) 100 runs of duration 100τ each.

it is correlated jump directions that produce the non-Gaussianity of the single particle displacement distributions observed at this temperature. Direct measurement of such directional correlations are recommended to verify this in the case that non-Poisson statistics are found for the number of moves per run.

Finally, we consider the distribution of move times, where the move time is defined as the time taken for a particle to move a distance of $R_{move} = 1$. Previously, we hypothesized that the propensity characterises the average waiting time and jump length. Here we test this hypothesis by considering the correlation between propensity and average move time with the jump length fixed at $R_{move} = 1$. We note that the propensities will only contain information about the average move time of those moves that are able to occur in the time period used to calculate the propensities. Hence it is only valid to compare the average move time obtained from runs of duration $1.5\tau_e$ with the propensities, since the same run times were used in calculating both quantities.

In Figure 2.18 we plot the propensity against the average move time $< t_{move} >$ for a configuration at $T = 0.5$. Only data for the 796 particles that moved in at least 50 of the total 1000 runs are plotted. This was done to ensure that there were adequate statistics to calculate the average move time for each particle. We find a moderate negative correlation between the propensity and the average move time. This provides some support for our previous hypothesis that the propensity characterises the average waiting time and jump length, but the broad scatter suggests that this is too simple a description to completely describe the data. It would be

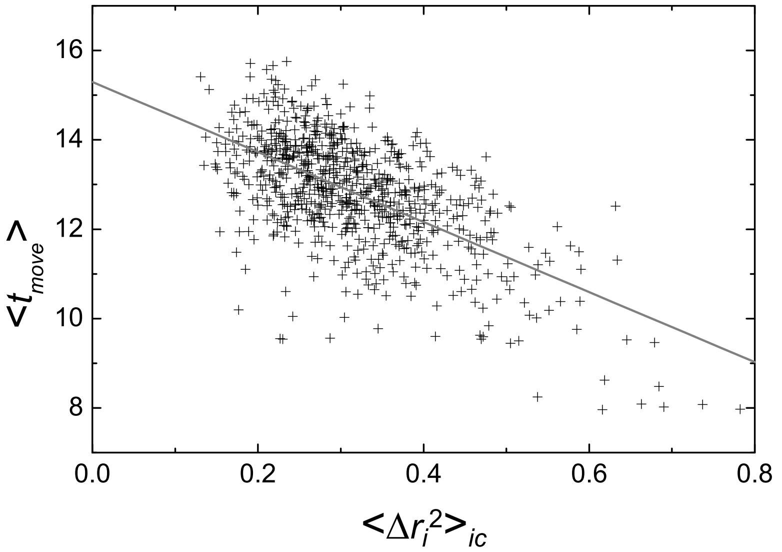

Figure 2.18: The relationship between propensity and average move time $< t_{move} >$ for 796 particles at $T = 0.5$. Properties were calculated using an ensemble of 1000 runs, and data points have only been plotted for particles that moved in at least 50 runs. The solid grey line is a linear fit to the data.

interesting to see if the correlation improves at lower temperature. At $T = 1$ we did not observe any correlation but this may have been due to a lack of data points (only 45 particles moved in at least 50 runs).

2.4.4 The Spatial Distribution of the Single-Particle Non-Gaussian Parameter

Given that the non-Gaussian $f_i(\Delta r)$ distributions represent a new piece of kinetic information, the spatial distribution of single-particle non-Gaussian parameters (α_i, defined in Eq. 2.3) may offer additional insight into the manner in which the configuration influences relaxation. Here we compare this distribution with the spatial distribution of dynamic propensity and discuss what insight may be gained from such analysis. Those particles with motion that varies the most from run to run can be thought of as having the least structural constraint on their mobility.

Figure 2.19 shows the spatial distribution of α_i and propensity for a configuration at $T = 0.4$. Regions with high propensity and particles with L06 topology (filled circles) tend to have low α_i, and particles with high α_i tend to have low propensity. Lines of high α_i appear to represent paths for rare motion in regions of low propensity,

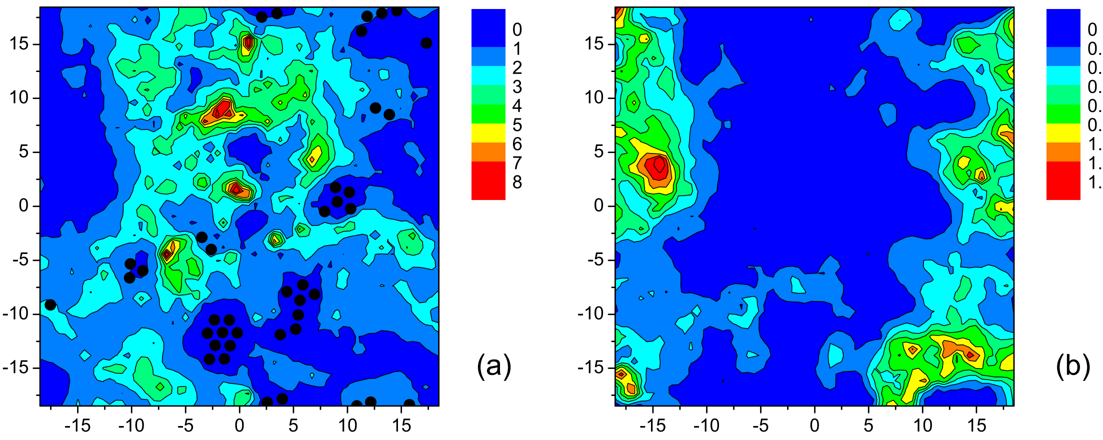

Figure 2.19: (a) The spatial distribution of the single particle non-Gaussian parameter α_i for a configuration at $T = 0.4$. The black circles indicate the positions of large particles with six large neighbours. (b) The propensity map for the same configuration used in (a). Quantities were calculated using ensembles of 100 runs.

and therefore a study of these may provide insight into mechanisms for relaxation of the slow regions.

2.4.5 Intermittency

One consequence of the high variability in particle motion from run to run, and the accompanying asymmetry of the displacement distributions, is that rare events (large displacements) have a significant impact on the mean squared displacement, i.e. the propensity. Other physical phenomena in which rare events have a significant influence on some mean property have previously been described as 'intermittent'. In particular, the term *intermittency* has been used to to describe distributions in which maxima in space or time are widely spaced and rare, but make a dominating contribution to the physical quantity of interest. See, for example, 'The Almighty Chance' [99] for an introduction to the concept of intermittency. The term was introduced by Batchelor and Townsend [100] for the patched temperature distribution in turbulence, and has been applied to the distribution of matter in space among other physical phenomena. The principal and characteristic property of intermittency is the abnormal relationship (when compared to the Gaussian one) between the consequent statistical moments.

In the present case, the rare events are not scattered in space or time, but over the isoconfigurational ensemble, i.e. over the space of possible futures. However, the abnormal relation between the statistical moments is similarly non-Gaussian. Another way of interpreting this is to say that the configuration expresses its character, or effect on the dynamics, intermittently.

The concept of intermittency has also recently been used to describe some experimental results on relaxation in glasses. Ciliberto et al. [101] have reported intermittent voltage noise signals characterised by rare large noise spikes above the regular fluctuations during dielectric studies of a colloidal glass of clay particles called Laponite. The result is a non-Gaussian distribution for the voltage noise which, based on numerical work, has been interpreted in terms of activated and spontaneous relaxation events [102]. However, discrepancies have been found between different experiments, and between simulations and theory, and this area appears to need further work to rationalise the contrasting findings. A review of recent experimental, numerical and theoretical work on the intermittency of relaxation in glassy soft matter can be found in ref. [15].

In terms of the present work, we suggest that another way of interpreting the intermittent manner in which the configuration affects the dynamics, and possibly also the intermittent voltage noise, is in terms of ‘stick’ and ‘slip’ events. Even high propensity regions are able to ‘stick’ particles, i.e. to not allow significant motion to occur, but occasionally ‘slips’ occur, i.e. large displacements take place during a run. The difference between high and low propensity regions in this picture is that the frequency (or probability) of slips is higher in the high propensity regions. Of course, this is a rather crude picture in the sense that the distribution of displacements for a particle tends to be continuous rather than forming two discrete peaks, but the basic picture of an increasing variability of particle motion as the system is cooled is consistent with our results.

2.5 Correlations in Particle Motion

The isoconfigurational ensemble technique can also be used to explore the character of the dynamics in the supercooled liquid. This can be done by exploring correlations in particle motion, for example between different particles within the same run or between the same particle (self-correlation) in different runs. Information about the lengthscale over which particle motion is correlated can also be obtained.

2.5.1 Self-Correlation within the Isoconfigurational Ensemble

Analysis of correlations between the motion of a particle and itself in different runs can give information on the degree to which the original configuration confers directionality on particle motion. By directionality we mean a tendency to move in a preferred direction. In particular, we investigate the following question: is the variation in propensity due to the tendency of some particles to have a strong directional preference?

We define the directionality d_i of a particle i as the mean dot product over all pairs of displacement vectors normalised by the propensity, i.e.

$$d_i = \frac{\frac{1}{N_{\alpha\beta}} \sum_{\alpha} \sum_{\beta>\alpha} (\Delta\vec{r}_{i,\alpha} \cdot \Delta\vec{r}_{i,\beta})}{< \Delta {r_i}^2 >} \tag{2.6}$$

where α and β are run indices, $N_{\alpha\beta} = {}^{N_{runs}}C_2$ is the number of distinct pairs of runs in the isoconfigurational ensemble, $\vec{r}_{i,\beta}$ is the displacement vector of particle i in run β, and $< \Delta {r_i}^2 >$ is the propensity of particle i. For a random distribution of displacements, the vector pairs will be evenly distributed in magnitude and in intervector angle. Therefore, we should have $d_i = \frac{1}{\pi} \int_0^\infty \cos\theta \; \mathrm{d}\theta = 0$. And if the particle moves in the same direction in every run, we should have $d_i = 1$.

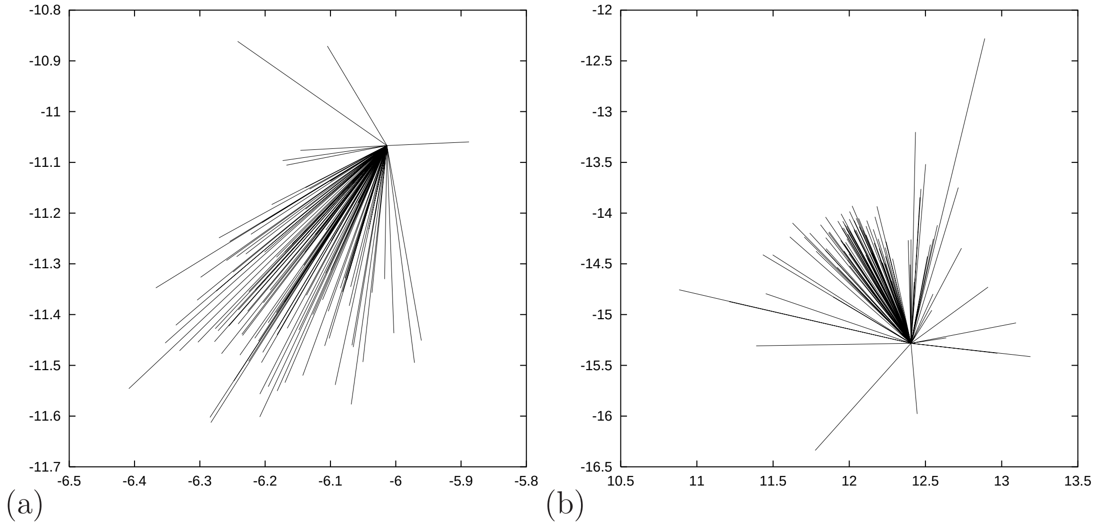

Figure 2.20: Displacement vectors for selected particles at $T = 0.4$ with high directionality and either (a) low or (b) high propensity. The vectors are from isoconfigurational ensembles of 100 runs.

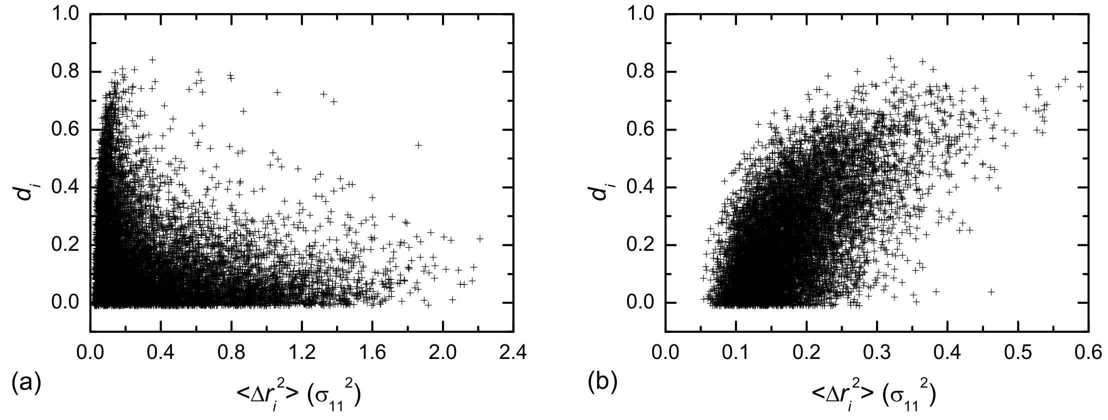

Figure 2.21: The particle directionality d_i as a function of propensity for ten configurations each at (a) $T = 0.4$ and (b) $T = 1$. Quantities were calculated using 100 runs. Note the different x-axis scales.

Figure 2.20 shows the displacement vectors for selected particles at $T = 0.4$. In particular, we considered an ensemble of 100 runs and selected particles with high directionality and either high or low propensity. We find that there are particles with $d_i > 0.8$, independent of propensity, whose displacement vectors fall almost exclusively within a 60° angle, i.e. that have strong directionality conferred upon their motion by the initial configuration.

An obvious question to ask is what role do particles with high directionality have in determining the propensity distribution. In Figure 2.21 we plot d_i against propensity, using data pooled from ten configurations each at $T = 0.4$ and $T = 1$. The configurations were separated from one another by $75\tau_e$, and the propensities and directionalities were calculated over ensembles of 100 runs. At $T = 1$, particles with high directionality have high propensity. This suggests that at high temperature the most mobile particles are those that have a high degree of directionality conferred upon their motion by the initial configuration. In contrast, at $T = 0.4$ the particles with high propensity generally have low directionality, suggesting that any directionality conferred by the initial configuration is rapidly 'forgotten' as a particle moves away from its initial position. Of course, this difference may be a consequence of how we have scaled the run time for the isoconfigurational ensemble. The mean collision time for this glass-former is 0.10τ for all $T \leq 1$ [89], therefore the run time at $T = 1$ is only one order of magnitude longer than this, compared to four orders of magnitude longer at $T = 0.4$.

The large number of particles with high directionality and low propensity at $T = 0.4$ could be explained by the following picture. At low temperature many particles remain trapped in the 'cage' formed by their neighbours. Since we are studying instantaneous configurations it is likely that some of these particles will be far from the centre of their local potential energy minimum (due to the cage) when the runs are begun, i.e. in the initial configuration. There is therefore a high probability that they will undergo mainly vibrational motion during the run and will consequently be found closer to the local potential energy minimum at the end of the run, thus resulting in a high directional bias in their motion.

We conclude that directional bias on particle motion due to the initial configuration is insufficient to explain the heterogeneity in the spatial distribution of propensities at low temperature. We do, however, note that some particles with high propensity also have high directionality. Given the increased clustering of high propensity particles at low temperature (see Figure 2.9), it is possible that these rare particles, with both high propensity and high directionality, have a role to play as initiators of motion in the high propensity regions. This could be an area for future research.

2.5.2 Correlation Between Motion of Unlike Particles

An analysis of correlations between the motion of unlike particles can yield information about the cooperativity of particle dynamics. For example, one can ask whether neighbouring particles move in the same direction, or investigate the lengthscale over which particle motion is correlated. This is an area that, as discussed in the introduction to Part I, has already been studied in much detail. The unique feature of the present analysis is that we average such measures over an isoconfigurational ensemble. This makes it possible, for example, to calculate the distance over which particle motion is correlated for individual particles in a given configuration.

Before discussing the distance over which particle motion is correlated, we present an analysis that can be used to identify particles whose motion is highly correlated with that of their neighbours. We define the flow f_i of a particle i as the mean dot product between the displacement vector of i and that of all its nearest neighbours, where the vectors are normalised and the isoconfigurational average is taken, i.e.

$$f_i = \left\langle \frac{1}{n_i} \sum_{j=1}^{n_i} \left(\frac{\Delta \vec{r}_{i,\alpha}}{|\Delta \vec{r}_{i,\alpha}|} \cdot \frac{\Delta \vec{r}_{j,\alpha}}{|\Delta \vec{r}_{j,\alpha}|} \right) \right\rangle \tag{2.7}$$

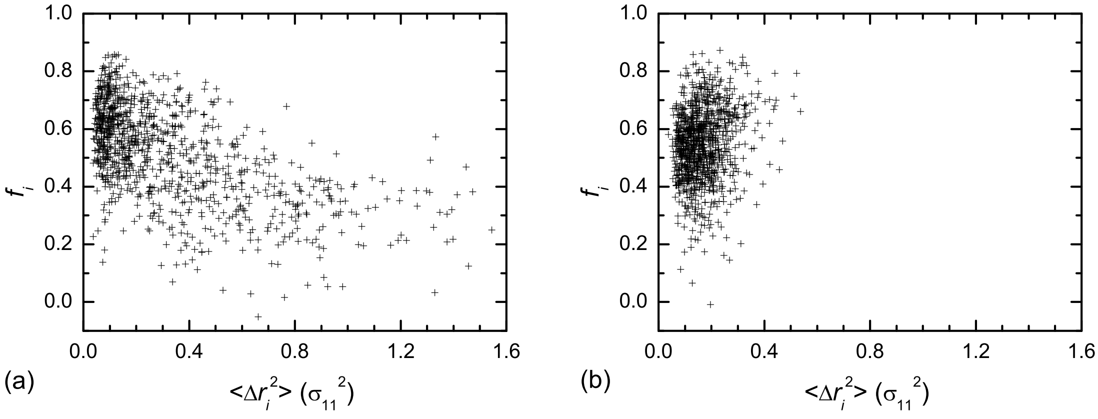

Figure 2.22: The particle flow f_i as a function of propensity for single configurations at (a) $T = 0.4$ and (b) $T = 0.6$. Quantities were calculated using 50 runs.

where α is the run index, n_i is the number of nearest neighbours of particle i, $\vec{r}_{i,\alpha}$ is the displacement vector of particle i in run α, and the angular brackets $<>$ represent an average over runs. If the motion of a particle i is uncorrelated with that of its neighbours then $f_i = 0$. On the other hand, if the motion of the particle is always in the same direction as that of its neighbours then $f_i = 1$.

In Figure 2.22 we plot f_i against propensity, for single configurations at $T = 0.4$ and $T = 0.6$. The propensities and flows were calculated over ensembles of 50 runs. While there is no strong correlation between propensity and flow, a few relations can be identified. Particles with high flow tend to be limited to those with $< \Delta r_i^2 >< 0.5$. The high flow of these low propensity particles may be due to normal modes or small hydrodynamic flows. There is also a strong change in the behaviour of high propensity particles upon cooling. At $T = 0.6$ there is a weak tendency for high propensity particles to have high flow, while at $T = 0.4$ there is a stronger tendency in the opposite direction, i.e. particles with high propensity tend to have lower flows on average than particles with low propensity. This relationship at $T = 0.4$ may be due to the large displacements and long run times involved compared to at $T = 0.6$. If several relaxation events take place in the same region over the course of many runs then the overall displacement vectors for these high propensity particles may no longer reflect the character of the motion during the individual relaxation events. This analysis may therefore be more useful at low temperature if applied to displacement vectors resulting from motion over shorter timescales.

Distance over which Motion is Correlated

Intuitively, it makes sense that if, in a dense supercooled liquid, one particle moves, then the particles nearby must also move to create the space needed for this particle to move into. One can ask over what distance such dynamical correlations persist. In this section we demonstrate how analysis of the isoconfigurational ensemble can be used to address this question.

Take a configuration and select a single particle i. Then, for each particle j, calculate the Pearson's correlation coefficient [90] K between the displacement magnitudes of particle i and particle j over an ensemble of 100 runs. Figure 2.23 shows the correlation coefficients for particles in a configuration at $T = 0.4$ as a function of their distance from particle i, where i is the high propensity particle at (-18,-15.5) in Figure 2.4. For distances greater than $5\sigma_{11}$ the correlation coefficient is scattered between -0.2 and 0.2 with an average value of about zero. The correlation coefficients are only greater than 0.2 for nearest neighbour particles, but the average correlation coefficient for particles at approximately the same distance (probably in the same coordination shell) remains greater than zero for distances up to at least $4\sigma_{11}$ and

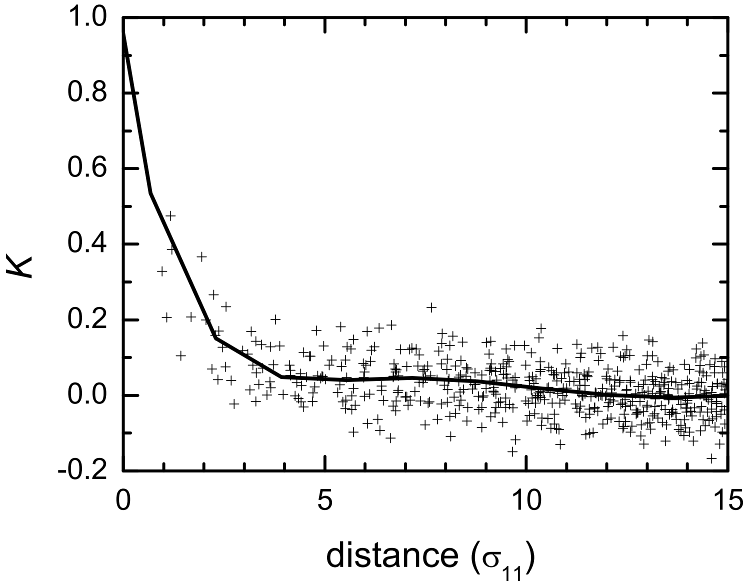

Figure 2.23: The correlation between the motion of a particle i and all other particles j as a function of the distance between i and j. The moving average has been indicated by a thick line, and the Pearson's correlation coefficient K between displacement magnitudes was calculated using data from an ensemble of 100 runs.

possible longer. Our results therefore suggests that the motion of i depends on the motion of at least some particles outside of its first coordination shell. This technique could be extended to calculate, for example, the mean distance over which particle motion is correlated for high and low propensity particles.

2.6 Discussion and Conclusions

Because the glass transition is defined by its dynamics, the task of establishing its structural origin requires us to begin with the dynamics and deduce what structures are responsible. This is an inversion of the usual problem in condensed matter physics and presents us with an important question, namely how trustworthy are the structural clues provided by the observed particle dynamics? In this chapter, we have demonstrated that there is considerable variation in the dynamical evolution of a specific particle configuration. We conclude that some aspects of the particle dynamics are not significantly correlated with the initial configuration and therefore cannot be ‘explained’ by reference to that configuration.

Through the introduction of the isoconfigurational ensemble, we have established that it is the spatial variation in the propensity for particle motion, rather than the motion itself, that is completely determined by the initial configuration. We find that, upon cooling, the spatial heterogeneity in the propensity increases both in amplitude and wavelength, i.e. the difference between high and low propensity increases and particles with similar propensity increasingly cluster together.

The increasingly large variation, upon supercooling, in an individual particle’s movement from run to run also represents an important new piece of kinetic information, distinct from the propensities and their spatial distribution. At high temperature all particles have a variability in their motion from run to run, relative to their propensity, that is typical for a particle undergoing a continuum random walk in 2D. As the temperature decreases particles increasingly have a variability from run to run that is higher than would be expected if they were undergoing a random walk, characterised by highly non-Gaussian single-particle displacement distributions.

In summary, the increasing variability in particle motion that we have characterised provides: the reason why the propensity is needed to characterise the effect of structure on dynamics; physical information on the process by which the configuration influences the dynamics; and a view of dynamics that may explain recent experiments describing the intermittency of relaxation events in colloidal clays. We have also outlined a number of ways in which further analysis of the variability of particle motion may provide additional insight into the process of relaxation and the role of structure in supercooled glass-formers.

The assignment of propensities to particles represents the major result of this chapter. This result provides a rigorous method for establishing the link between a given configuration and the subsequent dynamics. The remaining problem is to uncover the causal link between specific structural features of a configuration and the resulting propensities. A detailed account of the correlation between propensity and structure in the 2D mixture is presented in Chapter 3. Before moving on, however, we will discuss a number of other implications of the work presented in this chapter.

In the language of the jump model of particle motion [93], the propensity characterises the average waiting time and jump length, while the non-Gaussian character of the individual particle displacement distributions is a result of either displacement correlations between successive jumps and/or non-Poisson statistics for the number of jumps within the observation time. We have outlined how analysis of the isoconfigurational ensemble can directly test this conceptual view of dynamics in supercooled liquids.

A number of recent papers have characterised the transition in particle dynamics on supercooling as a transition from hydrodynamically-governed dynamics to landscape-dominated dynamics [86, 103]. The 'landscape' here refers to the potential energy surface over the configuration space. In this chapter we have arrived at an alternative description of this fundamental temperature dependent change, i.e. a transition, on cooling, from structure-independent (hence liquid-like) propensities for motion to structurally-determined propensities. One advantage of this new account over the landscape picture is that it refers directly to the behaviour of the liquid in real space rather than the abstract configuration space.

The propensity is related to the probability of a particle in a configuration undergoing a substantial displacement within a given time interval. Note that this is distinct from how far it is actually observed to move in a single trajectory. The propensity is therefore the starting point for several models of glass relaxation such as the facilitated spin models [71–73] and the cooperative lattice gas models [104–106]. In each of these, a set of rules determine the probability for movement based on the instantaneous configuration. In contrast, most models of molecular glass-formers are defined by a Hamiltonian and structural constraints. Uncovering the relationship between particle configurations and the probability of particle motion in these models represents a major challenge. Having now defined and described the dynamic propensity, we have taken a first and necessary step. In the next chapter we address our ultimate goal, which is to predict the spatial pattern of dynamic propensity from a given configuration.

Chapter 3

Predicting Dynamic Propensity

Having established the dynamic propensity as the part of the dynamics that must be due to a property of the structure, we now search for its specific structural origins. In particular, we test the ability of reduced measures of structure to predict the spatial variation in dynamic propensity. We consider the local coordination environment, local free volume, local potential energy, and coarse-grained versions of these, among others. While we find some correlations between structure and dynamics, none of these measures are able to predict the spatial variation in propensity. We therefore turn to the short-time dynamics as a direct measure of structural 'looseness'. We define a single-particle Debye-Waller factor and find that it is able to predict the spatial distribution of propensity. We suggest that this provides an upper bound on the predictive ability of any structural measure. We then use the Debye-Waller factor to study the time evolution of dynamic heterogeneity and obtain results that are at odds with a simple picture of defect diffusion. Finally, we test whether there is a microscopic basis for a relationship reported between short-time dynamics and the geometric free volume.

3.1 Introduction

Some aspect of the structure in a glass-forming alloy determines the observed slow particle dynamics. For example, strong correlations are observed between the increase in shear viscosity and large angle scattering structure in metallic alloys following a temperature quench [107]. In the previous chapter we have shown that there is also something in the structure that is responsible for the *spatial* variation in dynamics.

More precisely, the spatial variation in dynamic propensity is determined by the initial configuration. But what aspect of the initial configuration is responsible for the spatial variation in propensity? In this chapter we test the proposition that reduced measures of structure are able to predict the spatial variation in propensity.

Variations in local environment have been cited as important in a number of studies of the local connection between structure and dynamics. For example, in a study of the same 2D glass-former considered in this part of the thesis, Perera and Harrowell found that large particles with high local six-fold orientational order had, on average, longer relaxation times than large particles with low six-fold orientational order [44]. And in studies of a Lennard-Jones (LJ) liquid, Kob et al. found differences in the radially averaged structure about particles with different mobilities [46, 79]. The latter work also found a correlation between the average potential energy and the average mobility of particles divided into subsets according to their mobility. However, no correlations were found of sufficient strength to indicate a causal link, i.e. that the selected aspect of the local structure determined the local kinetics.

As briefly discussed in the previous chapter, a number of recent papers have characterised the transition in particle dynamics on supercooling as a transition from hydrodynamically-governed dynamics to landscape-dominated dynamics, where the 'landscape' refers to the potential energy surface over the configuration space. Sastry et al. [103, 108] have shown that changes in various dynamic properties of a glass-forming LJ liquid can be related to changes in the energy of the accessible part of the energy landscape. This conceptual picture therefore provides a link between dynamics and structure, albeit in the abstract configuration space. Heuer et al. [86, 109] and La Nave and Sciortino [110] have also reported correlations between the dynamics of small systems of 60–120 particles and the potential energy of the inherent structure (IS). These calculations did not examine whether the correlations extend to the spatial distribution of the two quantities, an issue that we address here.

Free volume [34] is a another widely used concept to explain the relationship between structure and dynamics. The generation or disappearance of free volume has been invoked to explain shear banding [111] and positron annihilation [112] in metallic glasses. The concept of 'shear transition zones' [113] is also used in the context of non-equilibrium mechanical response. Intuitively, it is easy to conceive that less crowded regions will have more space for particle motion and will therefore be 'looser' or more 'mobile'. This intuitive picture has been formalised in free volume theories, which are able to accurately describe some thermodynamic observations such as the temperature dependence of the viscosity (over more than 12 decades in magnitude for the viscosity in some cases [114]), and the dependence of T_g on quench rate [115]. A recent simulation study also found a strong correlation between the average free volume and the bulk averaged short-time mean squared displacement for monomers in a 'bead-spring' model of a glass-forming polymer over a range of temperatures [80]. Despite its popularity and the success of the free volume concept at a phenomenological level, there remains a persistent problem concerning the application of free volume to describe dynamics. In particular, what is the relationship between the geometric free volume - a quantity that can be well defined at the atomic scale - and the phenomenological free volume (a macroscopic quantity that is usually derived from the bulk density).

We begin by defining a measure of the local coordination environment and investigate the relationship between this and the propensity (Section 3.2.1). This is followed by a comparison of the spatial distribution of propensity and (i) the local potential energy (Section 3.2.2), and (ii) the local free volume (Section 3.2.3). In Section 3.2.4, we look at the effect of coarse graining the potential energy and the free volume on their spatial correlation with the propensity. We then consider a number of other structural measures (Section 3.2.5), including force networks and the proximity to crystalline clusters of large particles. In Section 3.3.1 we define a local Debye-Waller factor as a measure of structural 'looseness' and study its ability to predict the spatial distribution of propensity. We also use this quantity to study the time evolution of dynamic heterogeneities (in Section 3.3.2), and in Section 3.3.3 we investigate the ability of the geometric free volume to predict the spatial distribution of the short-time dynamics. Finally, we summarise the main results, draw some conclusions and suggest directions for future work (Section 3.4).

3.2 The Failure of Structural Measures to Predict the Spatial Variation in Propensity

Phenomenological correlations are the staple of the glass field. There is much evidence from experiments and simulations for correlations or anti-correlations between various bulk dynamic and thermodynamic properties (see, for example, ref. [116] and references therein). This is perhaps not surprising when one considers that, ultimately, it must be the interaction potential that determines all dynamic, thermodynamic and vibrational properties of glass-formers. However, it is important to recognise that a correlation between two variables does not necessarily imply that there is a causal link between the two, i.e. that a change in one property is responsible for the change in the other. We propose that it is necessary that a strong microscopic correlation exist for there to be a causal link between two properties. In particular, we are interested in establishing whether or not structural measures are able to explain the spatial variation in propensity in a dense amorphous alloy.

3.2.1 Local Coordination Environment

We investigate the local coordination environment of each particle by defining a measure in terms of the number of neighbours it has of each type. The particles of species a that are nearest neighbour to a particle of species b are defined as those that lie within a distance cut_{ab}, the distance to the first minimum in the appropriate partial pair distribution function (PPDF) $g_{ab}(r)$. The PPDFs for this model can be found in ref. [67]. For reference, the cutoff distances, cut_{ab}, used to define nearest neighbours for $T = 0.4$–1 were (cut_{11}, cut_{12}, cut_{22})=(1.45, 1.65, 1.85).

We identify a particular neighbourhood, or local environment, with the following notation: A small particle with m small neighbours and n large neighbours is designated as Smn and the analogous large particle is indicated as Lmn. For example, S14 indicates a small particle surrounded by 1 small and 4 large neighbours, and L06 indicates a large particle surrounded by 0 small and 6 large particles. In this way, all the particles are divided into subsets.

For the following analysis, we pool the data from ten well-spaced configurations of the 2D binary mixture, each separated by a run time of $75\tau_e$ from the previous one. Propensities were calculated using a total of 100 runs for each configuration.

Figure 3.1(b) shows the populations of the different environments at $T = 0.4$. The small particles have either five or six neighbours, while the large particles find themselves in six- or seven-fold environments. Hence the four distinct clumps in the distribution. Also note the large number of different environments. The purely steric interactions of the 2D binary mixture do not lead to any significant chemical ordering in the liquid, unlike, for example, the Kob-Andersen model. The fractions in (a), (b) and (c) are relative to the total number of particles in each distribution.

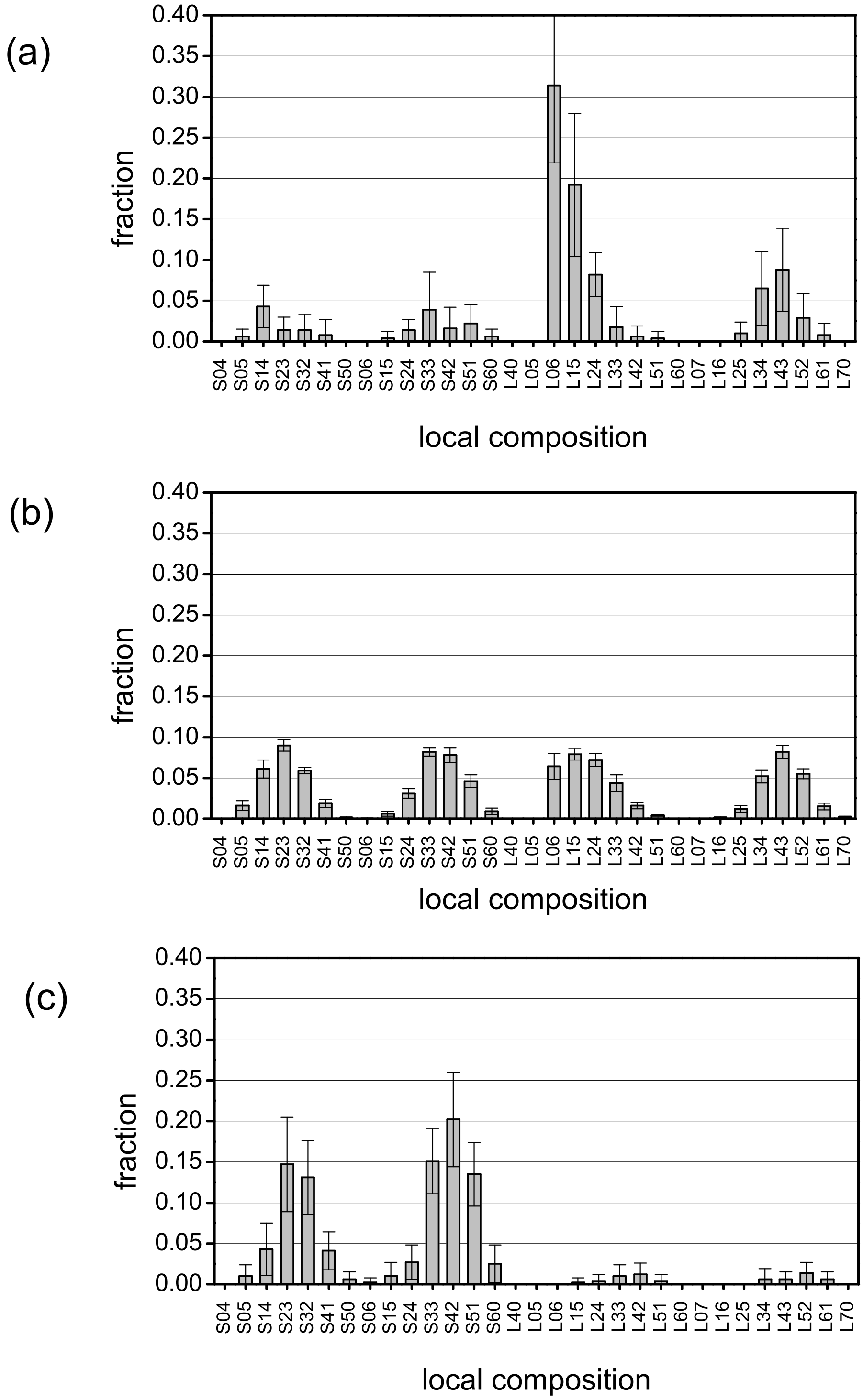

Figure 3.1: The distribution of local coordination environments in the binary mixture at $T = 0.4$ for (a) the slowest 5% of particles, (b) all the particles, and (c) the fastest 5% of particles. The environment code is explained in the text.

In Figure 3.1(a) we present the distribution of environments found among the slowest 5% of particles, i.e. the lowest 5% when ranked by their propensities. This subset is dominated by large particles, and in particular the L06 environment corresponding to local hexagonal packing of large particles. Particles with the L15 environment are also prominent. This finding is consistent with the earlier observation that large particles with high local six-fold orientational order had, on average, longer relaxation times than large particles with low six-fold orientational order [44].

More interesting perhaps, is the question of where motion will happen. Figure 3.1(c) shows the distribution of environments for the 5% fastest particles, i.e. the highest 5% when ranked by their propensities. This subset is clearly dominated by small particles, with a preference, relative to the total distribution in (b), for the more mixed environments: S23, S32, S33, S42, and S51.

Thus, we find some variation in the distribution of local environments between particles with high and low propensity, which is consistent with previous observations of differences in the radially averaged structure about particles with different mobilities [46,79]. However, consider a particle with a given coordination environment and it is clear that it may be present in either the high or the low propensity subsets, i.e. the local environment does not determine the variation in propensity. Another way to visualise this is to plot the distribution of propensities for the different environments.

The distribution of propensities for a selection of local environments are shown in Figure 3.2. While some environments, e.g. L06, provide a relatively strong constraint on particle motion, it is clear that most provide little constraint. Particles with low or high propensity can have almost any local environment. We conclude that some property other than the local coordination environment must be responsible for determining which of the particles exhibits high propensity.

While the local environment is unable to predict the spatial distribution of propensity, there is evidence for a general trend from lowest to highest average propensity as the number of large neighbours decreases and the number of small neighbours increases. Overall, particles with the L06 environment have the lowest propensity on average and particles with the S60 environment have the highest. That is, there is some correlation between local coordination environment and propensity when these variables are averaged over subsets of particles. However, we find no microscopic correlation of sufficient strength to indicate a causal link between the two.

For comparison, we plot the distribution of local coordination environments at

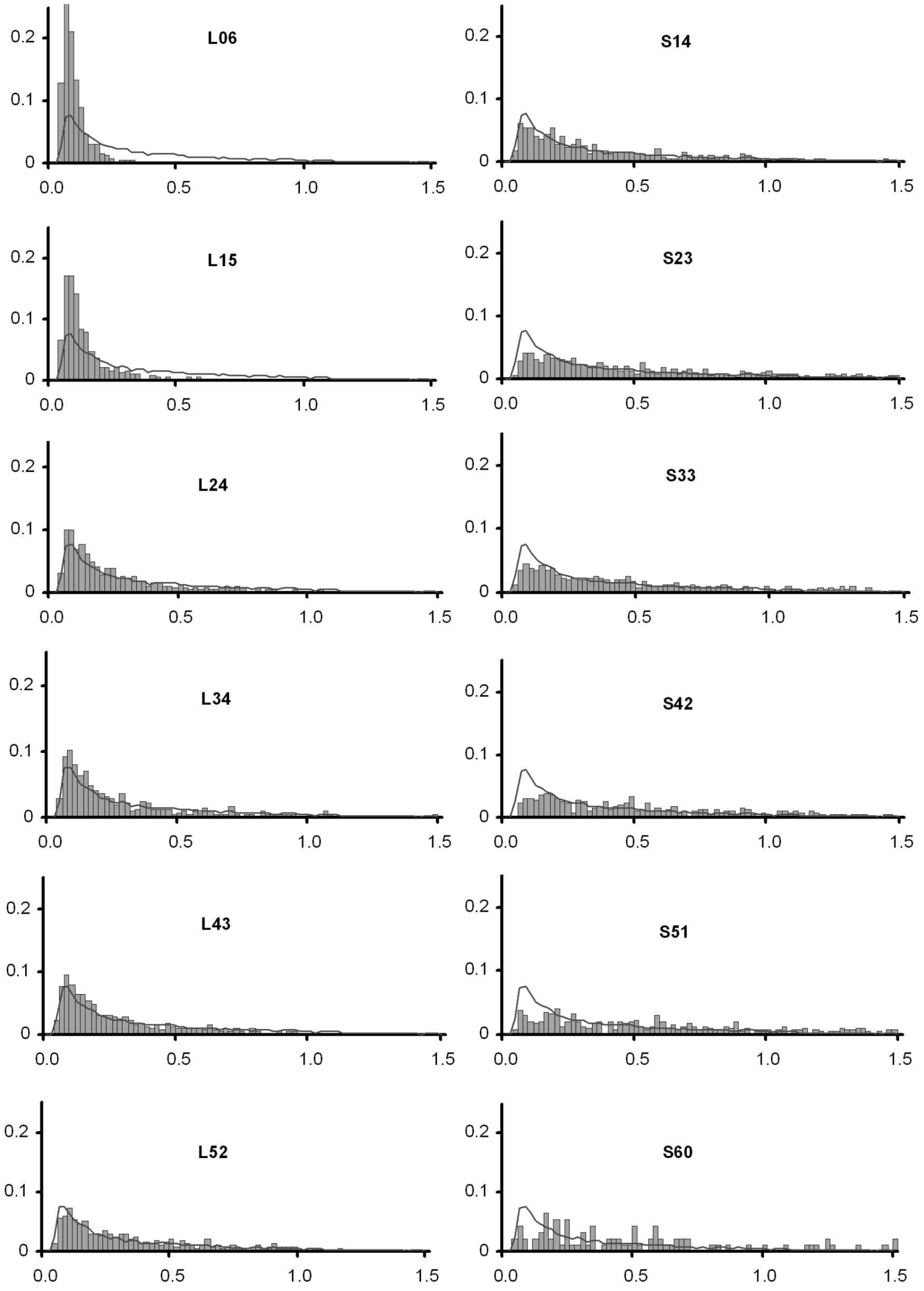

Figure 3.2: The distribution of particle propensities for selected local coordination environments at $T = 0.4$. The environment code is explained in the text, and the solid line indicates the propensity distribution over all particles.

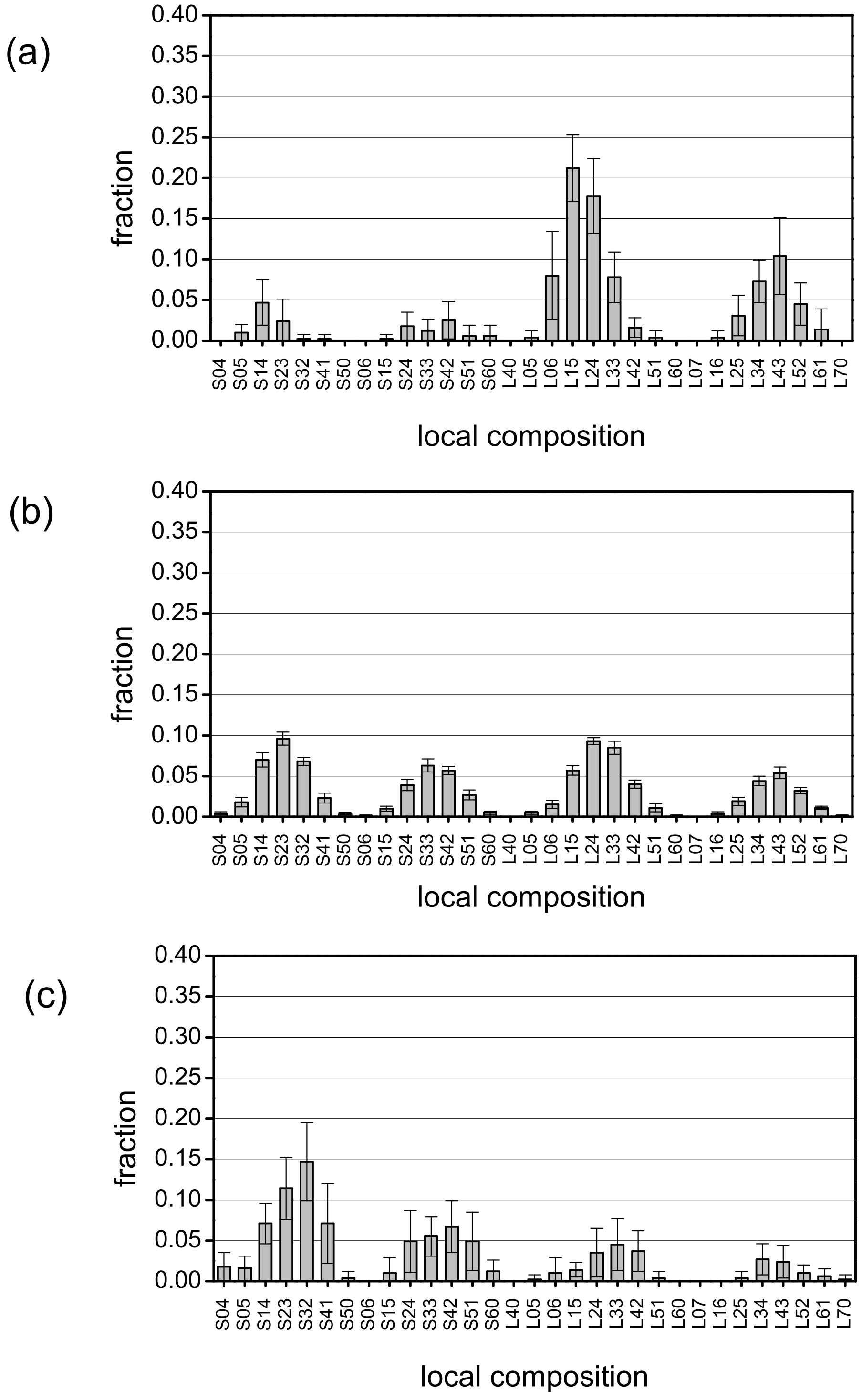

Figure 3.3: The distribution of local coordination environments in the binary mixture at $T = 1$ for (a) the slowest 5% of particles, (b) all the particles, and (c) the fastest 5% of particles. The environment code is explained in the text.

$T = 1$ in Figure 3.3. The proportion of L06 environments is now much smaller among the slowest 5% of particles, but the lowest and highest propensity subsets are still dominated by large and small particles, respectively, thus demonstrating that this is not a unique feature of low-temperature dynamics. It is also clear that the local environment does not provide a strong constraint on the propensity of a particle.

We therefore conclude that, while on average small particles tend to be more mobile than large particles, and the L06 environment is a good predictor of low propensity in the supercooled liquid, the local coordination environment is in general unable to predict the spatial distribution of dynamic propensity.

3.2.2 Potential Energy

We define the potential energy u_i of particle i as the sum over all potential interactions between it and its nearest neighbours (see Section 3.2.1 for the definition of nearest neighbours). We find that this local definition of the potential energy (PE) accounts for greater than 99.5% of the total potential energy in the soft-disc mixture at $T = 0.4$.

As described in the introduction, Doliwa and Heuer [86] and La Nave and Sciortino [110] have reported correlations between the dynamics of small systems and the inherent structure (IS) energy, but did not look at whether the correlation extends to the spatial distribution of these two quantities. We shall now examine the correlation between the spatial distribution of potential energy in the initial IS and the particle propensity. The inherent structures were obtained from the initial instantaneous configurations via a conjugate gradient minimisation of the energy and were used instead of the instantaneous configurations in order to remove the random effect of thermal fluctuations on the structure.

In order to aid in visualising the spatial variation of various quantities, we use contour plots. These are generated by interpolating the irregularly spaced particle properties onto a grid, as described for the propensity in Section 2.3. In Figure 3.4 we compare the spatial distribution of the IS potential energy and of the propensity for a configuration at $T = 0.4$. Note that the two maps are quite different, and that the spatial heterogeneities of the IS particle energies involve considerably shorter lengthscales than those of the propensity. We obtain similar results for nine other configurations at $T = 0.4$.

To quantify the spatial heterogeneity in a given property P, we use the following cluster analysis. The 10% of particles (102 particles in this case) with the largest

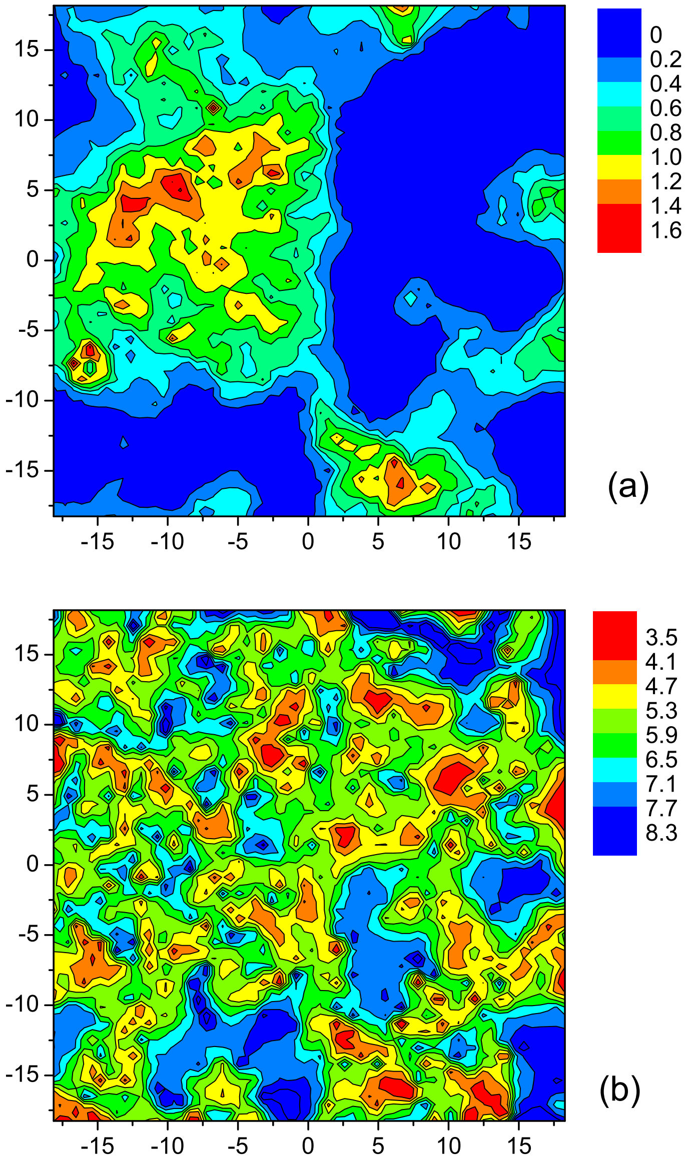

Figure 3.4: The spatial distribution of (a) dynamic propensity for a configuration taken from an equilibrated system at $T = 0.4$, and (b) potential energy per particle for the inherent structure of the same configuration used in (a). Propensities were averaged over 100 runs.

values of P are 'tagged'. Each tagged particle is then assigned to a cluster if it is a nearest neighbour to another tagged particle already in that cluster. When all tagged particles have been assigned to a cluster we count the number of clusters and calculate the variance in the number of particles per cluster. The maximum variance possible for a given number of clusters N occurs when $N - 1$ clusters consist of one particle

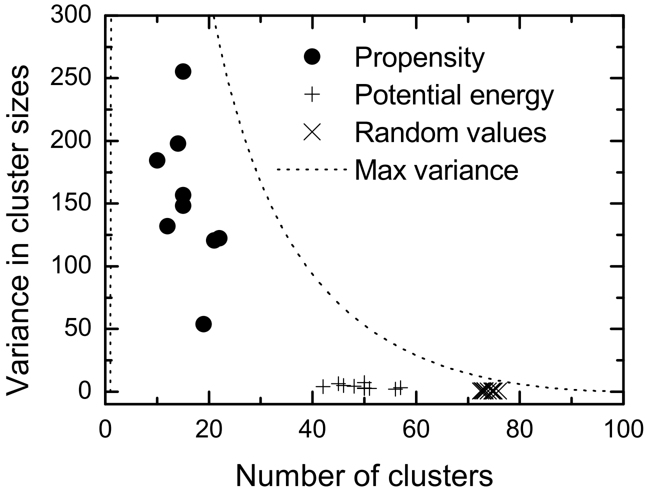

Figure 3.5: Cluster measures of spatial heterogeneity for particles with potential energies and propensities in the top 10%. Data points are shown individually for ten configurations at $T = 0.4$. Statistics obtained using random values are shown for comparison. The dotted line represents the maximum variance possible for a given number of clusters (see Eq. 3.1).

and one cluster consists of $102 - (N - 1)$ particles and is given by the relationship

$$\max(\sigma^2) = -205 - 10404/N^2 + 10608/N + N. \tag{3.1}$$

A random distribution without any spatial correlation will produce a large number of clusters with a correspondingly small variance, while a heterogeneous distribution will produce a smaller number of clusters.

In Figure 3.5 we plot the results of the cluster analysis for the propensity and the IS potential energy for ten configurations at $T = 0.4$. Particles with high potential energy cluster slightly more than an equal number of randomly selected particles, but significantly less than particles with high propensity.

These results highlight the absence of any significant spatial correlation between a particle's potential energy and its propensity. The apparent contradiction between our results and the previous reports [86, 110] underscores the difficulty in interpreting correlations. A correlation between *average* values of two quantities does not necessarily mean that a microscopic, and hence causal, relationship exists. Conversely, if no microscopic correlation exists then we can explicitly rule out a direct causal link between the two properties. These are both important steps en route to understanding the macroscopic correlations. In the remainder of this section we demonstrate

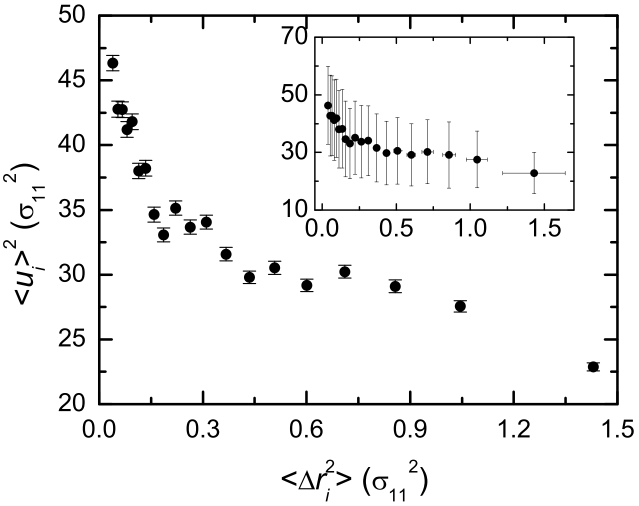

Figure 3.6: Potential energy per particle as a function of propensity. Data for ten configurations at $T = 0.4$ have been pooled together, and the particles divided into 20 subsets according to their propensities. Each subset is represented by a point in the graph. Note that we have plotted the square of the average potential energy $< u_i >^2$ in order to keep the units of the two axes the same. Error bars in the main graph represent one standard error. The inset shows the same data but with error bars corresponding to one standard deviation.

that correlations between suitably chosen averages also exist in the present system, despite their absence at a microscopic level.

If the particles are divided into 20 equal subsets according to their propensity, and the average propensity $< \Delta r_i^2 >$ and potential energy $< u_i >$ is calculated for each subset, then we do find a correlation. As shown in Figure 3.6, there is a clear increase in the average propensity as the average potential energy decreases. However, the size of the standard deviations (see inset) clearly demonstrates that it is impossible to predict the propensity of a particle from its potential energy. We have plotted the square of the average potential energy $< u_i >^2$ in order to keep the units of the two axes the same.

Kob et al. [79] have performed a similar analysis for an attractive Lennard-Jones liquid. They found that as the average potential energy increased, so too did the average mobility, and suggested that this was because particles with higher potential energy were able to find and move into more stable environments. For the repulsive 2D mixture that we have studied, the more stable environments - in the sense that they are less likely to be mobile - appear to be those with higher potential energy, i.e. the relationship between average potential energy and average mobility in the repulsive

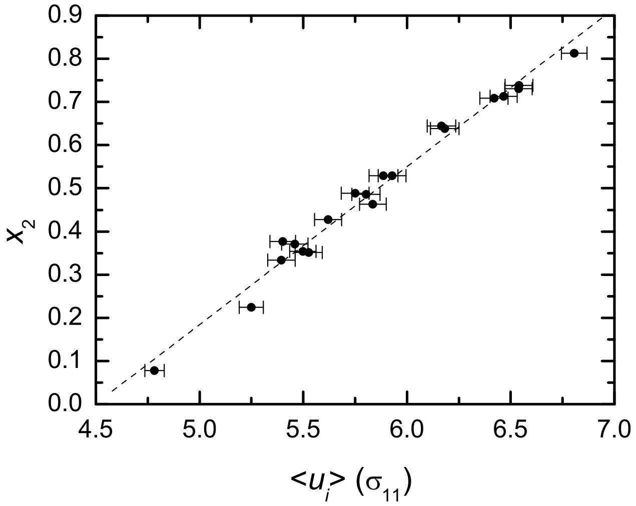

Figure 3.7: Average potential energy $< u_i >$ versus the fraction of large particles x_2 for the subsets considered in Figure 3.6. Each subset is represented by a point in the graph, and the error bars represent one standard error. There is a strong linear correlation between the two quantities as indicated by the dashed line.

soft-disc mixture is opposite to that in the attractive Lennard-Jones mixture.

We also find that, on average, small particles have lower potential energy than large particles, which is consistent with the observation in Section 3.2.1 that the subset of particles with the highest (lowest) 5% of propensities is dominated by the small (large) particles. To investigate this further, we again consider the propensity subsets but this time plot the average potential energy $< u_i >$ of each subset against the fraction of large particles x_2 in the subset. The results are plotted in Figure 3.7. There is a clear linear relationship between potential energy and composition, i.e. as the average potential energy increases so does the fraction of large particles in each subset.

In summary, correlations exist between average propensity and average potential energy, and between average potential energy and composition, when the particles are ordered by propensity and averages are taken over subsets. However, these correlations do not persist at a microscopic spatial level, and we conclude that local potential energy is unable to predict the spatial distribution of propensity. In Section 3.2.4 we consider the effect of coarse graining the potential energy, but first we investigate the spatial correlation between free volume and propensity.

3.2.3 Free Volume

Following Sastry et al. [117], we define the geometric free volume of a particle as the volume accessible to that particle with all its neighbours fixed. Our algorithm differs from that described in ref. [117] by considering overlaps between exclusion spheres rather than using the Voronoi construction. While this modified algorithm will not work well for systems with large voids, it provides an efficient method for calculating free volumes in the current system, and we expect it will work well for condensed phases consisting of mixtures of similarly sized particles. For the purpose of this calculation, we created a mapping to a hard-particle system by using a temperature dependent effective hard disc diameter corresponding to the distance of closest approach of two particles. We identified the closest approach by the distance at which the respective partial pair distribution function first exceeds 0.01. At $T = 0.4$ this corresponds to a distance of $0.9\sigma_{ab}$, where σ_{ab} is the lengthscale of the interparticle potential between particles of species a and b as listed in Section 2.2. We note that the relative ordering of particles by free volume, and in particular the spatial distribution of free volume, are both fairly insensitive to small changes in this effective hard disc diameter. Diameters of $0.85\sigma_{ab}$ and $0.8\sigma_{ab}$ resulted in changes in the relative ordering of free volumes by $+/-10\%$, but made little difference to their spatial distribution. And while values of $0.95\sigma_{ab}$ and σ_{ab} caused some particles to have zero free volume, those particles that still had non-zero free volumes were ordered similarly to what we found using other values.

We again consider the ten well-spaced configurations at $T = 0.4$ for which we calculated the propensity distributions. The distribution of free volume was calculated for each initial configuration and for its inherent structure, i.e. the local potential energy minimum obtained when the initial configuration is used as the start of a conjugate gradient minimisation of the energy. Slightly stronger correlations were observed using the inherent structures, therefore we present only the free volume analysis for these configurations.

To account for differences in particle size, we scale the free volume for each particle by $\pi.\sigma_{aa}^2/4$, where a is the particle species. The scaled free volume v_i has the added property that a very local correlation exists between this geometrical measure and the local potential energy (u_i) in both the inherent and instantaneous structures. In Figure 3.8 the raw and scaled free volumes are plotted against the local potential energies of particles in the inherent structure. Unlike the raw free volumes, the scaled

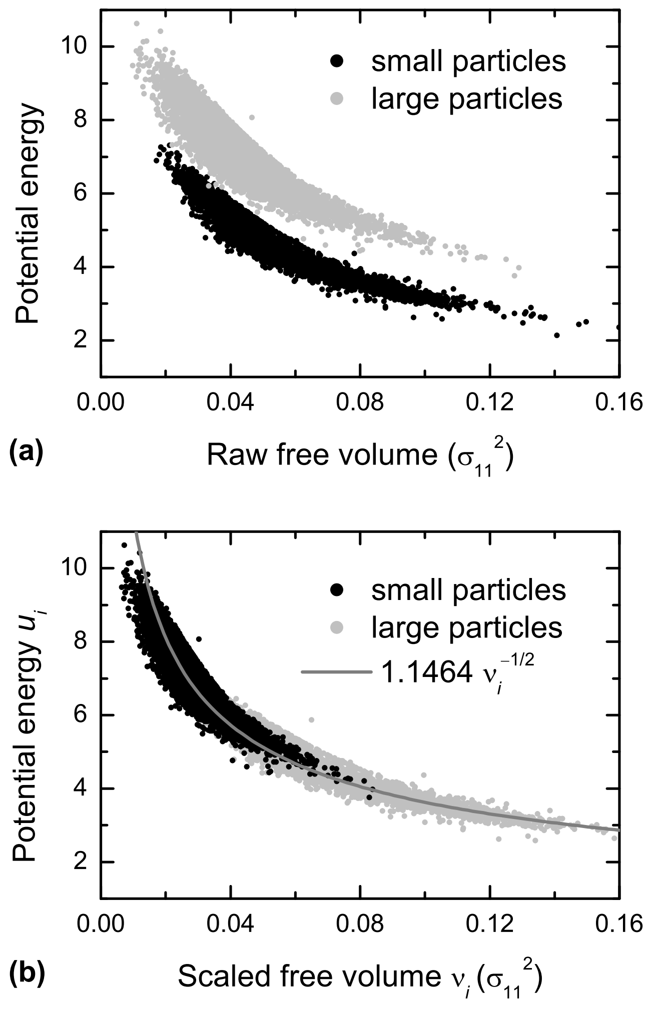

Figure 3.8: The relation between potential energy u_i and (a) raw free volume (b) scaled free volume v_i for particles in ten configurations at $T = 0.4$. Scaling the raw free volumes by $\pi.\sigma_{aa}^2/4$, where a is the species of each particle, collapses the data onto a single curve that is well described by the relation $u_i = 1.1464 v_i^{-1/2}$.

free volumes from the two particle species produce a single smooth curve when plotted against the energy. This curve is well described by the expression $u_i = 1.1464 v_i^{-1/2}$. As a consequence of this relation, most of the results described in this section are similar to those already presented for the potential energy. This will, of course, not necessarily be the case for all glass-forming liquids. From now on we consider only the scaled free volume, which we shall refer to simply as the free volume.

In Figure 3.9 we compare the spatial distribution of free volume and propensity for a configuration at $T = 0.4$. In spite of the coincidence of high propensity and

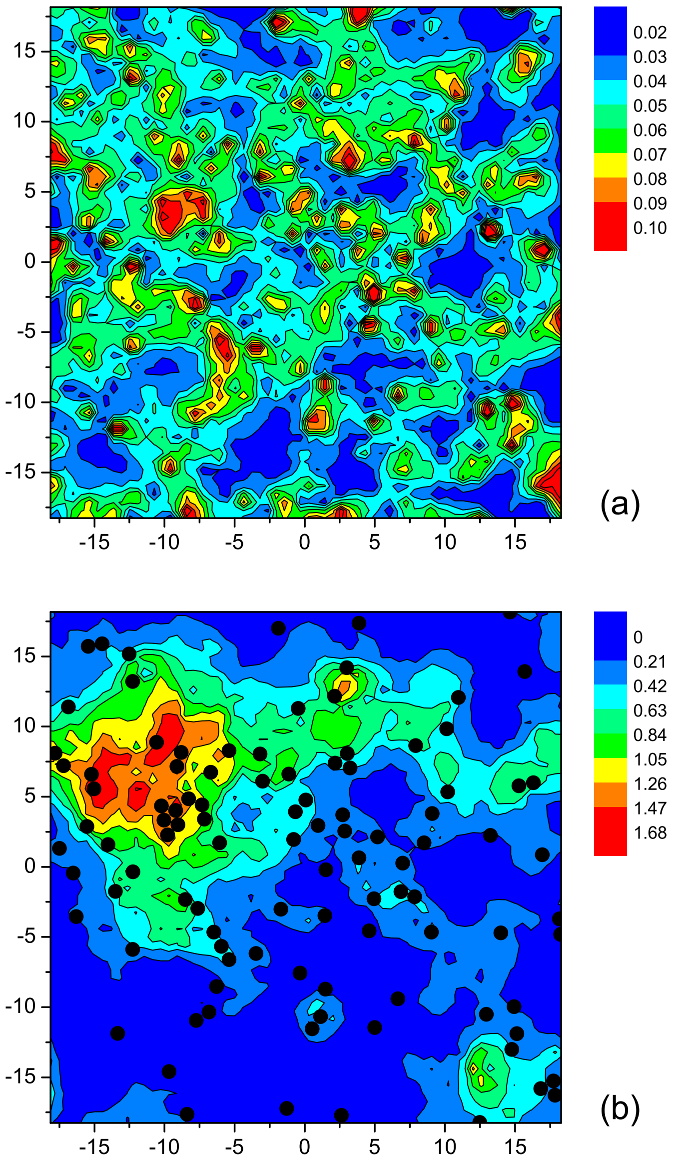

Figure 3.9: Contour plots of the spatial distribution of (a) free volume and (b) propensity for a configuration at $T = 0.4$. The black dots in (b) indicate the 10% of particles with the highest free volume. Propensities were averaged over 100 runs.

high free volume in some cases, there are clearly many ‘false positives’, i.e. particles with high free volume but low propensity. The spatial distribution of free volume and propensity are also clearly different. This is quantified in Figure 3.10(a) using the cluster analysis described in the previous section. Particles with high free volume cluster only marginally more than an equivalent number of randomly selected particles. For completeness, we repeat the subset analysis by dividing particles into 20 subsets

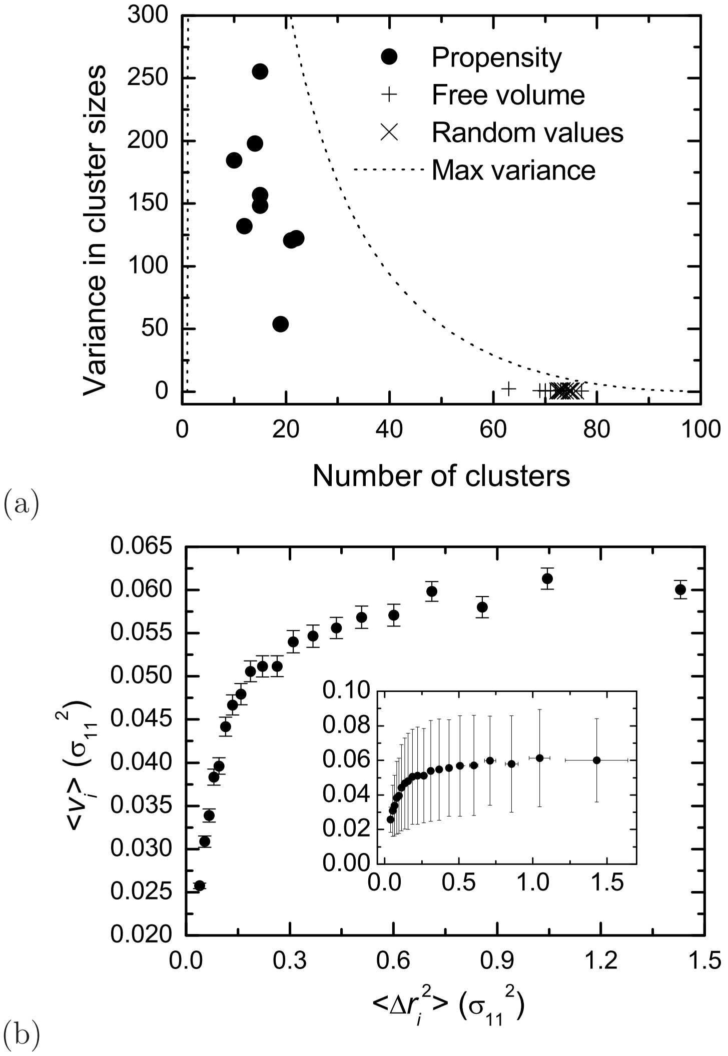

Figure 3.10: (a) Cluster measures of spatial heterogeneity for particles with propensities and free volumes in the top 10%. Data points are shown individually for ten configurations at $T = 0.4$. Statistics obtained using random values are shown for comparison. The solid line represents the maximum variance possible for a given number of clusters (see Eq. 3.1). (b) Free volume as a function of propensity. Data for ten configurations at $T = 0.4$ have been pooled together, and the particles divided into 20 subsets according to their propensities. Each subset is represented by a point in the graph. Error bars in the main graph represent one standard error. The inset shows the same data but with error bars corresponding to one standard deviation.

according to propensity and calculating the average free volume and propensity for each subset. The results are plotted in Figure 3.10(b). Similar to the potential energy analysis, there is an approximately linear correlation at low propensity followed by a rollover to a plateau with an asymptotic value of $v_i \approx 0.06$. However, the large standard deviations (see inset) clearly demonstrate that there is considerable overlap between the free volume of particles in the different propensity subsets.

In spite of this general failure of the free volume to exhibit any strong spatial correlation with the propensity, there appears to be some cause for hope. Referring to the contour plot of free volume in Figure 3.9(a), we note the presence of a significant number of isolated particles with a high free volume. These 'rattlers' are the source of most of the false positives in Figure 3.9(b). It seems reasonable to expect that the degree to which a particle can 'utilise' a neighbour's free volume depends upon the size of its own free volume. Based on this argument, one may hope to distinguish 'useful' free volume from that which cannot contribute to relaxation based on an analysis of clustering of particles with significant free volume. We therefore study the effect of coarse-graining.

3.2.4 The Effect of Coarse-Graining

Given that the local potential energy and the geometric free volume fail as predictors of the spatial variation in propensity, it makes sense to ask if we can improve the correlation by using a suitable spatial averaging. For example, Qian et al. [50] found that there was an optimal local averaging length (a coarse-graining length) for which the Pearson's correlation coefficient of density and a residence time was maximised in simulations of the low molecular weight glass-formers propylene carbonate and salol.

We coarse-grained the free volume, the potential energy and the propensity by assigning to each particle the value of the relevant property averaged over the local values for that particle and of the particles lying within a distance r of that particle. Values of r in the range $0 \leq r \leq 10\sigma_{11}$ were used. The degree of clustering, as measured by the cluster analysis described in Section 3.2.2, increases steadily with increasing r. This is a trivial consequence of the coarse-graining. The clustering observed in the particle propensity is approximately reproduced in the coarse-grained free volume and potential energy for $r = 2$.

To measure correlation, we use Spearman's rank-order correlation coefficient K [118]. This calculates a linear correlation coefficient of ranks rather than values. We use this method because it is more robust than standard linear correlation methods such as Pearson's. Also, because the distribution of ranks is known (they are uniformly distributed), it is possible to calculate the significance of non-zero values. Except for rare cases where $|K| < 0.1$, we typically obtain non-zero K values with

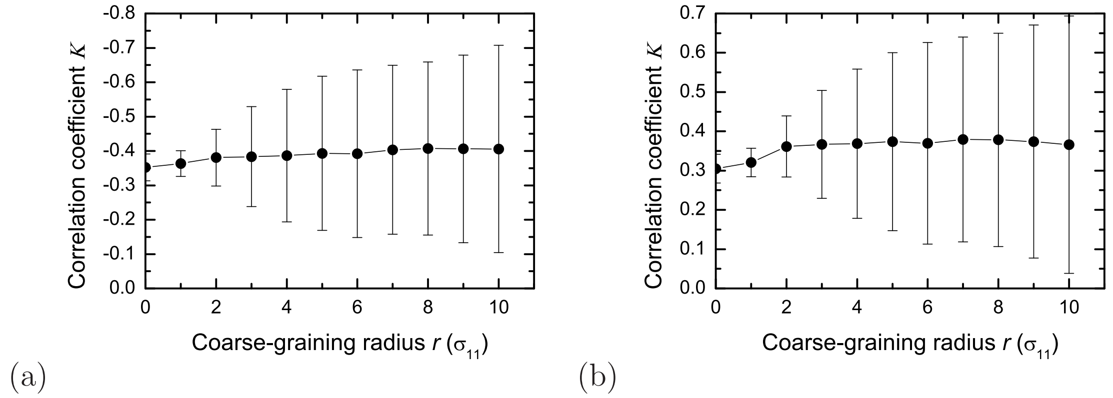

(a) (b)

Figure 3.11: Correlation between propensity and (a) potential energy, (b) free volume, as a function of coarse-graining radius r. Correlation coefficients (Spearman's rank-order correlation) have been averaged over ten configurations. Error bars represent one standard deviation.

greater than 99.9% significance. As for Pearson's correlation coefficient, K varies from -1 to 1, with 0 indicating that the two data sets are uncorrelated.

Figure 3.11(a) shows the correlation between potential energy and propensity as a function of coarse-graining radius. For the case without coarse-graining $K = -0.35$ averaged over the ten configurations studied (potential energy and propensity are anti-correlated). We find only a marginal increase in the average correlation on coarse-graining. The correlation between free volume and propensity as a function of coarse-graining radius is plotted in Figure 3.11(b). Without coarse-graining $K = 0.30$, averaged over the ten configurations studied, and there is only a small increase in the average correlation on coarse-graining. In particular, we note that while coarse-graining improves the correlation for some configurations it makes the correlation worse for others. This is evidenced by the growing standard deviation in the correlation coefficient with increasing coarse-graining radius, for both the potential energy and the free volume.

The average rank-order correlation coefficients that we find are equal to or larger than any of the (Pearson's) correlation coefficients obtained by Qian et al. [50]. Given that we find no spatial correlation between structure and dynamics in the present study, we suggest that it is unlikely that there will be any spatial correlation between the structural and dynamic measures considered in ref. [50].

In light of these results, and the analysis presented in the previous three sections, we conclude that neither the local coordination environment, local potential energy, geometric free volume, nor simple spatial averaging of the latter two, are able to predict the spatial distribution of propensity. This is despite finding correlations between all of these quantities and dynamics, as measured by the propensity, when suitable averages are taken. We find that the L06 local environment provides a strong constraint on the propensity, and that *on average* particles with lower propensity have higher potential energy, lower free volume and are dominated by large particles. However, our spatial analysis clearly demonstrates that there is insufficient correlation between these reduced measures of structure and the propensity on a *microscopic* level to be able to argue that the particular aspect of structure is the cause of the spatial heterogeneity in the propensity. While it is possible that more elaborate coarse-graining/clustering schemes may improve upon the correlation between propensity and structure, we consider it unlikely that any of these structural measures alone will be sufficient to explain the spatial distribution of dynamics.

3.2.5 Other Reduced Measures of Structure

This section describes some less common descriptions of structure that we also examined. Some interesting results are obtained, but the results are similarly negative or inconclusive as regards predicting the spatial distribution of propensity. In Section 3.3 we describe a different approach to the problem of predicting propensity.

Proximity to Particles with the L06 Environment

A number of studies suggest that relaxation times in amorphous materials are affected by proximity to boundaries. In the case of free-standing polymer films T_g is found to decrease [58], indicating that the relaxation time must be reduced by proximity to a free boundary. And a study of the correlation length of cooperative motion in the facilitated kinetic Ising model [119] found that the relaxation time close to a rigid/free wall was increased/decreased relative to the bulk. In addition, there are plenty of experimental results that find confinement of glass-formers can influence T_g [120]. Ref. [121] reviews recent computational work on the effect of confinement and also discusses some experimental results.

Therefore, motivated by the observation that a large proportion of low propensity particles have the L06 environment, and that the number of L06 particles and their degree of clustering increases with cooling, we consider the following hypothesis: that the spatial variation in dynamic propensity is dominated by the proximity of particles

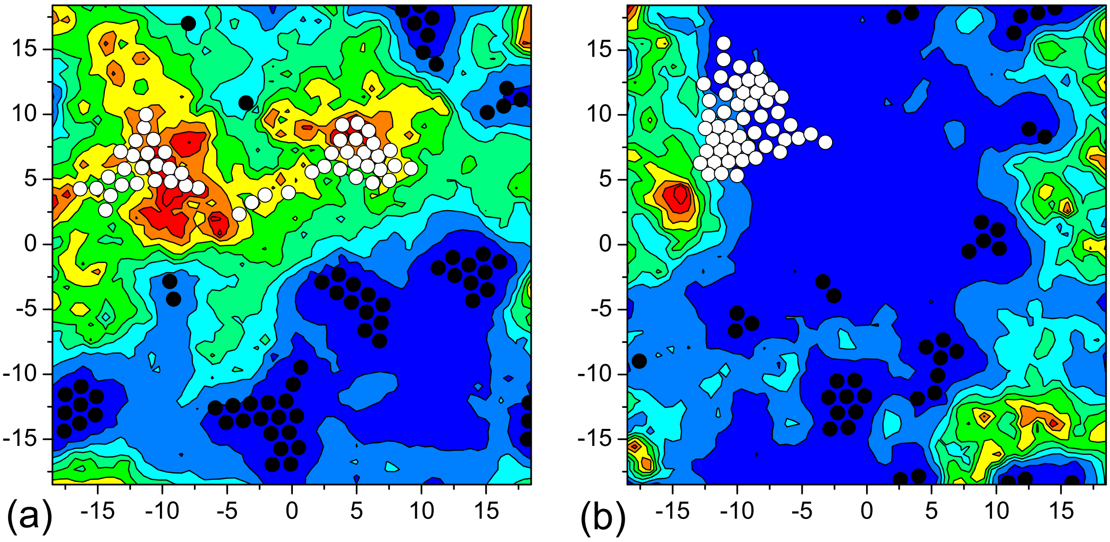

Figure 3.12: Distance from L06 particles as a predictor of the spatial distribution of dynamic propensity for two configurations at $T = 0.4$. The black circles indicate the positions of L06 particles, and the white circles indicate the 50 particles that lie furthest from these. The contour maps have been drawn to different scales to emphasise the spatial variation in propensity.

to crystalline L06 clusters, being higher in regions that are furthest away from these 'rigid walls'. We tested this hypothesis by plotting the location of L06 particles for ten configurations at $T = 0.4$ (the same configurations that were used previously) and compared their spatial distribution to the respective propensity maps. We also predicted the location of high propensity particles using several measures of distance from L06 particles. Finally, we considered the effect of including L15 particles in the analysis. The results shown here are for analysis of the inherent configurations, however very similar results are obtained from analysis of the instantaneous configurations since the local particle environments only change rarely during the conjugate gradient quench.

In Figure 3.12 we plot contour maps for the propensity for two configurations at $T = 0.4$ along with the location of particles with the L06 environment (black circles) and the location of the 50 particles (white circles) that lie furthest from *any* L06 particle. This measure does well at predicting the spatial distribution of propensity for the configuration plotted in (a), but poorly for the configuration plotted in (b). These results are typical of what we find for the other configurations. Sometimes distance from L06 particles is a good predictor of propensity and sometimes it is a poor predictor. Including particles with the L15 environment in the analysis, by identifying those particles furthest from any L06 or L15 particle, improves the prediction of high mobility for some configurations but does not work in general, e.g. for the configuration in (b).

We also considered a more complex scoring function for predicting the location of high propensity particles in the following. The score for each particle i is calculated as

$$P_i = \sum_{j=1}^{N} \exp^{-r_{ij}/\eta} \delta(\vec{r_i} - \vec{r_j}) \tag{3.2}$$

where the sum if taken over all the particles with the L06 local environment (or the L06 and L15 environments), $r_{ij} = |\vec{r_i} - \vec{r_j}|$ is the distance between particles i and j, η is a weight parameter for the distance, and the delta function ensure the score is 0 if $i = j$. The higher the score the more mobile the particle is predicted to be. We considered η values in the range 1–5, but found no improvement with this measure. With $\eta = 1$ we obtain results that are very similar to the simple minimum distance criterion used above, and we expect the results to approach those above as η approaches 0. And with $\eta = 5$ we found that the high propensity particles were predicted to lie in almost the same position for all configurations.

In general, clusters of hexagonally-packed large particles influence the dynamics by strongly defining where regions of high propensity cannot be located, however they do not appear to strongly influence which of the remaining configuration will have high propensity. We therefore propose that at low temperature there are special configurations that impart high mobility, e.g. when high propensity particles are found very close to L06 clusters they often appear to be part of a group of particles rotating about a single central particle.

The Force Network

Alexander [122] has argued that the relaxation of internal stresses is the most important mechanism in 'selecting' the structure of the amorphous state and in determining its stability. With this in mind, Kustanovich, Rabin and Olami [123] have studied atomic bond tensions in 2D and 3D binary Lennard-Jones glasses at zero temperature and argued that they are not randomly distributed, but instead associated with directional correlations in the nearest neighbour interactions. While they do not explicitly consider dynamics, they make the interesting point that isotropic measures

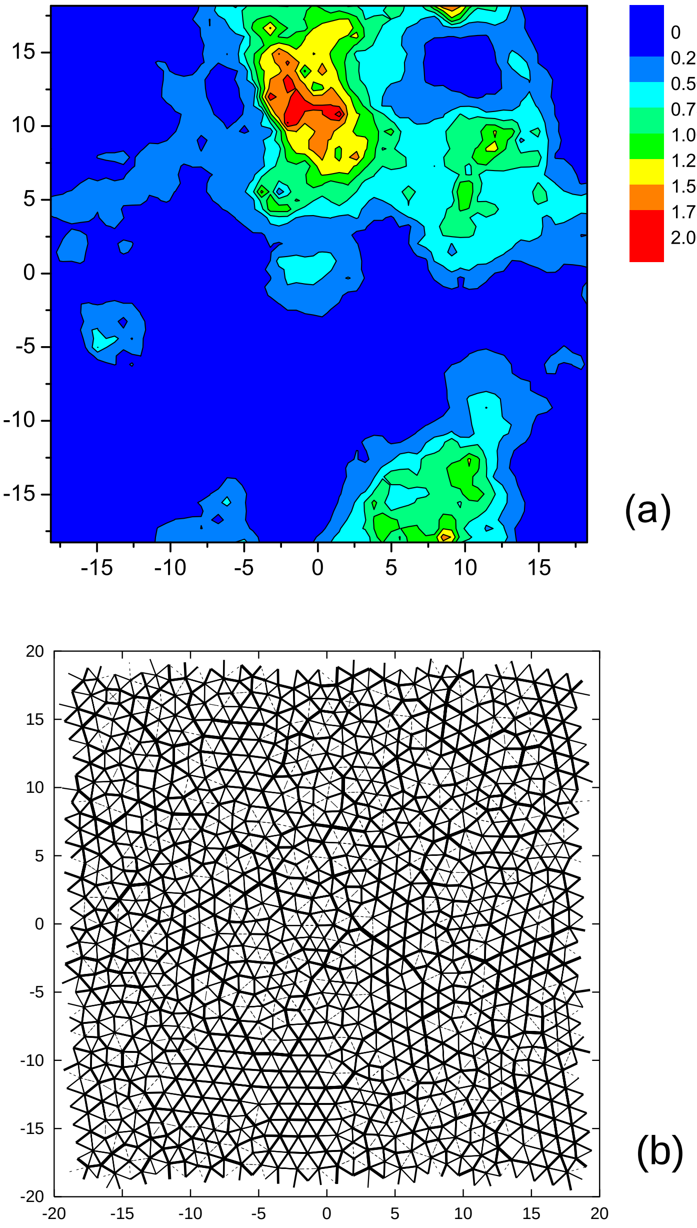

Figure 3.13: (a) The propensity map for a configuration at $T = 0.4$, and (b) the force network for the same configuration. The thickness of the lines connecting particles is proportional to the force between them. Propensities were averaged over 100 runs.

of disorder (which include free volume, local potential energy and local composition) will fail to take into account such correlations. We consider the relationship between the force network and the spatial distribution of propensity as a first step towards investigating whether anisotropic bond tensions are responsible for the spatial variation in dynamics. The results presented here do not form a complete study, but rather serve to indicate some directions in which this work could be continued.

In the purely repulsive soft-disc model that we study all ‘bond’ tensions are negative. We therefore consider the force network instead, where the force between two particles i and j is given by

$$F_{ij} = -\frac{dU(r_{ij})}{r_{ij}} = -J_{ij} \tag{3.3}$$

$U(r_{ij})$ is the interparticle potential, r_{ij} is the distance between i and j, and J_{ij} is the ‘bond’ tension. We calculate the force between each pair of neighbouring particles for the inherent structure of a configuration at $T = 0.4$. The force network, shown in Figure 3.13(b), is represented by connecting neighbouring particles with a line whose thickness is proportional to the force between them. The spatial distribution of propensity for the same configuration is shown in plot (a). While there is no obvious correlation between the force network and the propensities, it is difficult to analyse the anisotropy visually and further numerical analysis may yield more insight and may be worthwhile. Interestingly, we found no correlation between the magnitude of the net force on a particle (in the instantaneous configuration) and its propensity.

3.3 The Single-Particle Debye-Waller Factor as a Measure of Structural ‘Looseness’

As we have demonstrated, local structural measures fail to predict the spatial distribution of propensity. We therefore reconsider the question of what determines a particle’s ability to move. Ultimately, this must be associated with the degree to which particles are constrained by their surroundings. The hypothesis that potential energy or free volume would correlate with local mobility rests on the expectation that these local scalar measures capture an essential aspect of this constraint. Having found this not to be the case, we now consider the nature of local constraints explicitly.

Thorpe [124,125], building on earlier work of Maxwell [126] and Phillips [127], has shown how the lack of full constraint in network glass-formers is manifest as floppy modes, an observation that appears to offer a connection between a configuration and its dynamic heterogeneity. However, this constraint counting has not been applied to glasses stabilised by dense packing (as opposed to directional bonds) because of the unsolved problem of identifying local constraints in the former case. Brito and Wyart [128] have recently made some progress on this problem, reporting that the stability of a hard sphere glass can be related to that of networks of elastic bonds through the use of a time-averaged effective potential. On the other hand, Donev et al. [129] have developed an algorithm for testing whether a large continuous deformation of a hard-disc configuration is possible. These deformations, however, are highly collective and their algorithm is unable to single out dynamically significant motions associated with a small number of particles. We will sidestep this problem by looking directly for floppy modes, rather than trying to quantify the constraints responsible. The central question then becomes, is there a spatial correlation between the floppy modes (a measure of the short-time dynamics) and the propensity (a measure of the long-time dynamics)?

There is already experimental evidence that the short-time dynamics of particles can provide information about the long-time behaviour of a system. Buchenau and Zorn have reported that in selenium the mean-squared particle displacement, $< u^2 >$, scales with the viscosity, η, as

$$\eta = \eta_0 exp(C/[< u^2 >_{crystal} - < u^2 >_{liquid}]) \tag{3.4}$$

over many order of magnitude in η [130]. Subsequently, a range of polymeric and small molecule glass-formers have also exhibited strong correlations between the short-time fluctuations associated with the Debye-Waller (DW) factor and the viscosity [131]. And there are other reports in the literature of correlations between the DW factor and fragility [132], the non-ergodicity parameter and fragility [133], and between the shape of the interaction potential and both the fragility and the non-ergodicity, thus tying the latter two results together [116].

Here we provide evidence that such correlations between short- and long-time dynamics can exist at a *microscopic spatial level*. This is especially noteworthy considering that all the other macroscopic correlations that we have tested - between propensity and composition, free volume and potential energy - do not hold at the microscopic level.

3.3.1 Predicting Propensity on the Basis of Short-Time Heterogeneities

To characterise the short-time dynamics, we again consider an isoconfigurational ensemble of runs, all starting from the same 'equilibrated' configuration, with random initial momenta chosen from the appropriate Maxwell-Boltzmann distribution. However, in contrast to the propensity, we consider much shorter runs and study the variance in the particle positions. In this way, we define a particle Debye-Waller (DW) factor.

The DW factor is a standard measure of displacement fluctuations in solids, defined as the mean-squared deviation of an atom from its equilibrium position, averaged over all particles. Thus, one may write the DW factor as $<< (< \vec{r}_i > - \vec{r}_i(t))^2 >>$, where $\vec{r}_i$ is the instantaneous position of particle i, the inner angle brackets $<>$ and $< \vec{r}_i >$ refer to the time average and the outer brackets denote an average over particles. To calculate a DW factor for each individual particle in a configuration, we use a similar definition, except now the outer brackets indicate an average over an isoconfigurational ensemble of runs. We shall refer to this variance in the position of a single particle as the particle DW factor, i.e.

$$DW_i =<< (< \vec{r}_i >_{time} - \vec{r}_i(t))^2 >_{time}>_{ic}, \tag{3.5}$$

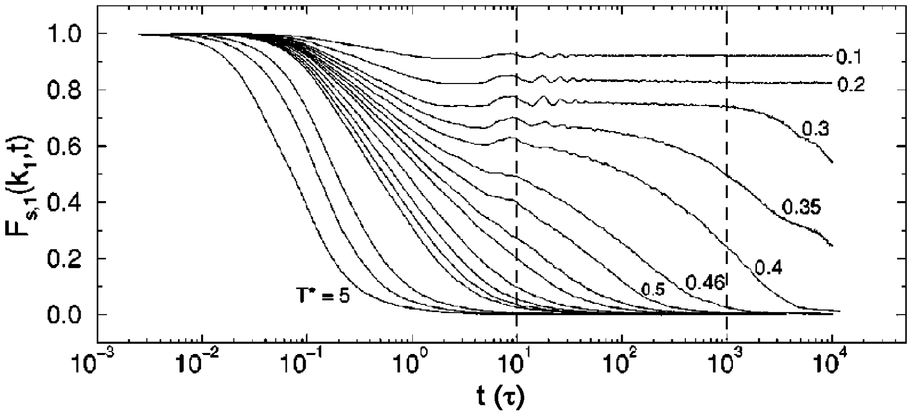

Figure 3.14: The incoherent scattering function as a function of temperature for the small particles in the 2D mixture. The times used to define the local DW factor (10τ) and the propensity (1000τ) at $T = 0.4$ are indicated by dashed vertical lines. Figure reproduced (with modifications) from ref. [44].

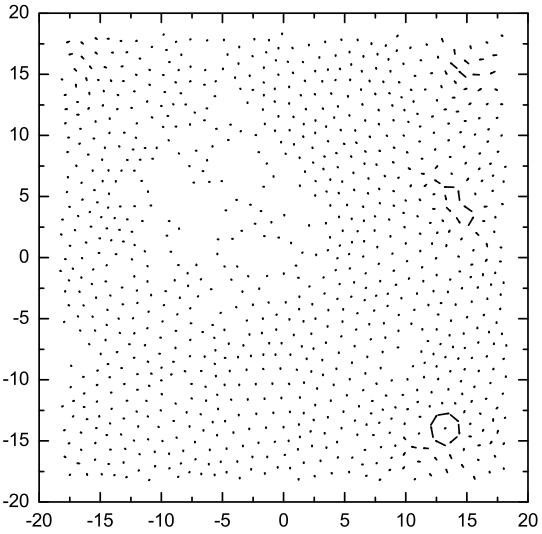

Figure 3.15: Particle displacement vectors connecting the inherent structures belonging to configurations at either end of a 10τ Debye-Waller run at $T = 0.4$. The vectors are drawn as arrows pointing from the initial to final particle positions.

where the time average is taken over the selected time interval and the isoconfigurational average is taken over the multiple trajectories. All results presented in this section are calculated using an ensemble of 100 runs.

We choose a runtime that lies in the middle of the characteristic plateau region in the log-log plot of the mean-squared displacement, and in the log-linear plot of the incoherent scattering function, and is therefore a characteristic time for fast β relaxation. At $T = 0.4$ we use a duration of 10τ to calculate the particle DW factors, which is two orders of magnitude shorter than the 1000τ runtime used to calculate the propensities. The incoherent scattering functions for the 2D mixture, with run times indicated, are shown in Figure 3.14. For reference, the structural relaxation time τ_e (the time at which the incoherent intermediate scattering function has decayed to $1/e$, and therefore a characteristic time for the primary α relaxation) is 673τ at $T = 0.4$.

From comparison of the inherent structure (IS) configurations at either end of the 10τ intervals, we find that this time roughly corresponds to the first 'escape' from the initial IS, involving a small localised reorganisation of particles. In Figure 3.15 we show the displacement vectors connecting IS configurations at either end of a DW run. Note the small localised rearrangements that consist mostly of displacements of less than one particle diameter. Analysing a small sample of runs we find they all end

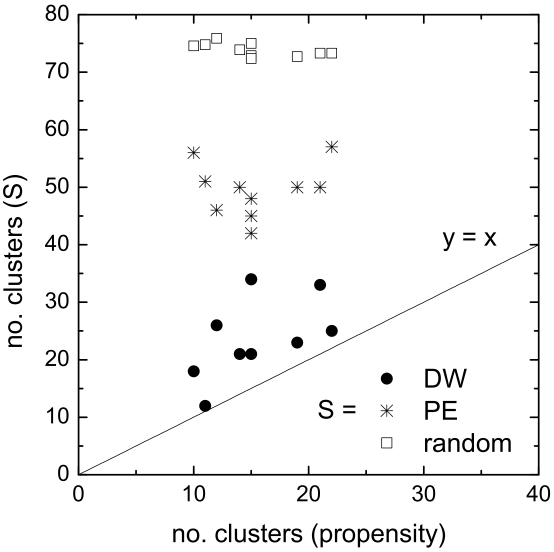

Figure 3.16: A cluster analysis of the spatial distribution of propensity, Debye-Waller factors (DW), and potential energy per particle (PE) for ten independent configurations at $T = 0.4$. 'Random' refers to the number of clusters generated by random samples of 102 particles.

up in different IS's to the initial configuration, and that most of these are unique.

We repeat the cluster analysis described in Section 3.2.2 for the particle DW factors, and compare the clustering of the DW in Figure 3.16. The DW factors result in a relatively small number of clusters, evidence of a substantial and non-trivial heterogeneity, and the number of these clusters is quite similar to that produced by the propensities and significantly smaller than that produced by the PE and random samples. Next we consider how well the local DW factors predict the spatial distribution of the propensity.

To use the DW factors as a predictor of propensity we shall require them to meet two criteria: they must exceed a Lindemann-like threshold of 0.035, which is similar to values obtained for a soft-sphere mixture near T_g [134], and the particles must be in a cluster of three or more particles. Our Lindemann-like threshold is inspired by the observation that crystals can sustain a maximum vibrational amplitude before they melt. This maximum vibrational amplitude, equivalent to the bulk DW factor relative to the interparticle spacing, is usually referred to as the Lindemann criterion [135]. Here we use a similar threshold with the aim of identifying local 'melting', in the sense of local particle mobility. We note that Stillinger [136] has suggested and studied an alternative definition of the Lindemann parameter, that can be extended into the high temperature liquid phase, based on intrabasin vibrational displacements of the inherent structures accessible at a given temperature. Our minimum cluster criteria is to reflect the fact that any substantial displacement in a dense liquid will require more than one particle to be mobile. In 2D the smallest group of particles that can locally rearrange is three.

We find that the selected particles do very well at predicting the spatial variation of the propensity. In Figure 3.17 we compare the prediction of high propensity using the particle DW factors (black circles) with the propensity maps for six independent configurations. Most regions of high propensity are identified by the selected particles, and very few points lie in regions of low propensity. Compare this to the predictions of high propensity based on the potential energy or free volume maps and the improvement is obvious.

Our data supports the proposition that the high DW regions represent the precursors to the long-time motion, and that the subsequent propagation of the consequences of these ‘seed’ motions is not readily accessible from the initial configuration, hence the coarse-grained character of the DW factors’ predictive success. Interestingly, in a study of a supercooled Lennard-Jones (LJ) liquid, Kob et al. [46] found that the *alpha*-relaxation time of particles with high mobility (measured on the timescale of the maximum in the non-Gaussian function) was on the order of the end of the *beta* relaxation time of the bulk. Thus, it appears likely that there will also be spatial correlation between the short-time and long-time dynamics in this attractive 3D glass-former. Additionally, Vollmayr-Lee et al. [137] have studied the same binary LJ system below the glass transition, characterising the particle mobility via a measure similar to our local Debye-Waller factor but averaged over multiple time intervals rather than multiple runs, and found that the dynamics was spatially heterogeneous. They found that those particles with high vibrational amplitude formed clusters that were compact relative to the lower-dimensional dynamic structures found for the same system above T_g. This is similar to our observation of relatively compact clusters of particles with similar mobility, as measured by the particle DW factor and propensity, relative to the structures found in single trajectories. Furthermore, Vollmayr-Lee and co-workers speculated that the clusters of highly mobile particles below T_g may be the nucleation point of the large scale motions found above T_g. Here, we have demonstrated that *above* T_g the short- and long-time propensities for motion are spatially correlated. We therefore conclude that it is likely that the compact

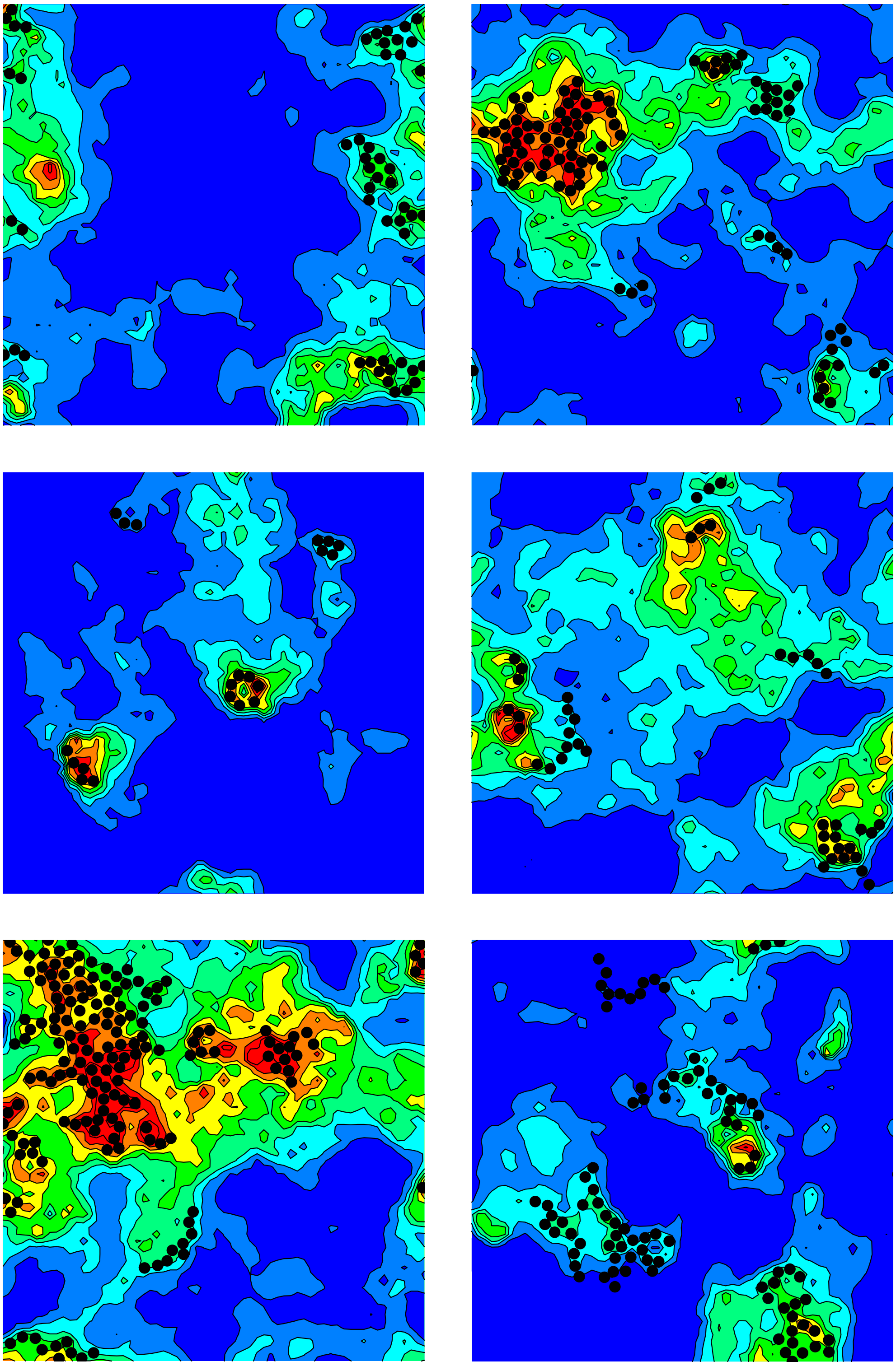

Figure 3.17: A comparison of the predictions of high propensity (filled circles) based on the local Debye-Waller data as described in the text with the actual propensity distributions for 6 independent configurations taken from an equilibrated system at $T = 0.4$. The colour scale is the same for all plots.

mobile clusters found in ref. [137] below T_g are indeed the nucleation point of the large scale motions found above T_g, and that the spatially heterogeneous distribution of these nucleation points is directly due to something in the structure. Laird and Schober [138] have reported spatial clustering of low-frequency modes in a quenched soft-sphere model glass, which suggests that the same relationship may also exist in one-component glass-formers. And Weeks et al. [139] have studied a colloidal glass-former and observed statistically similar clusters of mobile particles on the timescale of the β relaxation in *both* the supercooled liquid and glassy states. This could possibly be experimental evidence for the same relationship between structure and dynamics that we have described here.

3.3.2 Time Evolution of the Debye-Waller Factor

While much effort has gone into studying dynamic heterogeneities in supercooled liquids, little work appears to have been devoted to the time evolution of the dynamic heterogeneities in space. Doliwa and Heuer [47] have studied the time evolution of dynamic heterogeneities in a polydisperse hard-disc system. They found that clusters of slow particles can persist for very long times (up to $1300\tau_e$), that the dynamics of slow clusters are sub-diffusive and highly restricted in space, and that particles leave and join the cluster during its lifetime. In contrast, few particles leave and join clusters of fast particles during their comparatively short lifetime, and they undergo relatively little translational motion.

We have used our definition of a local DW factor to study the time evolution of dynamic heterogeneities at $T = 0.4$. In Figure 3.18, we plot the spatial distribution of DW factors for six configurations separated from each other by the timescale of a DW run (10τ). What is striking is that there are substantial changes in the spatial distribution of mobility over this short timescale. 'Loose' red regions disappear from one configuration to the next, sometimes to reappear again later. And new red regions appear that are not next to any existing red regions. Some configurations, such as the one in (f), have very few 'loose' regions. The timescale over which the distribution of DW factors changes is also significant. Although the system is able to move from one inherent structure (IS) to the next over 10τ, little diffusion of particles is able to take place during this time. Therefore, whatever it is that allows a susceptible subset of particles to become mobile must be able to be transmitted through space without the intervening particles moving substantially. This strongly suggests that the transfer

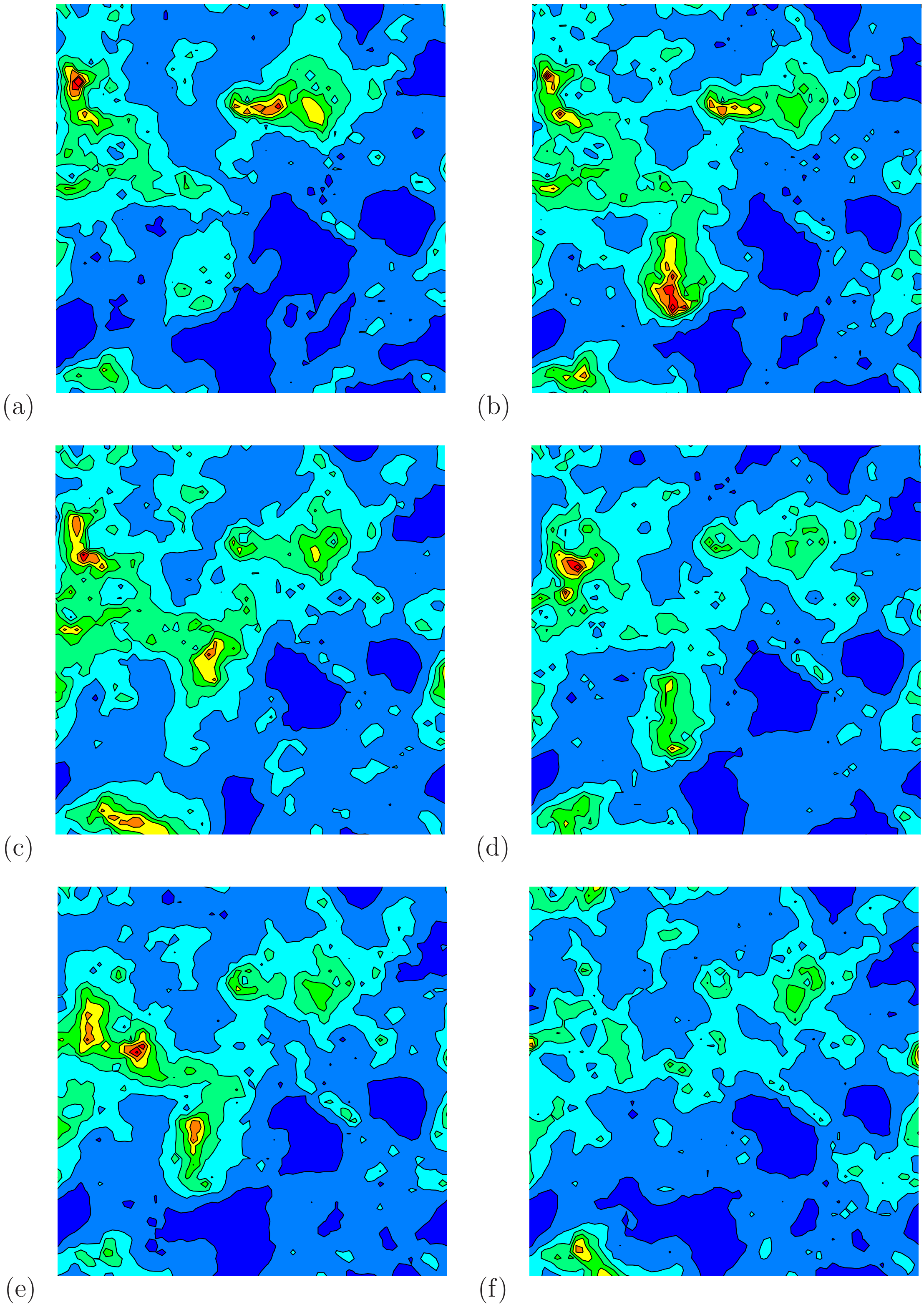

(a) (b)

(c) (d)

(e) (f)

Figure 3.18: Time evolution of the spatial distribution of DW factors at $T = 0.4$. The configurations used to generate plots (a)–(f) are separated from each other by 10τ, i.e. the timescale of a DW run. Ensembles of 100 runs were used to calculate the DW factors.

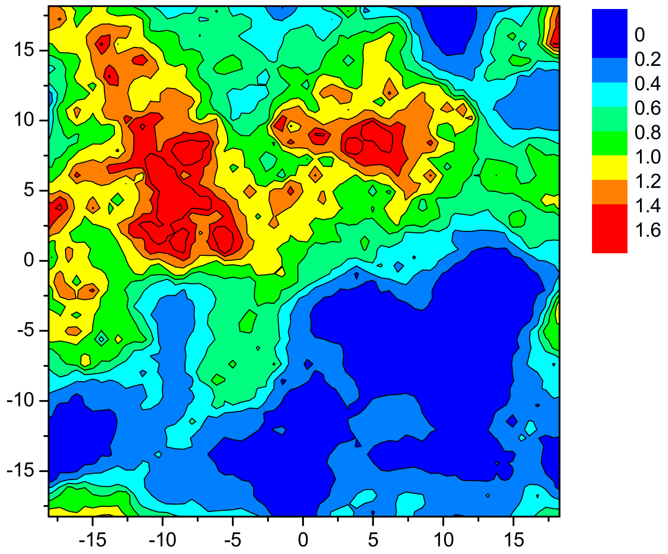

Figure 3.19: The spatial distribution of propensity at $T = 0.4$ for the configuration used to start the time series of DW maps shown in Figure 3.18. Propensities were calculated using an ensemble of 100 runs.

of mobility through the system cannot be explained simply in terms of the concept of defect diffusion [140], i.e. the transfer of some structural defect that allows for particle mobility. Note that it is this latter mechanism that operates in crystalline materials, in the form of the diffusion of vacancies and interstitials [141], and which, in a more abstract sense, is the picture built into facilitation models [71–73].

From the rapid change in the location of mobile regions in the DW maps it seems likely that the effect of the initial configuration on mobility changes faster than the timescale used to calculate the propensity. An obvious question to ask, then, is why does the DW factor predict the spatial distribution of propensity as well as it does? We suggest that this is because: (i) large regions of the structure, with low probability for motion, remain largely unchanged during most runs even after the longer α-relaxation time, and therefore still retain 'memory' of the initial configuration; (ii) as a result, the fast motion is confined to the remaining parts of the structure, resulting in the larger length scale of spatial heterogeneity in the propensity maps compared to the DW maps; and (iii) the propensity will retain 'memory' of the effect of the initial configuration on dynamics long after the instantaneous dynamics has forgotten about the initial structure, since the propensity will not become uniform until all regions have moved the same amount on average, i.e. the initial motion is included in the propensity and needs to be averaged out by motion that no longer remembers the initial configuration and this won't happen until some time *after* the slowest regions become fast. For comparison, we have plotted the propensity map for the initial configuration used to start the time series of DW maps in Figure 3.19.

Considering the time evolution of the DW maps and the propensity maps for different configurations at $T = 0.4$, a natural dynamic hierarchy of domains can be identified. On short times, these are those that never become mobile (e.g. regions of hexagonally packed large particles), those that are mobile at any given moment, and those that have the potential to become mobile. On the longer timescale of the propensity maps this hierarchy can be extended. The slowest regions to relax are the crystalline L06 clusters, which remain largely intact over the $675\tau_e$ that separate the configurations studied at $T = 0.4$. Then there are non-L06 regions that remain slow on the timescale of the propensity ($1.5\tau_e$), but which relax on a timescale shorter than the $75\tau_e$ between configurations. Next come the regions in the DW maps that have the potential to be 'loose' over short times, and finally those that have a high probability of significant relaxation over longer times (the high propensity regions). The similarity between the DW and propensity maps described in Section 3.3.1 tells us that although the spatial distribution of short-time mobility changes rapidly, the 'loose' spots remain confined to certain regions of the sample over much longer times.

In light of these results, the following questions still await a satisfactory explanation: (i) what determines the susceptibility of a particle region to mobility? and (ii) what is it that can allow a susceptible subset of particles to become mobile and that can be transmitted long distances through space without significant particle motion? Answers to these questions may also help to explain why some non-L06 regions remain slow on the timescale of the propensity.

Continuing the idea of 'stick' and 'slip' introduced in Section 2.4, we suggest that at $T = 0.4$ the most mobile regions can be viewed as marginally stable states in the sense that they are able to 'stick' the configuration, i.e. to not allow diffusional motion in a given run, but more often that not become mobile, i.e. 'slip'. Since their stability is not optimised their structure is also not likely to be unique. This wealth of structural possibilities may help to explain why none of the simple structural measures that we have tested have been able to predict the spatial distribution of propensity. The hierarchy of dynamic domains would then imply a hierarchy of states of different stabilities. This picture of marginally stable states would also explain why mobility is able to occur, and to be transferred, via small-scale rearrangements in the supercooled liquid. In contrast, in crystalline materials - which have unique optimised structures - motion can only occur via large-scale rearrangements. We note that Nagel and co-workers have also discussed the idea of marginal stable states in the context of granular materials and glasses. See ref. [142] and references therein.

Given that the DW factor is perhaps a better reflection of the effect that an instantaneous configuration has on the dynamics, one may ask whether the structural measures that we have considered are able to predict its spatial variation. The simple answer is, not in general. In the next section we present a direct comparison of the DW factor and free volume, since this directly addresses a correlation reported in the literature between the bulk averages of these two quantities. Additional spatial plots of propensity, DW factors, free volume, potential energy and inherent structures at $T = 0.4$ can be found in Appendix B.

3.3.3 Free Volume cannot Explain the Spatial Heterogeneity of Debye-Waller Factors

As described in the introduction, the free volume concept has been both popular and successful at a phenomenological level, yet there remains a persistent problem concerning the application of free volume to describe dynamics. In particular, what is the relationship between the geometric free volume - a quantity that can be well defined at the atomic scale - and the phenomenological free volume (a macroscopic quantity that is derived from the bulk density)? We address this question here.

For hard disc and sphere systems, and for systems that can be mapped to these, it is possible to define the local free volume unambiguously, as the volume accessible to a particle with all its nearest neighbours fixed in place [117]. Using this method, Starr et al. [80] recently found a power law relation between the average free volume and the bulk averaged short-time mean-squared displacement for monomers in a 'bead-spring' model of a glass-forming polymer over a range of temperatures. This success of the free volume idea was qualified by their failure to find any significant correlation between the mobility of a specific monomer and its local free volume. In this section we use our definition of the local DW factor to test for a causal relationship between the geometrical free volume and the short-time dynamics. We then discuss the relationship between the geometrical and the phenomenological free volume in the context of our results.

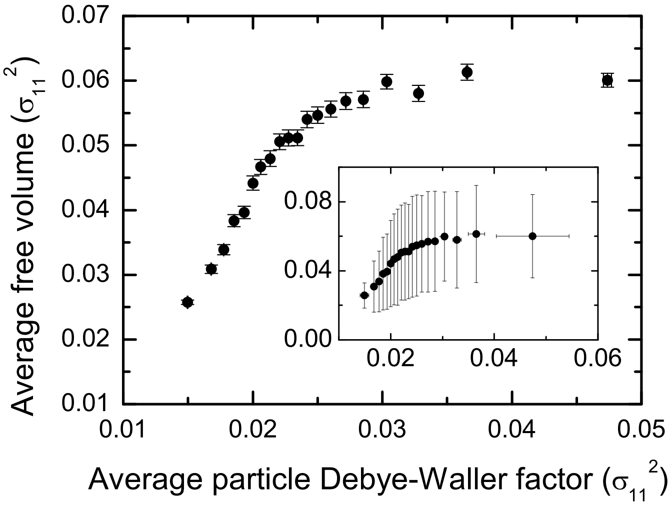

Figure 3.20: Free volume as a function of particle Debye-Waller factor. Data for ten configurations at $T = 0.4$ have been pooled together, and the particles divided into 20 subsets according to their DW factors. Each subset is represented by a point in the graph. Error bars in the main graph represent one standard error. The inset shows the same data but with error bars corresponding to one standard deviation.

We calculate the particle DW factors and local free volume, as described previously, for ten well-spaced configurations at $T = 0.4$. As shown in Figure 3.20, we find a smooth monotonic relation between the particle DW factor and the average free volume when particles are divided into 20 subsets according to their DW factors. For values of the DW factor up to about 0.022 this relationship is linear, a result analogous to that found in Starr et al. [80]. In addition, our work identifies an upper bound on the average particle free volume of about 0.06. This is visible as a plateau for DW factors above 0.03. We note that the maximum value of the DW factor, and hence the length of this plateau, increases with increasing time interval used to calculate the DW factor. For example, compare this plot to the one in Figure 3.10(b). Our results certainly support the phenomenological results of a strong connection between free volume and dynamics. The data also appear to support the idea that there is a well-defined threshold value of free volume or particle DW factor, above which large amplitude displacements occur.

This interpretation fails, however, when applied on a particle-by-particle basis. To see this, consider the standard deviation of the free volumes shown in the insert in Figure 3.20. Clearly, the free volume in a given dynamically defined subpopulation exhibits substantial fluctuations. Particles with wildly varying free volumes can

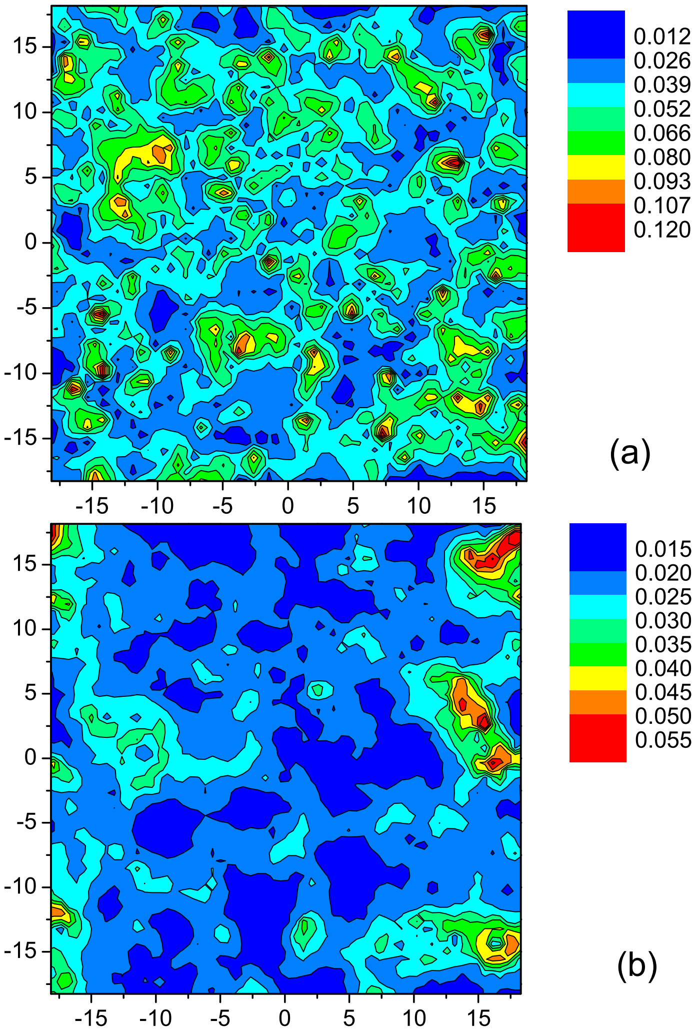

Figure 3.21: Contour plots of the spatial distribution of (a) free volume and (b) particle Debye-Waller factors for a configuration at $T = 0.4$. There is some spatial correlation between regions with low free volume and low DW factors but not in general between regions of high free volume and high DW factors.

exhibit similar values of the DW factor. We conclude that a particle's mobility, as characterised here by the DW factor, is not the result of its geometric free volume. As the amplitude of a particle's DW factor is a measure of the degree to which it is constrained by its surroundings, we conclude that the geometric free volume of that particle can only provide a haphazard glimpse of the degree of that constraint.

Our conclusion, that the variations between particles in terms of their geometric free volume cannot explain the variations observed in their DW factors, is supported by consideration of the spatial distribution of the two quantities. In Figure 3.21 we show contour maps for the free volume and the DW factor for a configuration

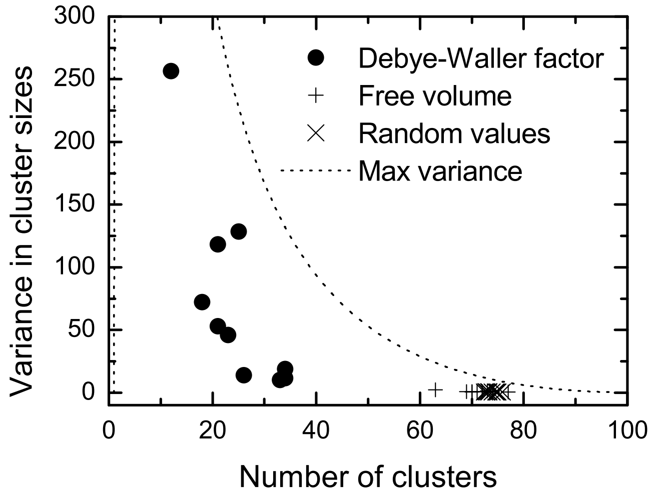

Figure 3.22: Cluster measures of spatial heterogeneity for particles with Debye-Waller factors and free volumes in the top 10%. Data points are shown individually for ten configurations at $T = 0.4$. Statistics obtained using random values are shown for comparison. The dotted line represents the maximum variance possible for a given number of clusters (see Eq. 3.1).

at $T = 0.4$. There is a clear difference in the characteristic length scales of the distributions with the DW factors exhibiting significantly stronger clustering than the free volume.

We have quantified this observation using the cluster analysis described previously (see Section 3.2.2). Figure 3.22 shows the results of the cluster analysis for the free volume and the particle DW factor for the ten configurations. Particles with high free volume show no significantly greater clustering than an equal number of randomly selected particles. In contrast, particles with high DW factor show significantly more clustering. These results, in addition to highlighting the absence of any significant correlation between a particle's free volume and its DW factor, point to the source of the problem. The clear spatial clustering of those particles with large DW factors is evidence of the cooperative character of even this short-time dynamics. The geometrical free volume fails to capture the subtle configurational features that result in enhanced local motion.

If the geometric free volume fails as a predictor of the local dynamic heterogeneity because the latter relies strongly on non-local correlations, can we improve the relevance of the free volume by using a suitable spatial average? For example, as mentioned in Section 3.2.4, Qian et al. [50] found that there was an optimal local

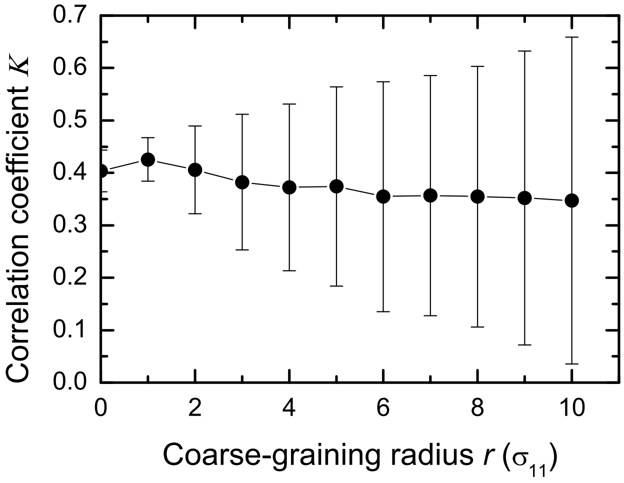

Figure 3.23: Correlation between free volume and particle Debye-Waller factor as a function of coarse-graining radius r. Correlation coefficients (Spearman's rank-order correlation) have been averaged over ten configurations. The error bars represent one standard deviation.

averaging length (a coarse-graining length) for which the Pearson's correlation coefficient of density and a residence time was maximised.

We have coarse-grained the free volume and the local DW factor, in the same way that we coarse-grained the propensity and local potential energy, by assigning to each particle the value of the relevant property averaged over the local values for that particle and of the particles lying within a distance r of that particle. We consider values of r in the range $0 \leq r \leq 10\sigma_{11}$. The degree of clustering as measured in Figure 3.22 increases steadily with increasing r. This is a trivial consequence of the coarse-graining. The clustering observed in the particle DW factor is approximately reproduced in the coarse-grained free volume for $r = 2$.

To measure correlation, we again used Spearman's rank-order correlation coefficient K [118]. This calculates a linear correlation coefficient of ranks rather than values. For the case without coarse-graining we find a value of $K = 0.40$, averaged over the ten configurations studied. Readers are reminded that we have already demonstrated that there is no strong correlation between the scaled free volume and the particle DW factor through the comparison of spatial maps and the cluster analysis. As shown in Figure 3.23, we find no increase in the average correlation between the free volume and the particle DW factor on coarse-graining. The short-comings of geometric free volume as a predictor of dynamics, we conclude, are not to be corrected by simple spatial averaging.

We conclude that, in this 2D glass-former, having a larger free volume does not cause a particle to exhibit larger amplitude fluctuations in position. Rather, as the correlation between averages over subsets indicates, it only increases the likelihood that the reduced local constraints necessary for large amplitude motion might apply. Even over the short timescales studied here, collective (i.e. non-local) processes are important and these are not well correlated with a purely local measure such as free volume. For this reason, we believe that the results reported here are likely to be common to many glass formers.

In most of its popular usages, however, the phenomenological free volume refers, not to an explicit geometrical volume, but to a reduction of mechanical constraints on particle motion. In this sense, the single particle Debye-Waller factor that we have defined in this chapter probably provides the better match, since it is an explicit measure of particle constraint, even if it lacks a purely geometric definition. If one accepts this proposition - that it is the particle DW factor rather than the geometrical free volume that provides the better microscopic expression of the phenomenological free volume - then the outstanding question for developing a microscopic treatment of dynamics in glassy materials is to see if there exists a method for predicting the particle Debye-Waller factors from a given configuration that is algorithmically simpler than the dynamic averages presented in Section 3.3.1.

3.4 Discussion and Conclusions

In this chapter we have sought to identify a measure of the configuration that can predict the spatial pattern of propensity for the 2D binary mixture. We have examined the local coordination environment, local potential energy and local free volume, and coarse-grained versions of these, as well as the proximity to 'rigid' L06 clusters. In addition, we have used our isoconfigurational approach to examine whether the correlations observed in simulations and experiments between bulk averaged quantities (structural versus dynamic, and dynamic versus dynamic) persist at a microscopic level, in the sense that they are spatially correlated. Such microscopic correlations, we argue, must be present for any causal relation to exist between the two quantities.

While we found that high and low propensity was clearly associated with small and large particles, respectively, and that the L06 local environment provides a strong constraint on the propensity, some property other than local coordination environment must also be involved. Most environments provide little constraint on the particle propensity, and particles with a given propensity can be found among most of the 23 different types of local environment. We also found that *on average* particles with lower propensity have higher potential energy, lower free volume and are dominated by large particles. However, our spatial analysis clearly demonstrates that there is insufficient correlation between these reduced measures of structure and the propensity on a *microscopic* level to be able to argue that any of these aspects of the structure are the cause of the spatial heterogeneity in the propensity.

This inability of local measures to predict the spatial distribution of propensity is perhaps not surprising. With increasing supercooling the particle motion becomes increasingly collective. The degree to which a particle is constrained must therefore depend not just on the arrangement of neighbours, but also on the degree to which those neighbours themselves are constrained, which in turn requires consideration of the neighbours' neighbours, and so on. Naively, one would expect coarse-graining to provide a non-local extension of, for example, the free volume that reflects this cooperativity and distinguishes 'rattlers' from those particles whose free volume is available for collective reorganisation. Yet we found that simple coarse-graining does not in general improve the correlation between structure and propensity. While the prediction of propensity improved for some configurations it become worse for others.

We therefore conclude that neither the local composition, local potential energy, geometric free volume, nor simple spatial averaging of the latter two, are able to predict the spatial distribution of propensity. The best we can say is that there are definite packings that in general inhibit motion, which can be topologically defined as L06 clusters. There also appear to be definite things in the structure that in general make motion more likely, however these cannot be simply understood in terms of accumulation of free volume, low potential energy, special environments, or distance from 'rigid' clusters.

With this failure of reduced measures of structure to predict the spatial distribution of propensity, we defined a direct measure of structural looseness in the form of the local Debye-Waller (DW) factor. Invoking criteria inspired by a heterogeneous extension of the Lindemann melting criterion for amorphous materials, we have shown that the DW factors provide an excellent predictor of the spatial distribution of the high propensity domains in each configuration studied. This success is the more striking when compared with the absence of any strong correlation between propensity and quantities like the local energy or free volume. We conclude that the initial configuration determines the local DW distribution (corresponding to the β process), which in turn is the precursor to the subsequent dynamic propensity (characteristic of the α process). These results extend the growing evidence from experiments [130–133] and simulations [116] for correlations between high and low frequency response to the spatial heterogeneities of the two processes. We also conclude that it is likely that the soft spots observed in several different glass-formers below T_g [137–139] are indeed the nucleation point of the large scale motions found above T_g, and that the spatially heterogeneous distribution of these nucleation points is directly due to spatial variations in the structure.

Given the subtlety of the collective mechanical constraints probed by the short-time dynamics, it is very unlikely that any measure of the initial configuration will provide a better prediction of the dynamic propensity than that provided by the spatial distribution of the DW factors. Subsequent answers may improve the algorithmic efficiency in mapping between configuration and the selected DW map, but it is also unlikely that they will improve upon the quality of the answer. If this proposal is accepted then one has, in this work, a sense of the limits one should expect in the answer to the core problem of the glass transition, i.e the causal connection between structure and dynamics. Wolfram [143, 144] has pointed out that there are phenomena in complex systems that are irreducible, in the sense that the future behaviour cannot be obtained by an algorithm more efficient than the solution of the equations of motion. Recently, Israeli and Goldenfeld [145] have qualified this observation by arguing that prediction is possible for suitably coarse-grained versions of the outcome. Our results certainly support the idea that judicious coarse-graining of the structure-dynamics problem is an important part of obtaining a satisfactory solution.

We also studied the time evolution of the DW factor and found that its spatial distribution changed significantly over times almost two orders of magnitude faster than the structural relaxation time. ‘Loose’ regions appeared and disappeared from one configuration to next, and were not present at all in some configurations. This suggests a hierarchy of dynamic regions on short times: those that are never mobile, those that have the potential to become mobile, and those that are mobile at any given time. These results indicate that whatever it is that allows a susceptible region to become mobile can be transferred through space without significant particle motion. This picture of dynamics is significantly different from that built into models of defect diffusion and facilitation.

Continuing the idea of 'stick' and 'slip' introduced in Section 2.4, we suggest that a distribution of states with differing stability may provide a better conceptual picture of the low-temperature dynamics. The most mobile regions can be viewed as marginally stable states, in the sense that they are able to 'stick' the configuration, i.e. to not allow diffusional motion in a given run, but more often that not become mobile, i.e. 'slip'. Since their stability is not optimised their structure is also not likely to be unique. This wealth of structural possibilities may help to explain why none of the simple structural measures that we have tested were able to predict the spatial distribution of propensity. The hierarchy of dynamic domains would then imply a hierarchy of states of different stabilities. And this picture of marginally stable states would also explain why mobility is able to occur, and to be transferred, via small-scale rearrangements in the supercooled liquid. In contrast, in crystalline materials, which have unique optimised structures, motion can only occur via large-scale rearrangements.

We also conclude that the success of the DW factor in predicting the spatial distribution of propensity is because large regions of the structure, with low probability for motion, remain largely unchanged during most runs even after the longer α-relaxation time, and therefore still retain 'memory' of the initial configuration. As a result, the fast motion is confined to the remaining parts of the structure, resulting in the larger length scale of spatial heterogeneity in the propensity maps compared to the DW maps. Furthermore, the propensity will retain 'memory' of the effect of the initial configuration on dynamics long after the instantaneous dynamics has forgotten about the initial structure, since the propensity will not become uniform until all regions have moved the same amount on average, i.e. the initial motion is included in the propensity and needs to be averaged out by motion that no longer remembers the initial configuration and this will not happen until some time *after* the slowest regions become fast.

Finally, we examined the microscopic relationship between the short-time dynamics and the geometrical free volume and found no correlation of sufficient strength to indicate a causal link. As discussed in Section 3.1, free volume has been invoked to explain a variety of dynamic changes in supercooled liquids, and at least one numerical study [80] has found a relationship between the average geometrical free volume and the bulk averaged short-time mean-squared displacement. While having a larger free volume might increase the likelihood that the reduced local constraints necessary for large amplitude motion will exist, we found that in this 2D alloy it does not cause a particle to exhibit larger amplitude fluctuations in position. Even over the short timescale of the DW factor, collective (i.e. non-local) processes are important and these are not well correlated with a purely local measure such as free volume. For this reason, we believe that the results reported here are likely to be common to many glass-formers. In most of its popular usages, however, the phenomenological free volume refers not to an explicit geometric volume, but to a reduction of mechanical constraints on particle motion. In this sense, the single particle Debye-Waller factor, that we have introduced in this chapter, probably provides the better match since it is an explicit measure of particle constraint, even if it lacks a purely geometric definition. If one accepts this proposition, i.e. it is the particle DW factor rather than the geometric free volume that provides the better microscopic expression of the phenomenological free volume, then the outstanding question for developing a microscopic treatment of dynamics in glassy materials is to see if a method exists for predicting the particle DW factors from a given configuration that is algorithmically simpler than the dynamic averages presented in this chapter.

There may be some value in the idea that the stability of the different regions is related to the symmetry of the bond tensions or forces around each atom. Certainly, the most stable L06 domains have the most symmetric local force networks. It is also possible that the relationship between structure and dynamics may be simpler in other glass-formers, for example those with strong chemical ordering, such as the Kob-Andersen model or the 2D glass-formers that we characterise in Part II. It will certainly be interesting to apply the tools developed in this part to the study of structurally different glass-formers.

Part II

Structural Phases in Non-Additive Soft-Disc Mixtures: Glasses, Substitutional Order, Random Tilings and Segregation

Chapter 4

Introduction and Overview of Results

Ultimately, all the structural, dynamic and thermodynamic properties of glass-formers must be determined by the interaction potentials acting between their constituent atoms or molecules. Therefore, one way to study the relationship between these properties is to systematically vary the interaction potentials and see what effect this has on the system. With this as motivation, we explore the parameter space of the binary soft-disc model. The goals of this work are: (i) to discover what other types of order and phase behaviour this model is able to reproduce; (ii) to gain some insight into the stability of the glass-forming system investigated in Part I; and (iii) to discover if there are related systems that can form amorphous solids, and to compare and contrast their structural and dynamic properties and thus gain further insight into the relationship between structure and glassy behaviour.

The binary soft-disc model that we explore in this part forms two-dimensional analogues of many of the structures observed in real alloys. To put our study into context, we therefore provide a brief introduction to the use of particulate models in structural studies and to the range of structures formed by alloys, with particular emphasis on amorphous alloys. We then provide an overview of our exploration of the parameter space of the binary soft-disc model (presented in detail in the following three chapters), including a discussion of the philosophical approach behind this work and a summary of the main results.

4.1 The Use of Particulate Models in Structural Studies

The use of simple models in the study of liquids and glasses has a long history. Bernal [146] introduced the idea of analysing random packings of spheres. Spheres were placed in bags, shaken and allowed to settle in various ways, before glue was poured over them. The geometry of the sphere-sphere contacts were then analysed in agonising detail. Such early geometric analysis gave birth to the concept of geometric frustration. The densest local packing of uniform spheres in 3D is the tetrahedron, however regular tetrahedra cannot pack together to fill space completely [147]. There is therefore competition between the densest local packing and the need to fill space resulting in frustration. Models of the glass transition have been based on this concept (see ref. [148] for a recent review).

Thermal effects were initially approximated crudely by shaking. In some cases elaborate mechanical devices were built to mix different sized spheres randomly and to shake planar arrays of such mixtures [149,150]. More recently, molecular dynamics simulations have allowed for the correct treatment of the equations of motion, and the use of more realistic models, including long-range potentials and the ability to study non-spherical molecules, e.g. water. However, the study of disc- and sphere-like 'atoms' has remained an important way to gain physical insight into the structure and dynamics of real systems. For example, such simple models can reproduce much of the phenomenology of real glass-formers and remain important tests for our understanding of the physics behind glass-formation. One of the most widely studied 3D glass-formers, introduced by Kob and Andersen [151], consists of a binary mixture of particles with spherically-symmetric Lennard-Jones interactions. Simple models also remain important for understanding the structural details of other processes, e.g. crystal nucleation and growth [152], and the competition between crystallisation and glass-formation [153]. Their continued relevance is perhaps because many properties of real materials, including alloys, appear to be dominated by packing effects.

4.1.1 Studies of 2D Models

Because of their relative simplicity, two-dimensional (2D) models have been important for addressing a wide range of problems in condensed matter physics. The most commonly studied models involve particles interacting via hard-disc (hard interactions), soft-disc (purely repulsive interactions) and Lennard-Jones (LJ) potentials. The LJ potential has both repulsive and attractive parts and is therefore the most similar of these to real atomic potentials. While these potentials are all isotropic, i.e. independent of direction, anisotropic potentials have also been investigated. Historically, single-component systems were studied first. However, binary and polydisperse mixtures tend to be more interesting because of their added structural and dynamic complexity. For example, binary mixtures are generally more suited to the study of glass-formation because the amorphous state is kinetically stabilised by the additional compositional fluctuations necessary for crystallisation to occur. Problems that have been addressed include the formation, structure and stability of crystals [154–158], quasicrystals [159–161] and glasses. In particular, glass-formation has been studied in binary hard disc mixtures [162], polydisperse hard disc mixtures [48], binary LJ mixtures [163–166], and binary soft-disc mixtures [44, 67, 167]. Recently, a 2D model consisting of LJ particles with an adjustable anisotropy has been shown to span the full range of glass behaviour from fragile to strong [168]. 2D models have also been used to study ordering in monolayers of charged colloids [169] and dipolar hard spheres [170], of interest for creating nanostructured devices through self-assembly. In the remainder of this section we briefly summarise some research on soft-disc systems, since the thesis constitutes a major extension of these studies. Additional discussion of relevant work can be found in Chapters 5–7.

The one component soft-disc model was studied by Broughton, Gilmer and Weeks [85, 171], who used molecular dynamics (MD) to characterise the melting and freezing transitions, and to calculate equations of state for the crystal and liquid phases along with the thermodynamic freezing temperature. And the additive binary mixture that we studied in Part I, has been studied before in the context of glass-formation by Muranaka and Hiwatari [167], and by Perera and Harrowell [44, 67]. Bocquet et al. [172] studied the effect of starting with a one-component system and gradually increasing the diameter of half the atoms while simultaneously reducing the diameter of the other half, keeping constant the mean diameter and the temperature. They found a discontinuous transition to an amorphous solid at a critical size ratio of the two species equal to 0.78. In comparison, non-additive soft-disc models have received almost no attention. Mountain and Harvey [173] used MD and Monte Carlo simulations to study a non-additive mixture with $\sigma_{12} > \sigma_{11} = \sigma_{22}$, in which they observed first-order fluid-fluid phase separation. We are not aware of any previous studies of ordered crystals, crystallisation or glass-formation in non-additive soft-disc mixtures, nor of any studies of ordered crystals or crystallisation in additive soft-disc mixtures.

Despite their simplicity, these models form many of the different types of order observed in real alloys, including substitutionally ordered crystals, quasicrystals and amorphous solids. We therefore provide a brief introduction to alloys and the range of structures that they form in the next section.

4.2 Alloys and Alloy Structures

Alloys are solutions or compounds of two or more elements, at least one of which is a metal. They have metallic properties and are usually designed to have properties which are more desirable than those of their components. For example, steel is harder than its principal component iron. In addition to forming a wide variety of periodic crystalline structures [174, 175], alloys also form more complex structures, including quasicrystals and glasses. Alloys can also micro-segregate when cooled from the melt, resulting in a composite of several different phases.

Periodic crystalline structures have long-range translational order that can be succinctly described by a relatively simple unit cell and rules for translating it to fill space. In substitutionally ordered crystals, the unit cell consists of two or more elements each with distinct environments, while in substitutionally disordered crystals the unit cell consists of a single solvent element with the other solute element(s) randomly substituting for it thus forming a solid solution. Structural defects are well-defined in crystalline alloys and many material properties are now well understood in terms of these [2]. The study of crystal nucleation and growth is an active area of research that we discuss further in Chapter 6.

Quasicrystals (QCs) belong to the family of aperiodic crystals. They produce sharp diffraction peaks just like periodic crystals, but lack long-range translational order. Quasicrystals are remarkable in that some of them display five-fold symmetry. Prior to their discovery in 1982 [176], it was thought that five-fold crystal symmetry could never occur, because there are no space-filling periodic tilings, or space groups, which have five-fold symmetry. They also have some potentially useful properties including low wettability in contact with most aqueous solutions, low coefficients of friction, and low thermal conductivity. Hence there is great interest in resolving the details of their physical structure. While the physical structure of quasicrystals is still an area of debate (which we discuss further in Section 5.1), a quasiperiodic pattern of points can be formed from a periodic pattern in some higher dimension. For example, to create the pattern for a one-dimensional (1D) quasicrystal, you can start with a regular grid of points in two-dimensional (2D) space. Let the 1D space be a linear subspace that passes through 2D space at an angle. Take every point in the 2D space that is within a certain distance of the 1D subspace. Project those points into the subspace. If the angle is an irrational number such as the golden mean, the pattern will be quasiperiodic. This geometric approach is a useful way to analyze physical quasicrystals. In a crystal, flaws are locations where the pattern is interrupted. In a quasicrystal, flaws are locations where the 1D 'subspace' is bent, or wrinkled, or broken as it passes through the higher-dimensional space. In 2D, a quasiperiodic structure can also be formed by a suitable tiling of squares and equilateral triangles. The relationship between quasicrystalline order, random tilings and amorphous solids is discussed further in Chapter 5.

Alloys can form another type of aperiodic crystal known as an incommensurately modulated structure (IMS). While modulated structures are not discussed further in this thesis, we describe them here for the sake of completeness. They can be considered as resulting from a 1D, 2D or 3D displacive and/or substitutional modulation of an underlying periodic structure. When the periods of the modulation wave and the basic structure are incommensurate to each other, an aperiodic crystal is formed, referred to as an IMS. The modulation wavevector may continuously vary with temperature or pressure running through all rational and irrational multiples of the lattice parameters. At low temperatures IMSs often undergo a transition to a periodic phase (the irrational wavevector locks in at a rational value), which can be described as a commensurately modulated phase.

Amorphous alloys, like other glasses, lack any form of long-range order. While the details of their structure is an unsolved problem, recent progress has been made which we review in the next section. Not only are they among the structurally simplest glasses, but they also have a number of useful properties - e.g. high strength, corrosion resistance and soft magnetism - the exploitation of which depends upon better understanding of their structure and phase behaviour. Questions of interest include how to make them more stable to crystallisation, and how to add small domains of crystalline order to improve their toughness. Many alloys, including the first one made in 1959 [177], require very high cooling rates to avoid crystallisation and can therefore only be formed in very thin strips. Recently, however, new alloys have been discovered that form glasses at much lower cooling rates [178, 179]. As these cooling rates can be achieved by simple casting into metallic molds it has become possible to make a much greater diversity of shapes. Perhaps the most useful property of bulk amorphous alloys is that they are true glasses, which means that they soften and flow upon heating. This allows for easy processing, such as by injection molding, in much the same way as polymers. As a result, amorphous alloys have been commercialised for use in sports equipment, medical devices, and as cases for electronic equipment [180]. However, metallic glasses at room temperature are not ductile and tend to fail suddenly when loaded in tension. Therefore, there is considerable interest in producing composite materials consisting of a metallic glass matrix containing particles or fibers of a ductile crystalline metal.

The structure that a particular alloy, or model, will adopt when cooled is determined by both thermodynamics (stability) and kinetics (speed of formation). Depending on their thermal history, many alloys will micro-segregate into a composite material consisting of two different phases. The interfaces between the two phases can be very elaborate [181], for example, steel can microsegregate into the crystalline phases ferrite and cementite in a layered (lamellar) pattern to form pearlite. In addition to segregation into different crystal phases, alloys may microsegregate in other ways, amorphous-quasicrystal (nanoquasicrystalline) and amorphous-crystal (nanocrystalline) materials being two recent discoveries [182, 183]. Such composite materials are often desirable because they combine good properties of both components, e.g. the hardness of metallic glasses with the toughness of ductile crystalline alloys. Consequently, the study of transitions between these different types of order is of interest for both practical [183, 184] and fundamental [185] reasons.

4.2.1 The Structure of Amorphous Alloys

The lack of long-range order in amorphous alloys led early researchers to compare their structure to Bernal's 'dense random packing of hard spheres in liquids' [186]. In this model, the larger solvent atoms are packed densely but randomly and the solute atoms fill the resulting cavities. Gaskell later proposed a stereochemically-defined model, in which the local packing consists of atom clusters in fixed ratios [187] with the same structure as that of crystalline compounds with similar composition. We now know that the attractive interactions between atoms of different types in amorphous alloys, and their differences in size, result in short-range order (SRO) that can be described by clusters of 'solute' atoms of one type surrounded by atoms of a more numerous species referred to as the solvent. However, amorphous alloys also possess medium-range order (MRO), typically over 3–5 atomic diameters. How the clusters of atoms interconnect to generate this MRO is only just starting to become clear, as we describe below.

Miracle [188] recently proposed a model in which face-centred cubic (fcc) packing of overlapping clusters is the building scheme for amorphous alloy structures. This model has been able to predict the compositions of most glass-forming alloys, and of alloys - known as eutectics - with lower melting points than any of their constituents [189], but has not been structurally verified. Sheng et al. have since used a combination of experimental and computational techniques to resolve the atomic level structure of a number of binary nickel-based and zirconium-based amorphous alloys with different ratios of atomic sizes and different solute concentrations [7]. They found that the SRO consisted of a large range of different solute-centred coordination polyhedra, but that these tend to be dominated by certain classes depending on the effective atomic size ratio (R) between the solute and solvent atoms. In order of decreasing R these were: the Frank-Kasper type; the icosahedral type; the bi-capped square archimedean antiprism; and the tri-capped trigonal prism. They also found that the MRO was dominated by three types of structures in order of increasing solute concentration: the icosahedral packing of solute-centred quasi-equivalent clusters; the dense packing of 'extended' clusters (pairs and strings); and a network-like arrangement of solute atoms. Additionally, they found that the fcc packing previously proposed gave a poorer fit to the experimental data for some transition metal-metalloid alloys. Fernandez and Harrowell have identified similar extended clusters in a well-known model of a metal-metalloid glass-former (the Kob-Andersen model) [190]. They found that the extended clusters were composed of local coordination polyhedra with shared triangular faces, and propose that it is the stability of these triangular-faced polyhedra that suppress crystallisation of the preferred CsCl crystal phase.

Thus, a clearer structural picture is gradually forming of both the SRO and MRO in amorphous alloys. This will likely be important for further applications involving these materials, which are already used commercially because of their special magnetic and mechanical properties. In particular, it appears that better understanding of the relationship between their structural and dynamic properties will be important. For example, more extensive use of their mechanical properties depends on better understanding of their plastic deformation [191]. And the path to understanding their stability to crystallisation in terms of their structure is already being forged [153, 190, 192–194]. The additional stability to crystallisation of the bulk metallic glasses is likely due to the addition of solute species of appropriate sizes and concentrations to fit into the holes left behind by the packing of solute clusters. Therefore a detailed understanding of the atomic packing geometry is likely to be important for the design of new bulk metallic glasses.

The work presented in this part of the thesis identifies, among other phases, a new set of structurally different but related model glass-formers. While we do not expect these to be good structural models for any real metallic glass-formers, we do expect they will help us to gain further insight into the physical principles behind the structure and dynamics of amorphous alloys and the relationship between the two. As stated previously, 2D models are especially attractive because, compared to 3D systems, it is relatively simple to directly visualise both the structure and the dynamics.

4.3 Overview of Model and Results

4.3.1 The Binary Soft-Disc Model

In this part of the thesis we explore the parameter space of the binary soft-disc model. This simple model consists of particles interacting via purely repulsive potentials of the form

$$u_{ab}(r) = \epsilon \left[\frac{\sigma_{ab}}{r}\right]^{12} \tag{4.1}$$

where the subscripts a and b specify particle types (either 1 or 2 for the binary model). Scaling the dimensions by σ_{11}, it is clear that there are only two independent lengthscales, σ_{12} and σ_{22}. The entire parameter space for the model is therefore a 3D space in σ_{22}, σ_{12} and x_1, the fraction of particles of type 1. For this study we fixed $\sigma_{22} = 1.4$, the value for the model glass-former studied in Part I, and investigated the effect of varying σ_{12} from 1.0–1.3. We considered both equimolar mixtures ($x_1 = 0.5$) and non-equimolar mixtures with $x_1 \approx 0.317$, and characterised the structure, dynamics and phase behaviour of the different systems. Figure 4.1 illustrates the

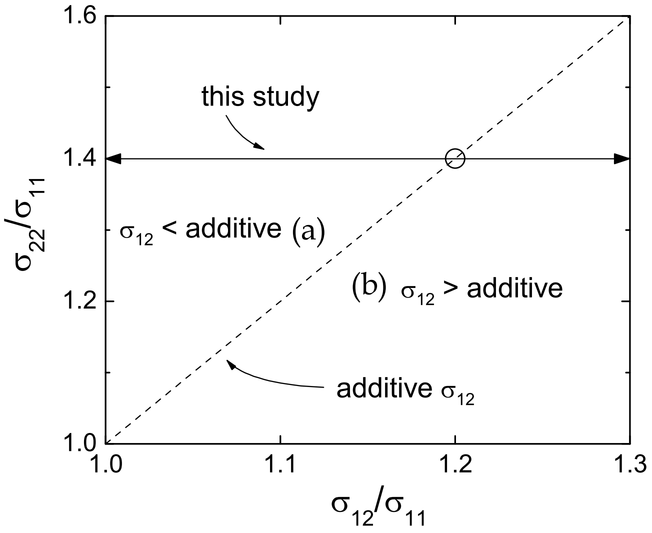

Figure 4.1: Parameter space of the two-component soft-disc model. The dashed line indicates the set of additive parameters, and divides the space into two regions: (a), in which there is an effective attraction between unlike particle species; and (b), in which there is an effective repulsion between unlike particle species. The solid line at $\sigma_{22} = 1.4$ indicates the part of the parameter space explored by the present work.

region of the parameter space that was explored.

It is interesting to study the variation of σ_{12} for several reasons. Firstly, while both the one-component and binary soft-disc models have been studied extensively, the effect of making the interparticle potential non-additive has received far less attention, as was discussed in Section 4.1.1. Secondly, by changing σ_{12} from additive (i.e. equal to $[\sigma_{11}+\sigma_{22}]/2$) to non-additive, it should be possible to tune the model from a system in which there is no chemical ordering to a system in which there is strong chemical ordering. Although this is a purely repulsive system, by decreasing σ_{12} it is possible to create an effective attraction between unlike species, since the PV term in the Gibbs free energy is able to be reduced when there are more contacts between unlike particle species. Similarly, by increasing σ_{12} it is possible to create an effective repulsion between like particle species. This is interesting because glassy alloys appear to fall into two main groups: (i) the random alloy glasses (RAGs) - generally metal-metal, in which chemical ordering is insignificant; and (ii) the chemically ordered glasses (COGs) - generally metal-metalloid, in which there is strong chemical ordering. The additive soft-disc system studied in Part I falls into the former group, while the Kob-Andersen model falls into the latter. The binary soft-disc model may therefore allow us to compare the relationship between structure and dynamics in several related, but structurally different, glass-formers.

In total, six systems were investigated. Detailed studies of these are presented in the following three chapters. First, however, we provide an overview of the phase behaviour of the different systems to illustrate some of the interesting comparisons that can be made between them. These comparisons are the ultimate goal of the work presented in this part of the thesis.

4.3.2 Low-temperature Phases

As our results demonstrate, this simple three-parameter model is able to form a wide variety of structurally distinct solid phases, including substitutionally ordered crystals, amorphous solids, random tiling-like structures and multiphase systems. Here we present an overview of the different types of low-temperature structures that were found. Representative configurations are shown in Figures 4.2. The equimolar mixtures with $\sigma_{12} = 1.0$ and 1.1 freeze to form substitutionally ordered crystals. Configurations corresponding to their ideal solid-state structures are shown in (b) and (d), which we will refer to as the S1 and H2 structures, respectively. They are related by a slight distortion and merging of adjacent square S1 unit cells. We investigate the process of freezing for the H2 crystal and discuss its stability to supercooling in Chapter 6. In contrast, when the non-equimolar mixtures with the same interparticle potentials are cooled they form solids lacking long-range periodic order, shown in (a) and (c). We argue that these are good glass-formers. For comparison, a configuration of the additive glass-former studied in Part I, i.e. the equimolar mixture with $\sigma_{12} = 1.2$, is shown in (f). The non-equimolar mixture with the same additive interparticle potential forms the structure shown in (e) when it is cooled gradually, i.e. it forms a partially phase separated multiphase system consisting of crystalline and amorphous regions, and offers the intriguing possibility of studying the coexistence between crystalline and amorphous states. Cooling of the equimolar mixture with the effectively repulsive interparticle potential $\sigma_{12} = 1.3$ results in liquid-liquid phase separation and freezing into two single-component crystalline phases, as shown in Figure 4.3.

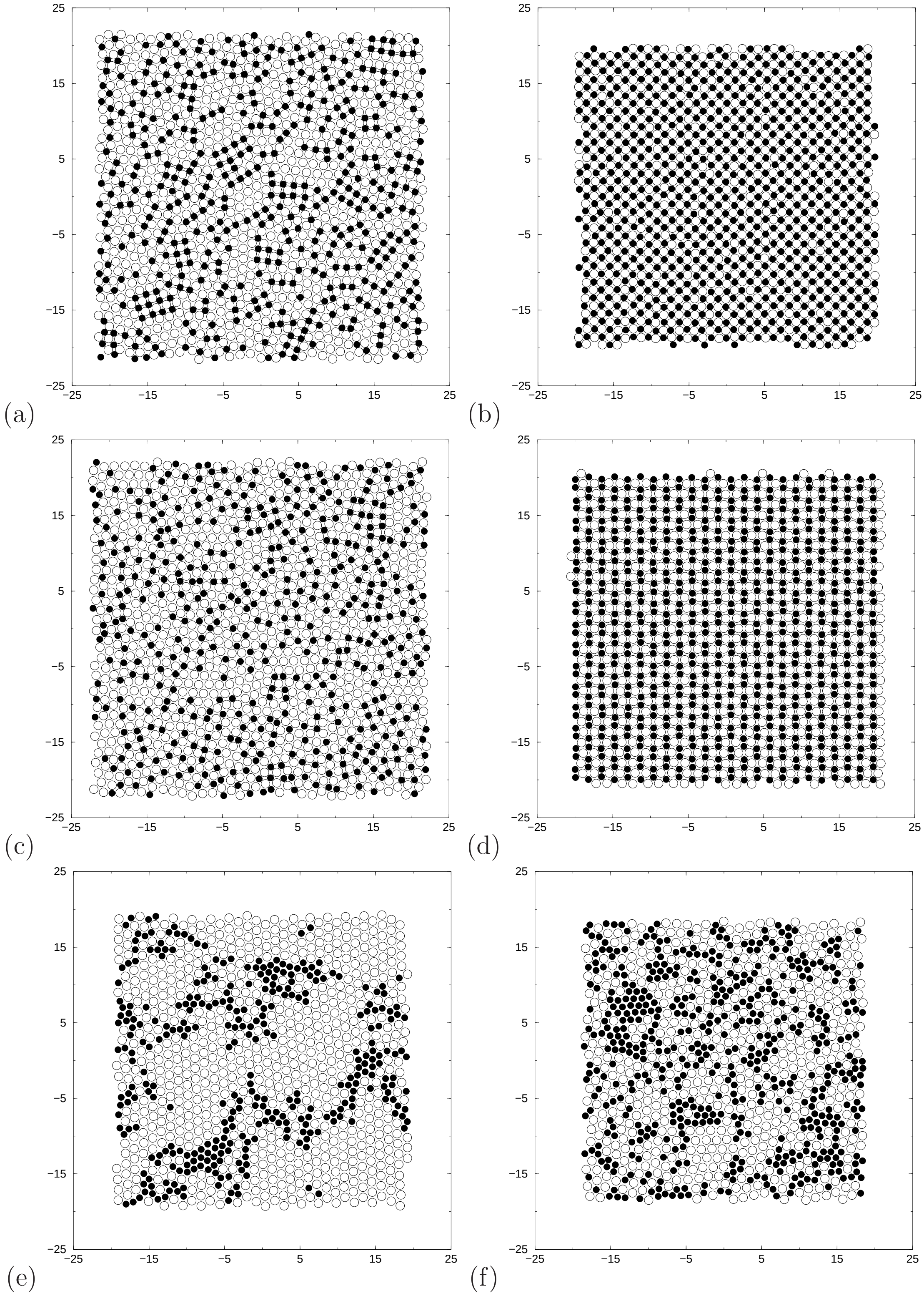

Figure 4.2: Low-temperature phases obtained upon cooling the following systems: (a) $\sigma_{12} = 1.0$, $x_1 = 0.3167$; (b) $\sigma_{12} = 1.0$, $x_1 = 0.5$; (c) $\sigma_{12} = 1.1$, $x_1 = 0.3167$; (d) $\sigma_{12} = 1.1$, $x_1 = 0.5$; (e) $\sigma_{12} = 1.2$, $x_1 = 0.3164$; and (f) $\sigma_{12} = 1.2$, $x_1 = 0.5$. The small and large particles are represented by filled and open circles respectively.

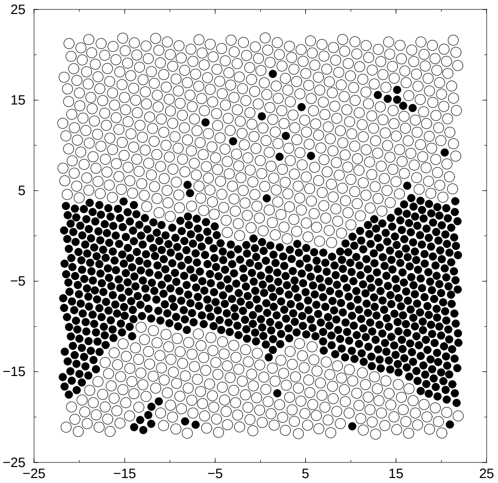

Figure 4.3: Low-temperature phase obtained upon cooling the system with $\sigma_{12} = 1.3$, $x_1 = 0.5$. The small and large particles are represented by filled and open circles respectively.

4.3.3 Comparison of Amorphous States as the Interparticle Potential is Varied

Representative low-temperature configurations for the two non-additive glass-formers identified by the present work, and for the additive glass-former studied in Part I, are shown in Figure 4.2, plots (a), (c), and (f). These form a complete structural range of alloy glasses from random alloy to chemically ordered. As the degree of chemical ordering increases, i.e. as σ_{12} decreases from additive, the number of dominant local environments decreases, the structure becomes more homogeneous, and the medium-range order becomes more defined. The structures also differ with respect to the amount of crystalline order that they incorporate. The random alloy - plot (f) - has substantial regions of large particle crystallites, while the glass-former with $\sigma_{12} = 1.1$ - plot (c) - shows very little sign of these or of the H2 crystal environment. And the glass-former with $\sigma_{12} = 1.0$ - plot (c) - is noteworthy because it appears to have very well-defined local order and obvious structural defects. Its structure can be described in terms of a decorated random tiling of squares and equilateral triangles with additional defects. The structural and dynamics properties of these new glass-formers are characterised in detail in Chapters 5 and 6.

As was discussed in Part I, the presence of structural variations in the random alloy glass-former has a significant impact on its dynamic properties. Therefore, given the structural differences just described, it should be insightful to use the tools developed in Part I to compare the effect of structure on dynamics over this range of glass-forming systems. In Chapter 8 we provide a taste of where this may lead.

4.3.4 Phase Diagrams for the Binary Soft-Disc Model

In Figure 4.4 we compare the different phases formed as a function of the interparticle potential σ_{12} and the composition x_1. The drawn lines are visual guides and do not necessarily correspond to actual phase boundaries. They do however suggest that the phase space is roughly divided into three regions: (i) a substitutionally ordered crystal region in the top left; (ii) a glass-forming region extending diagonally across the parameter space; and (iii) a phase separated region at the right. Intriguingly, the glass-former studied in Part I, i.e. the equimolar mixture with $\sigma_{12} = 1.2$, is balanced between the extremes of phase separation on the one hand, and formation of a substitutionally ordered crystal on the other [compare Figure 4.2(f) with Figures 4.3 and 4.2(d)].

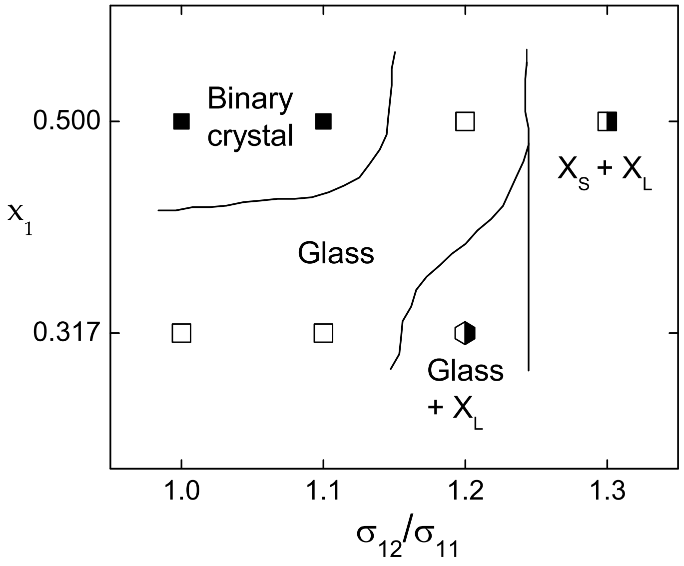

Figure 4.4: Different phases formed by the various soft-disc mixtures investigated in this work. Filled squares indicate substitutionally ordered crystals, open squares indicate glass-forming systems, the split hexagon indicates crystal-amorphous coexistence, and the split square indicates liquid-liquid phase separation resulting in coexistence between the single-component large- and small-particle crystal phases X_L and X_S, respectively. The lines are speculative phase boundaries and may not be correct.

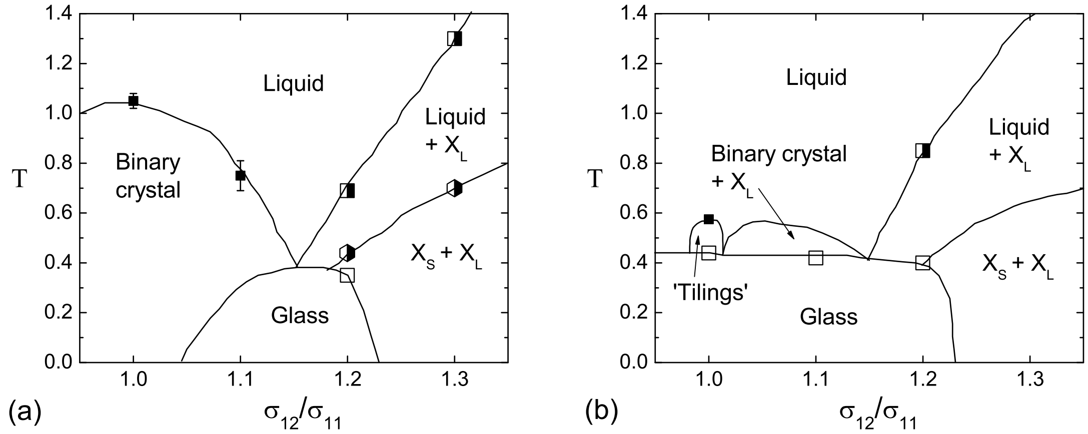

Figure 4.5: Phase diagrams for the binary soft-disc model with $\sigma_{22} = 1.4$ and (a) $x_1 = 0.5$ (b) $x_1 = 0.317$. The black squares represent the approximate melting point of different substitutionally ordered crystals (the error bars indicate the extent of the melting/freezing hysteresis region in our studies). The half-filled squares represent the freezing point of the large particle crystalline phase X_L, and the half-filled hexagons represent the freezing point of the small particle crystalline phase X_S. The open squares indicate when the supercooled liquid falls out of equilibrium, roughly the temperature at which $F_{s,1}(k, 10^4\tau) = 0.2$, where $F_{s,1}(k,t)$ is the incoherent scattering function for the small particles calculated at the wave vector corresponding to the largest peak in the respective structure factor $S_{11}(k)$. The lines roughly indicate proposed phase boundaries, and the regions in which we expect glass-formation to be possible.

We used our results to construct tentative phase diagrams for the binary soft-disc model as a function of σ_{12}. Figure 4.5(a) summarises the phase behaviour of the equimolar mixture, and Figure 4.5(b) summarises the phase behaviour of the $x_1 = 0.317$ mixture. Since the substitutionally ordered S1 and H2 crystals are related by a continuous deformation of the unit cell, we have indicated these by a single 'binary crystal' region. 'Tilings' refers to a large number of different structures that can be described as decorated tilings of squares and equilateral triangles. We expect the ground state for the non-equimolar mixture in the vicinity of $\sigma_{12} = 1.1$ to be coexistence between the binary crystal and the large particle crystalline phase X_L. For the equimolar additive mixture, we have used data from ref. [67] for the freezing points of the large and small particle crystalline phases. Given the small number of data points, the lines defining the stability of the different phases are highly speculative, especially as $T \to 0$. They do, however, provide a sense of the change in phase behaviour of the binary soft-disc model as the interparticle potential is varied, and of the relationship between the different phases.

Chapter 5

The S1 Crystal and a Defected Random Tiling ($\sigma_{12} = 1.0$)

The binary soft-disc mixture with $\sigma_{12} = 1.0$ *forms low-temperature structures that can be interpreted in terms of tilings of squares and equilateral triangles. Such tilings have previously been used as models for glass-formers and quasicrystals. We study the structure and dynamics of both equimolar and non-equimolar (*$x_1 = 0.3167$*) mixtures in the fluid-solid phase region. We find that the equimolar mixture readily freezes into a crystalline solid that we will refer to as the S1 crystal. Both cooling and heating traverses are characterised. In contrast, the non-equimolar mixture forms an amorphous solid state when cooled, yet a crystalline structure with almost identical composition is found to undergo a first order melting transition when heated. This leads us to speculate on the relationship between random tilings, quasicrystals and amorphous structures.*

5.1 Square-Triangle Tilings and Quasicrystals

The set of model parameters studied in this chapter allows four large particles to pack almost perfectly around one small particle (the ideal σ_{12} length with all else fixed would be $\sqrt{2 \times (1.4)^2}/2 \approx 0.9899$). Ideal particle packings for this system can therefore be described as decorated tilings of squares - decorated with 4 large and 1 small particle - and equilateral triangles - decorated with 3 large particles (see Figure 5.1(a)). These two structural units can further pack together to give a total of four different types of large-particle vertices, also shown in Figure 5.1, whose relative

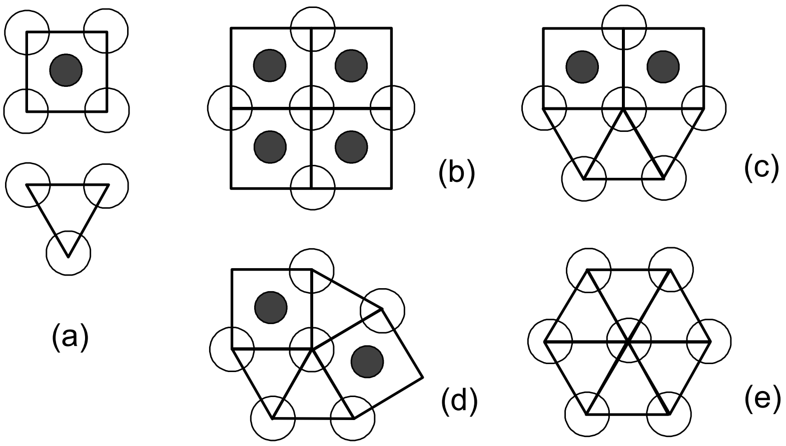

Figure 5.1: (a) Small particles (filled circles) and large particles (open circles) pack together to create square and triangular tiles (thick lines). These units can further pack together to form the local configurations around large particle vertices that are shown in (b)–(e). The central large particle and its nearest neighbours have been indicated to emphasise the local coordination environment.

abundance depends on the composition and particular arrangement of particles. Most compositions have the potential to form several different structures with unique vertex frequencies. This model may therefore be suitable for studying the physical effects of solid state entropy. Both regular tilings - with translational and rotational order - and random tilings - with only rotational order - can be constructed.

Square-triangle tilings have previously been used as structural models for real materials. Kawamura [195] studied the statistical mechanics of random square-triangle tilings in the context of amorphous systems, while Frank-Kasper phases [196] can be described in terms of ordered layers of particular square-triangle tilings. Random square triangle-tilings have also been used as a model for twelvefold-symmetric quasicrystals [197], and the structure of some alloys with twelvefold quasicrystalline order have been described in terms of dodecagonal tilings by equilateral triangles and squares [198, 199]. Intriguingly, a recent review [185] of phase transitions in metal alloys found that many alloys have amorphous to quasicrystal phase transitions upon de-vitrification suggesting that these two types of order may be strongly related.

We limit the current investigation to two compositions. An equimolar mixture that readily freezes into a 2D version of the CsCl lattice, which we will refer to as the S1 structure (after a similar packing constructed by Likos and Henley [155]), and a non-equimolar mixture whose composition $x_1 = 0.3167$ was specifically chosen to maximise the configurational entropy of the solid state. Nienhuis [200] has explicitly calculated the entropy of square-triangle tilings and shown that the configurational entropy is sharply peaked when the area occupied by triangles is equal to the area occupied by squares. It is straightforward to show that this corresponds to a number ratio of squares to triangles of $\sqrt{3}/4$, which with the particle decoration shown in Figure 5.1(a) corresponds to a small particle fraction of $x_1 = 0.31699$ (to 5 d.p.). It is an interesting question how the high configurational entropy of the solid state at this composition affects the nature of the fluid-solid phase transition.

Several particulate models that form square-triangle tilings are already known. Weber and Stillinger [158] studied the melting and freezing of a 2D binary mixture of Lennard-Jones (LJ) particles with 2- and 3-body interactions that crystallises into the same S1 structure as our equimolar mixture, and the structure of a dense randomly packed one-component 2D liquid has been interpreted in terms of tilings of squares and triangles [201]. Leung, Henley and Chester have made extensive use of another LJ model, with the same composition as our non-equimolar mixture, to investigate the stability of quasicrystals (see, for example, ref. [159]). The ratio of squares to triangles at which the maximal configurational entropy occurs also happens to be the ratio at which a subset of the tilings have quasicrystalline order.

Simulations of 2D binary LJ models have observed spontaneous formation of random-tiling like structures that lack ideal quasiperiodic order but which have long-range 10- or 12-fold orientational order and which produce quasicrystal-like diffraction patterns (with peaks that may be sharp or broad depending on the model) [159,160]. Widom et al. [160] have argued that one of these models is stabilised by the high configurational entropy of the random tilings, and in a later paper [161] demonstrated that its thermodynamic ground state was indeed crystalline.

In contrast, a recent review [202] of experimental work on quasicrystals provides strong evidence that: (i) at least one real quasicrystal has near-ideal quasiperiodic order (not just on average); (ii) that this structure can be well-described by a packing of overlapping symmetry-breaking decagons proposed by Grummelt [203]; and (iii) that this structure is energetically, not entropically, stabilised. They do, however, concede that the structure of some quasicrystals may be well described by a random packing of clusters which on average produce high symmetry. The precise structural and energetic relationship between 2D and 3D quasicrystals remains to be fully understood.

The rest of this chapter is structured as follows. The model and computational methods are described in Section 5.2, and in Section 5.3 we characterise the structural and dynamic properties of the equimolar mixture for both heating and cooling traverses. Our study of the non-equimolar mixture is presented in Section 5.4. We characterise the structural and dynamic changes during cooling from the liquid state to an amorphous solid, and in Section 5.4.4 we show that a periodic solid with similar composition undergoes a discontinuous melting transition. This is followed by a summary of the main results and a comparison of the structure and phase behaviour of the two mixtures in Section 5.5.

5.2 Model and Computational Details

We consider a 2D system consisting of a binary mixture of particles interacting via purely repulsive potentials of the form

$$u_{ab}(r) = \epsilon \left[\frac{\sigma_{ab}}{r}\right]^{12} \tag{5.1}$$

where $\sigma_{12} = 1.0 \times \sigma_{11}$ and $\sigma_{22} = 1.4 \times \sigma_{11}$. All units quoted will be reduced so that $\sigma_{11} = \epsilon = m = 1.0$ where m is the mass of both types of particle. Specifically, the reduced unit of time $\tau = \sigma_{11}\sqrt{m/\epsilon}$. A total of N particles were enclosed in a square box with periodic boundary conditions - except for one set of runs (described in Section 5.4.4) for which the particles were enclosed in a rectangular box with periodic boundary conditions.

The molecular dynamics simulations were carried out at constant number of particles, pressure ($P = 13.5$) and temperature using the Nosé-Poincaré-Andersen (NPA) algorithm developed by Laird et al. [83, 84]. This algorithm is discussed further in Appendix A, where we also list the equations of motion in 2D. The equations of motion were integrated using a generalised leapfrog algorithm [84]. The time step employed was 0.05τ for $T > 1$, and 0.01τ for $T \leq 1$. For argon units of $\epsilon = 120k_B$, $m = 6.6 \times 10^{-23}g$ and $\sigma_{11} = 3.4\mathring{A}$, these time steps correspond to approximately 10 and 20 femtoseconds respectively.

A non-equimolar mixture consisting of $N_1 = 456$ small particles and $N_2 = 984$ large particles (giving $N = 1440$ and $x_1 = 0.3167$ to 4 d.p.) was studied at 31 different reduced temperatures from $T = 5$ to $T = 0.2$. The starting configuration of the run at $T = 5$ was an equilibrated configuration at $T = 5$ for the equimolar system described in Chapter 6 with the appropriate number of small particles changed to large particles. The starting configuration of each lower temperature equilibration run came from the final configuration of the preceding higher temperature run. For $T \geq 0.5$, the equilibration times were longer than the times taken for all the dynamic correlation functions investigated to decay to zero. Below $T = 0.5$ the system is no longer able to reach equilibrium within the finite timescale of the simulations. Thus, the computer glass transition temperature for these simulations, defined as the temperature at which the system falls out of equilibrium, lies between $T = 0.5$ and $T = 0.45$. At all temperatures, the equilibration runs were taken out until steady state was achieved, i.e. until the average thermodynamic properties remained constant in time. Table C.6 (in Appendix C.2) lists the temperatures of each state studied as well as the equilibration and production times. The final configurations of the equilibration runs were used to start the production runs. The 'masses' of the Anderson piston and Nosé thermostat were $Q_v = 0.002$ and $Q_s = 1000$, respectively, for all temperatures.

Both cooling and heating traverses were studied for the equimolar mixture. Tables C.1 and C.2 (in Appendix C.1) list the temperatures of each state studied as well as the equilibration and production times for the cooling and heating traverses, respectively. The initial configuration for the cooling traverse was an equilibrated configuration at $T = 5$ for the equimolar system described in Chapter 6 with a total of $N = 1440$ particles, while the initial configuration for the heating traverse was the constructed periodic structure shown in Figure 5.4(a) that has a total of $N = 1444$ particles. The starting configurations for production runs and for lower (or higher) temperature equilibration runs are as described above for the non-equimolar mixture. The 'mass' of the Nosé thermostat was $Q_s = 1000$ for all temperatures. For the cooling traverse, the 'mass' of the Anderson piston was $Q_v = 0.0002$ for $T \geq 1.1$ and $Q_v = 10^{-6}$ for $T \leq 1.08$. For the heating traverse, $Q_v = 10^{-8}$ for all temperatures.

5.3 Freezing and Melting of the Equimolar Mixture ($x_1 = 0.5$)

5.3.1 Thermodynamic Properties

The thermodynamic averages for the potential energy per particle (U), energy per particle (E), enthalpy per particle (H), and number density per particle (ρ) are

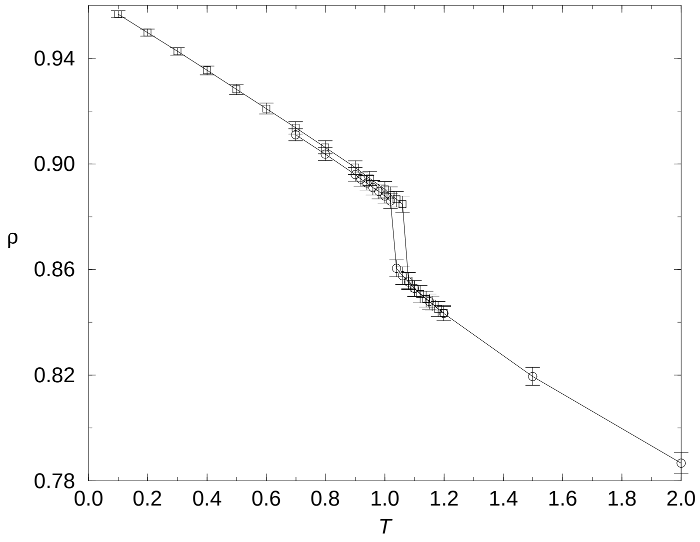

Figure 5.2: Isobaric ($P = 13.5$) phase diagram. Squares and circles indicate data points for the heating and cooling traverses, respectively. Error bars represent one standard deviation. The steps in density upon cooling and heating form a region of metastability extending from $T = 1.02$ to $T = 1.08$.

summarised in Table C.1 for the cooling traverse, and in Table C.2 for the heating traverse, for the range of temperatures that were investigated. Also tabulated are the compressibility factor ($Z = P/(\rho T)$), the coupling constant $\Gamma = \rho T^{-1/6}$, as well as the root mean square (rms) deviations of the instantaneous thermodynamic properties from their averages, calculated as $\sqrt{\langle x^2 \rangle - \langle x \rangle^2}$ where x is the property of interest and the angular brackets indicate an average over time.

The isobaric phase diagram for the equimolar mixture is shown in Figure 5.2. For the cooling traverse there is a clear step increase in density at $T = 1.02$, suggesting a first order freezing transition between $T = 1.02$ and $T = 1.04$. The resulting solid continues to have slightly lower density than the constructed perfect S1 crystal, which is consistent with the presence of defects that are frozen-in (see Figure 5.3 for representative configurations). When the constructed crystal is heated, there is a clear step decrease in density at $T = 1.08$, indicative of a first order melting transition between $T = 1.06$ and $T = 1.08$. The resulting liquid has the same density as the liquid for the cooling traverse. The different positions of the steps in density for the cooling and heating traverses indicate a region of hysteresis extending from $T =$ 1.02–1.08 over which the liquid and solid phases are metastable to supercooling and superheating, respectively. The thermodynamic freezing temperature T_f should lie somewhere in this region.

5.3.2 Structural Properties

Particle Configurations

Representative particle configurations from the cooling traverse are shown in Figure 5.3. Several changes in structure can be identified. At $T = 2$ the particles are well mixed and there is little recognisable order. Neither of the particle species form large clusters. By $T = 1.04$, i.e. just before freezing, there are large clusters of crystalline domains, characterised by squares of four large particles surrounding one small particle packed together. After the step increase in density at $T = 1.02$ (see Figure 5.2) there is obvious long-range order in the system, consistent with this being a

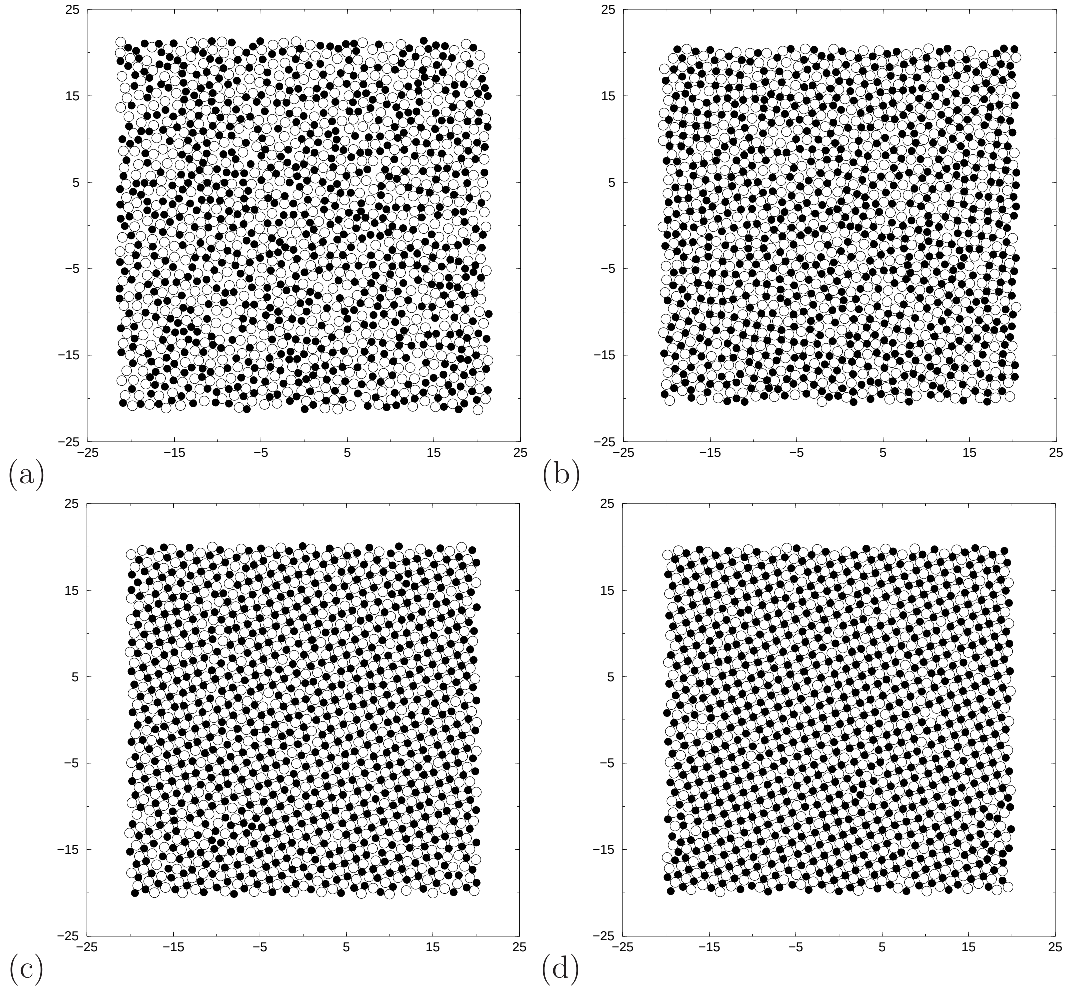

Figure 5.3: Representative particle configurations for the cooling traverse at (a) $T = 2$, (b) $T = 1.04$, (c) $T = 1.02$, and (d) $T = 0.7$. The small and large particles are represented by filled and open circles respectively.

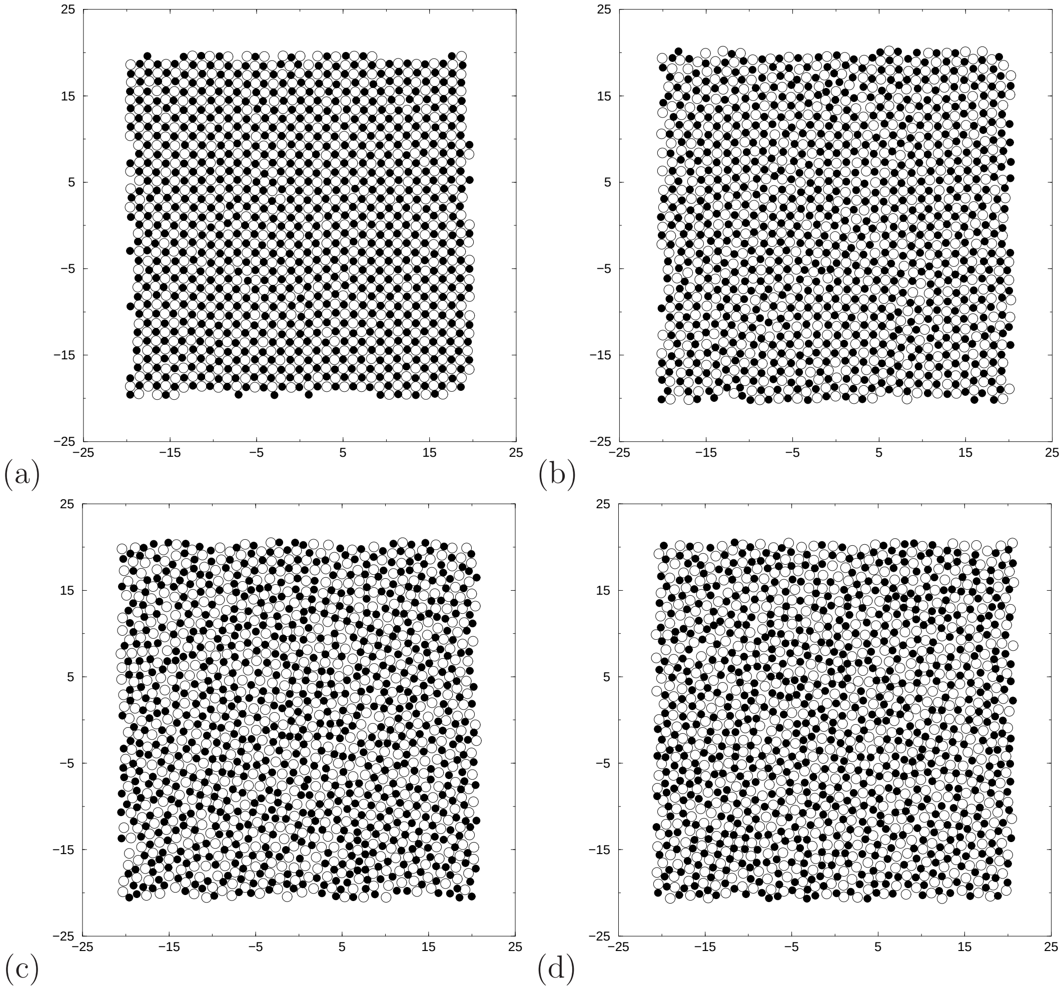

Figure 5.4: Representative particle configurations for the heating traverse at (a) $T = 0.4$, (b) $T = 1.06$, (c) $T = 1.08$, and (d) $T = 1.2$. The small and large particles are represented by filled and open circles respectively.

freezing transition. The units of S1 squares packed together are easy to identify. There are some defects in the crystal - mainly of the interstitial/vacancy and substitutional types - which appear to decrease in number with further cooling.

Representative particle configurations from the heating traverse are shown in Figure 5.4. The regular order of the equilibrated crystal at $T = 0.4$ has become somewhat less regular by $T = 1.06$, and a few defects are visible, but the long-range periodic order remains. At $T = 1.08$ there is still significant clustering of S1 units but the long-range order has been lost. This is where the step decrease in density occurs (see Figure 5.2, and is consistent with this being a melting transition. By $T = 1.02$ there is less crystalline order in the liquid.

Pair Distribution Functions

The pair distribution functions describe the radially averaged structure about particles. They are a useful way to identify long-range translational order and also contain much information about the local structure in a system. For an isotropic substance, the pair distribution function (PDF) is defined as

$$g_{all}(r) = \left\langle \frac{1}{N\rho} \sum_{i}^{N} \sum_{j \neq i}^{N} \delta[r - r_{ij}] \right\rangle , \tag{5.2}$$

where N is the total number of particles, ρ the number density, r_{ij} the separation between two particles, and the angular brackets denote an average over different configurations in time.

For two component systems, there are three partial pair distribution functions (PPDFs):

$$g_{ab}(r) = \frac{1}{x_a x_b N\rho} \left\langle \sum_{i}^{N_a} \sum_{j}^{N_b}{}' \delta[r - r_{ij}] \right\rangle \qquad a, b = 1, 2, \tag{5.3}$$

where ρ is the total number density, $x_a = N_a/N$ is the number fraction of species a with $N = N_1 + N_2$, and the prime in the second summation indicates that terms for which $i = j$ are omitted when $a = b$.

The PDF and PPDFs for the cooling traverse are plotted in Figures 5.5 and 5.6. They all show a clear transition from medium to long-range translational order between $T = 1.04$ and $T = 1.02$, which confirms a transition from liquid to crystalline order at $T = 1.02$ during the cooling traverse. There are also strong correlations prior to freezing, with solid-like structure in the PDFs extending out to at least $8\sigma_{11}$. Note, however, that there is significant change in $g_{11}(r)$ local structure both before and during freezing. The first peak shifts from $r = 1$ at high temperature to $r = 1.4$ in the crystalline state, with a change in peak intensity already visible prior to freezing. This can be explained by the disappearance of small particle nearest neighbours (with an expected separation distance of $r = 1$), to a local structure where small particles are contained in square cells of the type shown in Figure 5.1(a). When these are packed together the expected small-small separation is equal to $\sigma_{22} = 1.4$. To distinguish this change in local order, we use the first minimum in $g_{11}(r)$ at $T = 1.04$ as the cutoff for defining small particle nearest neighbours below $T = 1.04$. The definition of nearest neighbours is discussed further below. A consequence of this shift in peak

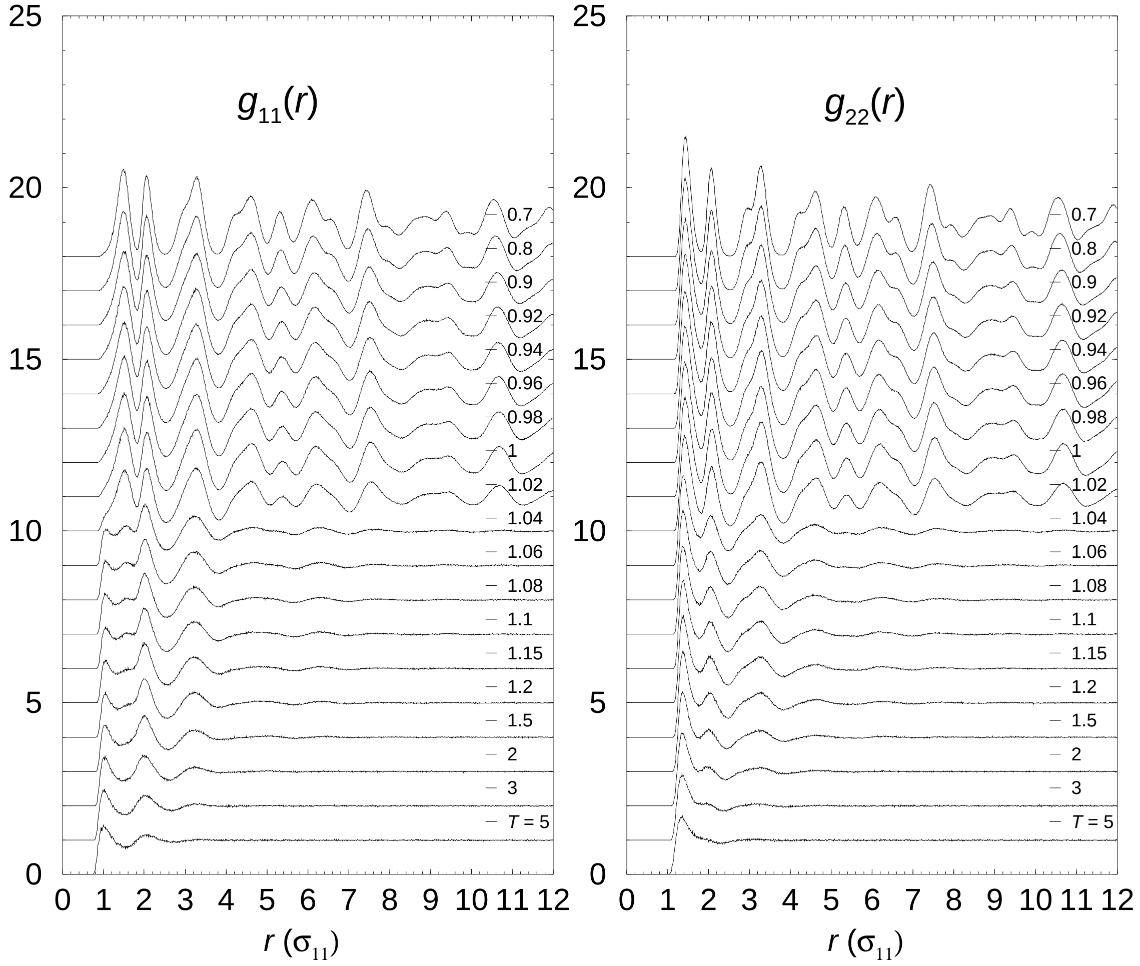

Figure 5.5: The partial pair distribution functions $g_{11}(r)$ and $g_{22}(r)$ for the cooling traverse as a function of distance from $T = 5$ down to $T = 0.7$. For $T \leq 3$, each curve has been shifted upwards by one unit from the higher temperature curve directly preceding it.

intensity - and the associated weak local ordering - is that for much of the liquid state the most intense peak in $g_{11}(r)$ is the third one. This is found at $r = 2$ and is likely due to a linear small-large-small particle arrangement. The lack of strong crystalline local ordering of the small particles prior to freezing (as evidenced by the significant change in $g_{11}(r)$) is rather unusual, especially in a 2D system. On the other hand, both $g_{12}(r)$ and $g_{22}(r)$ show strong local crystalline ordering prior to freezing.

The PDF and PPDFs for the heating traverse are plotted in Figures 5.7 and 5.8. These are very similar to those obtained for the cooling traverse at the same temperature, the major difference being that the transition from long-range to short-range translational order occurs between $T = 1.08$ and $T = 1.06$. As for the cooling

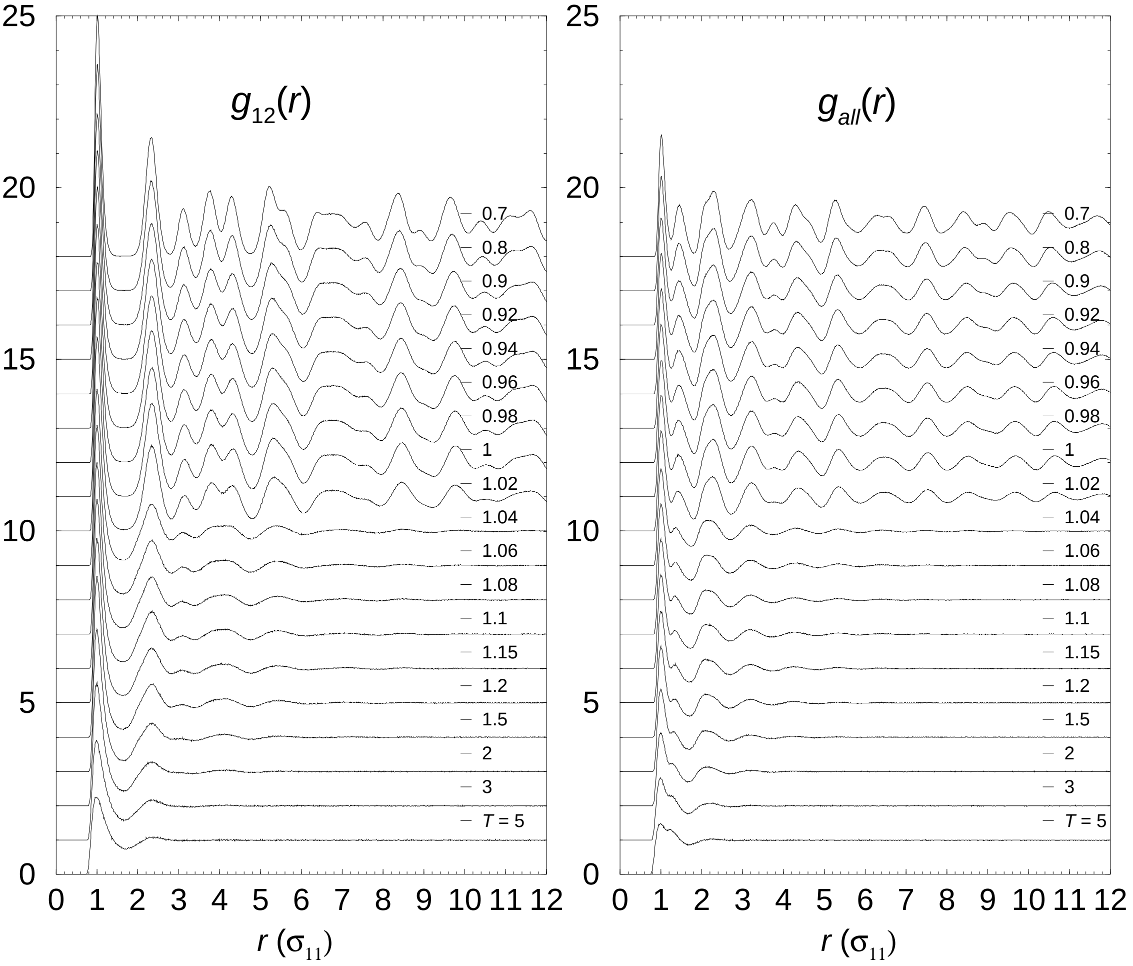

Figure 5.6: The partial pair distribution function $g_{12}(r)$ and the total pair distribution function $g_{all}(r)$ for the cooling traverse as a function of distance from $T = 5$ down to $T = 0.7$. For $T \leq 3$, each curve has been shifted upwards by one unit from the higher temperature curve directly preceding it.

traverse, this change in translational order coincides with a discontinuity in the density. Additional structure develops in the PDF and PPDFs at very low temperature, presumably due to a decrease in vibrational motion.

From this data we extract cutoff distances to use for defining nearest neighbours. Two particles of type a and b are defined to be nearest neighbours if they are separated by a distance less than cut_{ab}. This definition of nearest neighbours will be used when calculating various structural properties including the local coordination environment and orientational order parameters. We have generally used the position of the first minimum in $g_{ab}(r)$ as the value for cut_{ab}, as this distance usually allows for the best

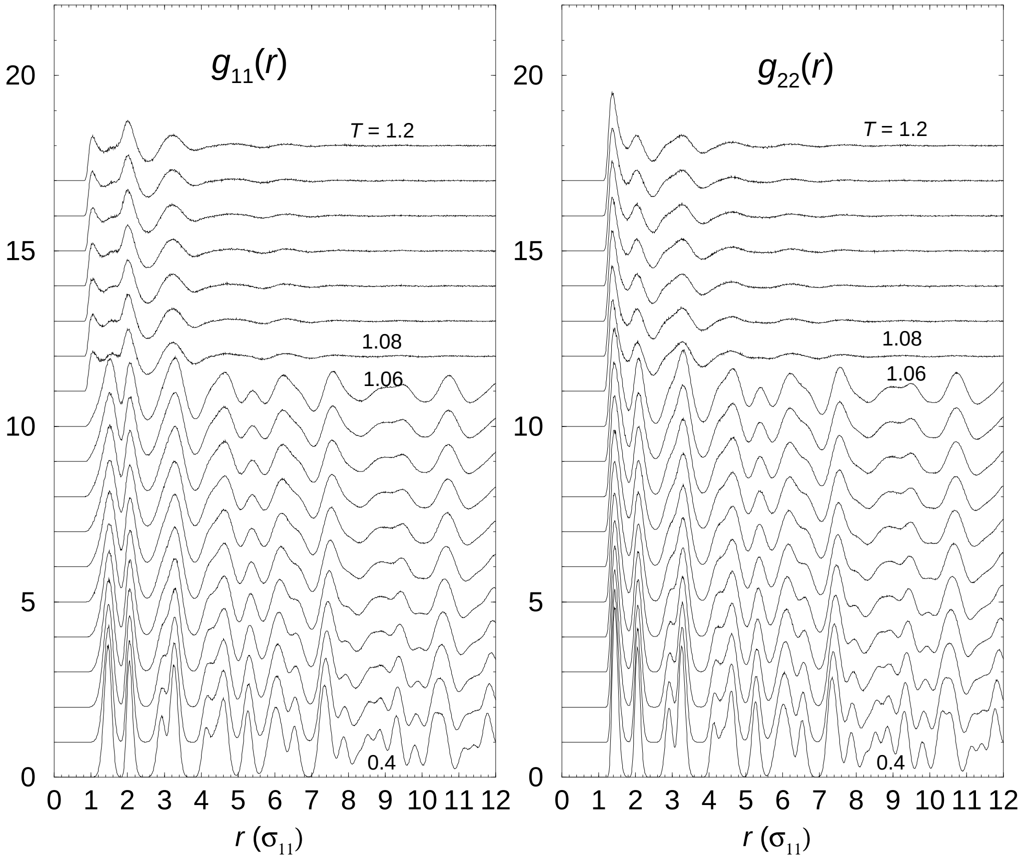

Figure 5.7: The partial pair distribution functions $g_{11}(r)$ and $g_{22}(r)$ for the heating traverse as a function of distance from $T = 0.1$ up to $T = 1.2$. For $T \geq 1.18$, each curve has been shifted upwards by one unit from the lower temperature curve directly preceding it.

distinction between the first and second coordination shells. That said, we have not followed this rule for the current model (with $\sigma_{11} = 1.0$) when defining cut_{11} at low temperature. This is because the first maximum in $g_{11}(r)$ shifts to a substantially larger distance at low temperature that can no longer correspond to a small-small nearest neighbour interaction, as has been explained above. To be able to identify this change in local structure about small particles, we have therefore set cut_{11} at low temperature equal to the smallest value of cut_{11} that was calculated from a minimum following a maximum in $g_{11}(r)$ corresponding to a nearest neighbour interaction.

Cutoff distances for the cooling traverse are listed in Table C.3. For cut_{11} at $T \leq 1.02$ we have used the position of the minimum in $g_{11}(r)$ at $T = 1.04$ for the reasons just explained. Cutoff distances used for the heating traverse were $cut_{11} = 1.32$, $cut_{12} = 1.66$ and $cut_{22} = 1.80$. The latter two values were obtained from the first

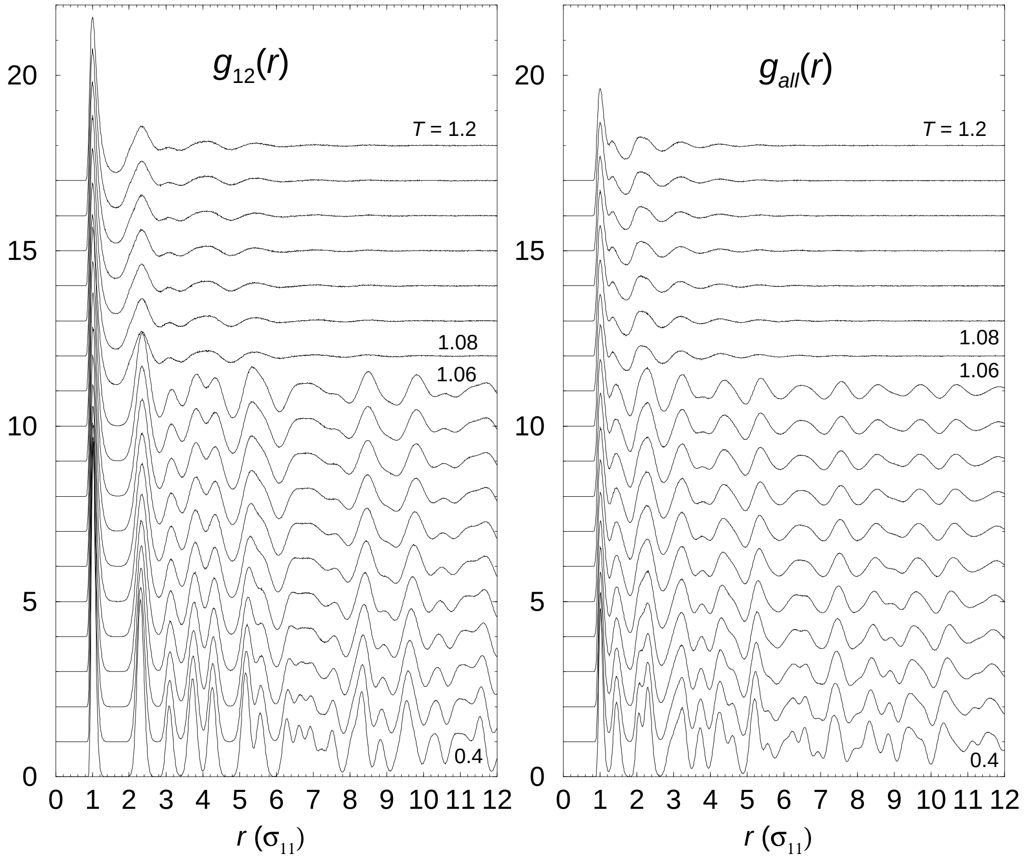

Figure 5.8: The partial pair distribution function $g_{12}(r)$ and the total pair distribution function $g_{all}(r)$ for the heating traverse as a function of distance from $T = 0.1$ up to $T = 1.2$. For $T \geq 1.18$, each curve has been shifted upwards by one unit from the lower temperature curve directly preceding it.

minima in the respective PPDFs, while the value for cut_{11} was set equal to the value obtained for the cooling traverse at $T = 1.15$.

Structure Factors

The partial structure factors can be calculated from the PPDFs as follows:

$$S_{ab}(k) = x_a \delta_{ab} + x_a x_b \rho \widehat{h}_{ab}(k), \quad a = 1, 2, \tag{5.4}$$

where $\widehat{h}_{ab}$ is the Fourier transform of the total correlation function $h_{ab}(r) = g_{ab}(r) - 1$ and has the form:

$$\widehat{h}_{ab} = \int_0^\infty r h_{ab} J_0(kr) dr \tag{5.5}$$

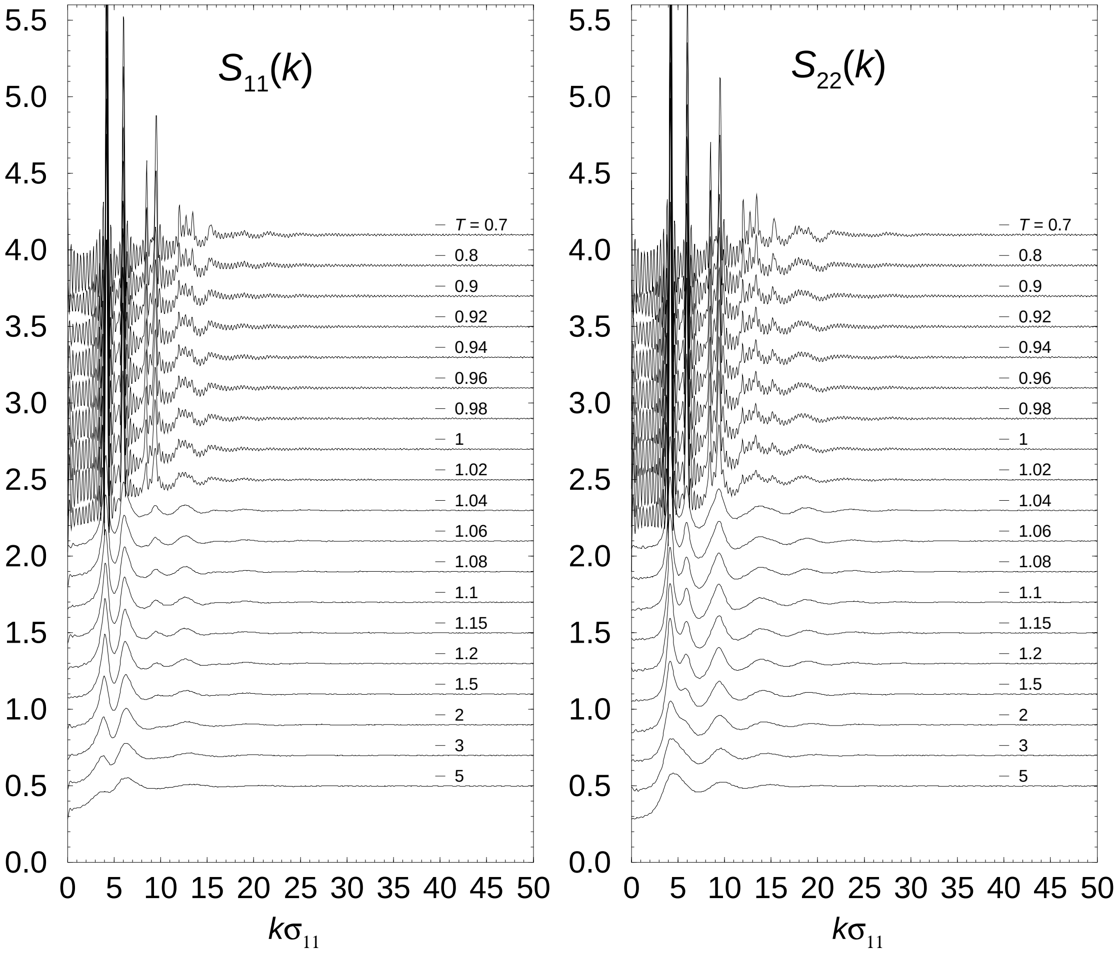

Figure 5.9: The partial structure factors $S_{11}(k)$ and $S_{22}(k)$ for the cooling traverse for temperatures from $T = 5$ down to $T = 0.7$. For clarity, each curve below $T = 5$ has been shifted upwards by 0.2 units above the higher temperature curve directly preceding it.

for a homogeneous fluid in 2D. J_0 is the Bessel function of order 0. We have also calculated the total structure factor

$$S_{all}(k) = 1 + \rho \widehat{h}_{all}(k) \tag{5.6}$$

where $\widehat{h}_{all}$ is the Fourier transform of $h_{all}(r) = g_{all}(r) - 1$. The integrals were evaluated using the extended Simpson's rule [204].

The structure factors for the cooling traverse, displaced vertically for clarity, are plotted in Figures 5.9 and 5.10. The oscillations at small k for $T \leq 1.02$ are artifacts of the Fourier transformation procedure due to the truncation of the long-ranged pair

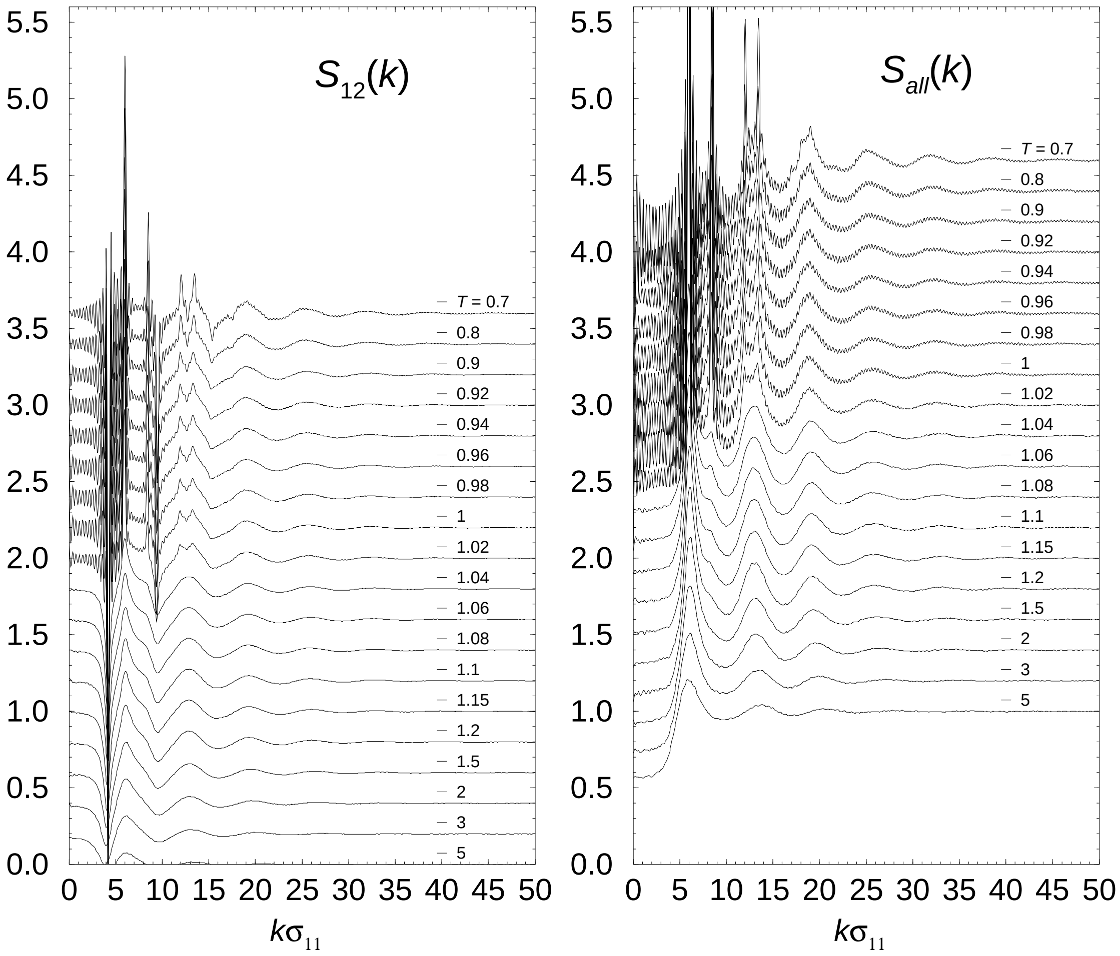

Figure 5.10: The partial structure factor $S_{12}(k)$ and the total structure factor $S_{all}(k)$ for the cooling traverse as a function of wave vector from $T = 5$ down to $T = 0.7$. For clarity, each curve below $T = 5$ has been shifted upwards by 0.2 units above the higher temperature curve directly preceding it.

distribution functions at non-zero values and should be ignored. As the temperature is lowered, the heights of the peaks become more pronounced, and at $T = 1.02$ they increase dramatically in height and become very sharp.

The location of the most intense peak (k_{max}) represents a characteristic length-scale for the dominant short-range ordering in the system. The decay of density correlation functions at wave vectors close to k_{max} therefore provides information about the main structural relaxation process in the system. As explained in Section 1.2, measurements of intermediate scattering by dynamic light scattering, inelastic neutron scattering and neutron spin-echo experiments are often made at wave vectors close to k_{max}. We therefore calculate the incoherent intermediate scattering functions (Section 5.15) at the wave vectors corresponding to the first maxima in $S_{11}(k)$ and $S_{22}(k)$. For reference, these are listed in Table C.4. We did not investigate structural relaxation in the solid state and have therefore not calculated structure factors for the heating traverse.

Local Structure Parameters

Several quantities were used to characterise the local structure of the equimolar mixture. In Figure 5.11 we present the 'bond' fractions n_{ab} for the cooling and heating traverses. The 'bond' fractions are defined as the fraction of all nearest neighbour particle pairs that occur between particles of type a and b (see Section 5.3.2 for the definition of nearest neighbours). They can be related to, and give similar information to, the first shell partial coordination numbers calculated previously for the equimolar mixture with $\sigma_{12} = 1.2$ [67].

The changes in local structure during the cooling and heating traverses are very similar. The majority of nearest neighbour interactions occur between unlike particle species (about 60%), with most of the remaining interactions being between large particles. During cooling, there is a sudden decrease in n_{11} at $T = 1.02$ that is accompanied by smaller step increases in n_{12} and n_{22}; and during heating, the reverse occurs at $T = 1.08$. These temperatures coincide with the temperatures at which there are sudden changes in the other properties already studied. In particular, the sudden decrease in small particle nearest neighbours at $T = 1.02$ is consistent with our interpretation that the first peak in $g_{11}(r)$ at this temperature is no longer due to small particle nearest neighbours.

Another way to characterise the change in local structure is via the local coordination environment. We have identified a particular neighbourhood with the following notation: a small particle with m small neighbours and n large neighbours is designated as Smn and the analogous large particle is indicated as Lmn. The distribution of these local environments is plotted as a function of temperature in Figure 5.12 for both the heating and cooling traverses. Only the most common environments are shown.

As the equimolar mixture is cooled, the fraction of S04 environments - corresponding to the square tile in Figure 5.1 - increases gradually until $T = 1.02$ at which point there is a sudden large increase, followed by a gradual increase as the temperature

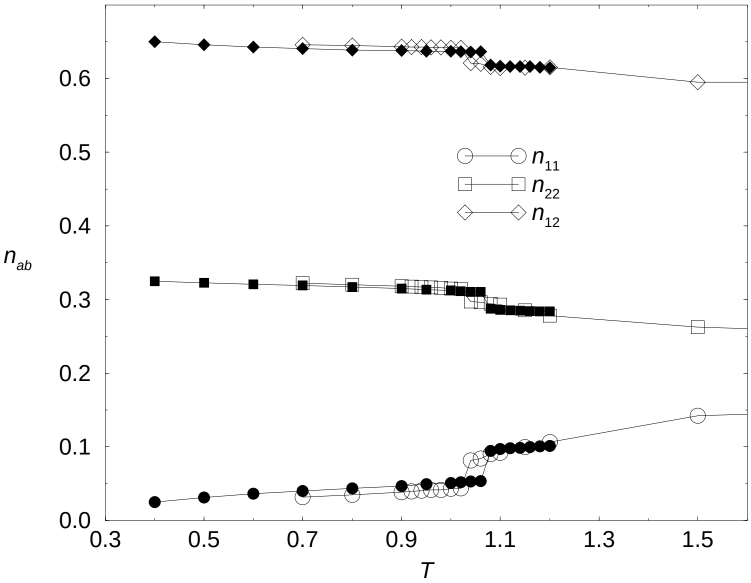

Figure 5.11: 'Bond' fractions as a function of temperature for the cooling and heating traverses. The filled symbols indicate data from the heating traverse. n_{ab} is the fraction of all nearest neighbours particle pairs that occur between particles of type a and b. Error bars represent one standard deviation.

is further reduced. There is a smaller increase in S14 until $T = 1.02$ after which the fraction of these environments begins to fall. Both these results are consistent with a freezing transition to the S1 crystal at $T = 1.02$; the S14 order could be due to a vibrational distortion of two square S04 environments packed together, which would explain why it decreases when the crystal is cooled. The main changes in large particle environments is a gradual increase in L43 until $T = 1.02$ at which point there is a sudden drop followed by a further gradual decrease with cooling. In a perfect S1 crystal the large particles will lie at the centre of four square unit cells packed together - corresponding to vertex (b) in Figure 5.1 - and will thus have an L44 environment. As this quantity was not calculated we can only speculate that the variation in L43 at low temperature is due to this being a vibrational distortion of the L44 environment. We do know that 52% of local environments are unaccounted for at $T = 0.7$. Since the S04 and S14 environments make up about 48% of all local environments at $T = 0.7$, and all 5-, 6- and 7-fold environments have been quantified, we assume that most of the remaining 52% is in the form of L44 environments. The other local environments present at high temperature make a neglible contribution below $T = 1.02$.

The heating traverse shows very similar variation in the distribution of local environments as a function of temperature. The major difference is that the sudden

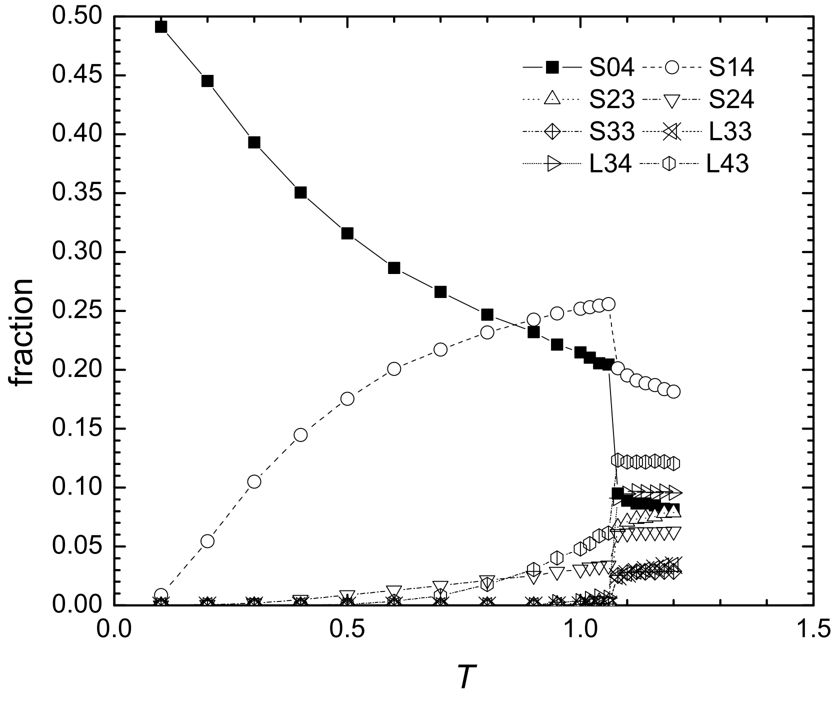

(a)

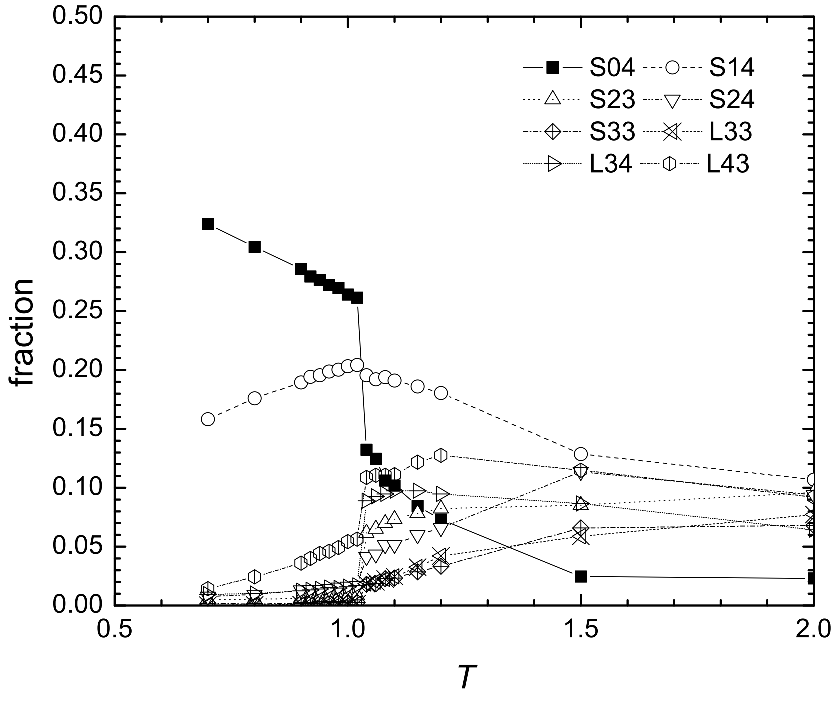

(b)

Figure 5.12: The distribution of local environments as a function of temperature for (a) heating, and (b) cooling traverses. We have identified a particular neighbourhood with the following notation: A small particle with m small neighbours and n large neighbours is designated as Smn and the analogous large particle is indicated as Lmn.

jumps now occur between $T = 1.06$ and $T = 1.08$. All the large particles must be in L44 environments at $T = 0.1$.

Orientational Order Parameters

We have already established that the equimolar mixture has long-range translational order at low temperature. Here we define a set of order parameters to investigate the local orientational order and long-range correlations between local environments. Following the definition of a hexatic order parameter by Broughton et al. [171], we define a set family of n-fold orientational order parameters for particle j as

$$\psi_n(\mathbf{r_j}) = \frac{1}{n_j} \sum_{k=1}^{n_j} \exp^{in\theta_{jk}} \tag{5.7}$$

where n_j is the number of nearest neighbours of particle j at position $\mathbf{r}_j$ and θ_{jk} is the angle (in radians) made by the bond between particle j and particle k and an arbitrary direction (here chosen to be the x axis). The order parameter equals one if particle j lies at the centre of a regular n-fold polygon made up of its neighbours.

A set of bulk averaged n-fold order parameters can then be defined as follows:

$$\Psi_n = \left\langle \frac{1}{N} \sum_{j=1}^{N} |\psi_n(\mathbf{r_j})| \right\rangle , \tag{5.8}$$

where the partial n-fold order parameters are given by

$$\Psi_{n,a} = \left\langle \frac{1}{N_a} \sum_{j=1}^{N_a} |\psi_n(\mathbf{r_j})| \right\rangle \qquad \text{with} \quad a = 1, 2. \tag{5.9}$$

The angular brackets represent an average over various configurations separated in time.

The bulk averaged n-fold order parameters Ψ_n probe the local orientational order. We consider the 4-, 6- and 12-fold order parameters. Both 4- and 6-fold local environments are common in the set of models that we have studied, and a random tiling of squares and triangles (a possible structure for the non-equimolar mixture explored in Section 5.4) will have long-range 12-fold order.

Their temperature variation is plotted in Figure 5.13 for both the heating and cooling traverses. $\Psi_{4,1}$ increases gradually below $T = 1.5$ and undergoes a sudden

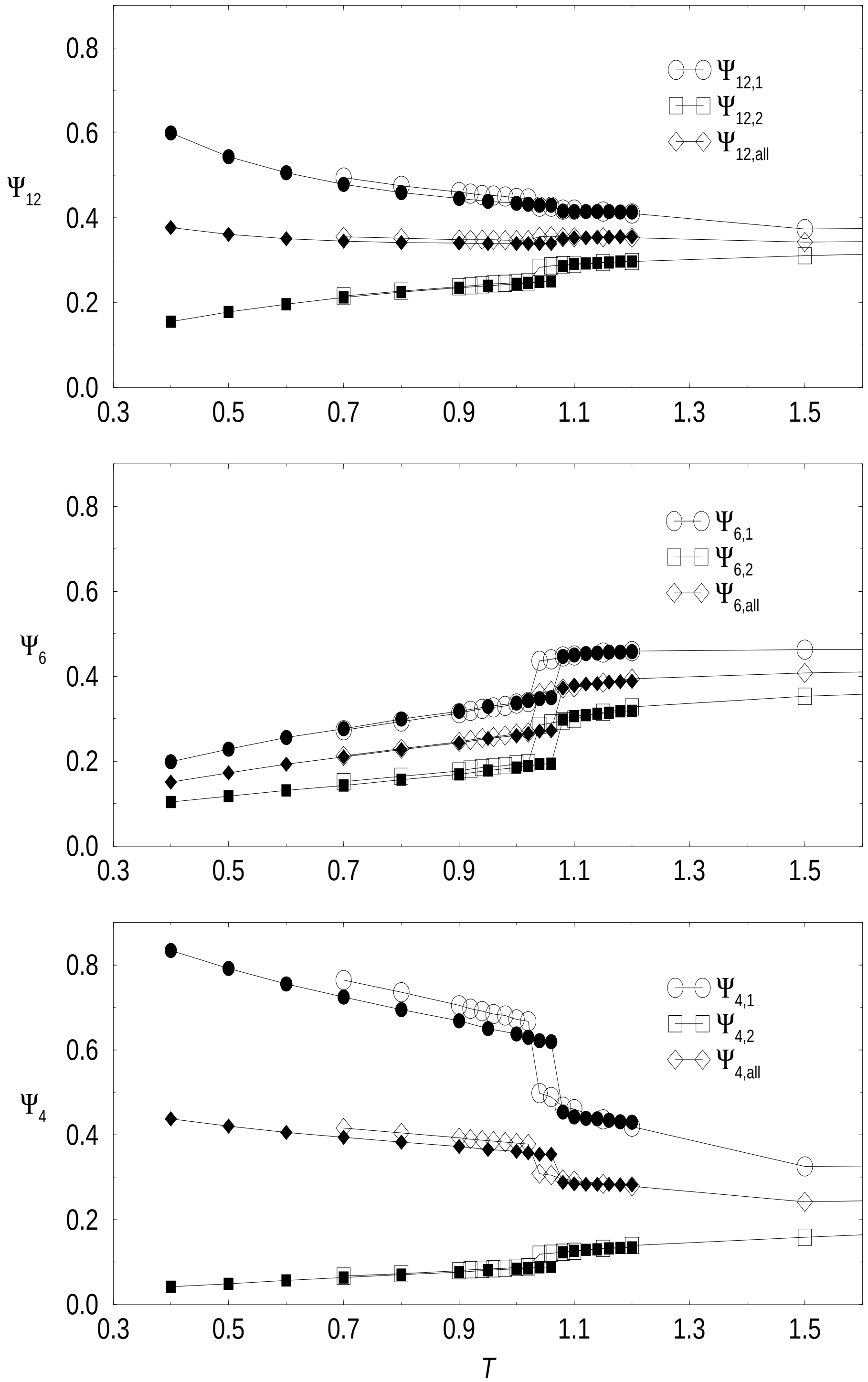

Figure 5.13: The temperature dependence of the bulk averaged n-fold order parameters Ψ_n, where $n = 4, 6, 12$, and their small ($\Psi_{n,1}$) and large ($\Psi_{n,2}$) particle contributions, for the cooling and heating traverses. The filled symbols indicate data from the heating traverse. The error bars represent one standard deviation about the average.

increase at $T = 1.02$ followed by a further gradual increase, very similar to the behaviour of the S04 environment. At the same time there is a decrease in $\Psi_{4,2}$, which can be explained by large particles increasingly finding themselves in vertices of type (b) (see Figure 5.1). The large particles at the centre of these vertices will have L44 environment which, having 8-fold orientational order, will result in $\Psi_{4,2} = 0$. The local 6-fold order decreases suddenly during cooling at $T = 1.02$. The variations in $\Psi_{12,a}$ appears to contain no additional information. The changes in bulk orientational order are similar for the heating traverse, except that the jump in properties now occurs at $T = 1.08$.

Next we test for the presence of long-range orientational correlation between local domains. The spatial correlation of the orientation of the local n-fold environments is measured by the associated correlation functions

$$C_n(r) = \left\langle \frac{1}{N\rho} \sum_{j=1}^{N} \sum_{k\neq j}^{N} \psi_n(\mathbf{r}_j)\psi_n^*(\mathbf{r}_k)\delta(r - |\mathbf{r}_j - \mathbf{r}_k|) \right\rangle \tag{5.10}$$

and

$$C_{n,a}(r) = \left\langle \frac{1}{N\rho {x_a}^2} \sum_{j=1}^{N_a} \sum_{k\neq j}^{N_a} \psi_n(\mathbf{r}_j)\psi_n^*(\mathbf{r}_k)\delta(r - |\mathbf{r}_j - \mathbf{r}_k|) \right\rangle \quad \text{with} \quad a = 1, 2. \tag{5.11}$$

These orientational correlation functions are weighted by the translational correlations. To see them free of this bias we plot the ratios $G_n(r) = C_n(r)/g_{All}(r)$, $G_{n,1}(r) = C_{n,1}(r)/g_{11}(r)$, and $G_{n,2}(r) = C_{n,2}(r)/g_{22}(r)$. We consider the cases where $n = 4, 6, 12$ for the reasons outlined above.

In Figure 5.14, we plot the partial 4-fold orientational correlation function $G_{4,1}(r)$ for both the cooling and heating traverses. We have not plotted $G_{4,2}(r)$ as there was no observable structure in this function. The functions have been displaced vertically for clarity. There is clearly long-range 4-fold orientational correlation between small particle environments for $T \leq 1.02$ during the cooling traverse, and $T \leq 1.06$ during the heating traverse, and only local order at higher temperature, which is consistent with the existence of the S1 crystal state at these temperatures. We have also calculated the 6- and 12-fold orientational correlation functions, however as they provide little additional insight we do not plot them. The 6-fold correlation functions have only a single peak and show little variation with temperature, while the 12-fold correlation functions are very similar to the 4-fold correlation functions and can be

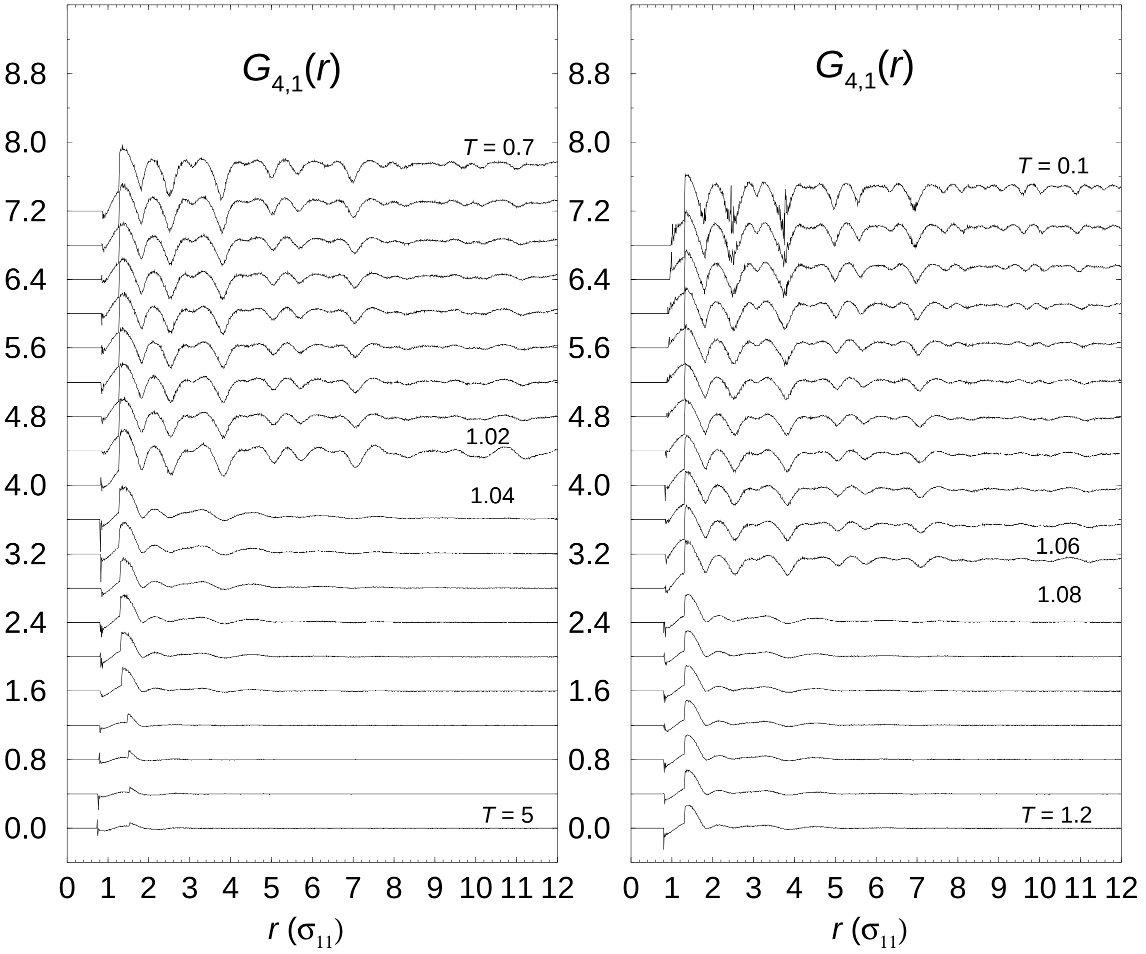

Figure 5.14: The partial 4-fold orientational correlation function $G_{4,1}(r)$ for the small particles, for the (left) cooling and (right) heating traverses. For clarify, functions have been offset vertically by 0.4 units above the preceding curve.

explained by the presence of 4-fold order in the system.

In summary, the equimolar mixture freezes at $T = 1.02$ into a largely defect-free S1 crystal structure. There appears to be substantial crystalline order in the liquid prior to freezing, in the form of S04 environments and a large uncounted fraction of local environments most of which are probably L44 environments. There is also evidence for medium-range packing of S04 cells, from the medium-range structure in the pair distribution functions, and from the high proportion of S14 environments. The structural changes during heating from a perfect S1 crystal are very similar, and confirm a region of metastability extending from $T = 1.02$–1.08.

5.3.3 Dynamics and Structural Relaxation

In this section, we present an analysis of the changes in particle transport and structural relaxation that occur upon cooling and heating of the equimolar mixture. We report some of the main time correlation functions that are routinely measured in MD simulations.

Intermediate Scattering Functions

The timescales of structural relaxation can be probed quite readily by computing density correlation functions such as the incoherent and coherent intermediate scattering functions. For the equimolar mixture, we have calculated the incoherent (or

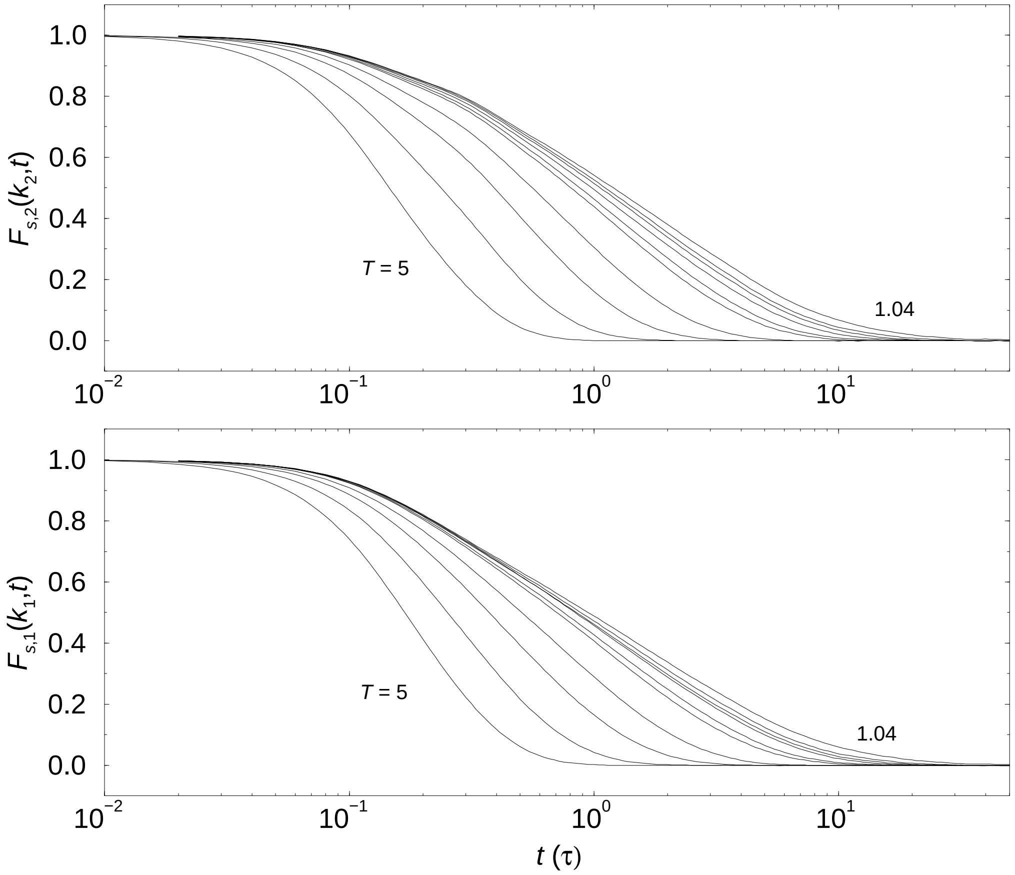

Figure 5.15: The incoherent scattering functions $F_{s,1}(k_1, t)$ and $F_{s,2}(k_2, t)$ for the small and large particles, respectively. The wave vectors k_1 and k_2 are the first peak positions in the respective partial structure factors (listed in C.4). From left to right the temperatures of the curves are $T = 5$, 3, 2, 1.5, 1.2, 1.15, 1.1, 1.08, 1.06, and 1.04.

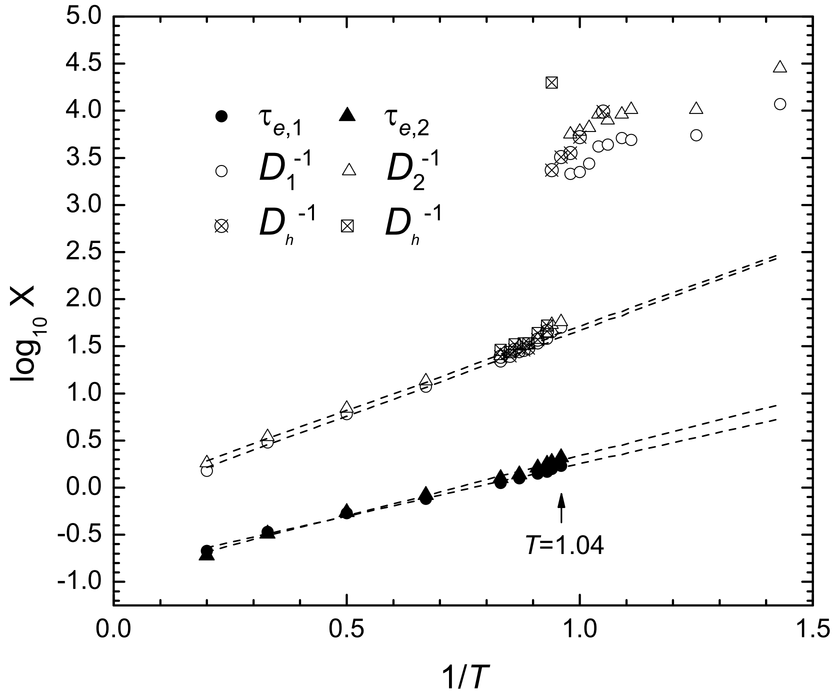

Figure 5.16: Arrhenius plot of the structural relaxation times $\tau_{e,1}$ and $\tau_{e,2}$ and the inverse diffusion constants D_1^{-1} and D_2^{-1} for the cooling traverse. Some inverse diffusion constants calculated for the heating traverse, $D_{h,1}^{-1}$ and $D_{h,2}^{-1}$, are also shown. The dashed lines are linear regressions through the cooling data for $T \geq 1.04$.

self) intermediate scattering functions

$$F_{s,a}(k,t) = \frac{1}{N_a}\left\langle \sum_{j=1}^{N_a} \exp(i\mathbf{k}.[\mathbf{r}_j(t) - \mathbf{r}_j(0)]) \right\rangle, \quad a = 1, 2 \tag{5.12}$$

for both particle species. The angular brackets denote an average over time origins and an angular average over the directions of the wave vector **k**. The magnitudes of **k** were chosen as the positions of the first maxima in the respective partial structure factors. The first peak was used since this is the largest one and therefore the best wave vector at which to monitor structural relaxation. Since the position of this peak varies significantly with temperature, we have used a temperature dependent magnitude for **k**, the values of which are listed in Table C.4.

We have only calculated incoherent scattering functions for the cooling traverse. These are plotted in log-linear form in Figure 5.15 for $T \geq 1.04$, i.e. for the liquid phase. It would be interesting to extend this analysis to the solid phase and to the heating traverse to further investigate the nature of defect motion in the S1 crystal. We find that the relaxation curves decay smoothly and broaden with decreasing temperature, until at $T = 1.04$ they span over two decades in time. There is no sign of a plateau region at intermediate times.

Structural relaxation times $\tau_{e,1}$ and $\tau_{e,2}$ are defined as the time taken for the incoherent scattering functions $F_{s,1}(k,t)$ and $F_{s,2}(k,t)$, respectively, to decay to $1/e$ of their initial values. The temperature dependences of these relaxation times, plotted in Figure 5.16, appear to be Arrhenius at all $T \geq 1.04$. This is consistent with the equimolar mixture existing as a normal liquid in this temperature range.

Mean-Squared Particle Displacements

The mean-squared displacement (MSD) can provide important information regarding the dynamics of particles on different length scales, and is defined as

$$R^2(t) = \frac{1}{N}\left\langle \sum_{i=1}^{N} |\mathbf{r_i}(t) - \mathbf{r_i}(0)|^2 \right\rangle, \tag{5.13}$$

where the angular brackets represent an average over time origins. The MSD is also a useful way to distinguish between a rigid system and a fluid one.

At very short times, the MSD has a power law dependence on time with an exponent of two, which corresponds to ballistic motion. A particle undergoes ballistic motion until it experiences its first collision with another particle, and such motion is therefore present even in systems that are configurationally frozen. The end of this region can therefore be used to estimate the first collision time. At much longer times, if the system is fluid, the MSD has a power law dependence on time with a slope of one, indicating diffusive motion.

A long-time diffusion constant can be extracted from the MSD. For the 2D system this is given by

$$D = \frac{1}{4}\lim_{t\to\infty}\frac{dR^2(t)}{dt} \tag{5.14}$$

Strictly speaking, the diffusion constant cannot be defined asymptotically in 2D as, according to the Landau-Peierls theorem [205], it diverges in the thermodynamic limit. However, in practice this is not an issue. The upward curve in the MSD at long times is so slow to appear that the diffusion constant is still well-defined and meaningful on the timescale of the simulations. A comparison of the diffusion constants and structural relaxation times can sometimes reveal interesting differences in the dynamics of incoherent processes on different length scales.

The MSDs over all particles $R^2(t)$, and averaged over the two particle species, ${R_2}^2(t)$ and ${R_1}^2(t)$ are plotted in Figure 5.17 for the cooling traverse and in Figure 5.18 for the heating traverse. All the plots are qualitatively very similar. At very short times, the curves have a power law dependence on time with an exponent of two, which corresponds to ballistic motion, while at much longer times, for sufficiently high temperature, the curves have a smaller slope of one indicating diffusive motion. The first collision time for this system is about 0.01τ. The sudden increase in ${R_1}^2(t)$ for the heating traverse at $T = 0.9$ is due to the appearance of defect approx. 2000τ into the production run.

Upon cooling, there is an increasing separation in timescales between ballistic and diffusive motion, accompanied by the sudden appearance of a plateau region at intermediate times at $T = 1.02$. This intermediate region is often associated with transient caging of particles by their neighbours. As we have already described, the structure of the equimolar mixture changes dramatically at $T = 1.02$, consistent with a freezing transition to a defected S1 crystal at this temperature. The MSD curves therefore suggest that there must be significant motion - presumably of the defects - in the S1 crystal. Additional cooling runs would be useful to investigate at what temperature the defect motion eventually stops.

During the heating traverse, only ballistic motion is present at low temperature. The constructed S1 crystal must therefore remain defect free. Eventually, at $T = 0.95$, ${R_1}^2(t)$ begins to rise again after about 100τ followed by ${R_2}^2(t)$ after about 1000τ. For $T \geq 1.08$ the MSD curves again show typical liquid behaviour with no plateau region at intermediate times. A survey of the equilibrated configurations show that the crystal structure remains defect free until $T = 0.95$ at which point a few defects appear. We therefore suggest that it is these defects that are responsible for the rise in the MSD at long times between $T = 0.95$ and $T = 1.06$. We therefore conclude that motion in the defected crystal is dominated by small particles. This contrasts with the behaviour observed after freezing during the cooling traverse when both particle species have similar mobility.

Diffusion constants were measured for both the cooling and heating traverses in the region where the MSD has reached its long-time constant value (${R_a}^2(t) > \sigma_{11}^2$). An Arrhenius plot of the inverse diffusion constants is shown in Figure 5.16. They

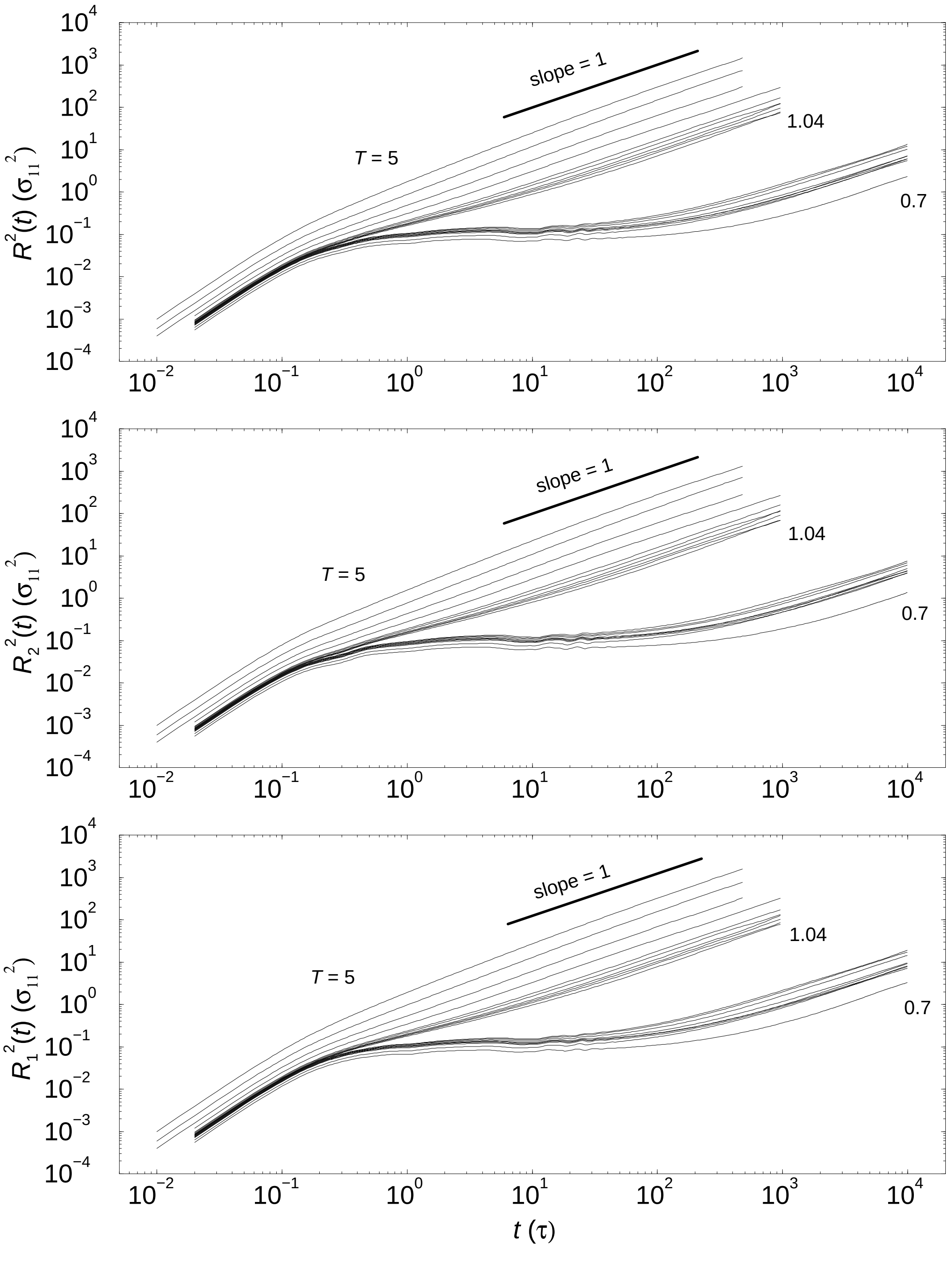

Figure 5.17: The time dependence of the MSD averaged over all particles $R^2(t)$, and averaged over the two particle species, ${R_2}^2(t)$ and ${R_1}^2(t)$ for the cooling traverse. The temperature of the curves from top to bottom is $T = 5$, 3, 2, 1.5, 1.2, 1.15, 1.1, 1.08, 1.06, 1.04, 1.02, 1, 0.98, 0.96, 0.94, 0.92, 0.9, 0.8, and 0.7.

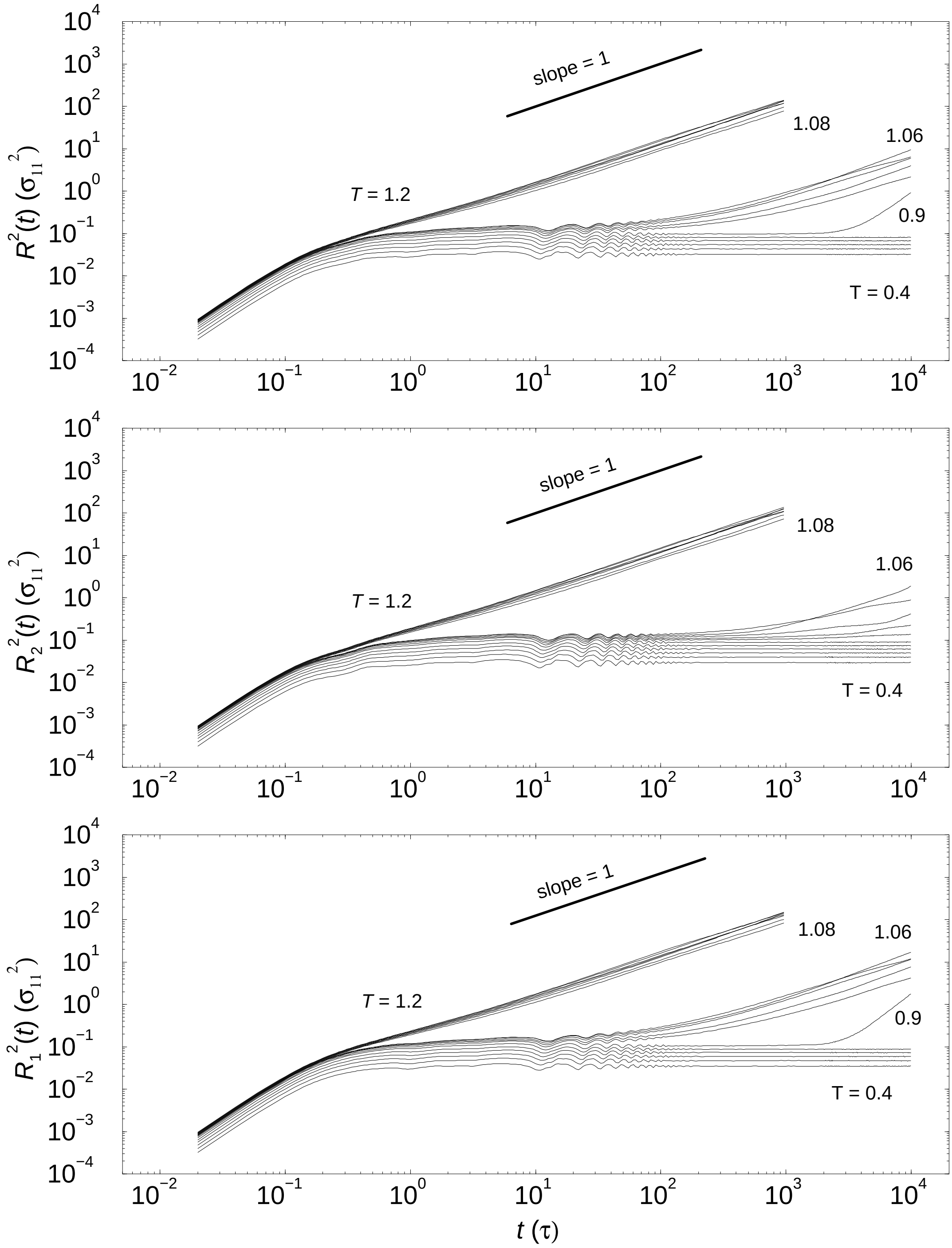

Figure 5.18: The time dependence of the MSD averaged over all particles $R^2(t)$, and averaged over the two particle species, ${R_2}^2(t)$ and ${R_1}^2(t)$ for the heating traverse. The temperature of the curves from top to bottom is $T = 1.2$, 1.18, 1.16, 1.14, 1.12, 1.1, 1.08, 1.06, 1.04, 1.02, 1, 0.95, 0.9, 0.8, 0.7, 0.6, 0.5, and 0.4. Note that the sudden increase in ${R_1}^2(t)$ at $T = 0.9$ is due to the appearance of a defect during the production run.

have Arrhenius temperature dependence for the entire liquid region ($T \geq 1.04$ for the cooling traverse, and $T \geq 1.08$ for the heating traverse). For reference, the structural relaxation times and diffusion constants are also listed in Table C.5. Diffusion constants measured for the defected crystals are generally two orders of magnitude smaller than for the low-temperature liquid.

The Non-Gaussian Parameter

In a harmonic solid, and in an equilibrium liquid at times sufficiently long for particles to randomise the initial distribution of momenta, the probability of a particle displacement of magnitude r is proportional to a simple Gaussian function $\exp(-Cr^2)$, where C is a constant that may depend on time. Substantial deviations from such Gaussian behaviour have been observed in many simulations of supercooled liquids at intermediate times. These deviations can be quantified by a non-Gaussian parameter [206] defined as

$$A(t) = \frac{R^4(t)}{C[R^2(t)]^2} - 1, \tag{5.15}$$

where $R^4(t) = \langle |\mathbf{r_i}(t) - \mathbf{r_i}(0)|^4 \rangle$ is the mean-quartic displacement, $R^2(t)$ is the mean-squared displacement, and the constant C equals 5/3 in 3D and 2 in 2D. For a Gaussian process $A(t) = 0$ for all times. Non-Gaussian parameters for individual particles species, represented by $A_a(t)$, can also be defined by averaging only over particles of type a.

Hurley and Harrowell [74], studying a model of particles undergoing a random walk in a dynamically heterogeneous environment, demonstrated that large values of $A(t)$ at intermediate times could be attributed to a broad distribution of local mobilities in the system. Thus, the non-Gaussian parameter can be used as a measure of the degree of dynamic heterogeneity. The maximum in $A(t)$ is expected to increase as the distribution of local relaxation times broadens.

We have calculated the non-Gaussian parameters for both the cooling traverse (plotted in Figure 5.19) and the heating traverse (plotted in Figure 5.20). During cooling, the non-Gaussian parameters remain very small at all times for $T \geq 1.04$. Suddenly, at $T = 1.02$, a large peak appears at intermediate times, and upon further cooling the amplitude of the peak and the time at which it occurs increase. During heating, the non-Gaussian parameters remain very small at all times for $T < 0.9$ and $T \geq 1.08$. At $T = 0.9$ a relatively narrow peak of large amplitude appears at relatively late time in $A_1(t)$ that can be attributed to the appearance of a defect in the crystal structure at about 2000τ into the production run. Between $T = 0.95$ and $T = 1.06$, a large peak again occurs at intermediate times with an amplitude that is larger at lower temperature. The unusually shaped peak at $T = 1.06$ can be attributed to a late onset of large particle defect motion. These results are all consistent with a freezing transition at $T = 1.02$ during cooling and a melting transition at $T = 1.08$ during heating. The appearance of the large peak at intermediate times in the non-Gaussian parameters coincides with the appearance of mobile defects in the crystal structure and can be explained by these. The peaks in $A_2(t)$ during the heating traverse appear at much later times, for the equivalent temperature, than during the cooling traverse. This suggests that the defect motion during the heating traverse is qualitatively different than during the cooling traverse.

Additionally, the large oscillations in $A_1(t)$ are visible between 10τ and 100τ during the heating traverse. These coincide with similar oscillations in the plateau region of ${R_1}^2(t)$ for all $T \leq 1.06$. Similar damped oscillations have been observed in the plateau region of the incoherent scattering functions for several glass-formers including the model studied in Part I. For that particular model, Perera and Harrowell [44] concluded that while system size could influence the frequency of these modes, their presence was a consequence of the transient rigidity of the liquid [44]. The present work demonstrates that such oscillations can also appear in a crystalline solid, either with or without defects. The unusually large size of the oscillations in $A_1(t)$ observed during the heating traverse may be related to the very small 'mass' used for the Anderson pressure piston Q_v (see Section 5.2).

Prior to freezing, the structural relaxation times follow an Arrhenius temperature dependence and the equimolar mixture shows typical liquid dynamics. In the solid phase, there is substantial defect motion in the high-temperature crystal, during both the heating and cooling traverses, as evidenced by a late rise in the MSDs and large peaks in the non-Gaussian parameters. During heating defects appear at $T = 0.9$ - initially due to small-particle motion, but at later times also due to large-particle motion. This reduced large-particle mobility contrasts with the frozen crystal in which the small and large particles have almost identical mobilities. The structural and dynamic data for both heating and cooling traverses is consistent with a transition from rigid S1 crystal to crystal with defect motion to normal liquid and vice versa. The equimolar mixture is discussed further in Section 5.5.

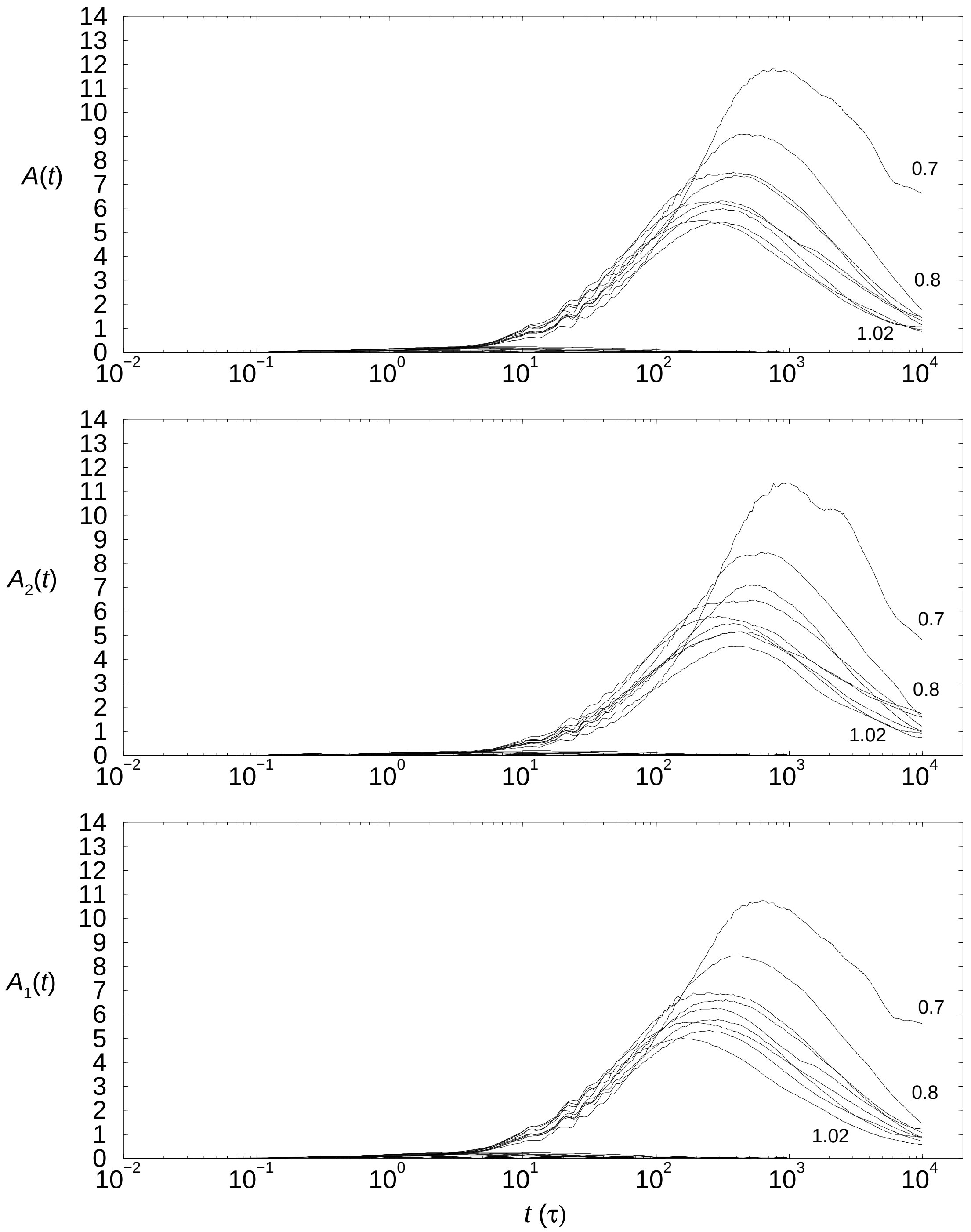

Figure 5.19: The non-Gaussian parameter averaged over all particles, $A(t)$, and averaged over only the small and large particles, $A_1(t)$ and $A_2(t)$, respectively, for the cooling traverse. The temperatures of the curves are as listed for Figure 5.17. Observe the sudden change in behaviour at $T = 1.02$.

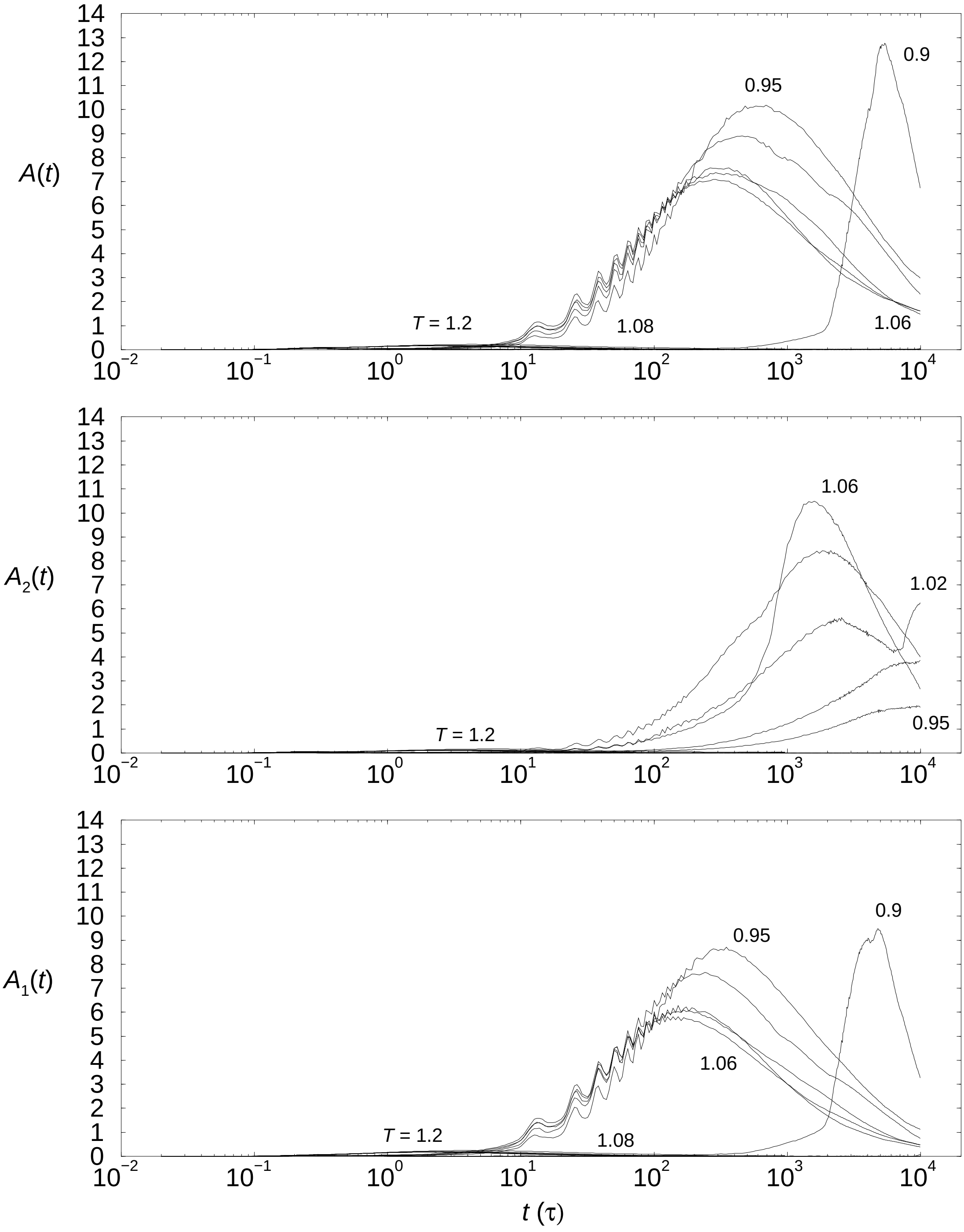

Figure 5.20: The non-Gaussian parameter averaged over all particles, $A(t)$, and averaged over only small and large particles, $A_1(t)$ and $A_2(t)$, respectively, for the heating traverse. The temperatures of the curves are as listed for Figure 5.18. Observe the sudden change in behaviour at $T = 1.08$. The sharp peak in $A_1(t)$ at $T = 0.9$ is due to the appearance of a defect during the production run.

5.4 Amorphisation and Melting of the Non-Equimolar Mixture ($x_1 = 0.3167$)

In this section we characterise the thermodynamic, structural and dynamic properties of the non-equimolar mixture. The composition ($x_1 = 0.3167$) was chosen to favour a random tiling with maximal configurational entropy as explained in Section 5.1. A 2D quasicrystal approximant can also be constructed at this composition [159]. When cooled from the fluid state, we find that the mixture forms an amorphous solid with well-defined local order and defects. In contrast, a periodic structure with similar composition melts discontinuously (see Section 5.4.4). This leads us to speculate on the relationship between random tilings, quasicrystal and amorphous solids.

5.4.1 Thermodynamic Properties

For reference, thermodynamic averages for the cooling traverse of the non-equimolar mixture are tabulated in Table C.6. The non-equimolar mixture was studied at many closely spaced temperatures, including at high temperature, to improve confidence in the nature of the transition from liquid to solid. Figure 5.21 shows the isobaric

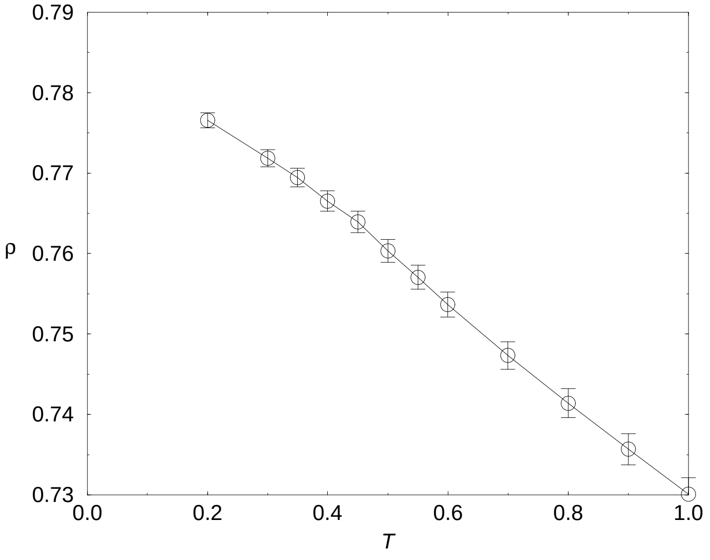

Figure 5.21: Isobaric ($P = 13.5$) phase diagram. Error bars represent one standard deviation. Note the lack of a step in density upon cooling.

phase diagram for the cooling traverse. The density increases smoothly indicating a continuous transition from the liquid to solid state. There is perhaps a small change in slope at $T = 0.45$, which is when the system falls out of local equilibrium. In the next section we characterise the changes in structure that occur during cooling of the non-equimolar mixture. Only data at selected temperatures ($T = 5$, 3, 2, 1, 0.9, 0.8, 0.7, 0.6, 0.55, 0.5, 0.45, 0.4, 0.35, 0.3, and 0.2) are plotted.

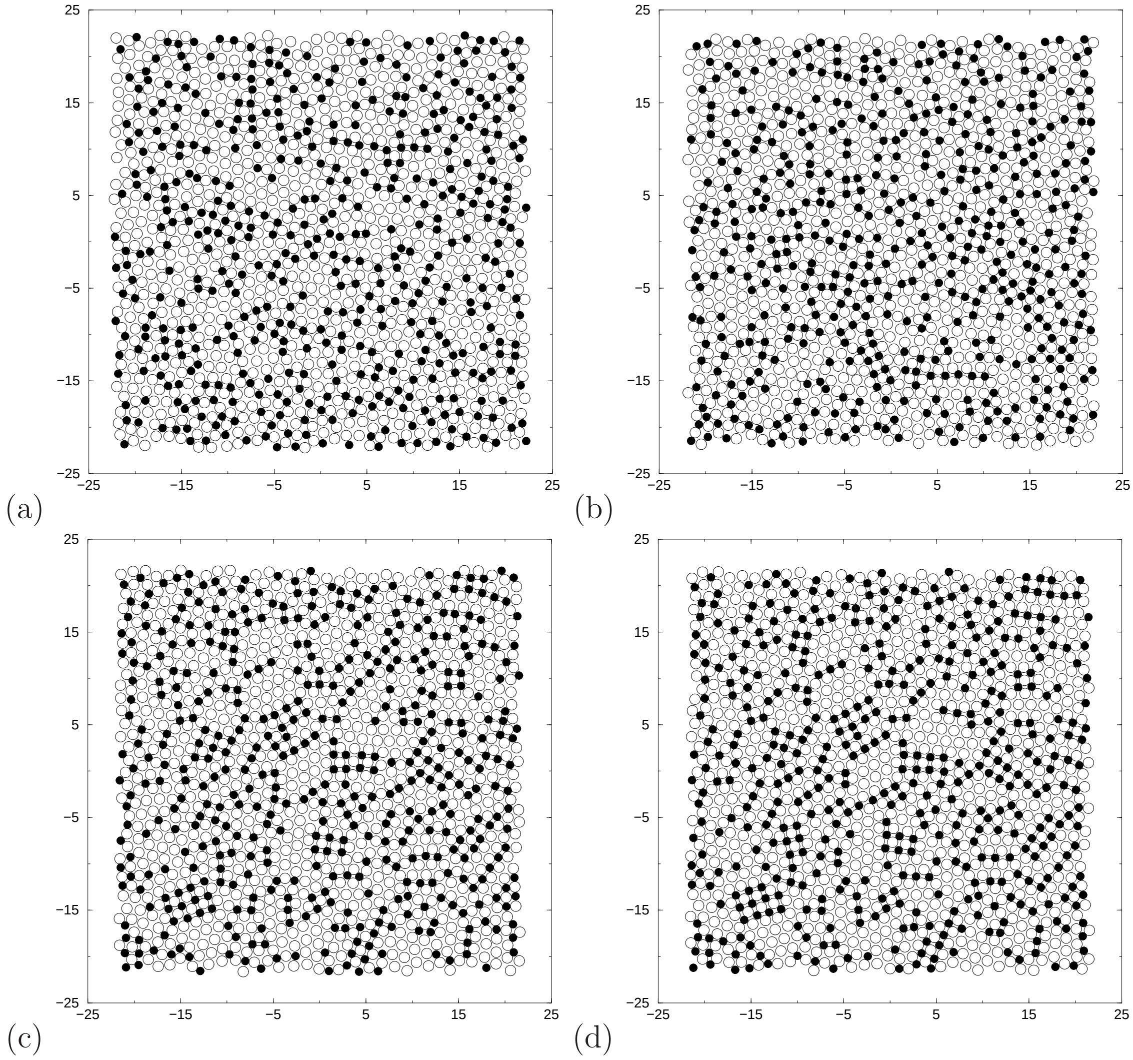

(a) (b) (c) (d)

Figure 5.22: Representative particle configurations at (a) $T = 1$, (b) $T = 0.7$, (c) $T = 0.4$, and (d) $T = 0.2$ for the cooling traverse. The small and large particles are represented by filled and open circles respectively.

5.4.2 Development of Random-Tiling Order

Particle Configurations

Selected particle configurations are plotted in Figure 5.22. At high temperature ($T = 1$) the liquid appears homogeneous but there is no clustering of small particles. By $T = 0.7$ local square and equilateral packings are apparent and small regions of S1 crystal order can be observed. These crystalline regions appear to have grown by $T = 0.4$ and the structure is now well described as a random tiling of squares and equilateral triangles with the occasional defect. Most of the structure is now rigid, as can be seen by comparing this configuration with the one after further cooling to $T = 0.2$. However, some changes are apparent in the lower left quarter of the structure indicating that motion is still possible at these very low temperatures.

Pair Distribution Functions

In Figures 5.23 and 5.24 we plot the pair distribution function (PDF) and the partial pair distribution functions (PPDFs), as defined in Section 5.3.2. It is clear that there is no development of long-range translational order on cooling. Some increase in local structure is apparent but this does not extend beyond $r = 7\sigma_{11}$. The most obvious change is that the position of the first peak in $g_{11}(r)$ shifts from $r = \sigma_{11}$ to $r = 1.4\sigma_{11}$ as the temperature is decreased. This is similar to what was observed for the equimolar mixture and can be explained by the disappearance of small particle nearest neighbours. As we demonstrate in Section 5.4.2, the small particles become surrounded by four large particles at low temperature forming the equivalent of square tiles resulting in a small particle closest interaction length of $\sigma_{22} = 1.4\sigma_{11}$. The large intensity of the peak around $r = 2\sigma_{11}$ relative to the first peak in $g_{11}(r)$ is due to a high relative proportion of linear small-large-small particle arrangements and can be explained by the majority of large particle vertices being of types (c) and (d) as illustrated in Figure 5.1. Thus the medium-range order in the non-equimolar mixture is quite different from that in the equimolar mixture. We explore this further in Section 5.4.2.

From these data we extract cutoff distances to use for defining nearest neighbours. We have generally used the position of the first minimum in $g_{ab}(r)$ as the value for cut_{ab}. The exception is for cut_{11} where we have used the position of the first minimum in $g_{11}(r)$ at $T = 1.5$ as the cutoff for all $T \leq 1$. This is necessary in order to distinguish

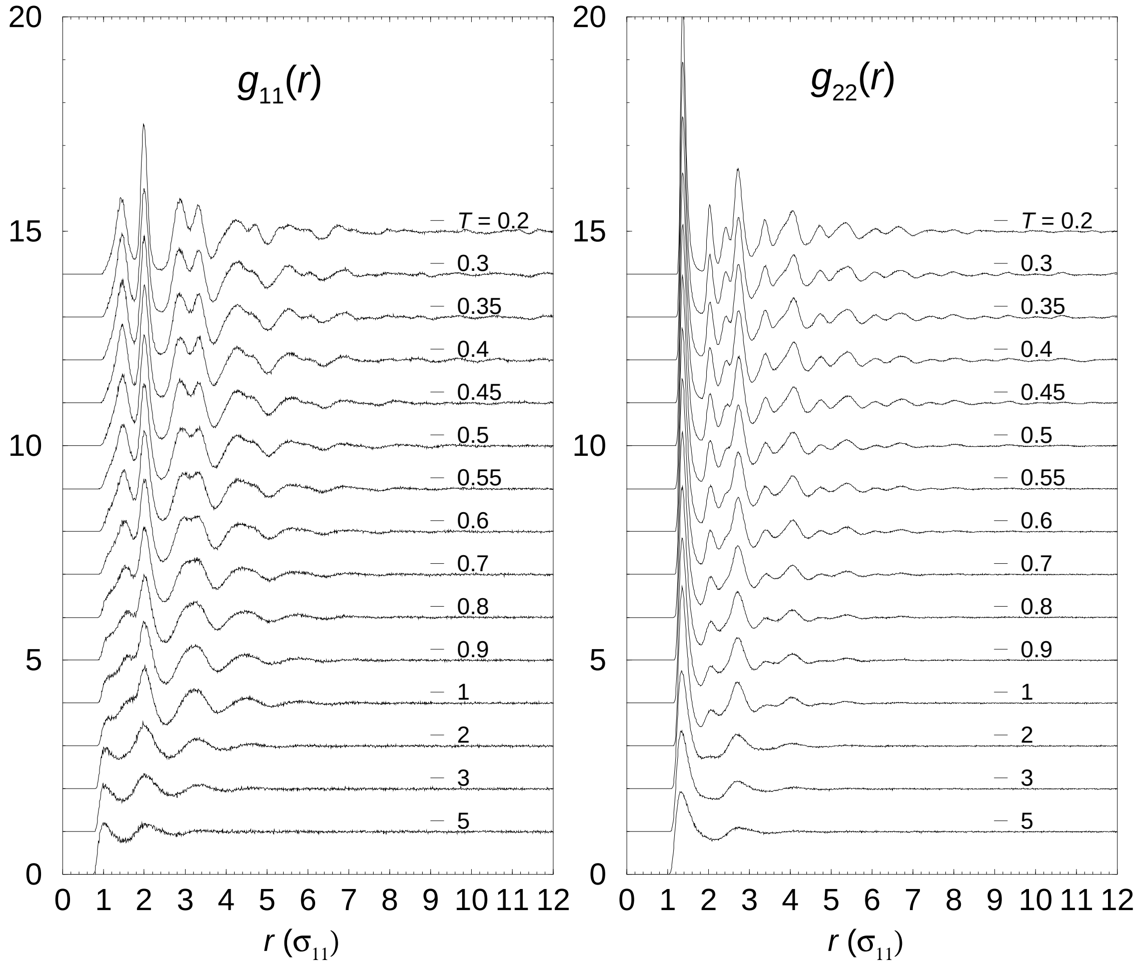

Figure 5.23: The partial pair distribution functions $g_{11}(r)$ and $g_{22}(r)$ as a function of distance from $T = 5$ down to $T = 0.2$. For $T \leq 3$, each curve has been shifted upwards by one unit from the higher temperature curve directly preceding it.

changes in local structure about small particles. Recall that as the temperature decreases there is a large shift in the position of the first peak to a value no longer corresponding to a nearest neighbour particle interaction. The following cutoffs were obtained: $(cut_{11}, cut_{12}, cut_{22}) = (1.44, 1.71, 2.06)$ for $T \geq 2$, and $(1.37, 1.61, 1.83)$ for $T \leq 1$.

The partial structure factors were calculated from the PPDFs as explained in Section 5.3.2. For reference, they are plotted along with the total structure factor in Figures C.1 and C.2.

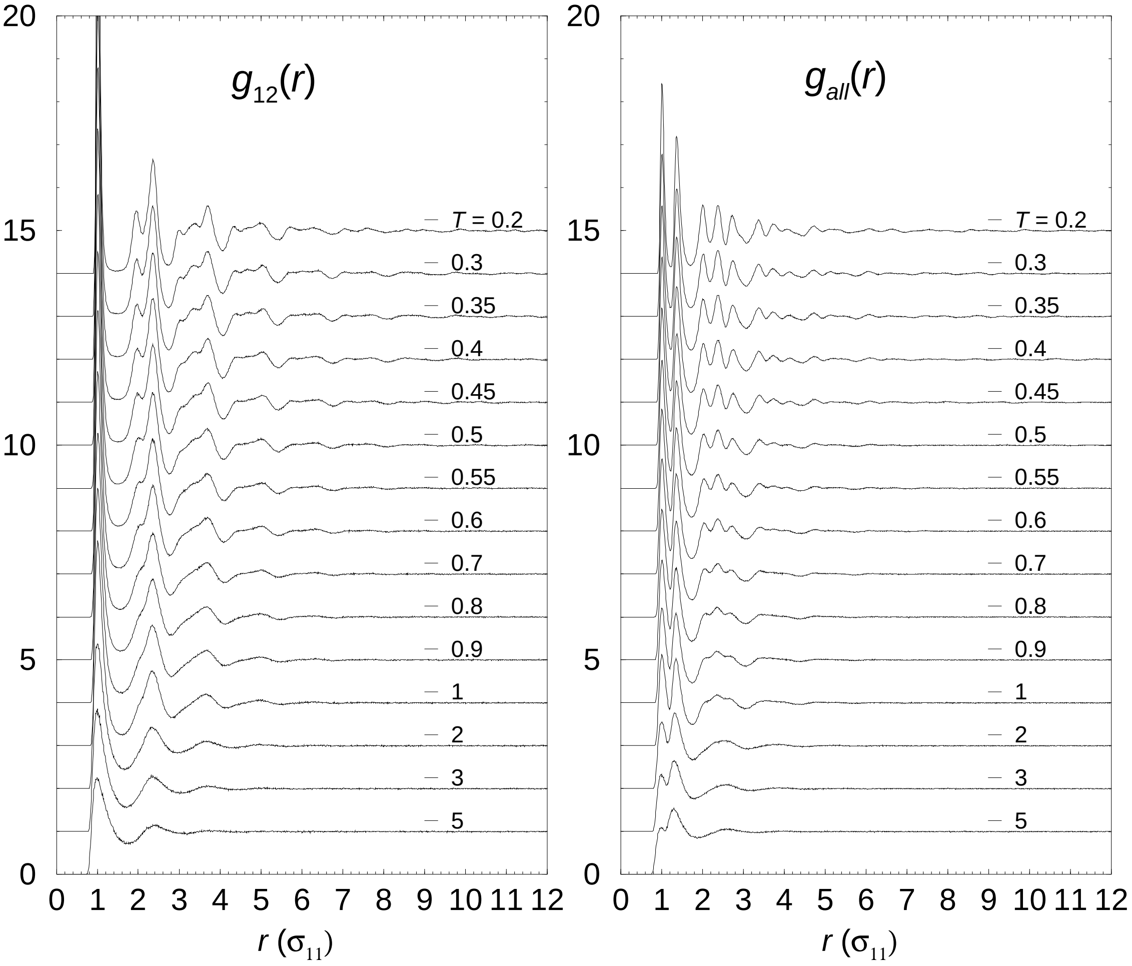

Figure 5.24: The partial pair distribution function $g_{12}(r)$ and the total pair distribution function $g_{all}(r)$ as a function of distance from $T = 5$ down to $T = 0.2$. For $T \leq 3$, each curve has been shifted upwards by one unit from the higher temperature curve directly preceding it.

Local Structure

Several quantities (defined in Section 5.3.2) were used to characterise the local structure of the non-equimolar mixture. The 'bond' fractions n_{ab} are shown in Figure 5.25. The majority of nearest neighbour interactions occur between large particles at all temperatures, closely followed by unlike particle interactions. Upon cooling below $T = 0.6$, there is a small step in n_{12} to lower values and a similar increase in n_{22}, consistent with a small increase in the clustering of large particles. n_{11} remains very low for all $T \leq 1$, indicating that small particles are separated from each other at these temperatures. This is consistent with the earlier observation that the peak in

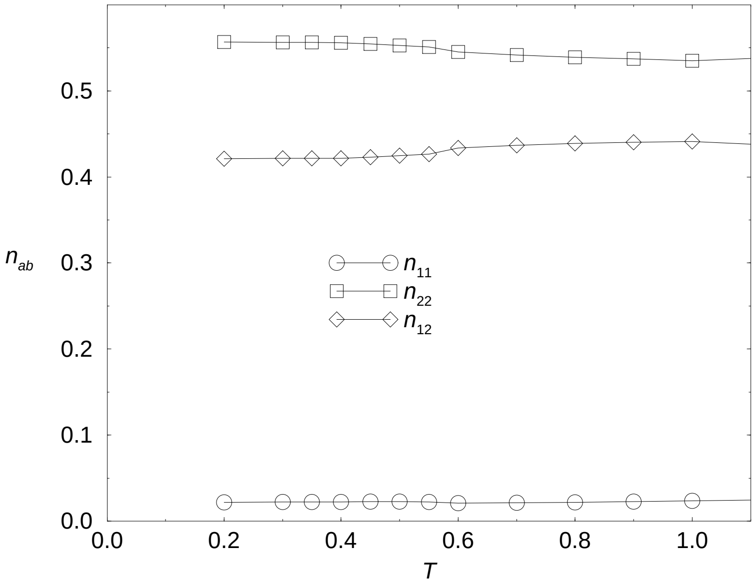

Figure 5.25: Nearest neighbour 'bond' fractions as a function of temperature for $T \leq 1$. n_{ab} is the fraction of all nearest neighbours particle pairs that occur between particles of type a and b.

$g_{11}(r)$ around $r = \sigma_{11}$ disappears when the mixture is cooled below $T = 2$ (see Figure 5.23).

In Figure 5.26 the distribution of local environments is plotted as a function of temperature. This analysis reveals that there is more variation in local structure during cooling than was picked up by the 'bond' fractions. There is a large gradual increase in the fraction of L25 environments between $T = 1$ and $T = 0.4$ that is accompanied by smaller smooth decreases in the fraction of L34, L24 and L15 environments. There is also a small increase in the fraction of L06 environments. Large particles at the centre of vertices of types (c) and (d) shown in Figure 5.1 will have L25 local order. Thus the increase in L25 order could be due to an increase in the formation of these types of vertices. The presence of some L16 order in the system could be due to slightly distorted L25 environments. The observation that L16 order decreases with temperature is consistent with these being vibrational distortions. The small increase in L06 environments could indicate an increase in the clustering of large particles or an increase in the number of isolated vertices of type (e) in Figure 5.1. Although not calculated, the fraction of L44 environments, corresponding to

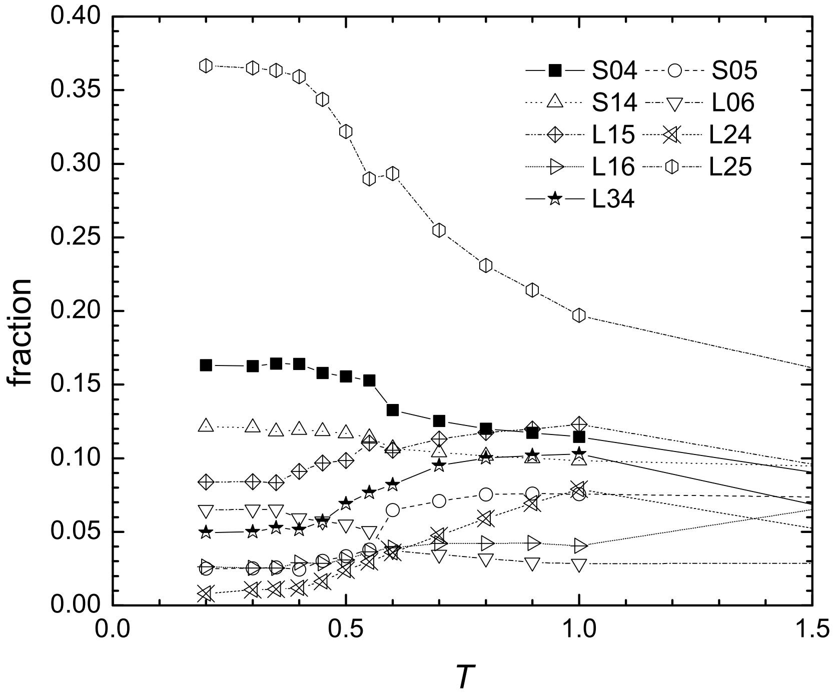

Figure 5.26: The distribution of local packing environments as a function of temperature. We have identified a particular neighbourhood with the following notation. A small particle with m small neighbours and n large neighbours is designated as Smn and the analogous large particle is indicated as Lmn.

vertex (b) in Figure 5.1, cannot account for more than 8% of the total. Therefore the majority of large particles vertices are of type (c) and (d), in contrast to the non-equimolar mixture where the structural data is consistent with the majority of large particle vertices being of type (b).

For small particles, the main changes during cooling are a sudden increase in S04 environments at $T = 0.55$ accompanied by a similarly sized decrease in S05 order. S04 order can be identified with the square tile shown in Figure 5.1(a), while the S05 environment is a non-ideal local packing. The substantial fraction of S14 order must be due to a vibrational distortion of two S04 units packed together, as the peak in $g_{11}(r)$ at $r = \sigma_{11}$ disappears on cooling and we observe no pentagonal S14 environments in the low-temperature configurations [see, for example, Figure 5.22(d)]. Reducing the cutoff distance used to define nearest neighbour interactions between small particles would help to better distinguish between S04 and S14 environments. Below $T = 0.4$ there is little change in any of the local environments, consistent with the structure being largely frozen below this temperature.

Orientational Order Parameters

In order to quantify the orientational order throughout the system we have introduced the n-fold orientational order parameters (see Section 5.3.2 for their definitions). The temperature variation for the 4-, 6- and 12-fold local order parameters is plotted in Figure 5.27. The major change upon cooling is an increase in the 4-fold order about small particles $\Psi_{4,1}$ below $T = 2$ from 0.4 to 0.7, and a decrease in $\Psi_{6,1}$ over the same temperature range from 0.45 to 0.25. There is also a small increase in 6-fold order about large particles from $T = 2$–1. There are no particles with 12 nearest neighbours so the increase in 12-fold bulk order must be due to the changes in 4- and 6-fold orientational order.

Next we test for long-range orientational correlation of the local domains. In Figure 5.28 we plot the partial 4-fold orientational correlation function about small particles $G_{4,1}(r)$ and the partial 6-fold orientational correlation function about large particles $G_{6,2}$. There was no structure in $G_{4,2}(r)$ and only a small first peak in $G_{6,1}$, so we do not plot these. Upon cooling, there is a small increase in orientational correlation between 4-fold environments about small particles. The peak structure is complex and different to that observed for the S1 crystal (see Figure 5.14). We therefore conclude that the medium-range order that develops about small particles is not of the S1 crystal type. There is also a similar but smaller increase in structure in $G_{6,2}$. This peak structure is different from that observed when there are substantial crystalline domains of large particles (see, for example, Figure 7.9), so we conclude that the medium-range order that develops about large particles is not due to crystalline domains of hexagonally-packed large particles, i.e. clustering of type (e) vertices. A random square-triangle tiling would be expected to have long-range 12-fold orientational order, so we plot the 12-fold orientational correlation function in Figure 5.29. There is some growth in the extent of 12-fold orientational correlations between both small and large particle environments, however there is clearly no long-range orientational order in the system. Therefore, we conclude that the local packing defects in this system are sufficient to disrupt this long-range orientational order.

We conclude that the non-equimolar mixture shows no sign of crystallisation or phase separation upon cooling from the liquid state. The low-temperature local structure is dominated by square S04 small particle environments, and L25 large particle

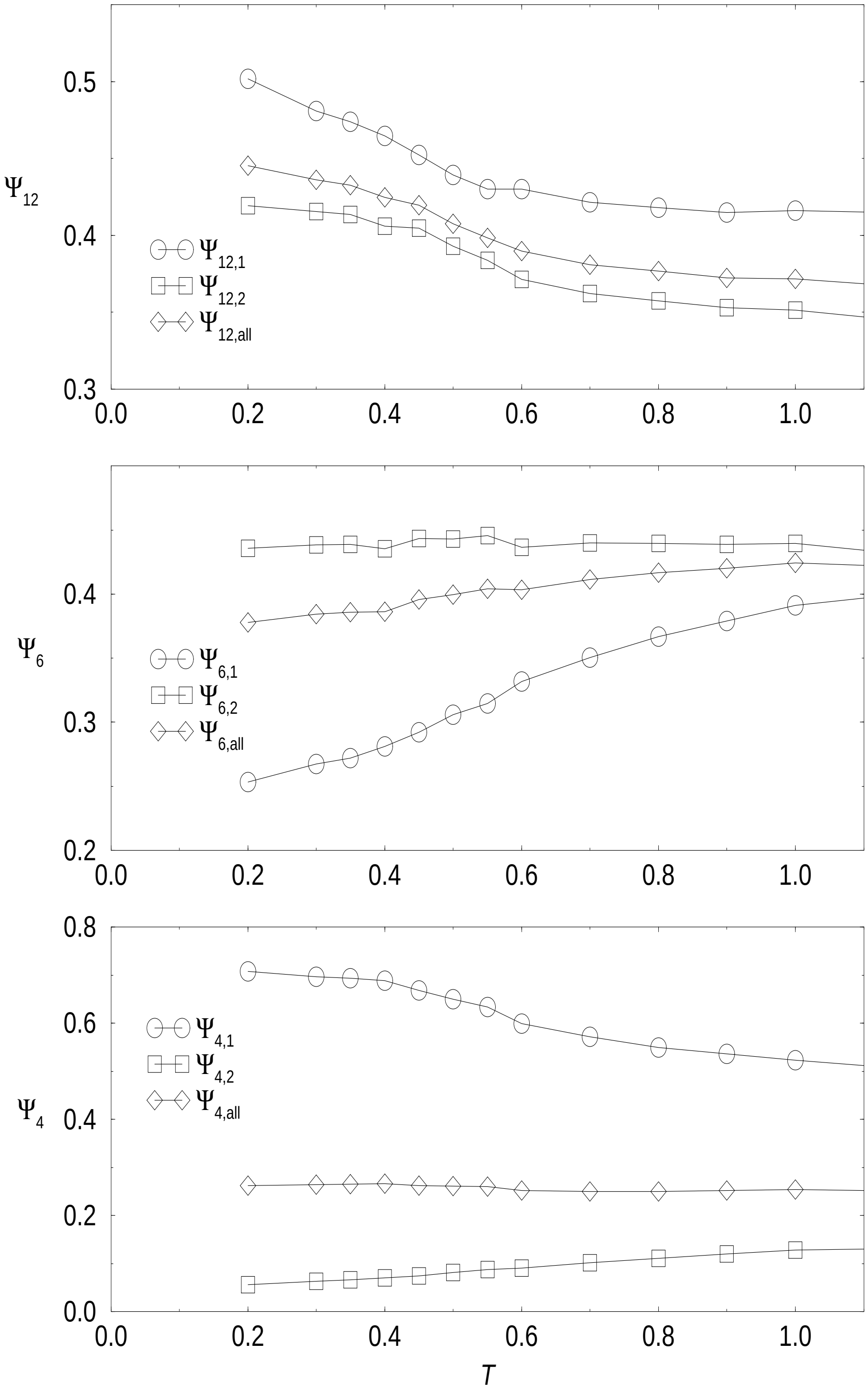

Figure 5.27: The temperature dependence of the bulk averaged n-fold order parameters Ψ_n, where $n = 4, 6, 12$, and their small ($\Psi_{n,1}$) and large ($\Psi_{n,2}$) particle contributions. Error bars represent one standard deviation.

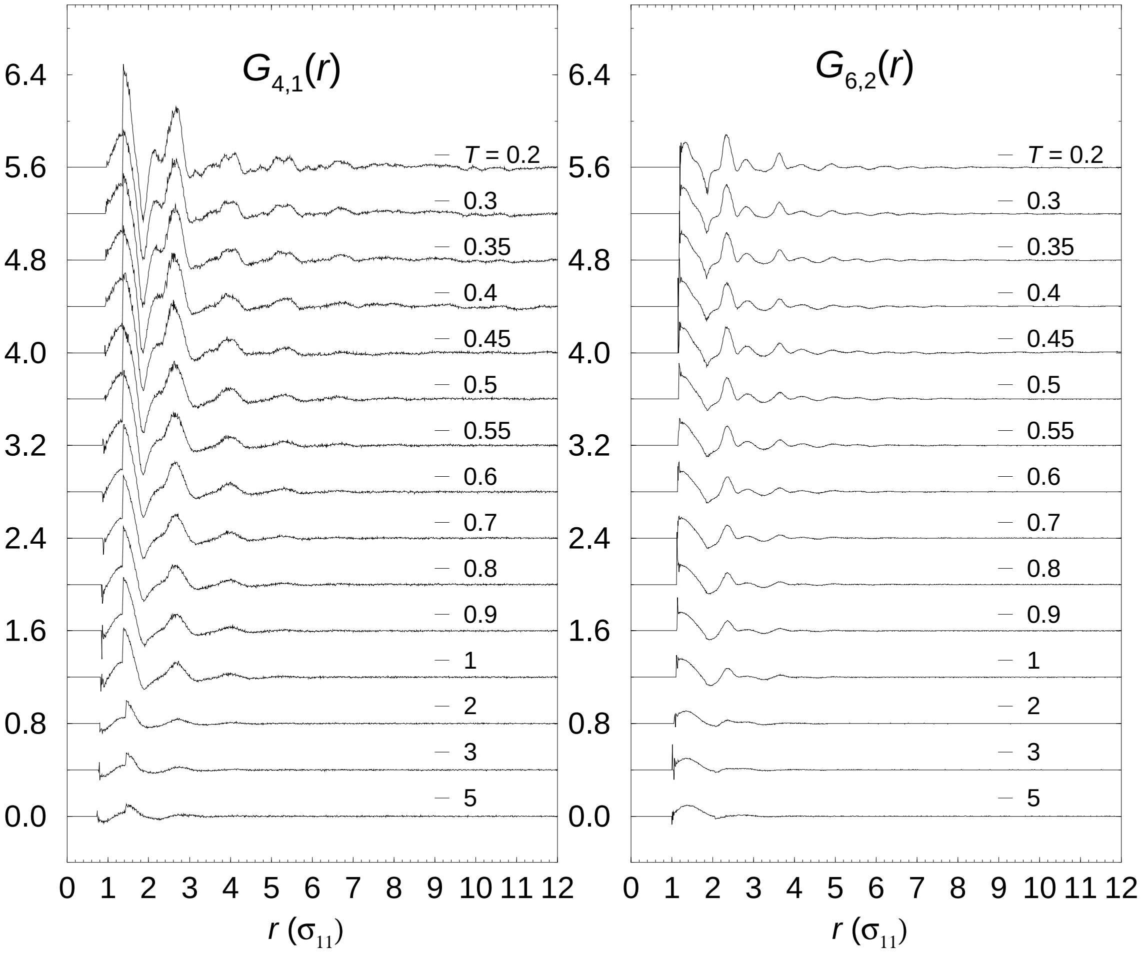

Figure 5.28: The partial 4-fold orientational correlation function $G_{4,1}(r)$ for the small particles (left), and the partial 6-fold orientational correlation function $G_{6,2}(r)$ for the large particles (right), as defined in the text. For clarify, functions have been offset vertically.

environments. Our results suggest that approximately 50% of large particles find themselves in vertices of type (c) and (d), with another 10-20% each in vertices of type (b) and (e), where the vertex types refer to those in Figure 5.1. Although only 3% of particles find themselves in pentagonal S05 environments, these appear sufficient to disrupt the formation of long-range 12-fold orientational order. In the next section, we present an analysis of the changes in particle transport and structural relaxation that occur during cooling.

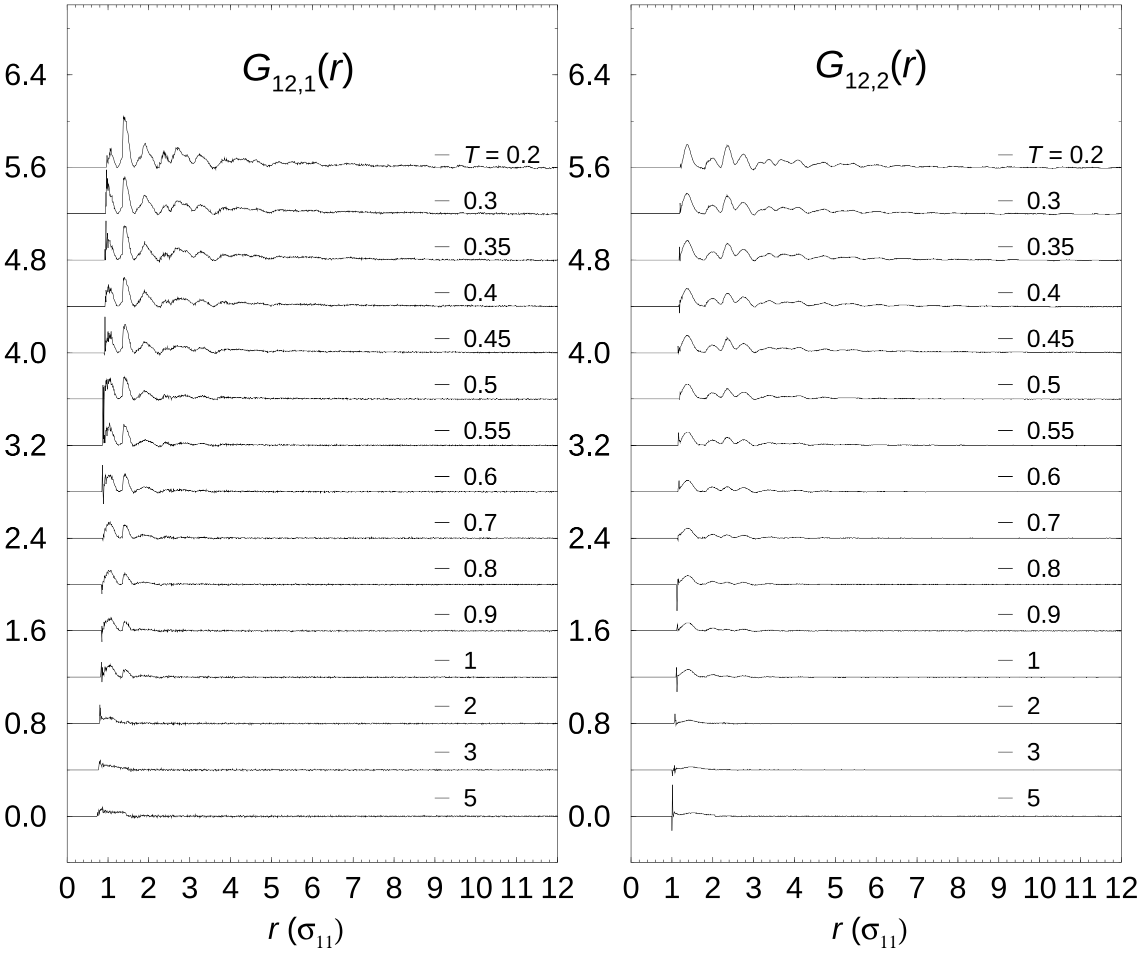

Figure 5.29: The partial 12-fold orientational correlation functions $G_{12,1}(r)$ and $G_{12,2}(r)$ for the small and large particles respectively, as defined in the text. For clarify, functions have been offset vertically.

5.4.3 Onset of Glassy Dynamics

Intermediate Scattering Functions

The timescales of structural relaxation can be probed quite readily by computing density correlation functions such as the incoherent and coherent intermediate scattering functions. For the non-equimolar mixture, we have calculated the incoherent (or self) intermediate scattering functions $F_{s,1}(k,t)$ and $F_{s,2}(k,t)$ for the small and large particles, respectively (see Section 5.3.3 for their definitions). $F_{s,1}(k,t)$ and $F_{s,2}(k,t)$ have been measured at the positions of the first maxima in the static structure factors $S_{11}(k)$ and $S_{22}(k)$ (plotted in Figure C.1). The positions of these maxima are weakly

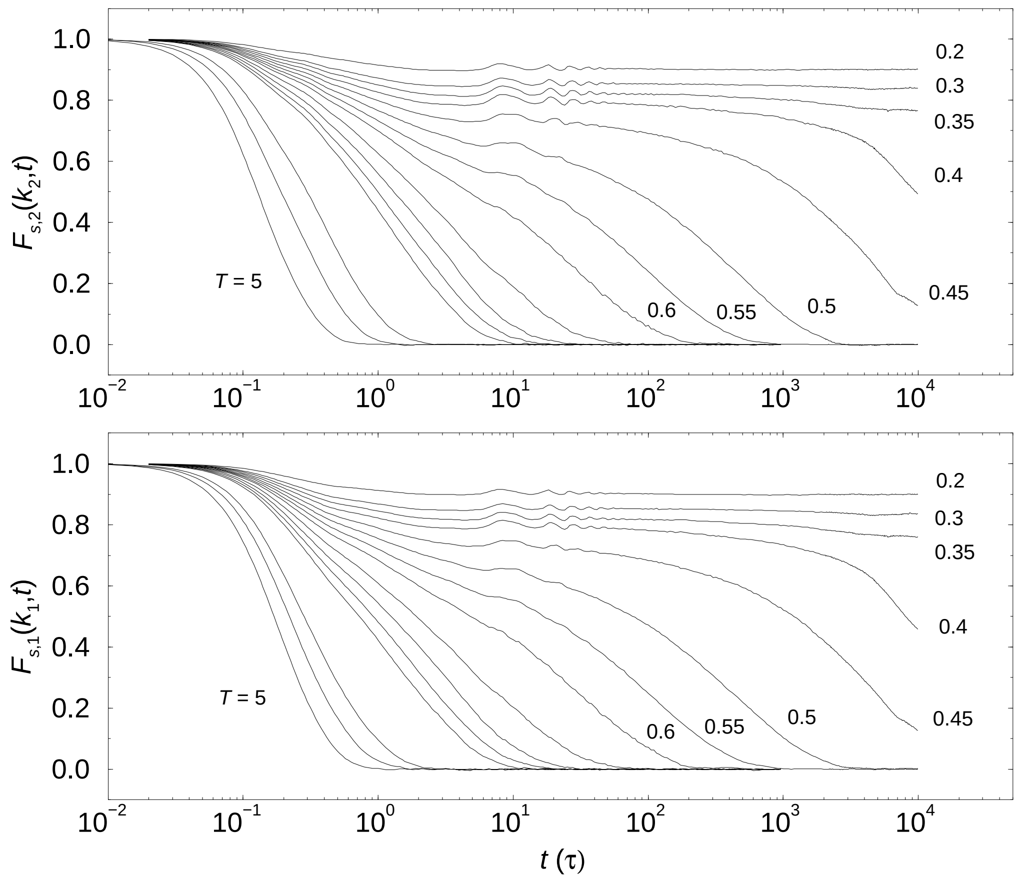

Figure 5.30: The incoherent scattering functions $F_{s,1}(k_1, t)$ and $F_{s,2}(k_2, t)$ for the small and large particles, respectively. The wave vectors k_1 and k_2 are the first peak positions in the respective partial structure factors (listed in Table C.7). From left to right the temperatures of the curves are $T = 5$, 3, 2, 1, 0.9, 0.8, 0.7, 0.6, 0.55, 0.5, 0.45, 0.4, 0.35, 0.3 and 0.2. Note the appearance of a two-step relaxation process at low temperature.

dependent on temperature and are listed in Table C.7.

Log-linear plots of the self intermediate scattering functions are shown in Figure 5.30. The relaxation curves broaden with decreasing temperature until below $T = 0.5$ they are no longer able to decay to zero within the finite time scale of the simulations. The relaxation functions already span over five decades in time at these temperatures. At $T = 0.6$ a step appears in the relaxation curves at intermediate times. This step broadens into a plateau with an amplitude that increases with decreasing temperature. The height of the plateau also increases with decreasing temperature. Such two-step relaxation functions have been observed in a wide range of glass-forming systems as discussed in Section 1.2. Damped oscillations are also observed in the

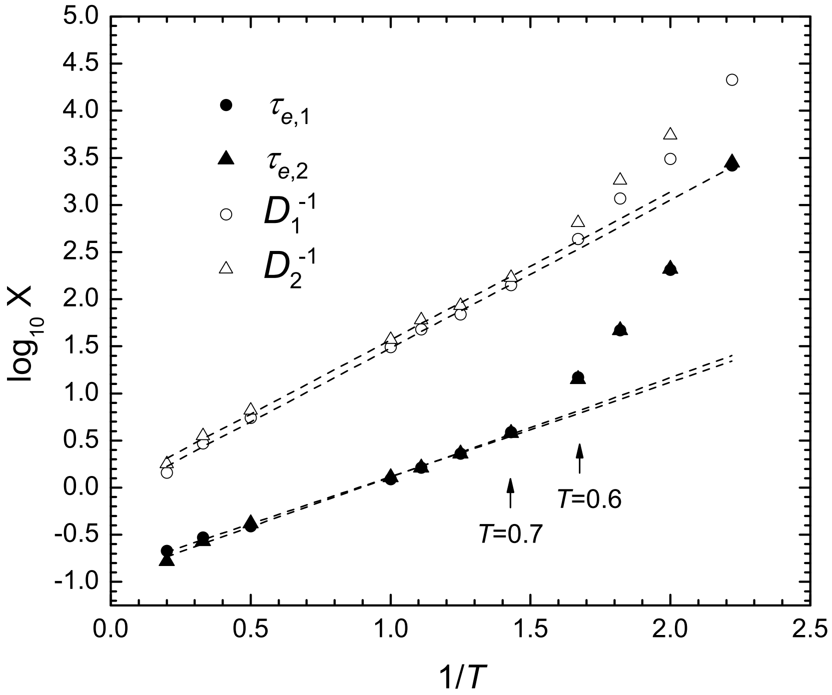

Figure 5.31: Arrhenius plot of the structural relaxation times $\tau_{e,1}$ and $\tau_{e,2}$ and the inverse diffusion constants D_1^{-1} and D_2^{-1}. The dashed lines are linear regressions through the data for $T \geq 0.7$. Note the divergence from Arrhenius behaviour at low temperature.

plateau region similar to what has been observed for other glass-formers including the model studied in Part I. Perera and Harrowell [44] concluded that while system size can influence the frequency of these modes, their presence is a consequence of the transient rigidity of the liquid.

Structural relaxation times $\tau_{e,1}$ and $\tau_{e,2}$ are defined as the time taken for the incoherent scattering functions $F_{s,1}(k,t)$ and $F_{s,2}(k,t)$, respectively, to decay to $1/e$ of their initial values. The temperature dependences of these relaxation times, plotted in Figure 5.31, appear to be Arrhenius at high temperature, but diverge strongly from Arrhenius dependence as the temperature drops below $T = 0.7$, behaviour typical of a fragile liquid. Note that the structural relaxation times for the small and large particles are almost identical, which is somewhat unusual.

Mean-Squared Particle Displacements

The mean-squared displacement (MSD) over all particles $R^2(t)$, and averaged over the two particle species, ${R_2}^2(t)$ and ${R_1}^2(t)$ are plotted in Figure 5.32. All three plots

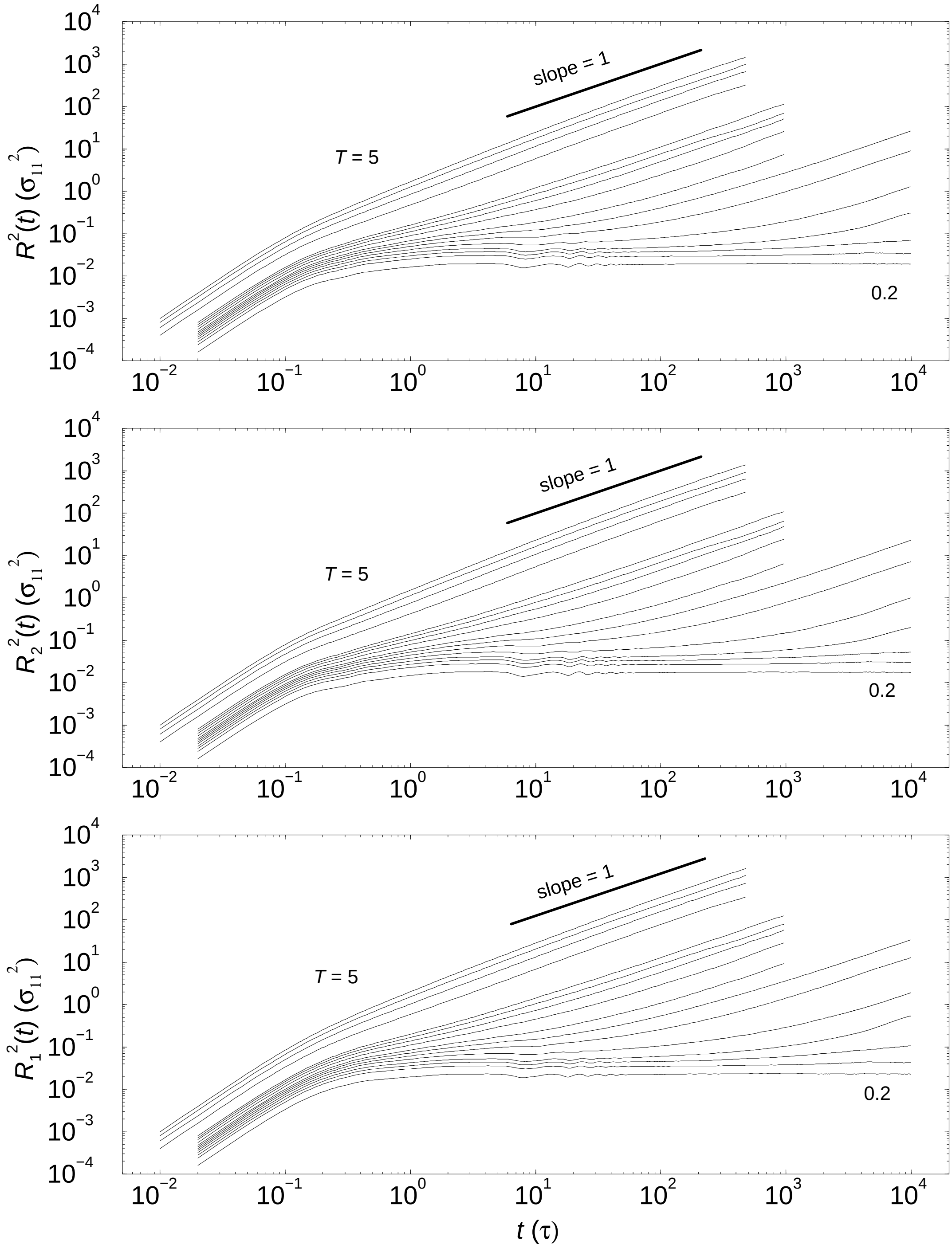

Figure 5.32: The time dependence of the MSD averaged over all particles $R^2(t)$, and averaged over the two particle species, ${R_2}^2(t)$ and ${R_1}^2(t)$. The temperature of the curves from left to right is the same as in Figure 5.30.

are qualitatively very similar. At very short times, the curves have a power law dependence on time with an exponent of two, which corresponds to ballistic motion, while at much longer times, for sufficiently high temperatures, the curves have a smaller slope of one indicating diffusive motion. Upon cooling, there is an increasing separation in timescales between ballistic and diffusive motion, accompanied by the appearance of a plateau region at intermediate times. This intermediate region is often associated with transient caging of particles by their neighbours. As for the relaxation curves, the MSDs also show behaviour that is typical of glass-forming systems.

Diffusion constants were measured in the region where the MSD has reached its long-time constant value (${R_a}^2(t) > \sigma_{11}^2$). The inverse diffusion constants are plotted against temperature in Figure 5.31. They show a weaker deviation from Arrhenius temperature dependence than the structural relaxation times, with the onset of this deviation occurring around the same temperature, i.e. $T = 0.6$. The ratio $D_1/D_2 \approx 1$ for $T \geq 0.7$ after which it increases slightly with further cooling, i.e. the diffusion constants, like the relaxation times, are almost identical for the small and large particles. For reference, the structural relaxation times and diffusion constants are also listed in Table C.8. In the next section we investigate the appearance of dynamic heterogeneity in the liquid.

Non-Gaussian Parameter

As explained in Section 5.3.3, the non-Gaussian parameters $A_a(t)$ can be used as a measure of the degree of dynamic heterogeneity in a sample. They are plotted for the present system in Figure 5.33. A rapid rise in non-Gaussian behaviour is observed at low temperature for both the large and small particle species. As expained earlier, large values at intermediate times can be attributed to a broad distribution of local mobilities. Therefore, this is evidence that the dynamics in the supercooled liquid is becoming heterogeneous. The maximum value of $A_1(t)$ increases rapidly below $T = 0.7$, while the maxima in $A_2(t)$ show a similar but smaller increase over the same temperature range. The trend is for the maxima to move to longer times as they increase in height; below $T = 0.4$ the finite observation time of the simulations is too short to observe them. $A_2(t)$ and $A_1(t)$ are no longer able to decay to zero below $T = 0.45$. From this, we conclude that the system falls out of equilibrium near this temperature.

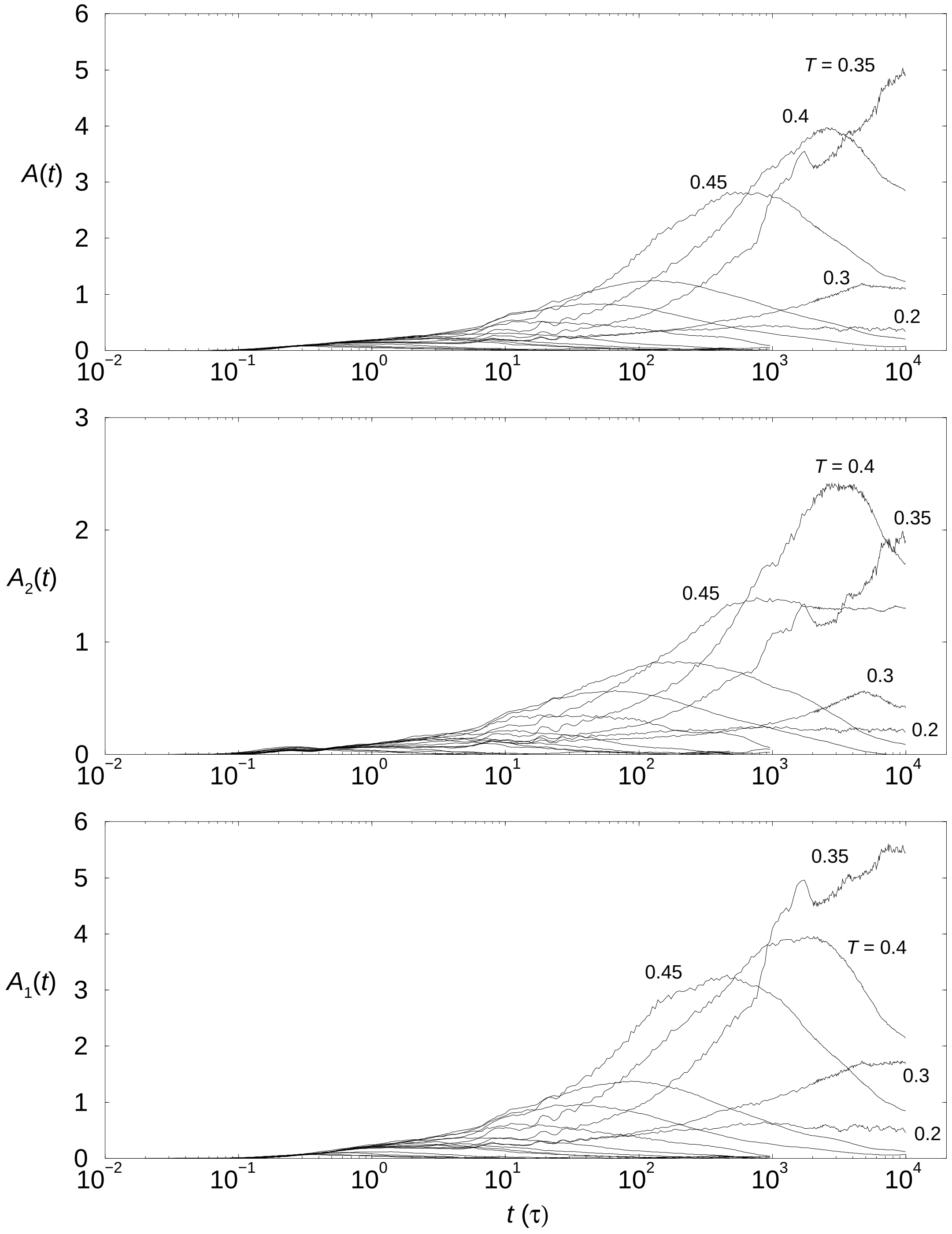

Figure 5.33: The non-Gaussian parameter averaged over all particles, $A(t)$, and averaged over small and large particles, $A_1(t)$ and $A_2(t)$, respectively. The temperatures of the curves are as listed in the caption for Figure 5.32. Observe the rapid increase in peak heights with decreasing temperature.

The changes in dynamic properties upon cooling of the non-equimolar mixture - the rapid increase in structural relaxation times, the appearance of a plateau in the incoherent scattering functions and MSDs, the non-Arrhenius temperature dependence of the structural relaxation times and inverse diffusion constants at low temperature, and the onset of non-Gaussian dynamics - are all consistent with what has been observed for other model glass-formers. Our structural analysis found no development of long-range translational or orientational order, or tendency to crystallise or phase separate. Thus the non-equimolar mixture appears to be a good glass-former.

5.4.4 Melting of a Periodic Structure

The continuous transition from fluid to amorphous solid for the non-equimolar system is intriguing. Why does it not freeze into a solid phase with perfect local packing, into either a random or ordered tiling with only square and triangular local order? How does the high configurational entropy of the solid state affect the nature of this phase transition? Is the presence of a few defects sufficient to disrupt a weak first-order transition?

As a first step towards addressing these questions, we constructed and heated a periodic structure with similar composition. The constructed particle packing is shown in Figure 5.34(a), and has vertex frequencies in the ratio $b : c : d : e = 0 : 6 : 6 : 1$, where the vertices are as drawn in Figure 5.1. The book 'Tilings and Patterns' [207] contains this and many other examples of periodic square-triangle tilings. In comparison, the ratio of vertex frequencies for a random tiling at this composition is $b : c : d : e = 0 : 1.26 : 11.6 : 1$ [198].

A total of $N = 1444$ particles were enclosed in a rectangular box with periodic boundary conditions in order to accommodate the rectangular unit cell of the crystal. We used a simulation cell with a fixed width:height ratio of $x/y = 0.866$, and the ratio of small to large particles was $N_1 : N_2 = 456 : 988$ giving a composition of $x_1 = 0.3158$. The model parameters and MD algorithm were as described previously in Section 5.2. The NPA Hamiltonian for independent scaling of x and y axes is given in Appendix A.

Only a limited set of equilibration runs were made to probe the nature of the solid to fluid phase transition. The system was equilibrated for 1000τ at reduced temperatures of $T = 0.2$, 0.25, 0.3, 0.35, 0.4, 0.45, 0.5, 0.55, 0.6, 0.65, 0.7, 0.75, 0.8, 0.85 and 0.9. The starting configuration of the run at $T = 0.2$ was the constructed

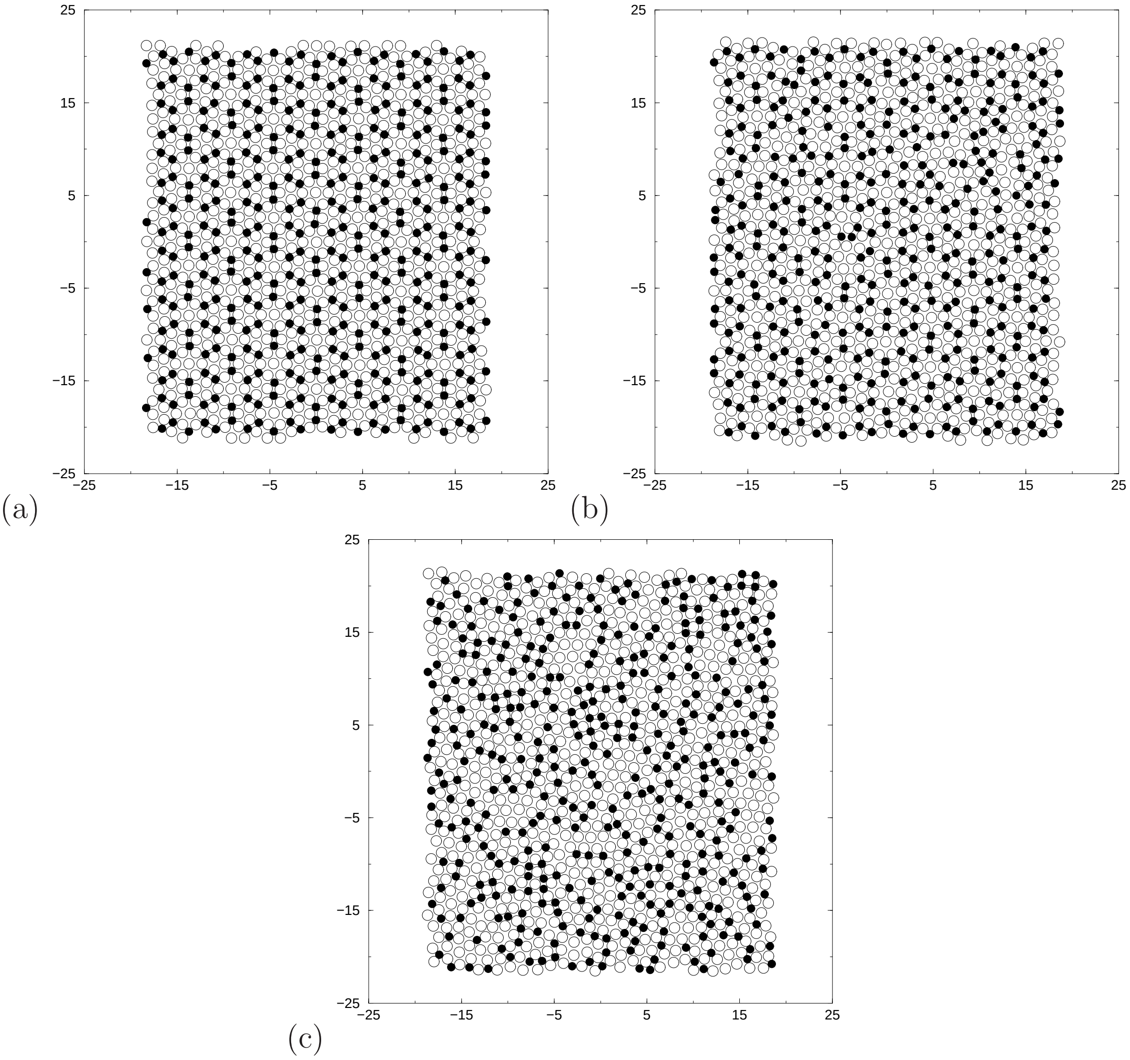

Figure 5.34: (a) The constructed periodic packing equilibrated at $T = 0.2$, and configurations (b) during and (c) after melting at $T = 0.6$. The small and large particles are represented by filled and open circles respectively.

periodic packing shown in Figure 5.34(a) whereas, for each of the higher temperatures, the initial configuration for the equilibration run came from the final configuration of the preceding lower temperature run. During these runs, the crystalline solid melted at $T = 0.7$. To test for stability to melting, additional $10,000\tau$ runs were made at $T = 0.65$, 0.6 and 0.55 starting from the final configuration of the initial 1000τ equilibration runs. The solid melted at both $T = 0.65$ and 0.6 but was stable at $T = 0.55$. We therefore conclude that the melting temperature lies somewhere between $T = 0.55$ and $T = 0.6$. There are some structural defects present at $T = 0.55$ in the form of particle packings that do not correspond to ideal tilings.

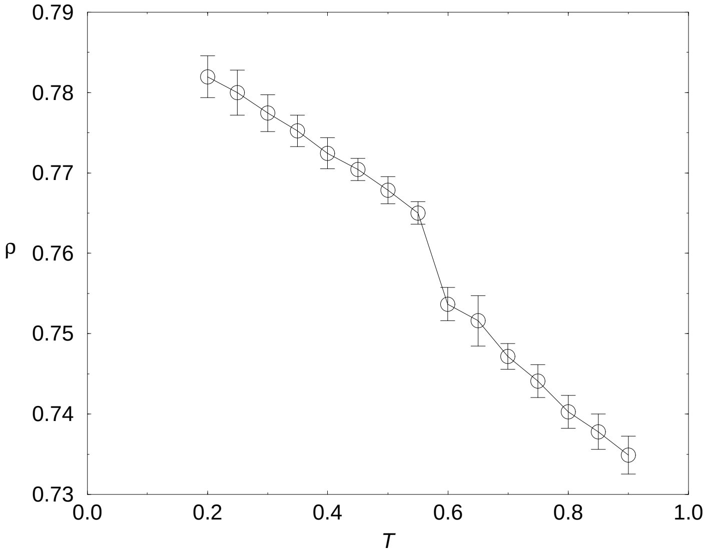

Figure 5.35: Isobaric ($P = 13.5$) phase diagram. Note the step in density upon cooling.

Selected configurations before, during, and after melting are shown in Figure 5.34. The latter part of the equilibration runs - when there was no longer any apparent change in thermodynamic properties - was used to obtain values for the equilibrium densities (shown in Figure 5.35). There is a clear step in density between $T = 0.6$ and 0.55. The densities of the liquid state points are very similar to those obtained previously upon cooling.

5.5 Discussion and Conclusions

The equimolar mixture freezes into a largely defect-free S1 crystal structure at $T = 1.02$. There appears to be substantial crystalline order in the liquid prior to freezing, in the form of S04 environments and a large unaccounted for fraction of local environments which are most likely L44 environments. There is also evidence for medium-range packing of S04 cells. The structural changes during heating from a perfect S1 crystal are very similar, and confirm a region of metastability extending from $T = 1.02$–1.08. Prior to freezing, the structural relaxation times follow an Arrhenius temperature dependence and the equimolar mixture shows typical liquid dynamics.

In the solid phase, there is substantial defect motion in the high-temperature crystal, during both the heating and cooling traverses. During heating, defects appear at $T = 0.9$, initially due to small-particle motion, but at later times also involving large-particle motion. This reduced large-particle mobility contrasts with the frozen crystal in which the small and large particles have almost identical mobilities. The structural and dynamic data for the heating traverse is consistent with a transition from rigid S1 crystal to crystal with defect motion to normal liquid and vice versa for the cooling traverse.

In contrast, the non-equimolar mixture shows no sign of crystallisation or phase separation upon cooling from the liquid state. The low temperature local structure is dominated by square S04 small particle environments, and L25 large particle environments. Our results suggest that approximately 50% of large particles find themselves in vertices of type (c) and (d), with another 10-20% each in vertices of type (b) and (e), where the vertex types refer to those in Figure 5.1. Although only 3% of particles find themselves in pentagonal S05 environments, these appear sufficient to disrupt the formation of long-range 12-fold orientational order. The changes in dynamic properties upon cooling below $T = 0.7$ - the rapid increase in structural relaxation times; the appearance of a plateau in the incoherent scattering functions and MSDs; the non-Arrhenius temperature dependence of the structural relaxation times and inverse diffusion constants at low temperature; and the onset of non-Gaussian dynamics - show behaviour typical of supercooled glass-forming liquids. Since our structural analysis found no development of long-range translational or orientational order, or tendency to crystallise or phase separate, we conclude that the non-equimolar mixture is a good glass-former.

This behaviour is rather surprising, as the model parameters are almost ideal for the formation of local square and triangular structures with the ability to tile space. It is also surprising given that a periodic structure with similar composition undergoes a first-order melting transition when heated from the solid state. We have not looked at heating a solid structure corresponding to an ideal random tiling - due to the time constraints of this project and the non-trivial problem of constructing such a configuration - but we suspect that it would also undergo a discontinuous transition to the liquid state despite its lack of long-range translational order. So is there another reason for the glass-forming ability of the non-equimolar mixture? The dynamics indicate that the liquid is supercooled below $T = 0.7$, and the equilibration runtimes remain sufficiently long for both the intermediate scattering functions and non-Gaussian parameters to decay to zero above $T = 0.45$ (which is when the system falls out of local equilibrium). And yet a substantial fraction of non-ideal packings remain at $T = 0.5$, which ultimately are sufficient to disrupt the formation of long-range orientational order. Perhaps these defects are stabilised because the particle numbers that we have chosen cannot form an ideal random tiling that fits perfectly into a square simulation cell. In this case, the absence of larger domains with ideal 12-fold orientational order indicates that the random tiling structure is not substantially favoured relative to the amorphous structure.

Many models of glass-formers are based on particle interactions that encourage local ordering that cannot pack to fill space, for example the Dzugutov model [208]. In comparison to these, the non-equimolar mixture is noteworthy because it extends glass-formation to a model in which the interparticle potentials favour local ordering that can pack to fill space. In this latter case, it appears to be the large configurational entropy of the solid state that stabilises the amorphous state. Recall that we have chosen the composition that can decorate a square-triangle tiling ratio with maximal configurational entropy. In addition, this work suggests that metal alloys that form quasicrystals may also be good glass-formers, and that their structures may be related. Certainly, there is evidence for nanoquasicrystalline materials [183], and amorphous to quasicrystal transitions are often observed in metallic glasses upon devitrification [185].

The low temperature dynamics of the non-equimolar system are also interesting. The structural relaxation times of the small and large particles remain equal at all temperatures and the diffusion constants are equal until $T = 0.7$, below which they diverge slightly. This coupling of mobility and relaxation of both species in the present system may be explained by the lack of small particle nearest neighbours, since this implies that for a small particle to move or for its local structure to change, a large particle must also move. Structural relaxation of both particle species is also coupled in the equimolar mixture. The low-temperature dynamics of the non-equimolar mixture are also interesting. While we have not presented the results here, videos of the low-temperature particle motion (below $T = 0.5$) show that the main mechanism for motion is via a local distortion that allows a small particle to move from a square S04 environment into a neighbouring triangle of large particles, thus converting the initial square S04 environment into a triangular tile and the initial triangular packing into a square S04 tile. This mechanism appears to be enhanced by nearby defects, e.g. S05 environments. This would also explain the enhanced mobility of small particles relative to large particles at low temperature. Kawamura [195] and Henley et al. [155, 159] both describe the minimum rearrangement that must take place to convert one ideal random square-triangle tiling into another. This involves the motion of at least 6 small and 6 large particles and is thus expected to have a high activation energy. Therefore the significant motion, and mechanism, that we observe at low temperature strongly suggests that the activation energy for structural rearrangements is significantly lowered in the presence of non-ideal packings. These may therefore be entropically stabilised.

Chapter 6

The Asymmetric H2 Crystal and a Chemically Ordered Glass ($\sigma_{12} = 1.1$)

We study the structure and dynamics of both equimolar and non-equimolar mixtures with $\sigma_{12} = 1.1$ *in the fluid-solid phase region. The equimolar liquid is relatively stable to supercooling but eventually freezes into a substitutionally ordered crystal with an elongated hexagonal unit cell. Both heating and cooling traverses are characterised and the process of crystallisation is investigated. In contrast, the non-equimolar mixture shows no sign of crystallisation and forms an amorphous solid state when cooled. We argue that this system is a good glass-former and structurally distinct from the model with additive interparticle potential that was investigated in Part I.*

6.1 Introduction

Although highly metastable to supercooling, the equimolar mixture of the present model eventually forms a crystal phase that can be described as a tiling of the plane by unit cells consisting of two small particles surrounded by six large particles in an elongated hexagonal arrangement. This unit cell, illustrated in Figure 6.3(a), has previously been described by Likos and Henley [155], who investigated the phase diagram of binary hard-disc mixtures but did not perform any simulations. We will follow their convention and refer to the local hexagonal unit as the H2 unit cell and the crystal as the H2 crystal. A 2D binary Lennard-Jones (LJ) mixture studied in the context of quasicrystal stability also has the H2 crystal as one of its ground states [161], however this LJ model has substantially different interactions lengths and forms structures not observed in the present system. We characterise the structure and dynamics of the equimolar mixture in Section 6.3.

The non-equimolar mixture (with composition $x_1 = 0.3167$) is noteworthy for its ability to form an amorphous solid that is structurally more homogeneous than the equimolar model studied in Part I, despite over two-thirds of its components being of the same species. It also has less diversity of local coordination environments and a medium-range order that can be described in terms of favoured packings of local environments. Surprisingly, it shows little sign of the H2 crystal order present in the equimolar liquid, with dynamic behaviour that is typical of other glass-forming liquids. We characterise the structure and dynamics of this system in Section 6.4.

While the main object of the present study is to characterise the changes in phase behaviour and dynamics that occur as the interparticle potential σ_{12} is varied, we also spend some time in this chapter studying the process of crystallisation in the equimolar mixture. This work is presented in Section 6.3.4. This is not meant to form a comprehensive study of nucleation and crystallisation, but rather to demonstrate that non-additive soft-disc mixtures may serve as useful model systems for such work. To put this into context, we give a brief introduction to the study of crystallisation in the remainder of this section.

Crystal nucleation is an important phenomenon in many processes, yet scientific understanding of its molecular mechanism remains incomplete. Despite progress, many open questions concerning crystallisation phenomena still remain, including the rate of formation of the crystal phase, structure and composition of the critical nucleus, role of solvents and foreign objects etc. Crystals can take many forms, only one of which is the most stable. However it is usually not known in advance which structure will form upon nucleation. Ostwald's rule of stages [209] states that the crystal phase that nucleates from a supercooled liquid is the one that is closest to the liquid state in its free energy. Hence crystallisation via nucleation may yield the metastable form instead of the most stable structure. This issue is particularly important, for example, in the pharmaceutical industry where the same drug molecule can have different properties due to differences in its crystal structure.

A fundamental understanding of the nucleation, growth kinetics, and morphology of crystals grown from the melt requires a detailed microscopic description of the crystal-melt interface [210–213]. However, such information is difficult to obtain experimentally. For example, it is difficult to detect the presence of small nuclei, and it is difficult to probe the crystal-melt interface, especially at the high melting/freezing temperatures typical of metal alloys. Not surprisingly, computer simulations have played a leading role in the determination of the microscopic structure, dynamics, and thermodynamics of such systems [214]. The majority of simulation studies so far have focused on single component systems, ranging from simple models such as hard spheres [214–217] or LennardJones [218, 219] to more 'realistic' systems, such as water [220–222], silicon [223, 224] or simple metals [225, 226]. In contrast, there have been relatively few studies of multicomponent systems [152, 227–232], despite the reality that most materials of technological interest are mixtures (for example, doped semiconductors, alloys, and intermetallic compounds).

We therefore suggest that the ordered S1 and H2 crystal phases, characterised in this chapter and in Chapter 5, offer valuable models systems in which to further our understanding of crystallisation. These non-additive soft-disc mixtures have the added complexity of two particle species with the simplicity of two dimensions and purely repulsive potentials. They may also be viewed as model systems for the study of ordering in monolayers. We are not aware of any previous studies of ordered crystals, crystallisation or glass-formation in non-additive soft-disc mixtures, nor of any studies of ordered crystals or crystallisation in additive soft-disc mixtures.

The rest of this chapter is structured as follows. In Section 6.2 we describe the model and computational methods used. We characterise the structural and dynamic properties of the equimolar mixture in Section 6.3 and, in Section 6.3.4, study the process of crystallisation for this system. Our study of glass-formation in the non-equimolar mixture is presented in Section 6.4. This is followed by a summary of the main results and a comparison of the structure and phase behaviour of the two mixtures in Section 6.5.

6.2 Model and Computational Details

We consider a 2D system consisting of a binary mixture of particles interacting via purely repulsive potentials of the form

$$u_{ab}(r) = \epsilon \left[\frac{\sigma_{ab}}{r}\right]^{12} \tag{6.1}$$

where $\sigma_{12} = 1.1 \times \sigma_{11}$ and $\sigma_{22} = 1.4 \times \sigma_{11}$. All units quoted will be reduced so that $\sigma_{11} = \epsilon = m = 1.0$ where m is the mass of both types of particle. Specifically, the reduced unit of time $\tau = \sigma_{11}\sqrt{m/\epsilon}$. A total of $N = 1440$ particles were enclosed in a square box with periodic boundary conditions.

The molecular dynamics simulations were carried out at constant number of particles, pressure ($P = 13.5$) and temperature using the Nosé-Poincaré-Andersen (NPA) algorithm developed by Laird et al. [83, 84]. This algorithm is discussed further in Appendix A, where we also list the equations of motion in 2D. The equations of motion were integrated using a generalised leapfrog algorithm [84]. The time step employed was 0.05τ for $T > 1$, and 0.01τ for $T \leq 1$. For argon units of $\eta = 120k_B$, $m = 6.6 \times 10^{-23}g$ and $\sigma_{11} = 3.4\mathring{A}$, these time steps correspond to approximately 10 and 20 femtoseconds respectively.

A non-equimolar mixture consisting of $N_1 = 456$ small particles and $N_2 = 984$ large particles (giving $x_1 = 0.3167$ to 4 sig. fig.) was studied at 16 different reduced temperatures from $T = 5$ to $T = 0.2$. The starting configuration of the run at $T = 5$ was an equilibrated configuration at $T = 5$ for the equimolar system described in this chapter with the appropriate number of small particles changed to large particles. The starting configuration of each lower temperature equilibration run came from the final configuration of the preceding higher temperature run. For $T \geq 0.45$, the equilibration times were longer than the times taken for all the dynamic correlation functions investigated to decay to less than 0.1. Below $T = 0.45$ the system is no longer able to reach equilibrium within the finite time scale of the simulations. Thus, the computer glass transition temperature for these simulations, defined as the temperature at which the system falls out of equilibrium, lies between $T = 0.45$ and $T = 0.4$. At all temperatures the equilibration runs were taken out until steady state was achieved, i.e. until the average thermodynamic properties remained constant in time. Table C.15 (in Appendix C.4) lists the temperatures of each state studied as well as the equilibration and production times. The final configurations of the equilibration runs were used to start the production runs, and the 'masses' of the Anderson piston and Nosé thermostat (see Appendix A) were $Q_v = 0.002$ and $Q_s = 1000$, respectively, for all temperatures.

Both cooling and heating traverses were studied for the equimolar mixture (with $N_1 = 720$ small particles and $N_2 = 720$ large particles). Tables C.9 and C.10 (in Appendix C.3) list the temperatures of each state studied as well as the equilibration and production times for the cooling and heating traverses, respectively. Full production runs were not performed for cooling runs at $T < 0.6$ and heating runs at

$T > 0.7$. In these cases the thermodynamic averages were calculated during the latter part of the equilibration run after there was no further change in average properties. These 'production' runs are indicated by an asterisk (*) after the production runtime. No further properties, structural or dynamic, were calculated at these temperatures. The initial configuration for the cooling traverse was a previously equilibrated configuration at $T = 5$, while the initial configuration for the heating traverse was the constructed periodic structure shown in Figure 6.2(e). The starting configurations for production runs and for lower (or higher) temperature equilibration runs are as described above for the non-equimolar mixture. For the cooling traverse, the 'masses' of the Anderson piston and Nosé thermostat were $Q_v = 0.0002$ and $Q_s = 1000$, respectively, for all temperatures. For the heating traverse, we used $Q_v = 0.0002$ for $T \leq 0.62$ and $Q_v = 0.000001$ for $T \geq 0.64$, and $Q_s = 10$ for $T \leq 0.2$ and $Q_s = 1000$ for $T \geq 0.3$. At low temperatures the kinetic energy fluctuations for the crystal phase became regular unless Q_s was reduced, and at high temperatures the density fluctuations became regular unless Q_v was reduced. We note that changing Q_s and Q_v generally has little effect on the thermodynamic averages, except near a critical point where increasing the size of the fluctuations can cause one phase (usually the solid) to become unstable with respect to the other.

6.3 Metastability and Freezing of the Equimolar Mixture ($x_1 = 0.5$)

6.3.1 Thermodynamic Properties

For reference, thermodynamic averages are listed in Table C.9 for the cooling traverse, and in Table C.10 for the heating traverse. The isobaric phase diagram for the equimolar mixture is shown in Figure 6.1 for $T < 1.1$. Upon cooling, the density increases smoothly at a greater than linear rate. Given sufficient time, the system crystallises at $T = 0.6$ into a labile crystal, a representative configuration of which is shown in Figure 6.2(d). The density of this defected crystal is indicated by the filled diamond in the isobaric phase diagram (Figure 6.1). Heating of the crystalline configuration shown in Figure 6.2(e) reveals a hysteresis region in the isobaric phase diagram extending from $T = 0.6$ to $T = 0.8$. This is very large compared to the hysteresis regions observed for freezing/melting in the single-component soft-disc system

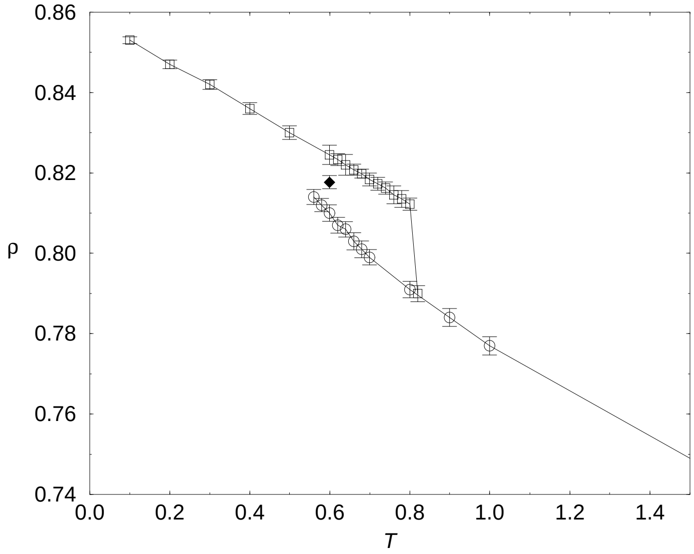

Figure 6.1: Isobaric ($P = 13.5$) phase diagram. Squares and circles indicate data points of the heating and cooling traverses, respectively. The filled diamond indicates the final density after a freezing transition at $T = 0.6$. Error bars represent one standard deviation. Note the large region of metastability extending from $T = 0.6$ to $T = 0.8$.

at the same pressure and for the S1 crystal phase studied in Chapter 5. For the former, the region extends from $T = 0.95$–0.98, and for the latter, it extends from $T = 1.02$–1.06. We have heated the defective crystal shown in Figure 6.2(d) and found that melting occurs at $T = 0.7$ but not at $T = 0.68$. The true thermodynamic melting/freezing temperature should therefore lie somewhere in the range $T = 0.69$–0.8. The apparent high metastability of the liquid phase to supercooling is investigated in the following work. We also study the process of crystallisation at $T = 0.6$.

In the next section we characterise the changes in structure that occur during heating and cooling of the equimolar mixture. Note that structural properties have only been calculated for the heating traverse in the range $T = 0.1$–0.7.

6.3.2 Development of Crystalline Order

Particle Configurations

Representative particle configurations from the cooling and heating traverses are shown in Figure 6.2. We draw attention to several important features. The small

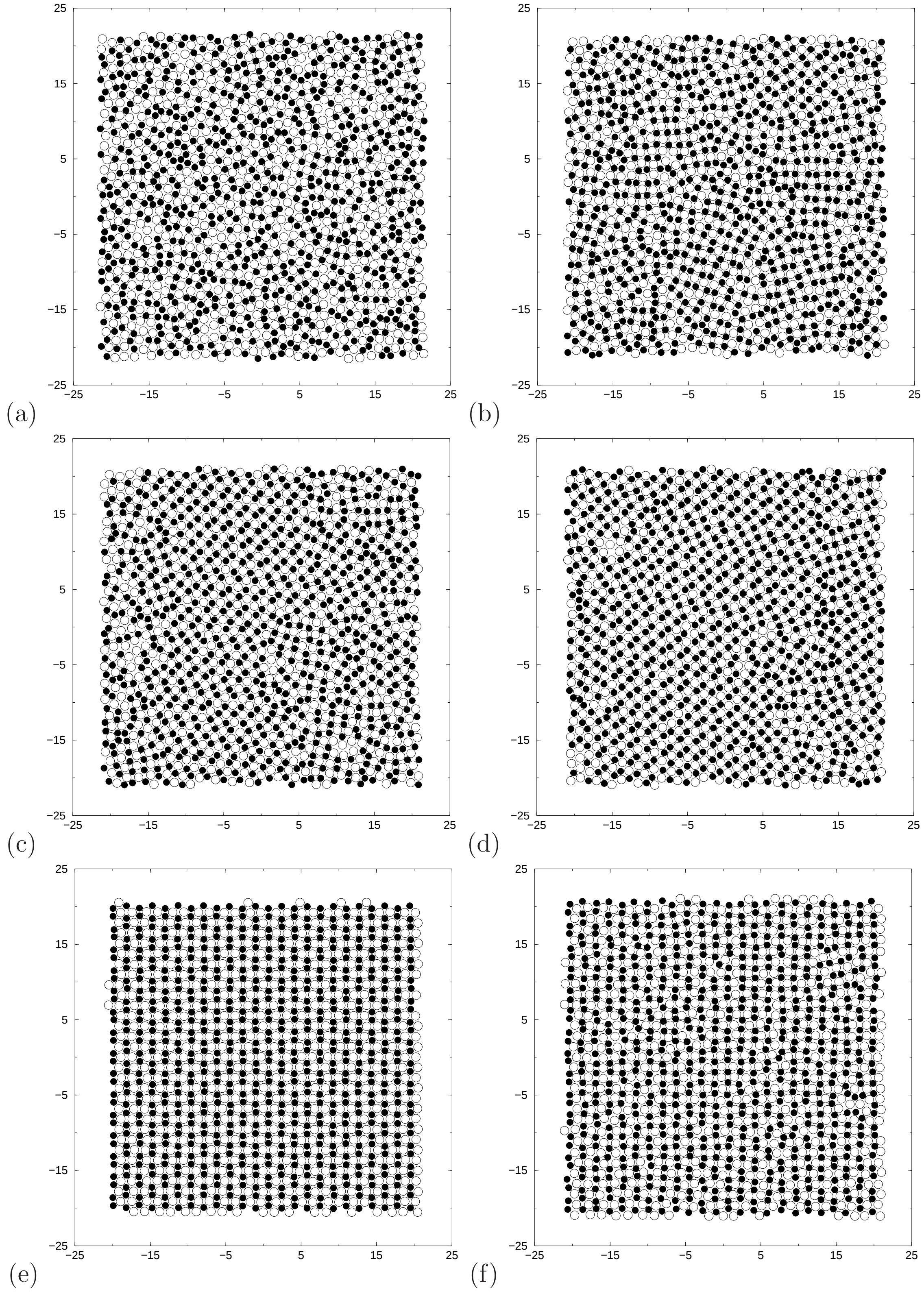

Figure 6.2: Representative particle configurations: during cooling at (a) $T = 1$, (b) $T = 0.6$ before freezing, (c) $T = 0.6$ during freezing, and (d) $T = 0.6$ after freezing; and during heating at (e) $T = 0.1$ and (f) $T = 0.8$. The small and large particles are represented by filled and open circles respectively.

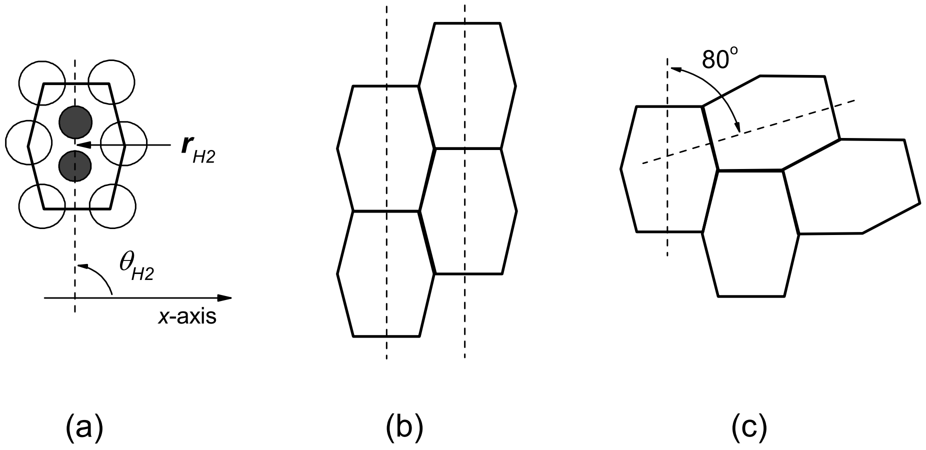

Figure 6.3: Drawing of (a) the H2 unit cell and (b) parallel and (c) herringbone packings of these. The filled and open circles represent small and large particles, respectively, and the thick line represents the H2 unit cell. The dashed line, passing through the two small particles, is the cell axis, θ_{H2} is the orientation of the cell, and $\mathbf{r}_{H2}$ is the midpoint of the line joining the two small particles.

and large particles species appear to be well-mixed at all temperatures, consistent with an effective attraction between unlike particle species. During cooling, the initially disordered liquid (a) appears to develop large quantities of crystalline-like order (b) prior to freezing. The crystal that is formed consists of elongated hexagonal unit cells, of the type illustrated in Figure 6.3(a), that we will refer to as H2 unit cells. These pack together in both parallel and near-perpendicular (herringbone-like) arrangements, as represented schematically in Figure 6.3(b)-(c).

The structure of the growing crystal appears to be quite labile; some of the herringbone packing present during crystallisation [Figure 6.2(c)] has changed to parallel packing by the time the main crystallisation event is complete (d). There are still small amorphous regions in (d). A perfect crystalline configuration of parallel-packed H2 cells fits well into a square simulation box and was used for the heating traverse. The constructed crystal (e), with all unit cells packed in a parallel fashion, is stable right up to $T = 0.8$ (f), the only defects present being a couple of substitutions and some herringbone packing in the upper right-hand corner. We note that because the H2 unit cells are able to pack together in both parallel and herringbone alignments without constraints on the periodicity of these, it is theoretically possible for this system to form a solid state with perfect H2 local order, and long-range orientational order, yet lacking in long-range translational order. The relative stability of such configurations could be investigated by using a simulation algorithm that allows for the box shape to change, for example that of Melchionna et al. [233].

Pair Distribution Functions

The pair distribution functions (PDFs), defined in Section 5.3.2, describe the radially averaged structure about particles. The PDFs for the cooling traverse are plotted in Figures 6.4 and 6.5. Also shown, for comparison, are the respective PDFs at $T = 0.6$ during the heating traverse. For reference, the complete PDFs for the heating traverse are plotted in Figures C.3 and C.4.

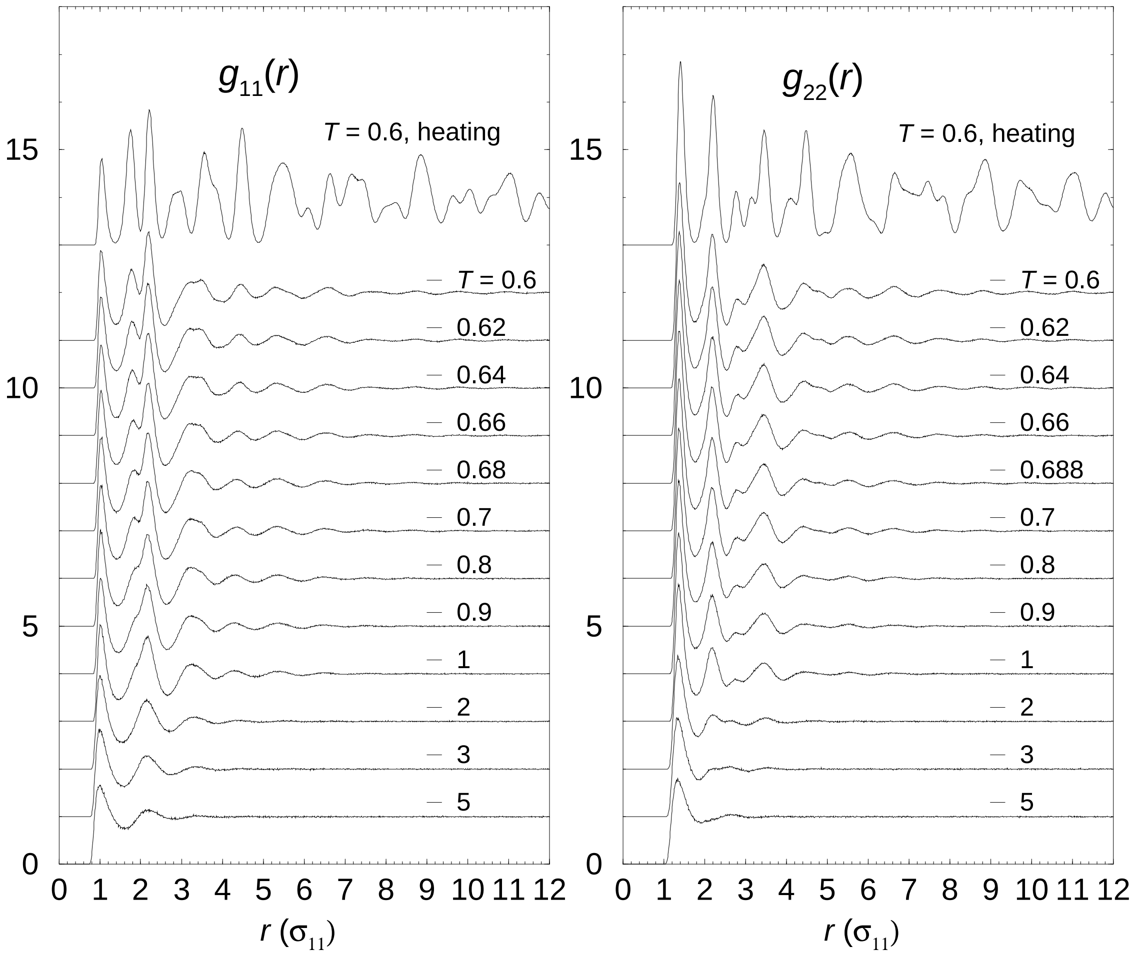

Figure 6.4: The partial pair distribution functions $g_{11}(r)$ and $g_{22}(r)$ for the cooling traverse as a function of distance from $T = 5$ down to $T = 0.6$. For $T \leq 3$, each curve has been shifted upwards by one unit from the higher temperature curve directly preceding it. For comparison, the respective functions at $T = 0.6$ during the heating traverse have also been plotted.

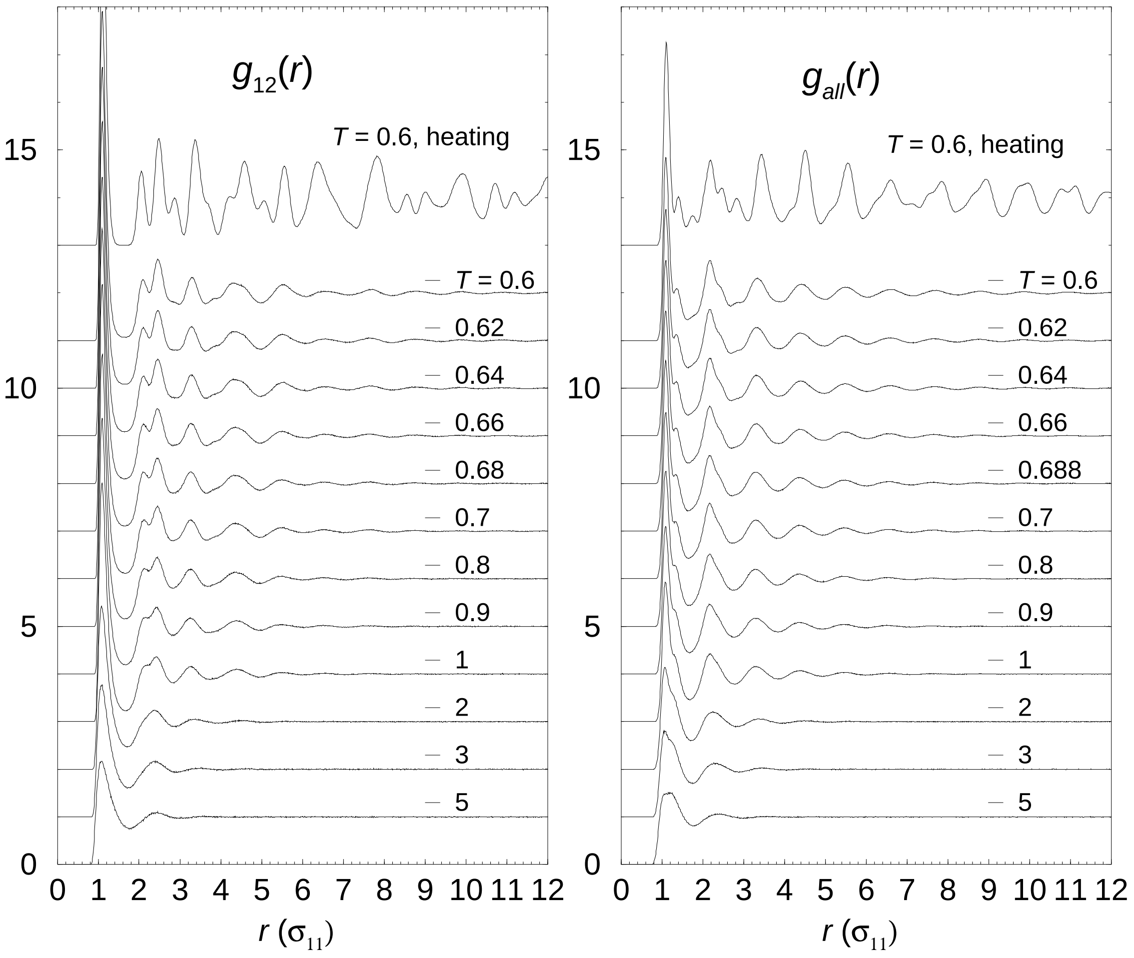

Figure 6.5: The partial pair distribution function $g_{12}(r)$ and the total pair distribution function $g_{all}(r)$ for the cooling traverse as a function of distance from $T = 5$ down to $T = 0.6$. For $T \leq 3$, each curve has been shifted upwards by one unit from the higher temperature curve directly preceding it. For comparison, the respective functions at $T = 0.6$ during the heating traverse have also been plotted.

Upon cooling, the liquid shows increasing local ordering until at $T = 0.6$ there are undulations in the PDFs out to $r = 8\sigma_{11}$. The initial peak structure is similar to that in the solid-state PDFs at the same temperature, but there are significant differences beyond $r = 2.5\sigma_{11}$. For example, the fourth peaks in the crystalline partial pair distribution function (PPDFs) are absent in the liquid state PPDFs. Therefore, whatever crystalline order is present in the liquid prior to freezing must be in very small domains or involve herringbone packing, as the latter would result in a different peak structure to the parallel-packed crystal used for the heating traverse.

The partial structure factors were calculated from the PPDFs, using the method explained in Section 5.3.2. They are plotted along with the total structure factor in Figures C.5 and C.6. We did not investigate structural relaxation in the solid-state and have therefore not calculated structure factors for the heating traverse.

We further investigate the local order in the liquid and solid states using a number of measures built upon nearest neighbour interactions. Two particles of type a and b are defined to be nearest neighbours if they are separated by a distance less than cut_{ab}, where cut_{ab} is the distance at which the first minimum in the respective partial PDF, $g_{ab}(r)$, occurs. For reference, cutoff distances obtained for the cooling and heating traverses are listed in Tables C.11 and C.12, respectively.

Local Structure Parameters

In Figure 6.6 we plot the distribution of local packing environments as a function of temperature. The main change during the cooling traverse is a rapid increase in the fraction of L43 and S14 environments below $T = 1$; by the time freezing

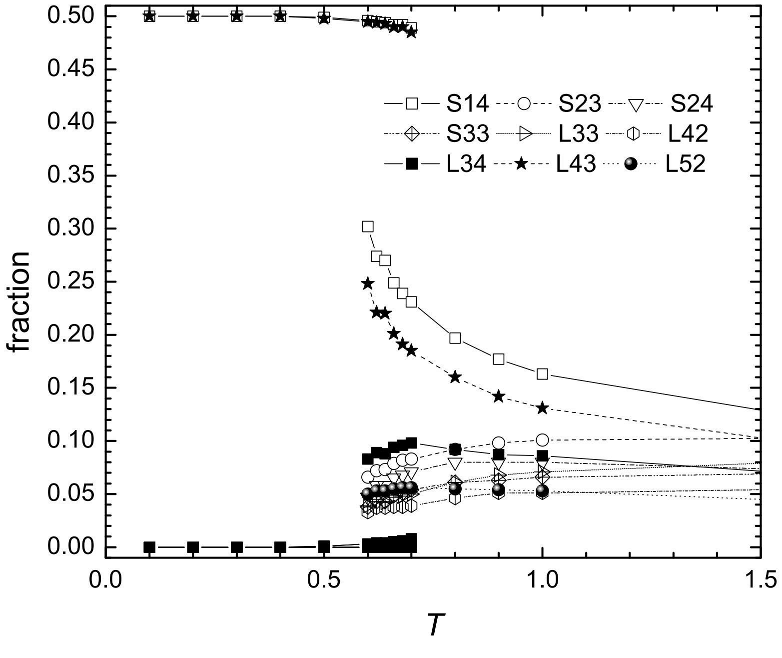

Figure 6.6: The distribution of local packing environments as a function of temperature. We have identified a particular neighbourhood with the following notation: A small particle with m small neighbours and n large neighbours is designated as Smn and the analogous large particle is indicated as Lmn.

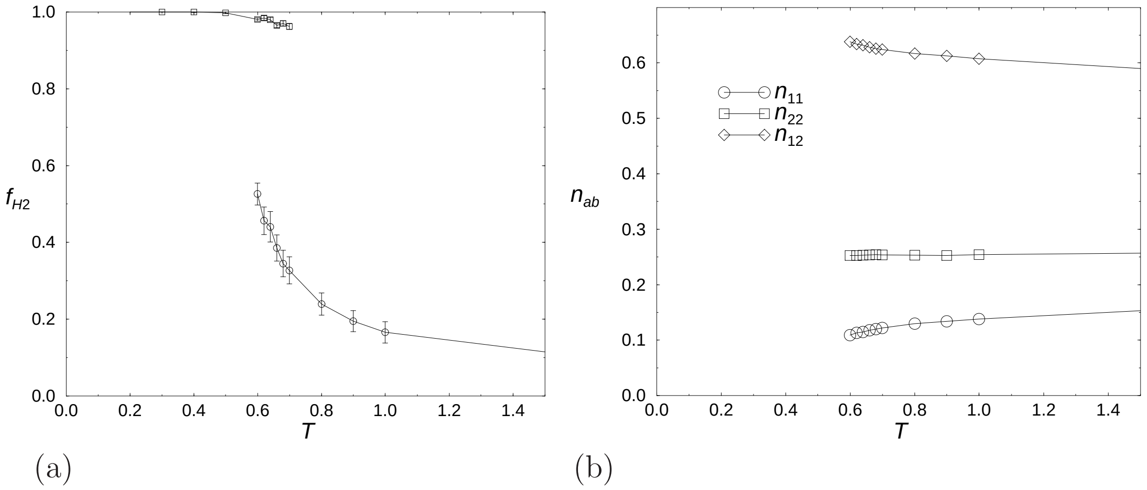

(a) (b)

Figure 6.7: (a) The fraction of particles in H2 unit cells (f_{H2}) as a function of temperature during the cooling and heating traverses. (b) 'Bond' fractions as a function of temperature. n_{ab} is the fraction of all nearest neighbour particle pairs that occur between particles of type a and b. Results are only shown for $T \leq 1$, and the error bars represent one standard deviation.

commences, over half the particles are in these environments. Analysis of the H2 crystal (both parallel and herringbone packings) shows that all the small particles have S14 environments and all the large particles have L43 environments. Therefore, these results indicate that there may be a high degree of crystalline order in the low-temperature liquid phase. As expected, the solid phase during the heating traverse is composed almost entirely of L43 and S14 environments. Above $T = 0.6$, there is a small decrease in the fraction of these environments that is most likely due to vibrational distortions, as substitutional defects do not appear until $T = 0.7$.

To resolve to what extent the S14 environments pack together to form H2 unit cells [see Figure 6.3(a)], we consider the fraction of particles in H2 cells f_{H2} as a function of temperature. An H2 cell is defined as a small particle with S14 local environment whose neighbouring small particle also has the S14 local environment. Figure 6.7(a) clearly demonstrates that f_{H2} also rises rapidly prior to freezing. In contrast, the distribution of nearest neighbour interactions n_{ab} between particles of type a and b, plotted in Figure 6.7(b), shows relatively little change with temperature. From these results we conclude: (i) that the liquid has a high degree of crystalline-like local structure prior to freezing; and (ii) that the dominant change in local structure on cooling is a change in the *topology* (spatial distribution) of nearest neighbour interactions, rather than a change in their relative abundance.

Orientational Order Parameters

To investigate the orientational correlation between H2 cells, we define a new set of order parameters. The ‘orientation’ of an H2 cell θ_{H2} is defined as the angle subtended by the x-axis and the line running through the two small particles in the H2 cell, in the range $0^o \leq \theta_{H2} < 180^o$. And the ‘location’ of the H2 cell $\mathbf{r}_{H2}$ is defined as the midpoint of the line joining the two small particles. See Figure 6.3(a) for a graphical representation of these quantities. Using them, we define an orientational distribution function for H2 cells as

$$P_{H2}(\theta) = \left\langle \frac{1}{N_{H2}} \sum_{j}^{N_{H2}} \theta_{H2,j} \quad \delta(\theta - \theta_{H2,j}) \right\rangle , \tag{6.2}$$

where N_{H2} is the total number of H2 cells, $\theta_{H2,j}$ is the orientation of the jth H2 cell, and the angular brackets denote an average over different configurations in time.

We also define a pair distribution function for H2 cells as

$$g_{H2}(r) = \left\langle \frac{1}{N_{H2}\rho_{H2}} \sum_{i}^{N_{H2}} \sum_{j \neq i}^{N_{H2}} \delta[r - r_{H2,ij}] \right\rangle , \tag{6.3}$$

where N_{H2} is the total number of H2 cells, $\rho_{H2} = V/N_{H2}$, $r_{H2,ij} = |\mathbf{r}_{H2,i} - \mathbf{r}_{H2,j}|$ is the separation between the ith and jth H2 cells, and the angular brackets denote an average over different configurations in time.

We test for the presence of long-range orientational correlation between H2 domains by defining an orientational correlation function as

$$C_{H2}(r) = \left\langle \frac{1}{N_{H2}\rho_{H2}} \sum_{j=1}^{N_{H2}} \sum_{k \neq j}^{N_{H2}} \cos[2(\theta_{H2,j} - \theta_{H2,k})] \quad \delta(r - |\mathbf{r}_{H2,j} - \mathbf{r}_{H2,k}|) \right\rangle , \tag{6.4}$$

where the angular brackets again indicate an average over time origins. This orientational correlation function is weighted by the translational correlations. To see it free of this bias we plot the ratio $G_{H2}(r) = C_{H2}(r)/g_{H2}(r)$. If all the H2 cells at a given separation r lie parallel to each other then $G_{H2}(r) = 1$, while if they all lie perpendicular to each other then $G_{H2}(r) = -1$.

In Figure 6.8 we plot the distribution of H2 cell orientations during the cooling and heating traverses. Plot (b) shows that during the heating traverse the H2 cells remain in a parallel alignment perpendicular to the x-axis, as indicated by the peak

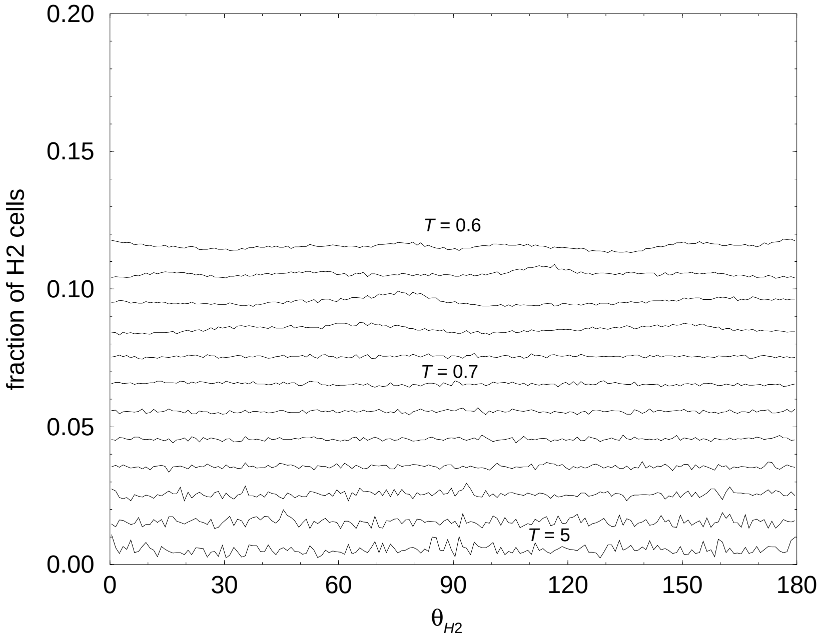

(a)

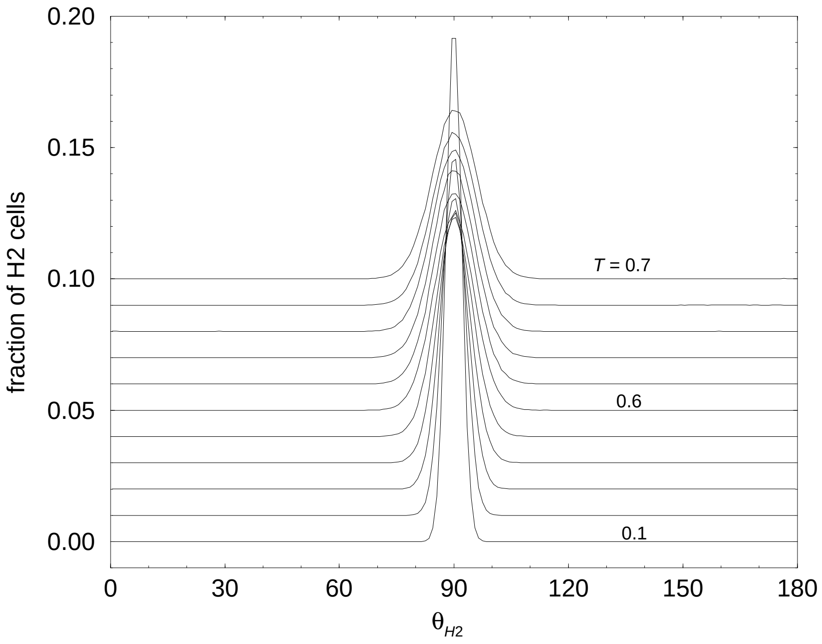

(b)

Figure 6.8: The temperature dependence of the distribution of H2 cell orientations during the (a) cooling and (b) heating traverses. The absolute value of the fraction depends upon the size of the binning over angles and is therefore unimportant. For clarity, each curve in (a) below $T = 5$ has been shifted upwards by 0.01 units above the higher temperature curve directly preceding it, and each curve in (b) above $T = 0.1$ has been shifted upwards by 0.01 units above the lower temperature curve directly preceding it.

around $\theta_{H2} = 90^o$. As the temperature increases the peak broadens, presumably due to vibrational motion. We find no evidence of herringbone packing in the temperature range studied. In contrast, during cooling [plot (a)], there is no strong alignment of H2 cells. Some small undulations appear below $T = 0.68$, often separated by an angle around 80^o, but it is clear that the majority of H2 cells are not aligned with respect to each other.

The orientational correlation functions G_{H2} for the cooling traverse are plotted in Figure 6.9(a). Also shown for comparison - plot (b) - are the pair distribution functions $g_{H2}(r)$ at $T = 0.6$ during both heating and cooling traverses. Note that C_{H2} for the heating traverse is almost identical to $g_{H2}(r)$ since all H2 cells are parallel to one another; G_{H2} for the heating traverse therefore contains no additional information and has not been plotted. We find that during the heating traverse there is clear long-range structure in $g_{H2}(r)$ extending the full length of the simulation cell. An example at $T = 0.6$ is shown in plot (b). In contrast, there is no long-range orientational order between H2 cells during cooling. There is, however, increasing structure at small separations as the temperature is reduced. The maxima in $G_{H2}(r)$ near $r = 2.2$, 2.8, 3.5 and 4.5 match the expected nearest and next-nearest neighbour separations of H2 cells in perfect parallel packing, and also appear as sharp peaks in $g_{H2}(r)$ during the heating traverse. We therefore conclude that these are due to the presence of small clusters of H2 cells packed in parallel. Furthermore, the minima in $G_{H2}(r)$ around $r =$ 2.5 and 4.0 match the expected nearest and next-nearest neighbour separations of H2 cells in herringbone packing, and also appear as additional peaks in $g_{H2}(r)$ during the cooling traverse that are absent during the heating traverse. The near-perpendicular alignment of H2 cells in herringbone packing would also explain the negative values of these minima. We therefore conclude that in the liquid phase below $T = 0.7$ there are clusters of aligned H2 cells that are 3–4 H2 units across. The increasing fluctuations at higher temperature indicate poor statistics, probably due to the increasingly small number of H2 cells in the sample.

This result, along with the increase in the fraction of particles in H2 order and the lack of any strong angular preference for H2 cells, suggests that before freezing commences there is a significant amount of H2 order in small domains that are unaligned with respect to each other.

We also tested for the presence of 4-, 6- and 12-fold orientational order in the system (see Section 5.3.2 for the definition of the orientational order parameters).

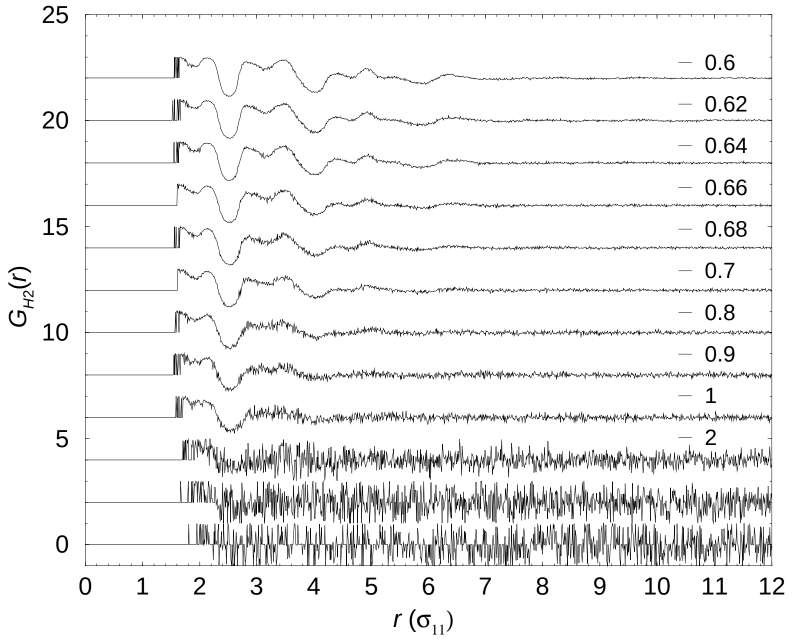

(a)

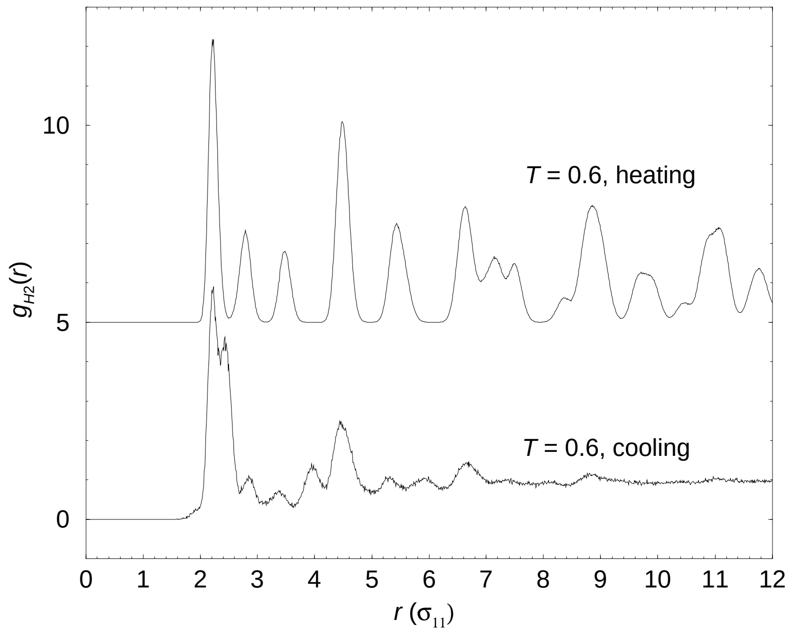

(b)

Figure 6.9: (a) The temperature dependence of the orientational correlation function for H2 cells $G_{H2}(r)$ during the cooling traverse. (b) The pair distribution function for H2 cells $g_{H2}(r)$ at $T = 0.6$ during the cooling and heating traverses. For clarity, functions have been offset vertically from each other.

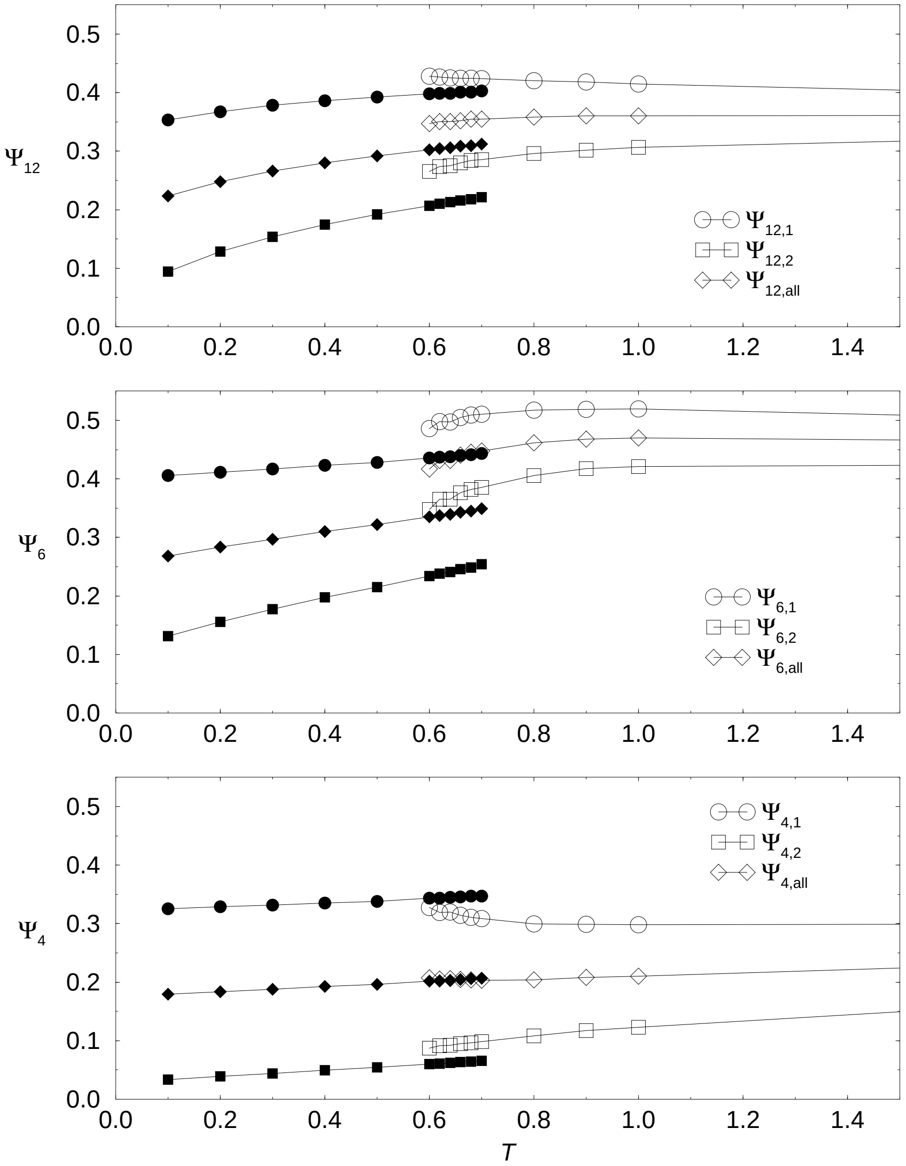

Figure 6.10: The temperature dependence of the bulk averaged n-fold order parameters Ψ_n, where $n = 4, 6, 12$, and their small ($\Psi_{n,1}$) and large ($\Psi_{n,2}$) particle contributions, for the cooling and heating traverses. The filled symbols indicate data from the heating traverse.

The bulk averaged n-fold order parameters Ψ_n are plotted in Figure 6.10 for both the heating and cooling traverses. The major change upon cooling is a decrease in 6-fold order below $T = 1$. This is likely caused by the rapid increase in 5-coordinated S14 environments and 7-coordinated L43 environments (see Figure 6.6), which must also explain the discontinuity in the bulk 6-fold order between the liquid and solid phases. The increase in $\Psi_{4,1}$ below $T = 1$ must also be related to the increase in S14 environments, as S04 environments make up less than 2% of the total. The changes in 12-fold order are likely due to the changes in 4- and 6-fold orientational order.

The n-fold orientational correlation functions $G_n(r)$ test for long-range orientational correlation of the local n-fold domains. During the cooling traverse, we find that $G_{4,1}(r)$, $G_{6,1}(r)$ and $G_{6,2}(r)$ develop very weak correlations (out to $r = 5\sigma_{11}$). The peak structure of these functions is very similar to that observed at small r during the heating traverse (for which $G_{4,1}(r)$, $G_{6,1}(r)$ and $G_{6,2}(r)$ have very weak long-range correlations). We therefore conclude that the 4- and 6-fold orientational correlations observed in the liquid phase are simply a reflection of the H2 order in the system, and do not include these plots.

At low temperatures, the liquid phase contains a very high degree of local crystalline-like order, with over 50% of particles in H2 unit cells. However, these cells appear only to form small clusters, usually less than 3 units across, that remain unaligned with respect to each other.

6.3.3 Dynamics and Structural Relaxation

In this section, we present an analysis of the changes in particle transport and structural relaxation that occur upon cooling of the equimolar mixture.

Intermediate Scattering Functions and Arrhenius Plot

For the equimolar mixture, we have calculated the incoherent (or self) intermediate scattering functions $F_{s,1}(k,t)$ and $F_{s,2}(k,t)$ for the small and large particles, respectively (see Section 5.3.3 for their definitions). $F_{s,1}(k,t)$ and $F_{s,2}(k,t)$ have been measured at the positions of the first maxima in the static structure factors $S_{11}(k)$ and $S_{22}(k)$, which are weakly dependent on temperature and are listed in Table C.13. Log-linear plots of the self intermediate scattering functions are shown in Figure 6.11. The relaxation curves broaden with decreasing temperature and, below $T = 0.7$, develop an increasingly prominent shoulder near 10τ. The appearance of a shoulder in the intermediate scattering function is often a sign of supercooled liquid behaviour. For example, glass-formers typically develop two-step relaxation functions upon supercooling as discussed in Section 1.2. Interestingly, $F_{s,1}(k,t)$ and $F_{s,2}(k,t)$ decay at almost the same rate at a given temperature.

The structural relaxation time $\tau_{e,1}$ is defined as the time taken for the incoherent scattering function $F_{s,1}(k,t)$ to decay to $1/e$. The temperature dependence of

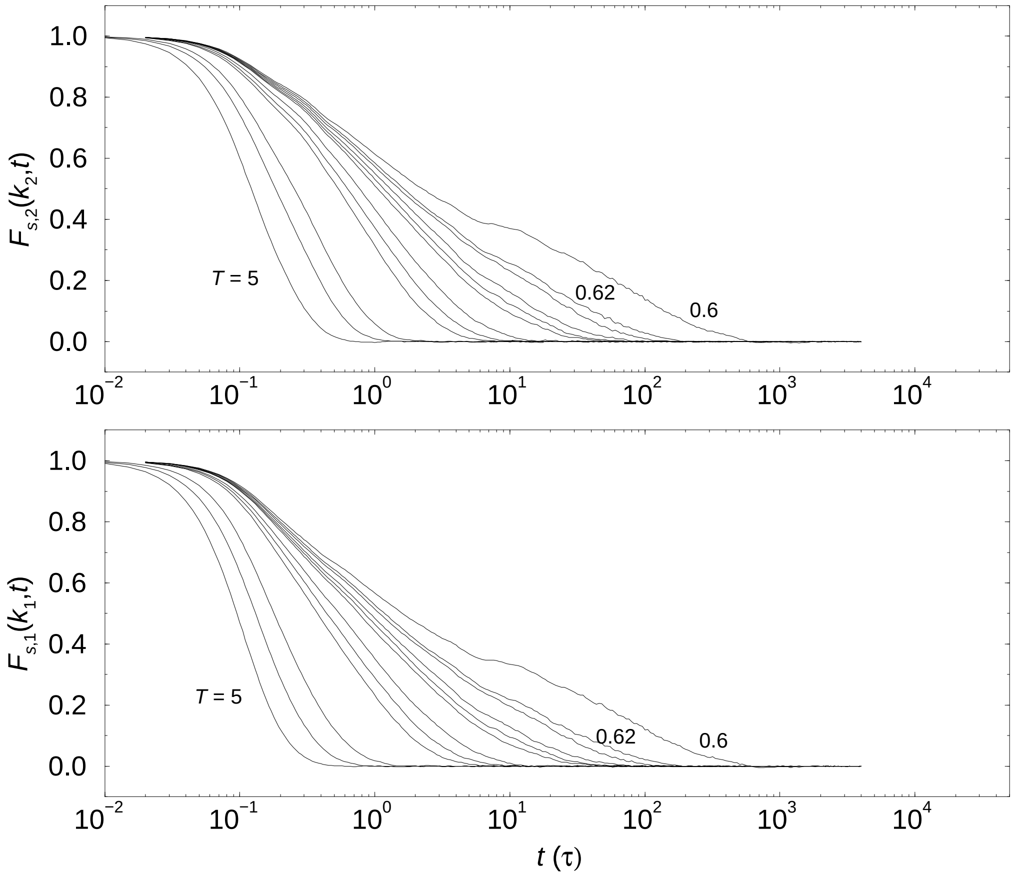

Figure 6.11: The incoherent scattering functions $F_{s,1}(k_1, t)$ and $F_{s,2}(k_2, t)$ for the small and large particles, respectively. The wave vectors k_1 and k_2 are the first peak positions in the respective partial structure factors (listed in Table C.13). From left to right the temperatures of the curves are $T = 5$, 3, 2, 1, 0.9, 0.8, 0.7, 0.68, 0.66, 0.64, 0.62, and 0.6. Note the appearance of a shoulder in the curves below $T = 0.7$.

this relaxation time, plotted in Figure 6.12, is Arrhenius at high temperatures, but diverges weakly from Arrhenius behaviour as the temperature drops below $T = 0.7$. This deviation from Arrhenius behaviour also resembles the dynamic behaviour of supercooled fragile glass-formers. Similarly, the diffusion constants - measured in the region where the mean-squared displacement (MSD) has reached its long-time constant value ($R_a^2(t) > \sigma_{11}$) - also show a strong deviation from Arrhenius temperature dependence, with the onset of this deviation occurring just below $T = 0.7$. The diffusion constants for the small and large particle species remain approximately equal at all temperatures. For reference, the MSDs are plotted in Figure C.7, and the structural relaxation times and diffusion constants are listed in Table C.14.

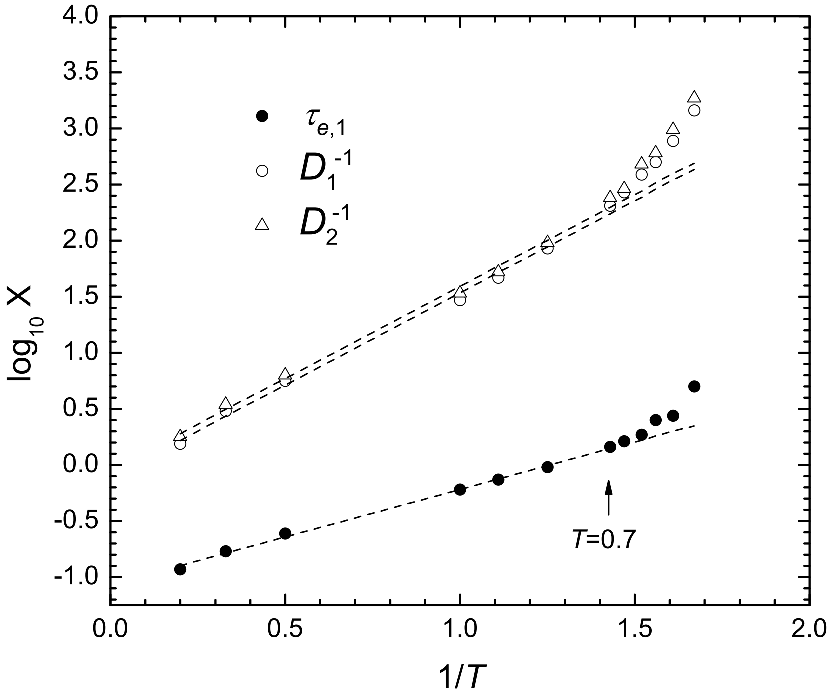

Figure 6.12: Arrhenius plot of the structural relaxation time $\tau_{e,1}$ and the inverse diffusion constants D_1^{-1} and D_2^{-1}. The dashed lines are linear regressions through the data for $T > 0.7$. Note the divergence from Arrhenius behaviour at low temperatures.

Non-Gaussian Parameter

As explained in Section 5.3.3, the non-Gaussian parameters $A_a(t)$ can be used as a measure of the degree of dynamic heterogeneity in a sample. Large values at intermediate times can be attributed to a broad distribution of local mobilities. The non-Gaussian parameters for the present system are plotted in Figure 6.13. A rapid rise in non-Gaussian behaviour is observed at low temperatures for both the large and small particle species; the trend is for the maxima to move to longer times as they increase in height. Given that we found no evidence of crystallisation during these runs, we attribute the non-Gaussian behaviour to an increasing heterogeneity in the liquid dynamics at intermediate times. Furthermore, at all temperatures the non-Gaussian parameters appear able to decay to zero over the timescale of the equilibration runs, indicating that the equilibration times were long with respect to structural relaxation.

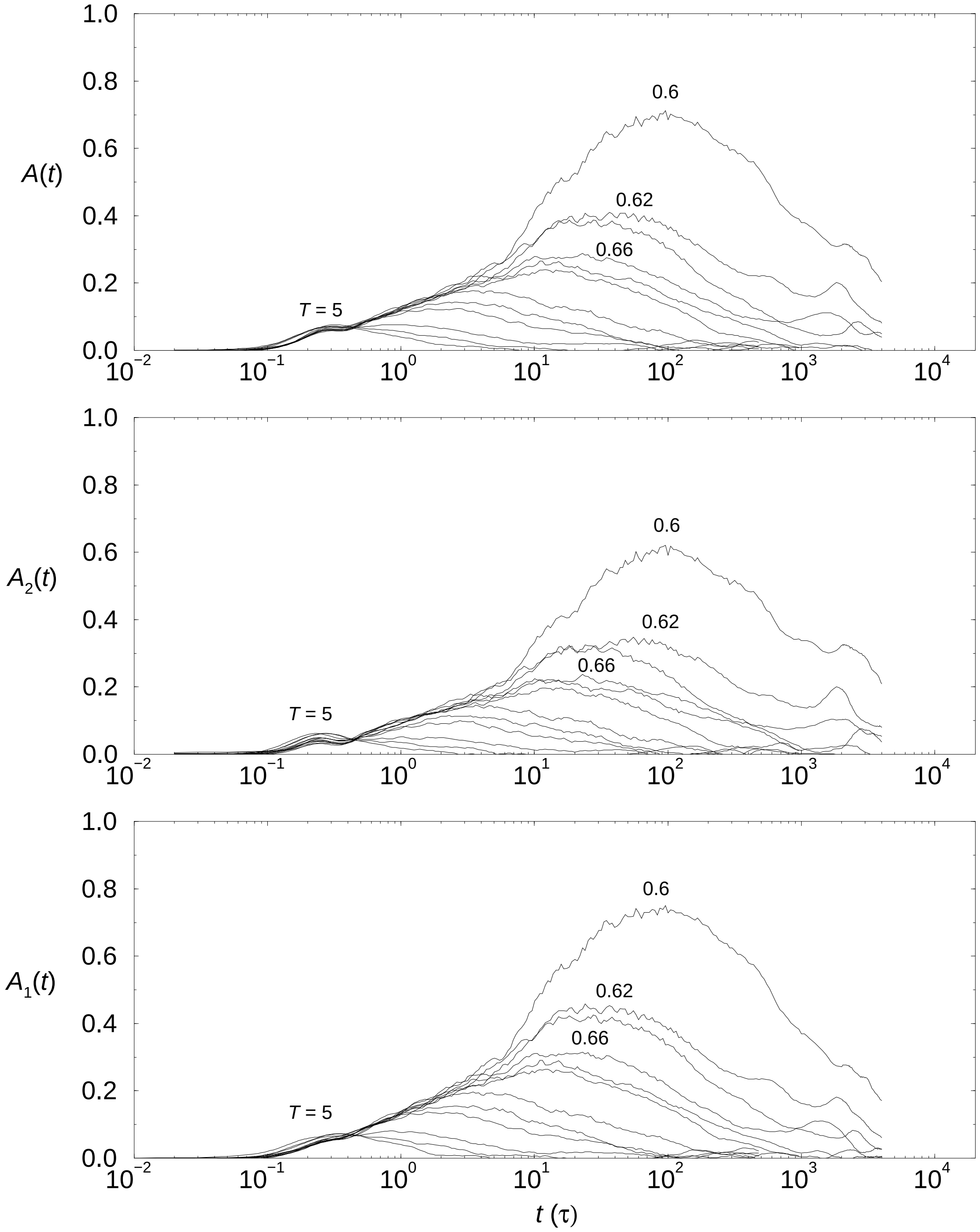

Figure 6.13: The non-Gaussian parameter averaged over all particles, $A(t)$, and averaged over small and large particles, $A_1(t)$ and $A_2(t)$, respectively. The temperatures of the curves are as listed in Figure 6.11. Observe the rapid increase in the peak heights with decreasing temperature.

Upon cooling below $T = 0.7$, the liquid phase increasingly shows dynamic behaviour typical of a supercooled liquid; the diffusion constants and structural relaxation times deviate from Arrhenius behaviour, the non-Gaussian function develops an increasingly large peak at intermediate times, and a shoulder appears in the intermediate scattering function. The observation that the defected H2 crystal melts near $T = 0.7$ also suggests that the thermodynamic melting/freezing temperature T_f lies somewhere near this temperature. Yet the liquid remains stable to crystallisation over equilibration times that are sufficiently long for the average particle to travel 5–$10\sigma_{11}$, and for all the particles to randomise their initial kinetic state (the non-Gaussian function decays to approximately zero). We investigate the origin of this metastability further in the next section, by studying the process by which crystallisation eventually proceeds.

6.3.4 Alignment of Unit Cells During Crystallisation

As discussed in the Section 6.1, the mechanism by which crystallisation proceeds in substitutionally ordered crystals appears to have received relatively little attention. In this section we present a brief investigation into the process of crystallisation in the H2 system. In particular, we wish to uncover the rate-limiting step in order to gain some insight into the large metastability of this system to supercooling despite the high degree of crystalline order in the liquid. We also propose a reason for the relatively slow process by which crystallisation eventually proceeds.

We consider several properties investigated above, as well as a number of new measures of H2 unit cell aggregation, and study the change in these properties before, during and after crystallisation over the course of a $50,000\tau$ run. The starting configuration for this run was the final configuration of the $10,000\tau$ equilibration run at $T = 0.6$.

In Figure 6.14 we plot the change in several thermodynamic properties as a function of time. The quantities undergo large fluctuations but some clear trends can be observed. After about $6,000\tau$ the fraction of nearest neighbour interactions between different particle species n_{12} starts to increase. Soon after, the density ρ starts to increase. Both n_{12} and ρ increase fairly continuously until about $28,000\tau$ after which time they return to fluctuations about a constant value. In contrast, the potential energy (PE) shows only a small change relative to the magnitude of its fluctuations. Therefore, the crystallisation process appears to last from about 6,000–$28,000\tau$, and

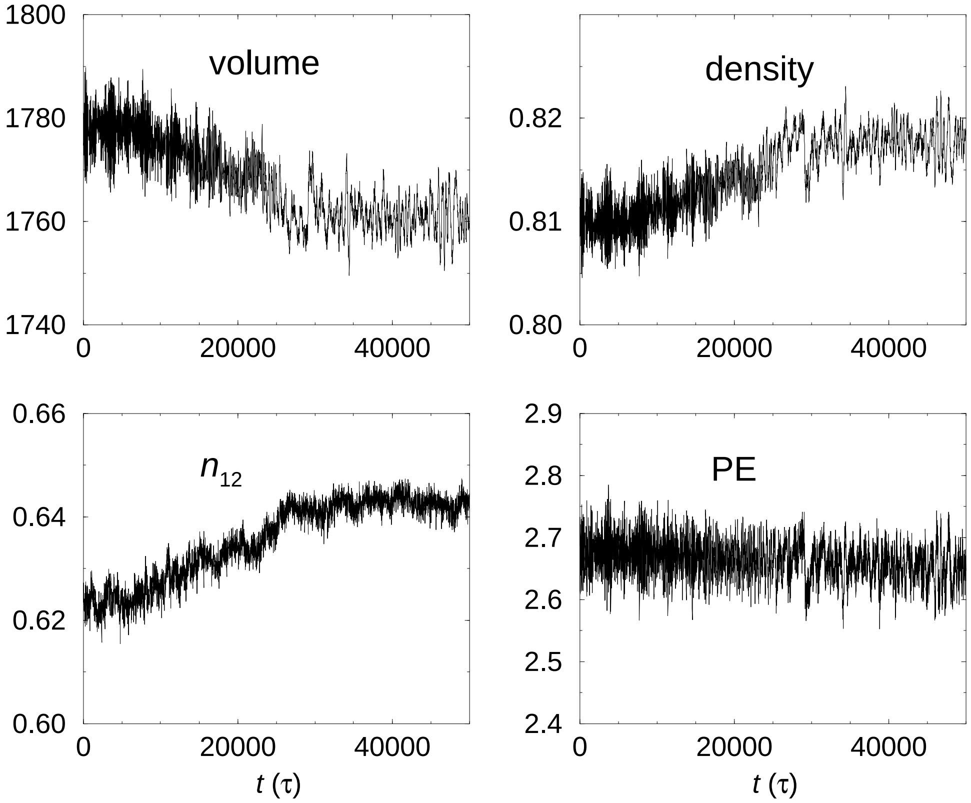

Figure 6.14: The change in volume, density, n_{12} and potential energy as a function of run time before, during and after crystallisation at $T = 0.6$.

does not commence until $16,000\tau$ after the start of equilibration at $T = 0.6$.

Figure 6.15 shows the change in H2 cell orientation and the fraction of particles in H2, S14 and L43 local order during the run; and Figure 6.16 shows the change in the number of H2 clusters, the mean number of particles per H2 cluster, and the distribution of cluster sizes over the duration of the run. We define the mean number of particles per H2 cell as the total number of particles in H2 cells divided by the total number of H2 cells. When H2 cells pack together they share particles, the result being that the mean number of particles per H2 cell decreases. This therefore provides a measure of the degree to which H2 cells cluster together. We also calculate the total number of H2 clusters and the distribution of cluster sizes. Two H2 cells with indices i and j are defined as belonging to the same H2 cluster if $|\mathbf{r}_{H2,i} - \mathbf{r}_{H2,j}| \leq 3.1$, where $r = 3.1$ is the position of the minimum between nearest and next-nearest neighbour peaks in $g_{H2}(r)$.

From 0–10,000τ, the size of the largest H2 cluster undergoes large fluctuations

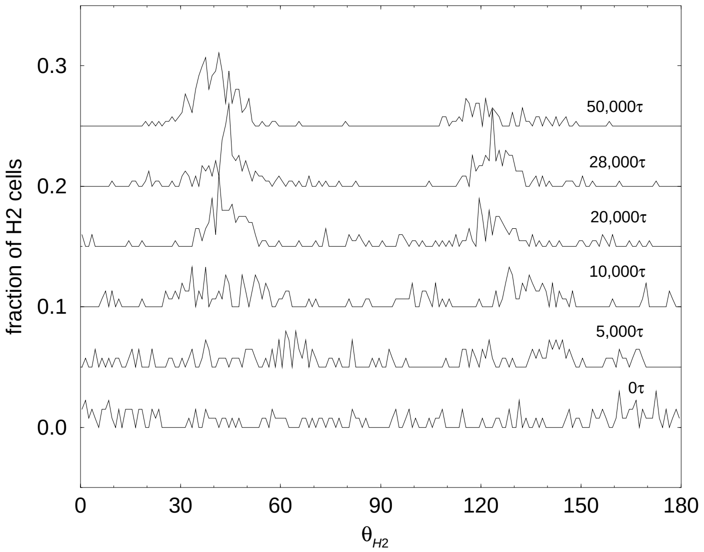

(a)

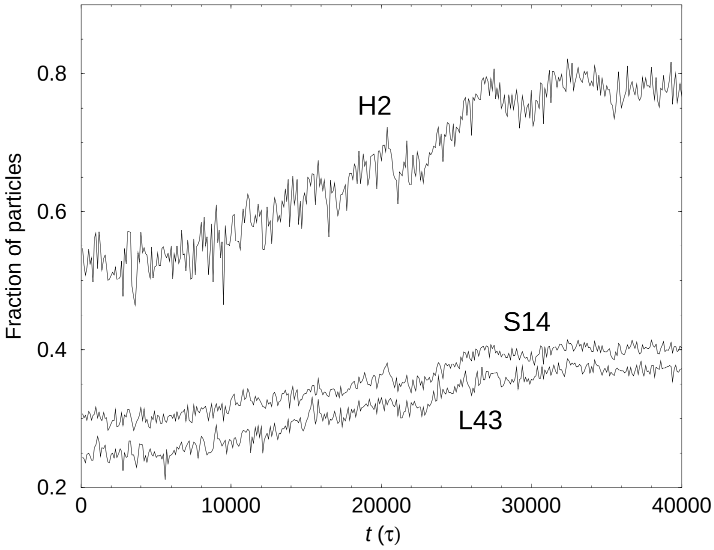

(b)

Figure 6.15: The change in (a) the distribution of H2 cell orientations, and (b) the fraction of particles in H2 unit cells and in S14 and L43 local environments, as a function of run time before, during and after crystallisation at $T = 0.6$. For clarity, the curves in (a) have been displaced vertically from each other.

between 25 and 105 particles, before jumping to a size of 125 particles from which growth proceeds. The critical nucleus therefore appears to be around 115 particles in size. However, simply reaching a critical cluster size cannot be what is responsible for

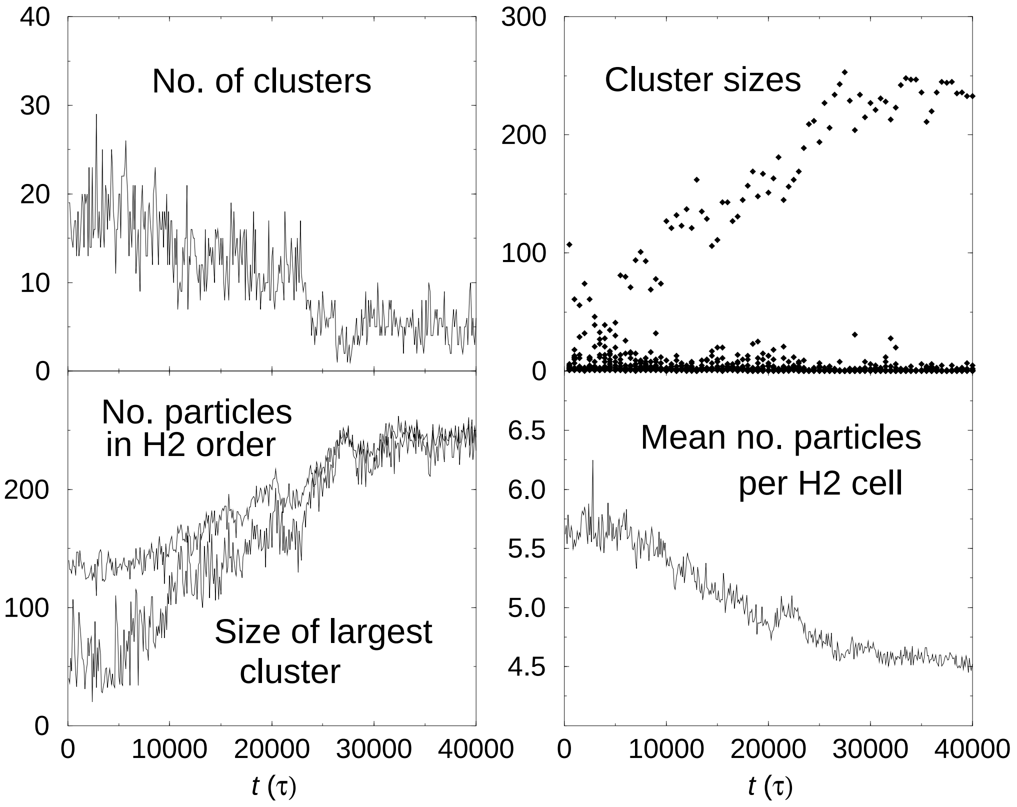

Figure 6.16: The change in the clustering of H2 cells as a function of run time before, during and after crystallisation at $T = 0.6$.

initiating crystallisation. The number of particles in H2 order (and in S14 and L43 order) starts to increase around $7,000\tau$, i.e. before the largest cluster has exceeded 115 particles, and even after crystallisation has begun the largest cluster size drops below 115 particles. The angle distribution of H2 cells supplies the answer. At 0τ the angle distribution is very broad with no clear peaks, but after $5,000\tau$ two small peaks near 65^o and 140^o are now visible. By $10,000\tau$ more clustering of angles is apparent, which with time form two peaks separated by an angle of about 80^o, consistent with the development of herringbone packing of H2 cells. There is also a small decrease in the mean number of particles per H2 cell around $6,000\tau$, indicating a small increase in the clustering of H2 cells at this time. Small drops in the total number of clusters and in the mean number of particles per H2 cell near $10,000\tau$ are consistent with a larger growth event involving the aggregation of two smaller (aligned) clusters. This scenario is supported by the lack of an equivalent sudden increase in the number of particles in H2 order near $10,000\tau$. We therefore conclude that the rate limiting step

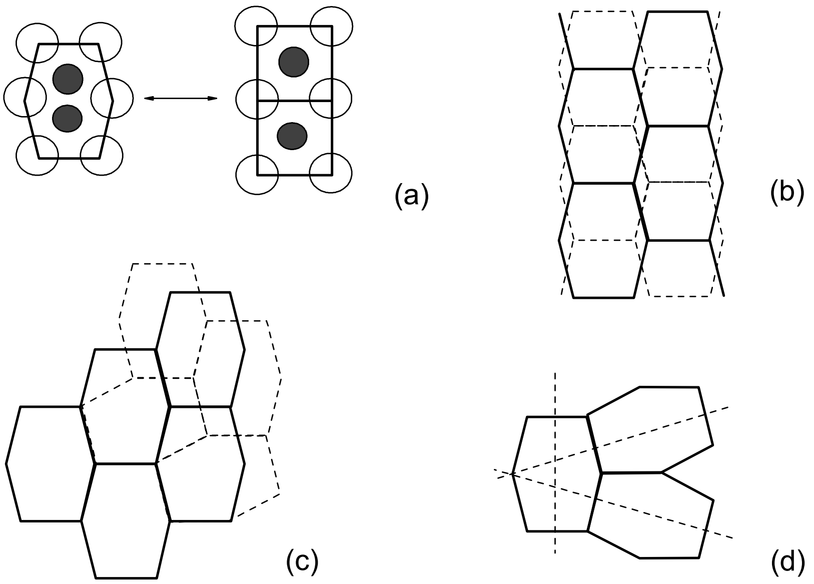

Figure 6.17: (a) The hexagonal H2 unit cell is related to two square S1 unit cells via a simple distortion. (b)-(c) Different crystalline packings of H2 cells can interconvert via distortions like the one illustrated in (a). (d) H2 cells can also stack together in 'frustrated' packings that cannot grow to fill space. The filled and open circles represent small and large particles, respectively, and the thick line represents the H2 and S1 unit cells.

is the alignment of H2 cells. Once sufficient cells become aligned, the fraction of crystal-like local environments starts to increase, eventually resulting in aggregation of two or more existing aligned clusters.

Crystallisation is a slow process, lasting for at least $22,000\tau$, and appears to proceed irregularly. The size of the largest cluster again increases suddenly around $18,000\tau$ and $24,000\tau$. The former appears to be mainly a growth event (the number of particles in H2 order increases suddenly while the total number of clusters fluctuates about an approximately constant value), while the latter appears to be a combination of both growth (f_{H2} increases) and aggregation (the total number of clusters decreases). These interpretations are supported by changes in the mean number of particles per H2 cell: as the cells aggregate, more particles become shared between H2 cells and the value decreases. Finally, we note that between $28,000\tau$ and $50,000\tau$, i.e. after the main crystallisation event appears to be complete, there is a shift from herringbone packing towards parallel packing of H2 cells; the peak in the H2 angle distribution function near 40^o grows while the peak near 125^o shrinks. Therefore, we conclude that the most stable packing is the parallel one, and suggest that the herringbone packing provides a kinetically favourable interface for crystal growth.

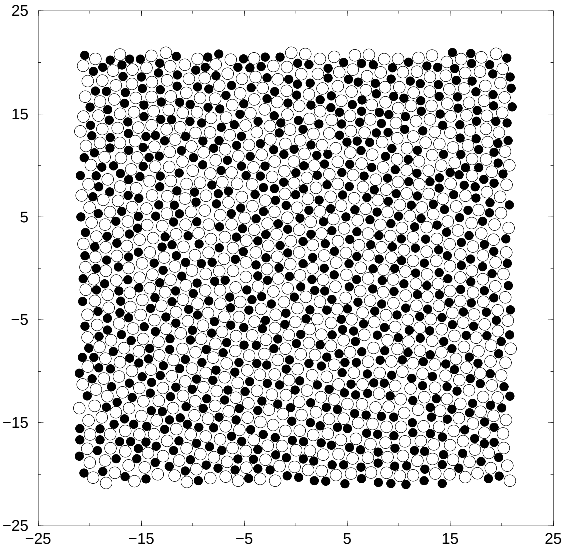

Figure 6.18: A configuration after a freezing transition at $T = 0.58$. Note the presence of grain boundaries between unaligned crystalline domains.

Figure 6.17 illustrates how different packings of H2 cells might interconvert via simple distortions. Small changes in particle position can convert an asymmetric H2 unit cell into two symmetric S04 environments, i.e. two S1 unit cells. Different S1 cells may then recombine resulting in interconversion between different parallel packings of H2 cells (b) or between parallel and herringbone packings (c). Of course, this interconversion may proceed in a step-like manner rather than all at once. Frame (d) illustrates one possible reason for slow crystal growth. H2 cells may pack together in arrangements that cannot grow to fill space.

Finally, while crystallisation occurs at $T = 0.6$ given sufficient time, the liquid phase is stable for long times even at lower temperatures. If, after $10,000\tau$ equilibration at $T = 0.6$, the liquid is cooled to $T = 0.58$ it is stable for a further $10,000\tau$ before crystallisation commences. And if cooled to $T = 0.56$ at this time it takes a further $12,000\tau$ before crystallisation starts. At these lower temperatures, crystallisation appears to proceed simultaneously via several different nucleation events. Following crystallisation, the final structure, shown in Figure 6.18 for $T = 0.58$, consists of several unaligned crystalline domains separated by grain boundaries.

In summary, we conclude that the rate-limiting step for nucleation is the alignment of a sufficient number of H2 cells in an arrangement that can grow to fill space, i.e. either in herringbone or parallel packing of a combination of these. At $T = 0.6$, growth then proceeds via the creation of new crystalline order in the liquid phase and the occasional attachment of existing crystalline clusters to the growing nucleus. In addition to the alignment of existing H2 cells, growth may be slowed via the compositional changes needed to create new crystalline local order and by false starts leading to packing of H2 cells in arrangements that cannot grow to fill space. Additionally, the growing crystal is quite labile, its structure interconverting between different parallel and herringbone packings. The interior of the final crystal is dominated by parallel packing which leads us to believe that this is the energetically preferred arrangement of H2 cells. At lower temperatures, there appear to be multiple nucleation events, resulting, at least initially, in a structure with many grain boundaries.

6.4 Glass-Formation in the Non-Equimolar Mixture ($x_1 = 0.3167$)

6.4.1 Thermodynamic Properties

The isobaric phase diagram is plotted in Figure 6.19. The density increases smoothly with cooling, showing no sign of a first order phase transition. There is, perhaps, a small change in slope between $T = 0.45$ and $T = 0.4$, which coincides with the

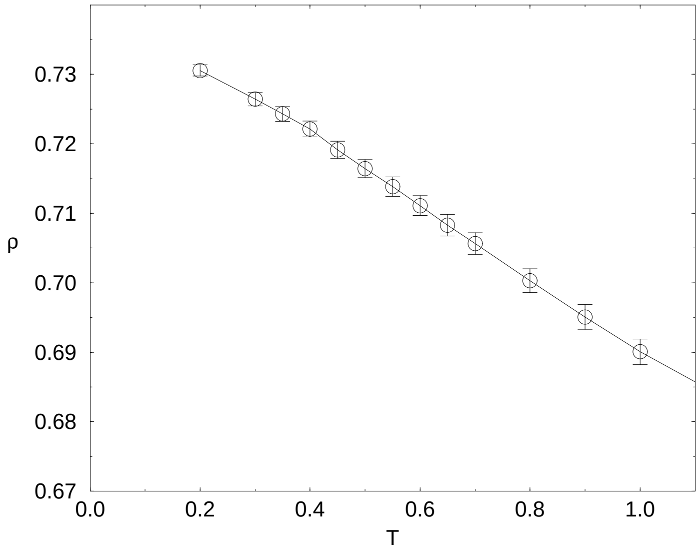

Figure 6.19: Isobaric ($P = 13.5$) phase diagram. Error bars represent one standard deviation. Note that the density increases smoothly with cooling.

temperature at which the system falls out of equilibrium. For reference, the thermodynamic averages for the potential energy per particle (U), energy per particle (E), enthalpy per particle (H), and number density per particle (ρ) are summarised in Table C.15 for the range of temperatures that were investigated.

6.4.2 Development of Short- and Medium-Range Order

Particle Configurations

Representative particle configurations are shown in Figure 6.20. There is little change in structure with temperature. The local structure becomes more regular upon cooling, but the small particles appear evenly dispersed throughout the sample at all

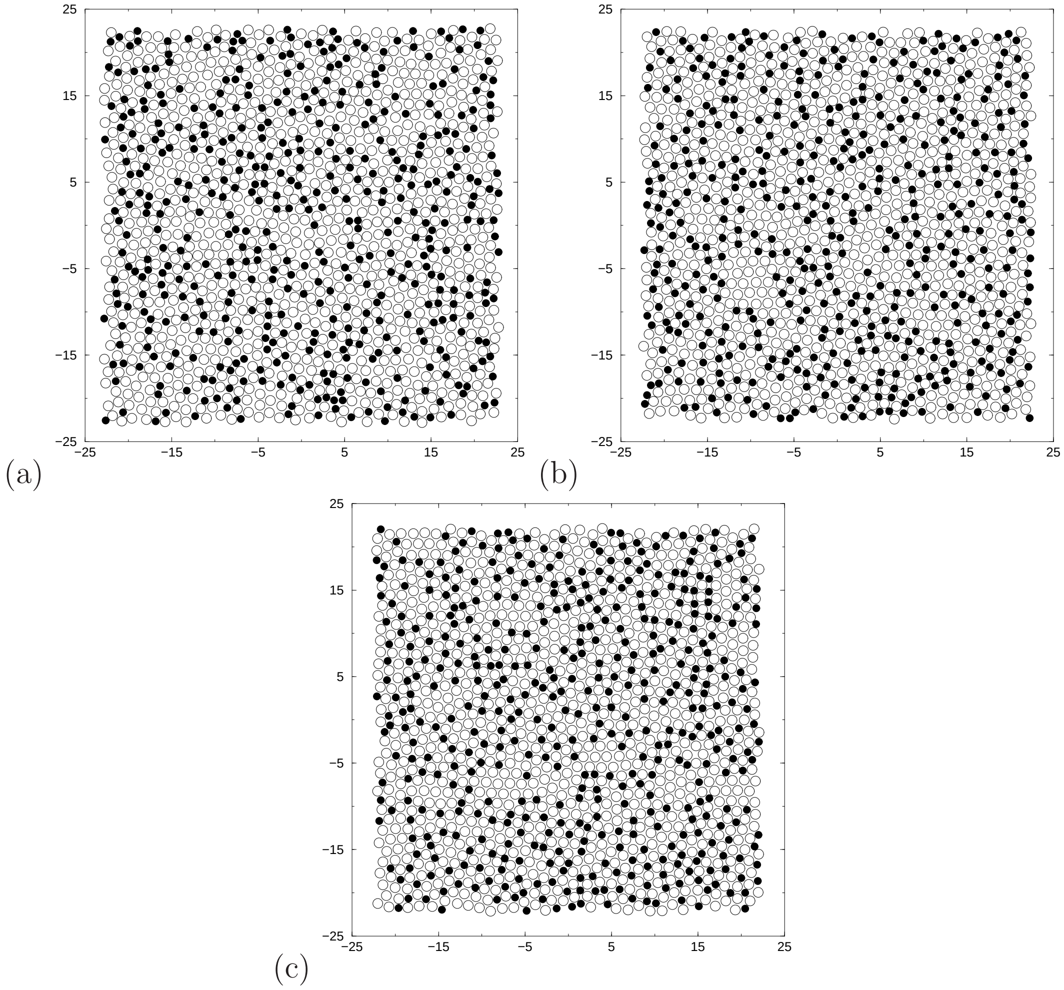

Figure 6.20: Representative particle configurations at (a) $T = 1$, (b) $T = 0.6$, and (c) $T = 0.2$. The small and large particles are represented by filled and open circles respectively.

temperatures. Rather than forming large crystalline clusters, the large particles remain dispersed as the system is cooled.

Pair Distribution Functions

The pair distribution function (PDF) and the partial pair distribution functions (PPDFs), defined in Section 5.3.2, are shown for the non-equimolar mixture in Figures 6.21 and 6.22. Upon cooling, the PDFs develop structure over increasing lengthscales (out to about $6\sigma_{11}$), but there is clearly no long-range translational order in the system. There are some similarities to the PDFs calculated for the equimolar mixture

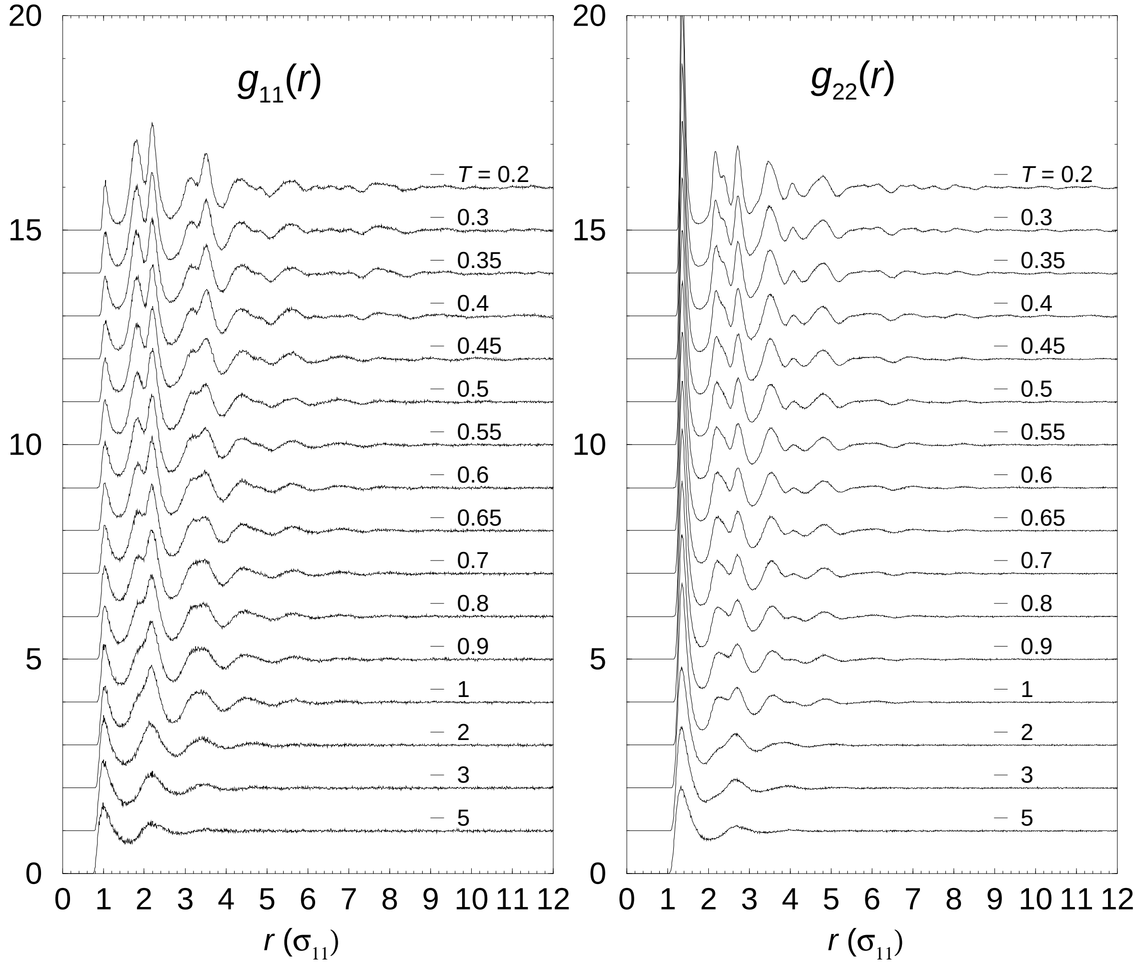

Figure 6.21: The partial pair distribution functions $g_{11}(r)$ and $g_{22}(r)$ as a function of distance from $T = 5$ down to $T = 0.2$. For $T \leq 3$, each curve has been shifted upwards by one unit from the higher temperature curve directly preceding it.

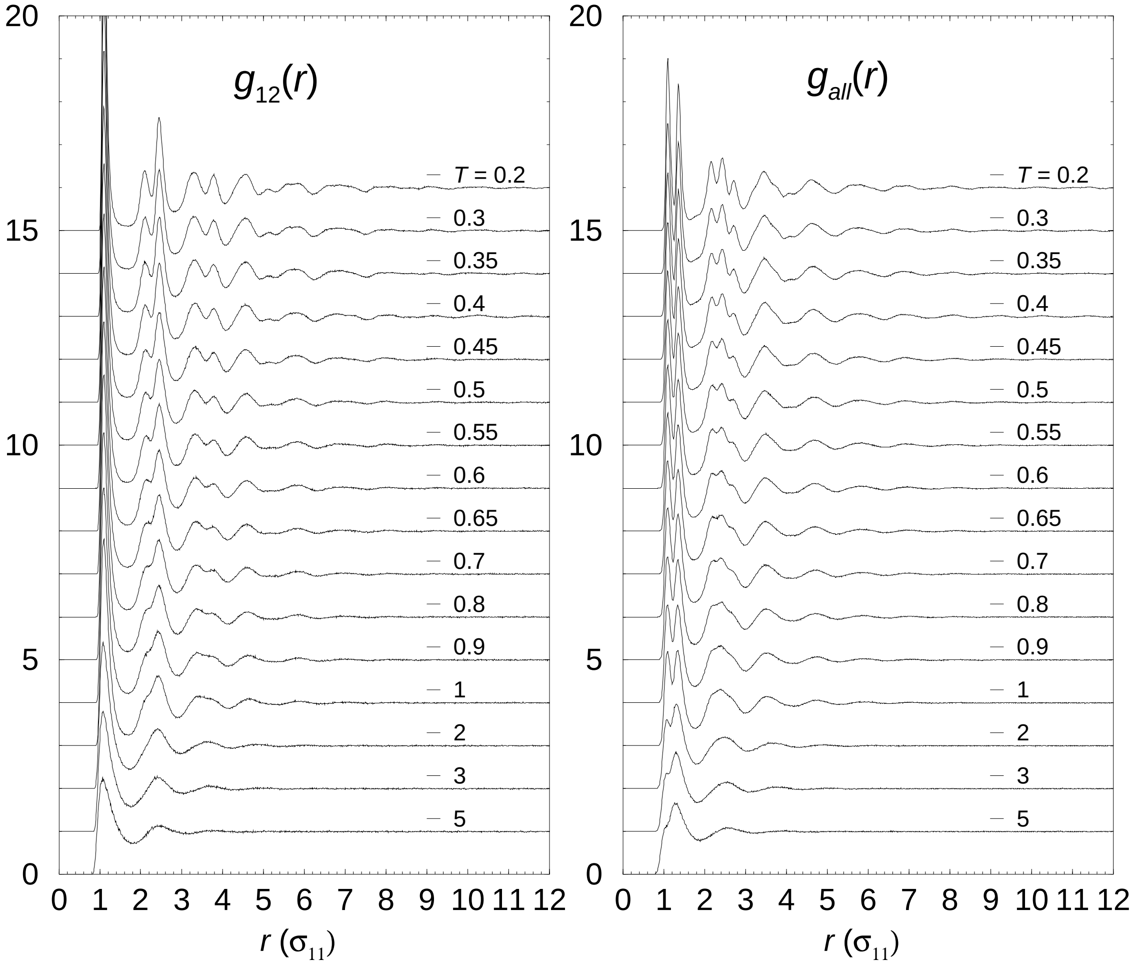

Figure 6.22: The partial pair distribution function $g_{12}(r)$ and the total pair distribution function $g_{all}(r)$ as a function of distance from $T = 5$ down to $T = 0.2$. For $T \leq 3$, each curve has been shifted upwards by one unit from the higher temperature curve directly preceding it.

but also some notable differences: $g_{11}(r)$ has a smaller first peak, indicating that there are less nearest neighbour contacts between small particles; $g_{12}(r)$ has an additional peak at $3.8\sigma_{11}$; and $g_{22}(r)$ has an additional peak at $2.4\sigma_{11}$ and extra peak intensity at $2.8\sigma_{11}$ that can be explained by the presence of hexagonal packing of large particles.

We used the positions of the first minima in the PPDFs as cutoff distances for defining nearest particle neighbours when calculating the local coordination environments and the various orientational order parameters. For reference, these are listed in Table C.16.

Structure Factors

The partial structure factors were calculated from the PPDFs as explained in Section 5.3.2. They are plotted along with the total structure factor in Figures 6.23 and C.8. We note that $S_{11}(k)$ has very weak structure, indicating the lack of a strong characteristic lengthscale for short-range ordering about the small particles. Also, the second peak in $S_{22}(k)$ does not show the splitting characteristic of crystalline domains of large particles (see discussion in Section 7.2.3), indicating the absence of such crystalline domains.

The first peaks in $S_{11}(k)$ and $S_{22}(k)$ are the most intense, and show very little

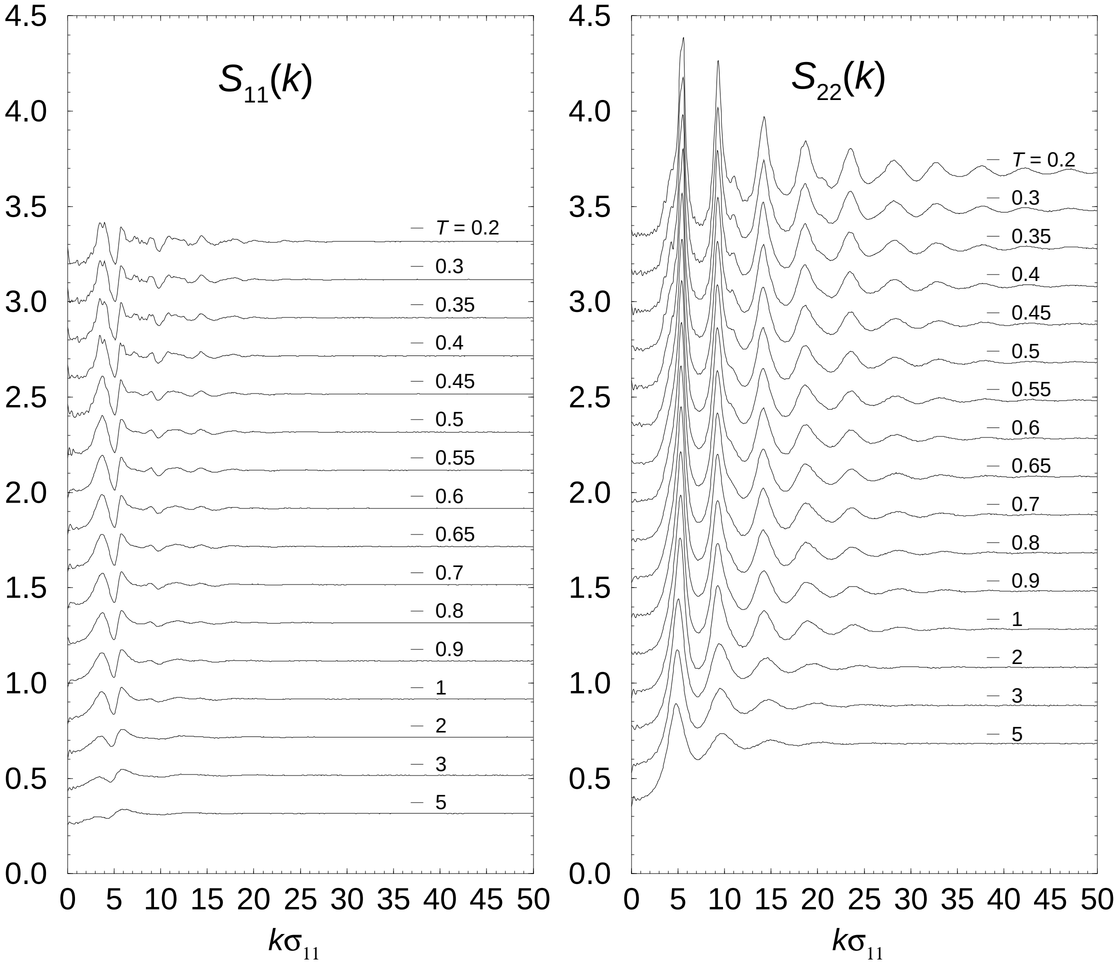

Figure 6.23: The partial structure factors $S_{11}(k)$ and $S_{22}(k)$ for temperatures from $T = 5$ down to $T = 0.2$. For clarity, each curve below $T = 5$ has been shifted upwards by 0.2 units above the higher temperature curve directly preceding it.

variation with temperature. Their approximate positions are given by the wave vectors $k_1 = 3.64\sigma_{11}^{-1}$ and $k_2 = 5.5\sigma_{11}^{-1}$, respectively. We have used these wave vectors to calculate the incoherent scattering functions presented in Section 6.4.3.

Local Structure

Several quantities were used to characterise the local structure of the non-equimolar mixture. In Figure 6.24 we present the 'bond' fractions n_{ab}, defined as the fraction of all nearest neighbours particle pairs that occur between particles of type a and b (see Table C.16 for nearest neighbour cutoff lengths). Upon cooling below $T = 1$, there is a small increase in n_{12} and an associated decrease in n_{11}. However, the dominant interactions in the system are in roughly equal measure large-large and large-small, at all temperatures.

To investigate the local structure in more detail we consider the local environment about each particle. In Figure 6.25 the distribution of local packing environments is plotted as a function of temperature. There is no clearly dominant environment at low temperature. At $T = 0.2$, five environments make up 75% of the local structure, and a further four environments contribute a further 20%. Still, the structure appears

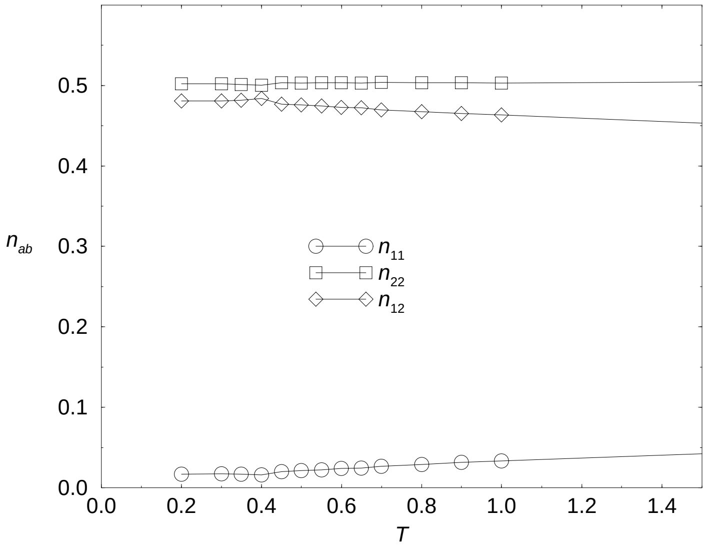

Figure 6.24: 'Bond' fractions as a function of temperature for $T \leq 1$. n_{ab} is the fraction of all nearest neighbours particle pairs that occur between particles of type a and b. Error bars represent one standard deviation.

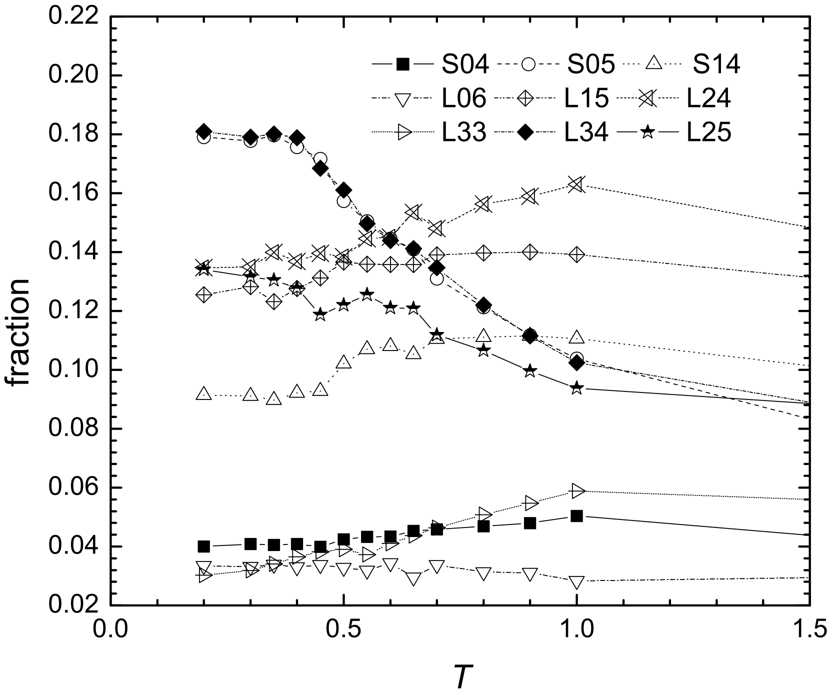

Figure 6.25: The distribution of local packing environments as a function of temperature. We have identified a particular neighbourhood with the following notation: A small particle with m small neighbours and n large neighbours is designated as Smn and the analogous large particle is indicated as Lmn. Only the most common environments are shown.

more homogenous, and the distribution of local environments is less diverse, than in the equimolar additive glass-former studied in Part I. For comparison, the latter has over 20 different local environments with none contributing more than 10% of the total.

There is little sign of H2 crystalline order in the system; below $T = 0.6$ the fraction of particles in S14 environments decreases sharply and less than 5% of large particles are in L43 environments. There is also little sign of crystallisation of the large particle fraction; the L06 environment, corresponding to a hexagonal cluster of large particles, shows only a small increase upon cooling and never constitutes more than 5.5% of large particle environments.

That said, there are some significant changes in local structure upon cooling. Below $T = 1$, the fractions of S05 and L34 environments rise dramatically and, intriguingly, become equal. Analysis of a configuration at $T = 0.2$ [Figure 6.20(c)] suggests that the reason for this is that the L34 environment is strongly associated

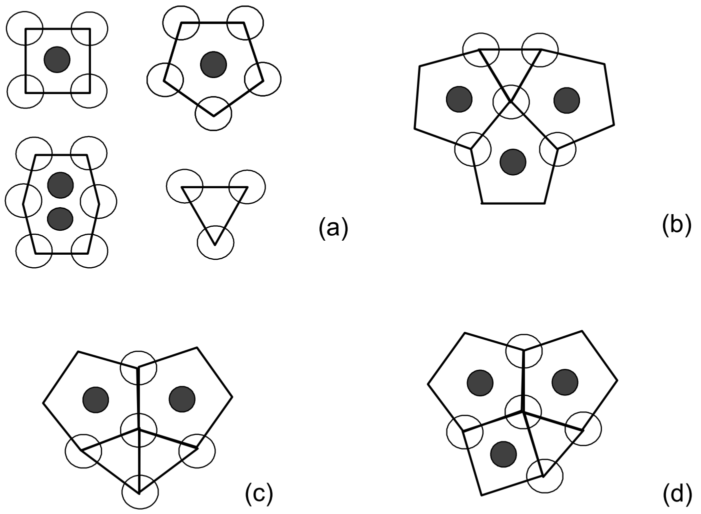

Figure 6.26: (a) Small particle environments in the low-temperature liquid, and (b)-(d) some common ways in which these pack together to form vertices about large particles. The filled and open circles indicate small and large particles, respectively. Note that the large particles at the centre of (b) and (d) both have $L34$ local environments. Occasionally an H2 cell, consisting of two overlapping $S14$ environments, replaces the square cell in structure (d).

with the packing of pentagonal S05 units together with triangular units of three large particles and, occasionally, square S04 units and pentagonal S14 units. These local structural units are illustrated in Figure 6.26(a), and some of their more common packings are illustrated in Figure 6.26(b), (c) and (d). Observe that the large particles at the centre of (b) and (d) both have L34 local environments. Occasionally an H2 cell, consisting of two overlapping S14 environments, replaces the square cell in structure (d).

The preference for the S05 environment over the S14 environment is at first surprising. When all interparticle distances are set equal to σ_{ab}, the $S14$ environment has an angle sum about the small particle of 363°. In contrast, the S05 environment has an angle sum of 395°. We propose that the reason for this preference is that a higher proportion of S14 environments would force an increase in the number of large-large particle contacts which, due to the non-additive interparticle potential, would result in an increase in the system volume. This hypothesis would also explain the very low number of small particles with more than one small neighbour and the absence of a larger increase in L06 environments upon cooling. Glass-formation in this system may therefore be related to the idea of 'frustration', i.e. competition between optimal local and global packings.

Orientational Order Parameters

In order to quantify the orientational order in the system, we used the n-fold orientational order parameters, defined in Section 5.3.2. The bulk averaged n-fold order parameters Ψ_n probe the local orientational order, and are plotted in Figure 6.27. The major change upon cooling is a large decrease in $\Psi_{6,1}$ below $T = 1$. This, together with a small decrease in $\Psi_{4,1}$, is consistent with the large increase observed in S05 environments which are expected to have roughly 5-fold local orientational

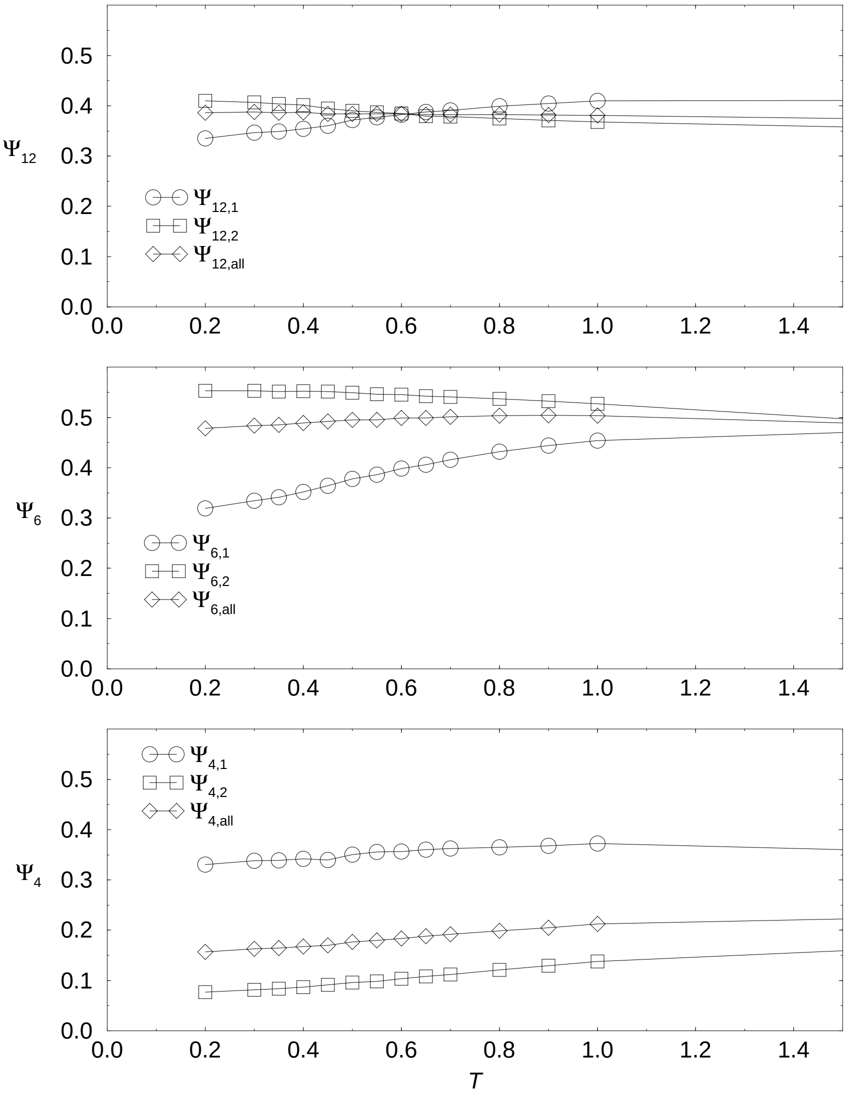

Figure 6.27: The temperature dependence of the bulk averaged n-fold order parameters Ψ_n, where $n = 4, 6, 12$, and their small ($\Psi_{n,1}$) and large ($\Psi_{n,2}$) particle contributions. The error bars represent one standard deviation about the average.

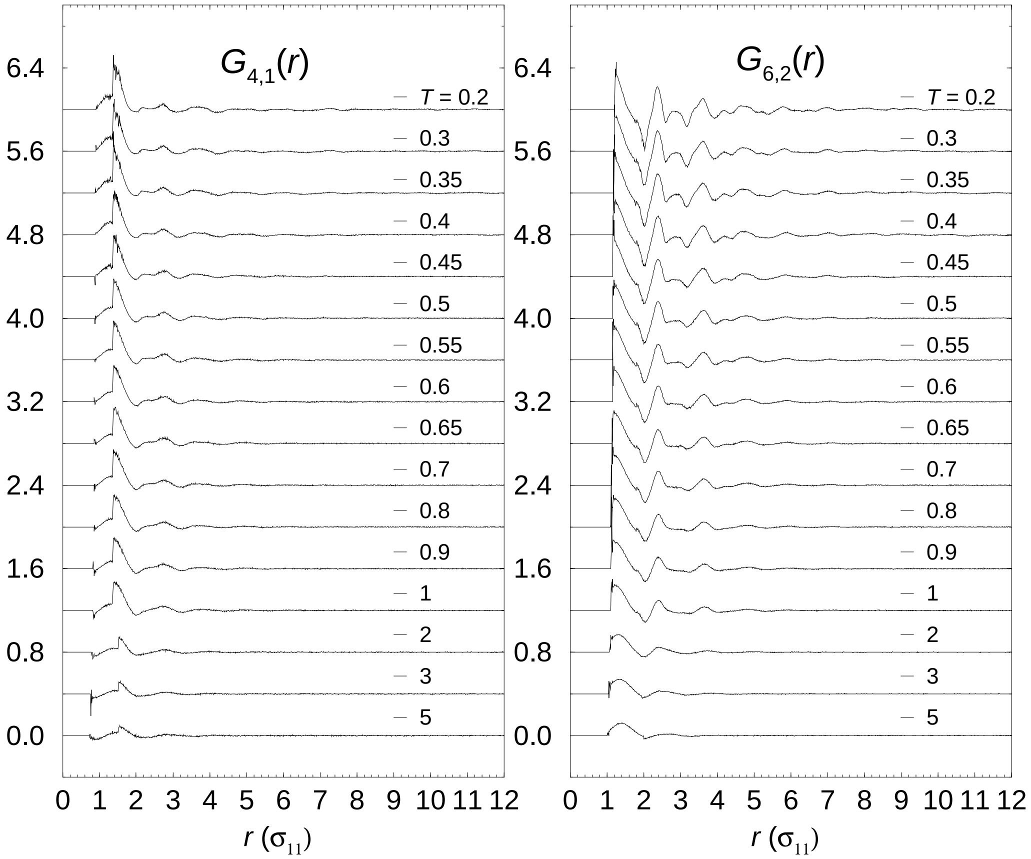

Figure 6.28: The partial 4-fold orientational correlation function about small particles $G_{4,1}(r)$, and the partial 6-fold orientational correlation function about large particles $G_{6,2}(r)$. For clarify, functions have been offset vertically by 0.4 units above the preceding curve.

order. $\Psi_{6,2}$ is quite high but shows only a small increase below $T = 1$. This, together with the large decrease in $\Psi_{6,1}$, indicates that there is no significant growth of a substitutionally disordered large-particle crystal phase.

We also tested for long-range orientational correlations between the local n-fold domains (defined in Section 5.3.2). We found no structure in $G_{4,2}(r)$ and only a single peak in $G_{6,1}(r)$ at all temperatures. Figure 6.28, shows the partial 4-fold orientational correlation function about small particles $G_{4,1}(r)$ and the partial 6-fold orientational correlation function about large particles $G_{6,2}(r)$. Some weak local correlations develop upon cooling, however there is clearly no long-range 4-fold orientational order in the system. There is also no sign of long-range 6-fold order in the system, but $G_{6,2}(r)$ develops structure out to $r = 6$–$8\sigma_{11}$ upon cooling, with a peak structure similar to that observed in systems with substantial hexagonal crystalline domains of large particles (see, for example, Figure 7.9). Considering the lack of a substantial increase in $\Psi_{6,2}$ and in $L06$ environments upon cooling, this change must be mainly due to an increase in the orientational order within existing clusters of hexagonally-packed large particles.

We conclude that the non-equimolar mixture shows no sign of crystallisation or phase separation upon cooling from the liquid state. The low-temperature structure appears to be dominated by two types of medium-range order, small domains of hexagonally-packed large-particles, and larger domains of pentagonal S05 environments packed together with each other and with some S04 environments, H2 units and triangular packings of large particles. In the next section, we present an analysis of the changes in particle transport and structural relaxation that occur during cooling.

6.4.3 Supercooled Liquid Dynamics

Intermediate Scattering Functions and Arrhenius Plot

The timescale of structural relaxation can be probed quite readily by computing density correlation functions such as the intermediate scattering functions (see Section 5.3.3 for their definitions). Log-linear plots of the self intermediate scattering functions are shown in Figure 6.29, and have been measured at the positions of the first maxima in the static structure factors $S_{11}(k)$ and $S_{22}(k)$. The positions of these maxima are independent of temperature and are listed in the caption to Figure 6.29. The relaxation curves broaden with decreasing temperature until below $T = 0.45$ they are no longer able to decay to zero within the finite time scale of the simulations. The relaxation functions already span over five decades in time at this temperature. Below $T = 0.6$, a step appears in the relaxation curves at intermediate times. This step broadens into a plateau with an amplitude that increases with decreasing temperature. The height of the plateau also increases with decreasing temperature. Such two-step relaxation functions have been observed in a wide range of glass-forming systems as discussed in Section 1.2. Damped oscillations are also observed in the plateau region similar to what has been observed for the equimolar mixture with $\sigma_{12} = 1.2$ [44].

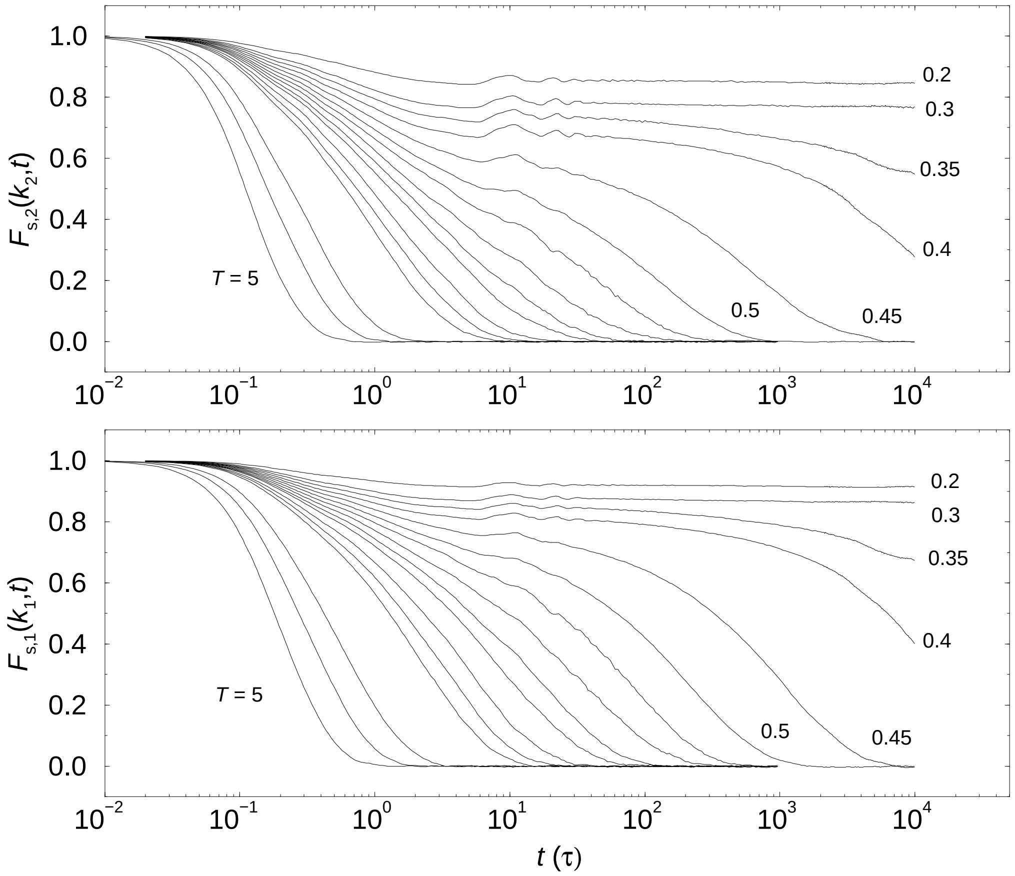

Figure 6.29: The incoherent scattering functions $F_{s,1}(k_1, t)$ and $F_{s,2}(k_2, t)$ for the small and large particles, respectively. The wave vectors $k_1 = 3.64\sigma_{11}^{-1}$ and $k_2 = 5.5\sigma_{11}^{-1}$ are the first peak positions in the respective partial structure factors. From left to right the temperatures of the curves are $T = 5$, 3, 2, 1, 0.9, 0.8, 0.7, 0.65, 0.6, 0.55, 0.5, 0.45, 0.4, 0.35, 0.3, and 0.2. Note the appearance of a two-step relaxation process in the intermediate scattering functions.

Interestingly, $F_{s,2}(k, t)$ decays substantially faster than $F_{s,1}(k, t)$ at a given temperature. The height of the plateau in $F_{s,2}(k, t)$ is also substantially lower than the height of the plateau in $F_{s,1}(k, t)$ at the same temperature. This indicates that the large particles are able to relax their local structure *faster* than the small particles, which is rather unusual.

The temperature dependences of the structural relaxation times, plotted in Figure 6.30, appear to be Arrhenius at high temperatures, but diverge strongly from Arrhenius dependence as the temperature drops below $T = 0.65$. In contrast, the diffusion constants - measured in the region where the mean-squared displacement (MSD) has reached its long-time constant value ($R_a^2(t) > \sigma_{11}$) - show a weaker deviation from

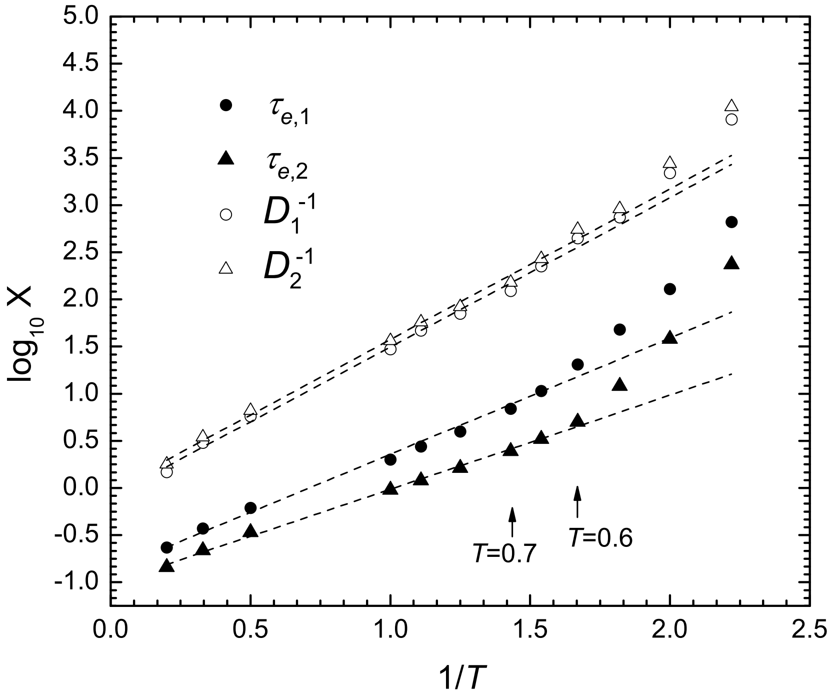

Figure 6.30: Arrhenius plot of the structural relaxation times $\tau_{e,1}$ and $\tau_{e,2}$ and the inverse diffusion constants D_1^{-1} and D_2^{-1}. The dashed lines are linear regressions through the data for $T \geq 0.65$. Note the divergence from Arrhenius behaviour at low temperatures.

Arrhenius temperature dependence, with the onset of this deviation occurring below $T = 0.6$. The diffusion constants for the small and large particle species remain approximately equal at all temperatures. The shorter structural relaxation times for the large particles, and the similar diffusion constants for the two species, suggest that although large particles are able to relax their local environments faster, the motion of both species becomes coupled at longer times and lengthscales.

For reference, the mean-squared displacements (MSDs) are plotted in Figure C.7, and the structural relaxation times and diffusion constants are listed in Table C.14. we note that the MSDs also show typical supercooled liquid behaviour.

The Non-Gaussian Parameters

The non-Gaussian parameters are plotted in Figure 6.31. A rapid rise in non-Gaussian behaviour is observed at low temperature for both the large and small particle species. The maximum values of the parameters increase rapidly below $T = 0.55$, with the peaks being slightly larger for the small particles. The trend is for the maxima to

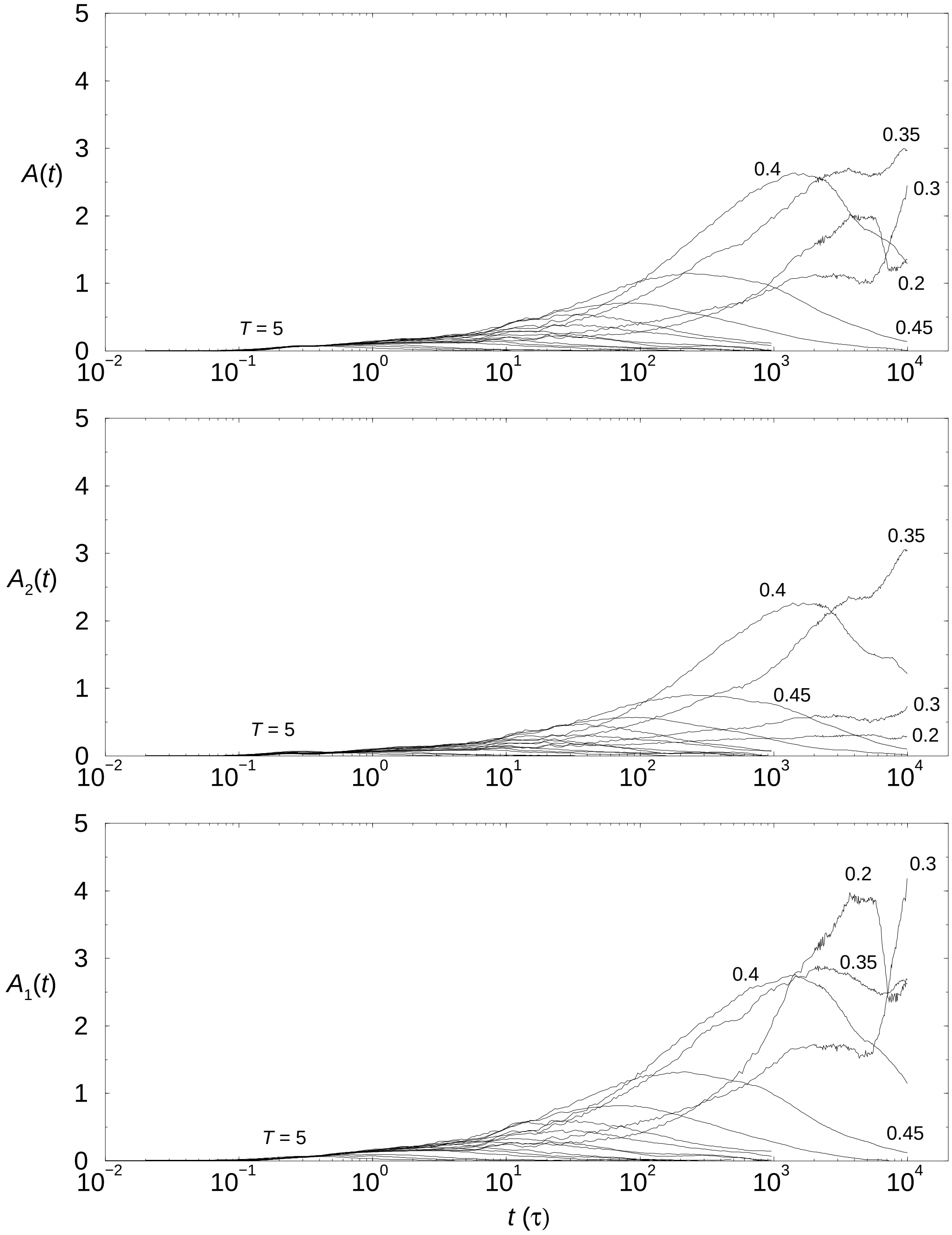

Figure 6.31: The non-Gaussian parameter averaged over all particles, $A(t)$, and averaged over small and large particles, $A_1(t)$ and $A_2(t)$, respectively. The temperatures of the curves are as listed in Figure 6.29. Observe the rapid increase in the peak heights with decreasing temperature.

move to longer times as they increase in height. Below $T = 0.4$ the finite observation time of the simulations is too short to observe the maxima. $A_2(t)$ and $A_1(t)$ are no longer able to decay to zero for $T < 0.45$. From this, and the behaviour of the intermediate scattering functions and MSDs, we conclude that the system falls out of equilibrium somewhere near $T = 0.45$.

In summary, the non-equimolar mixture shows changes in dynamic behaviour upon cooling that are typical of fragile glass-forming liquids. This, together with the lack of any sign of crystallisation or development of long-range order in the liquid, lead us to conclude that this model is a good glass-former.

6.5 Discussion and Conclusions

The equimolar mixture forms a substitutionally ordered crystal phase when cooled at a constant pressure of $P = 13.5$. The crystal can be described as a tiling of the plane by a unit cell consisting of two small particles surrounded by six large particles in an elongated hexagonal arrangement. This H2 unit cell has been predicted to form one of the ground states for binary hard disc mixtures [155]. We find that the unit cells pack together both in parallel, and in a herringbone arrangement where the cells lie at approximately 80^o to each other. From analysis of rearrangements in the growing crystal, it appears that the parallel arrangement is the more stable one. However, the herringbone arrangement is present in high concentration in the crystal nucleus and at the crystal-liquid interface and we therefore postulate that it is a kinetically preferred structure, and that it provides a kinetically preferred growth interface. The parallel arrangement has also been found to be one of the ground states for a 2D binary Lennard-Jones model studied in the context of quasicrystal stability [161]. This latter model, however, has significantly different interaction lengths to the present model and forms a wide variety of other structures that were not observed in the present system.

Heating of a crystal consisting of a perfect parallel packing of H2 cells revealed a hysteresis region in the isobaric phase diagram extending from $T = 0.6$ to $T = 0.8$. This is very large compared to the hysteresis regions observed for freezing/melting in the single-component soft-disc system at the same pressure, extending from T =0.95–0.98, and for the S1 crystal phase studied in Chapter 5, extending from $T = 1.02$–1.06. When a defective crystal was heating from $T = 0.6$ we found that melting occurred at $T = 0.7$ but not at $T = 0.68$. The true thermodynamic melting/freezing temperature is therefore expected to lie somewhere between $T = 0.69$ and $T = 0.8$. We found that the low-temperature liquid exhibited dynamic behaviour typical of supercooled systems: the structural relaxation times and diffusion constants depart from an Arrhenius temperature dependence below $T = 0.7$, the maximum in the non-Gaussian function at intermediate times increases rapidly in magnitude at low temperature, and the intermediate scattering function has a clear step in the decay curve at $T = 0.6$. Below $T = 1$, the proportion of local crystalline environments in the liquid also rises rapidly, and at $T = 0.6$ over 50% of particles are in H2 cells. Yet, the supercooled liquid remains stable to crystallisation over timescales that are at least 2 orders of magnitude longer than the structural relaxation times and over which the average particle travels 3.5–10 diameters.

The high metastability of the supercooled liquid phase appears to be due to the slow process by which H2 cells align correctly for crystal growth to proceed. Although the majority of particles are in local H2 order at $T = 0.6$, these form only small clusters, on average 3–4 H2 units across, that remain unaligned with respect to each other. Only after more than 3,000 structural relaxation times ($\tau_{e,1}$) do a sufficient number of H2 cells align for the fraction of local crystalline environments to start increasing. Close-packing of H2 clusters in arrangements that cannot grow to fill space may be a reason for the slow rate of alignment of H2 cells. Crystal growth then appears to proceed via both aggregation events, involving the joining of several crystalline domains, and addition events involving the formation of new crystalline order in the liquid adjacent to the growing crystal. The initial crystal nucleus and the growing crystal contain a high proportion of herringbone packing of H2 cells, but the fraction of parallel packing appears to increase once the main growth event is complete, i.e. the crystal is quite labile to interconversion between different parallel and herringbone packings. Small distortions in the local coordination environment about small particles - from the S14 to S04 environment - may form a pathway for such interconversions to take place.

In contrast, the non-equimolar mixture shows little sign of H2 crystal order or phase separation into single component crystalline domains. The low-temperature structure is instead dominated by S05 environments and an equal number of L34 environments. The equal occurrence of these two environments appears to be due to the specific way in which the pentagonal S05 environments pack together with each other and with occasional S14 and S04 environments. This system shows dynamic behaviour typical of other glass-forming liquids: the structural relaxation times and diffusion constants depart from an Arrhenius temperature dependence below $T = 0.6$, the maximum in the non-Gaussian function at intermediate times increases rapidly in magnitude around the same temperature, and the intermediate scattering function develops a clear two-step decay in the low-temperature liquid state. We therefore conclude that this model is a good glass-former. In contrast to the equimolar glass-former studied in Part I, this system has a more homogeneous structure and less diversity of local environments. It will therefore be interesting to compare the spatial distribution of dynamic heterogeneity in this system with that found for the structurally different glass-former in Part I.

Chapter 7

Nanocrystallinity and Phase Separation

In this chapter we present studies of two further soft-disc mixtures. The non-equimolar mixture with composition $x_1 = 0.3164$ *of the additive system, i.e. with* $\sigma_{12} = 1.2$*, and the equimolar mixture of the non-additive system with* $\sigma_{12} = 1.3$*. We find that the former undergoes phase separation into an apparently stable crystal-amorphous composite, while the latter undergoes liquid-liquid phase separation before freezing of first the large-particle and then the small-particle fractions.*

7.1 Introduction

As discussed in Section 4.2, amorphous alloys are of great technological interest because of their exceptional hardness, among other unusual properties. Pure metallic glasses, however, are also brittle, i.e. once they reach their elastic limit they fracture easily. To make them more suitable for a variety of applications, people have sought to improve their toughness by finding ways of forming crystalline domains that remain distributed within the amorphous matrix. Such nanocrystalline materials fall into the broader class of multiphase alloys [181,234] that include micro-segregated crystal-crystal composites such as the famous and beautiful Damascus steel swords [235,236].

The equimolar soft-disc mixture studied in Part I, with additive interparticle potential $\sigma_{12} = (\sigma_{11} + \sigma_{22})/2 = 1.2$, has previously been characterised as a good glass-former [44,67]. Here we study a non-equimolar mixture with composition $x_1 = 0.3164$ with the same set of interaction potentials, and find that, upon cooling, it undergoes partial phase separation into a stable crystal-amorphous composite. This system may therefore be a useful model with which to increase our understanding of nanocrystalline materials, including both the relationship between their microscopic and mechanical properties and how to stabilise them.

We also study the phase behaviour of the equimolar mixture with interparticle potential $\sigma_{12} = 1.3$, which being greater than additive, results in an effective repulsion between unlike particle species. Not surprisingly, we find that this mixture undergoes liquid-liquid phase separation before freezing of first the large particle fraction and then the small particle fraction. In terms of interparticle potential, this places the glass-forming alloy studied in Part I between the competing extremes of phase separation, on the one hand, and formation of a substitutionally ordered crystal, on the other. The latter, of course, refers to the H2 crystal characterised in Chapter 6.

The rest of this chapter is structured as follows. In Section 7.2 we characterise the changes in structure and dynamics during cooling of the non-equimolar additive mixture, and in Section 7.3 we present a brief study of the phase behaviour of the equimolar mixture with $\sigma_{12} = 1.3$. This is followed by a short discussion and summary of the main results.

7.2 Crystal-Amorphous Coexistence in the Non-Equimolar Mixture with $\sigma_{12} = 1.2$

7.2.1 Model and Computational Details

We consider a 2D system consisting of a binary mixture of particles interacting via purely repulsive potentials of the form

$$u_{ab}(r) = \epsilon \left[\frac{\sigma_{ab}}{r}\right]^{12} \tag{7.1}$$

where $\sigma_{12} = 1.2 \times \sigma_{11}$ and $\sigma_{22} = 1.4 \times \sigma_{11}$. All units quoted will be reduced so that $\sigma_{11} = \epsilon = m = 1.0$ where m is the mass of both types of particle. Specifically, the reduced unit of time $\tau = \sigma_1\sqrt{m/\epsilon}$. A total of $N = 1024$ particles were enclosed in a square box with periodic boundary conditions.

The molecular dynamics simulations were carried out at constant number of particles, pressure ($P = 13.5$) and temperature using the Nosé-Poincaré-Andersen (NPA) algorithm developed by Laird et al. [83,84]. The equations of motion were integrated using a generalised leapfrog algorithm [84], and are provided for 2D simulations in Appendix A along with further details of the NPA algorithm. The time step employed was 0.05τ for $T > 1$, and 0.01τ for $T \leq 1$. For argon units of $\eta = 120k_B$, $m = 6.6 \times 10^{-23}g$ and $\sigma_{11} = 3.4\mathring{A}$, these time steps correspond to approximately 10 and 20 femtoseconds respectively.

A non-equimolar mixture consisting of $N_1 = 324$ small particles and $N_2 = 700$ large particles (giving a composition of $x_1 = 0.3164$ to 4 d.p.) was studied at 16 different reduced temperatures from $T = 5$ to $T = 0.3$. The starting configuration of the run at $T = 5$ was an equilibrated configuration at $T = 5$ for the equimolar mixture described in Chapter 2 with the appropriate number of small particles changed to large particles. The starting configuration of each lower temperature equilibration run came from the final configuration of the preceding higher temperature run. At all temperatures the equilibration runs were taken out until steady state was achieved, i.e. until the average thermodynamic properties remained constant in time. The equilibration run times were longer than the times taken for all the dynamic correlation functions investigated to decay to zero for $T \geq 0.7$, and were at least an order of magnitude longer than the structural relaxation times for $T \geq 0.45$ / $T \geq 0.55$ for the small/large particles. Table C.18 (in Appendix C.5) lists the temperatures of each state studied as well as the equilibration and production times. The final configurations of the equilibration runs were used to start the production runs. The 'masses' of the Anderson piston and Nosé thermostat were $Q_v = 0.0001$ and $Q_s = 1000$, respectively, for all temperatures.

7.2.2 Thermodynamic Properties

The isobaric phase diagram is plotted in Figure 7.1. The density increases smoothly with cooling showing no sign of a first order phase transition, although there is perhaps a small change in slope between $T = 0.5$ and $T = 0.6$. The thermodynamic averages for the potential energy per particle (U), energy per particle (E), enthalpy per particle (H), and number density per particle (ρ) are listed for reference in Table C.18. An equation of state has previously been calculated for this system [67] using data obtained for the equimolar mixture. We have verified that this equation of state is consistent with the thermodynamic results obtained at the current composition.

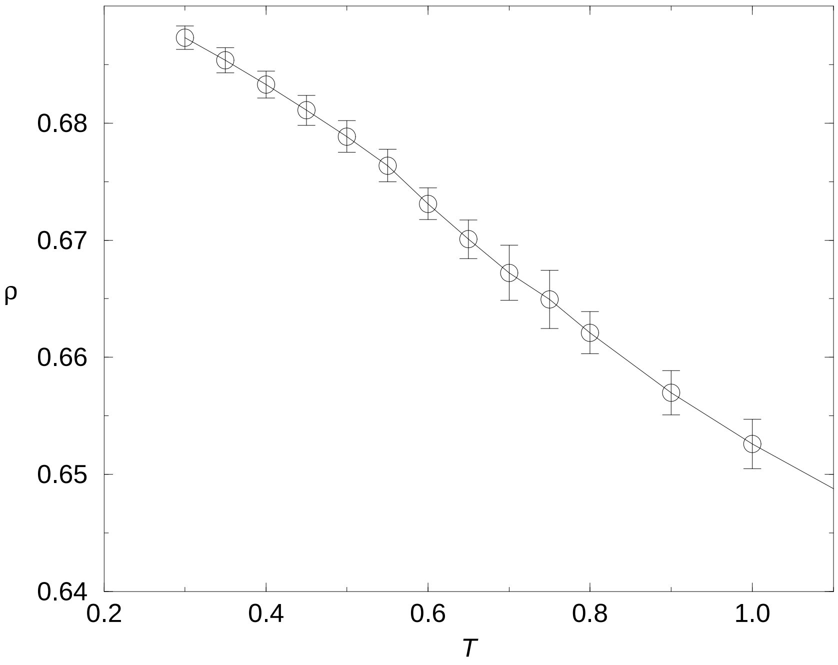

Figure 7.1: Isobaric ($P = 13.5$) phase diagram. Error bars represent one standard deviation. Note that the density increases smoothly with cooling.

7.2.3 Growth of Crystalline Domains During Cooling

Particle Configurations

Several changes in structure occur as the system is cooled (representative particle configurations are shown in Figure 7.2). The initially homogeneous liquid (a) appears to separate into regions of hexagonally packed large particles and an amorphous phase consisting of both small and large particles but the separation is incomplete and the two phases remain intermixed. By $T = 0.55$ crystalline domains of large particles have formed (b), but do not appear to grow (c) despite the apparent high mobility of the intermixed amorphous phase. At $T = 0.3$ (d), the entire structure is rigid and the phases remain intermixed.

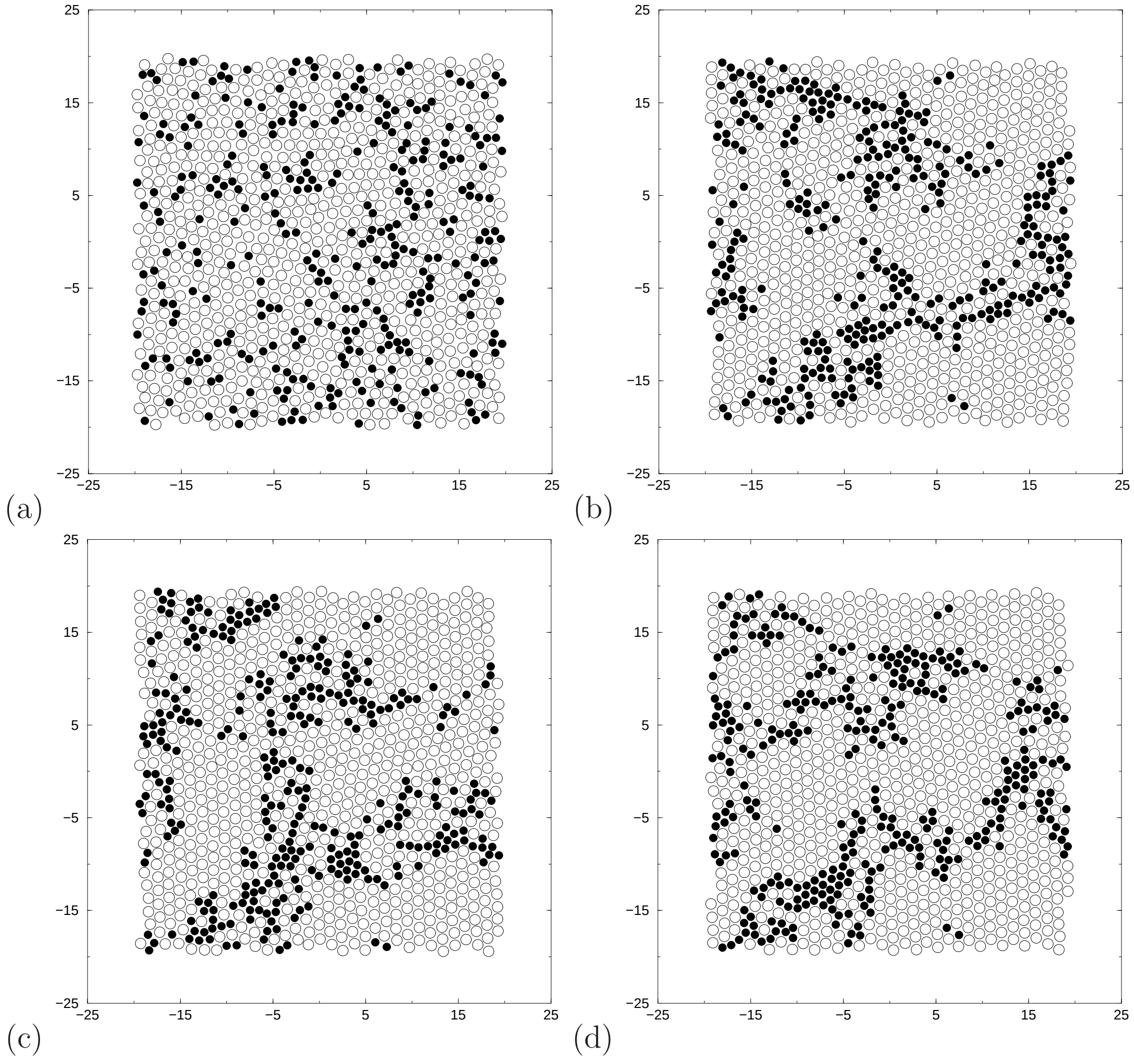

Figure 7.2: Representative particle configurations at (a) $T = 1$, (b) $T = 0.55$ after $50,000\tau$ equilibration, (c) $T = 0.55$ after $100,000\tau$ equilibration, and (d) $T = 0.3$. The small and large particles are represented by filled and open circles respectively.

Pair Distribution Functions

The pair distribution function (PDF) and the partial pair distribution functions (PPDFs) have been defined in Section 5.3.2. They are shown for the current system in Figures 7.3 and 7.4. Upon cooling, $g_{22}(r)$ develops structure over increasing lengthscales until by $T = 0.55$ there is still structure at $r = 10\sigma_{11}$, suggesting that there is some translational correlation between the large particle domains. There is no evidence of long-range translational order in the other PPDFs. The PDFs are also sensitive measures of local compositional correlations. For example, integrating

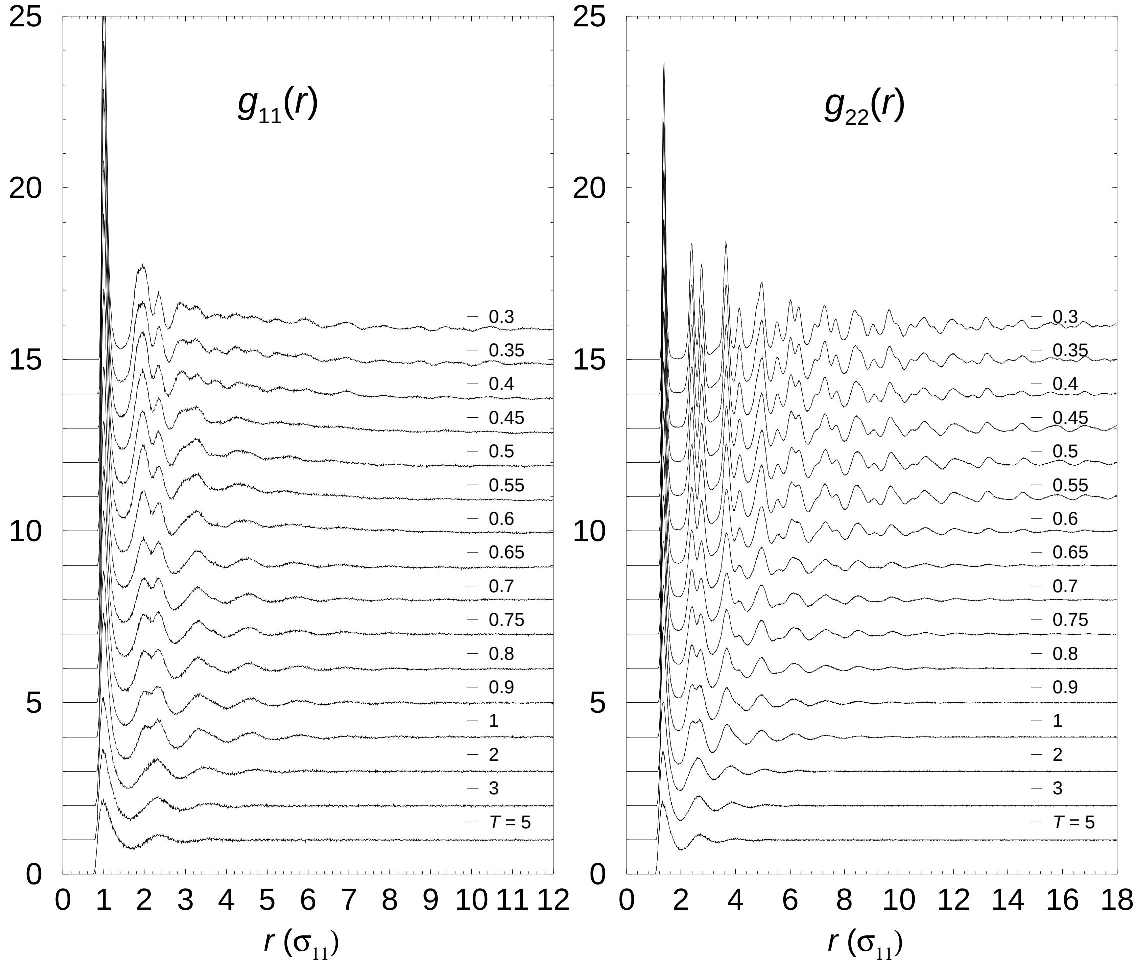

Figure 7.3: The partial pair distribution functions $g_{11}(r)$ and $g_{22}(r)$ as a function of distance from $T = 5$ down to $T = 0.3$. For $T \leq 3$, each curve has been shifted upwards by one unit from the higher temperature curve directly preceding it. Note the different x-axis scales.

under the first peak of the distribution functions out to the first minimum provides the partial coordination numbers, which are calculated in slightly different form in Section 7.6. We extract the positions of the first minima in the PPDFs (listed in Table C.19) to use as cutoff distances for defining nearest particle neighbours when calculating the local coordination environments and the various orientational order parameters.

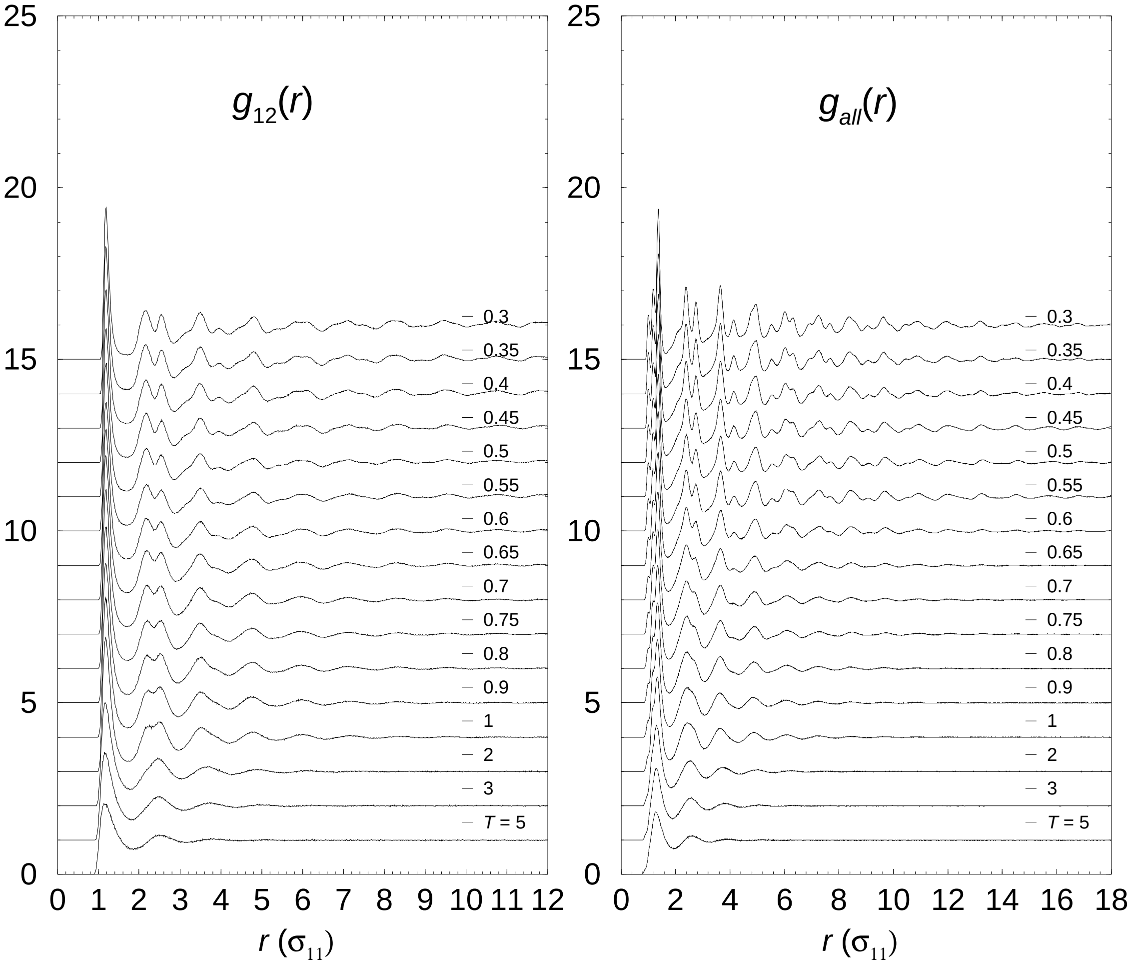

Figure 7.4: The partial pair distribution function $g_{12}(r)$ and the total pair distribution function $g_{all}(r)$ as a function of distance from $T = 5$ down to $T = 0.3$. For $T \leq 3$, each curve has been shifted upwards by one unit from the higher temperature curve directly preceding it.

Structure Factors

The partial structure factors were calculated from the PPDFs as explained in Section 5.3.2. They are plotted along with the total structure factor in Figures 7.5 and C.10. The oscillations at small k below the first maxima are artifacts of the Fourier transformation procedure (due to truncation of the PDFs at non-zero values) and should be ignored. For $S_{22}(k)$, the second peak is split into two components at all but the highest temperatures. The components of the bimodal second peak in $S_{22}(k)$ occur at wave vectors that coincide with the second and third peaks (at $k \approx 9.2\sigma_{11}^{-1}$ and $k \approx 10.5\sigma_{11}^{-1}$, respectively) in the static structure factor of a single component

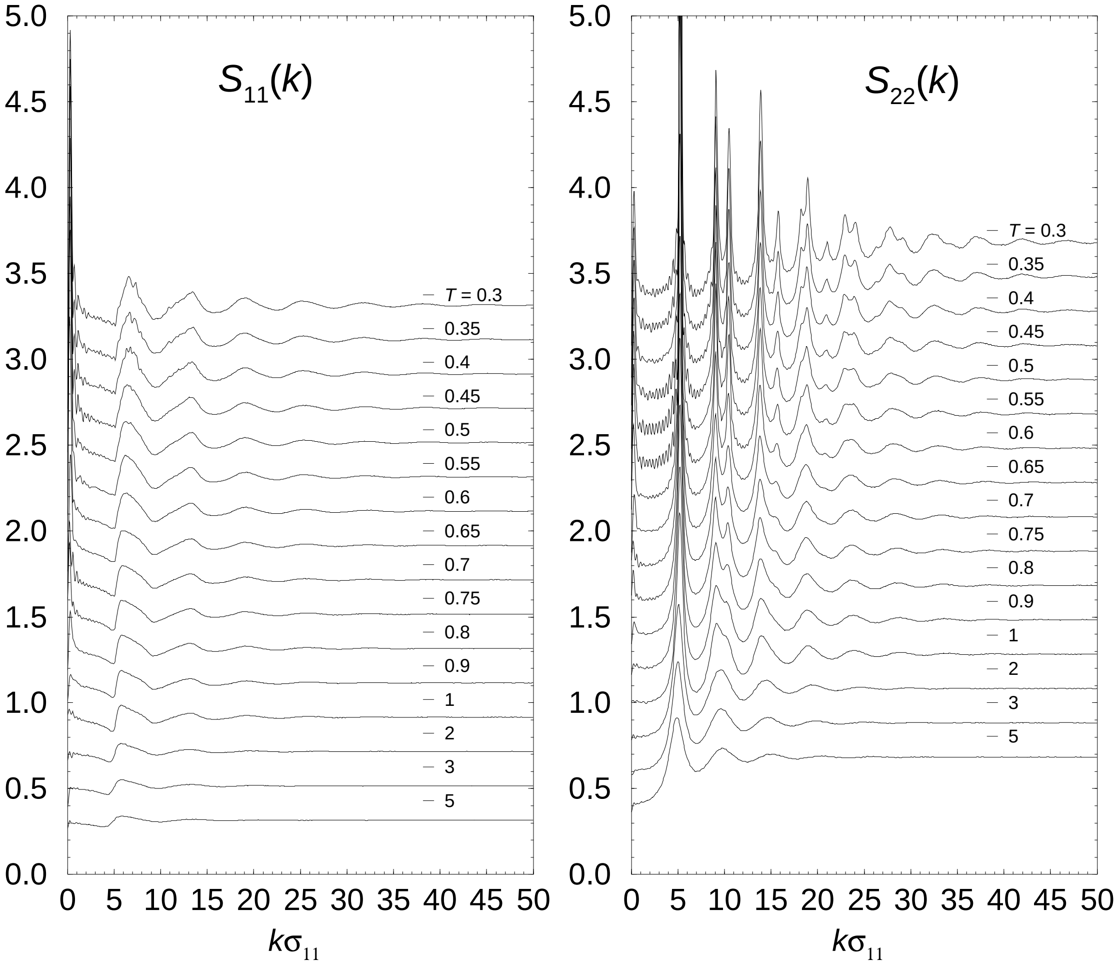

Figure 7.5: The partial structure factors $S_{11}(k)$ and $S_{22}(k)$ for temperatures from $T = 5$ down to $T = 0.3$. For clarity, each curve below $T = 5$ has been shifted upwards by 0.2 units above the higher temperature curve directly preceding it.

crystal of large particles. We conclude that this feature is due to the presence of crystalline domains of large particles at low temperatures.

Local Structure Parameters

Several quantities were used to characterise the local structure of the non-equimolar mixture. In Figure 7.6 we present the 'bond' fractions n_{ab}, defined as the fraction of all nearest neighbours particle pairs that occur between particles of type a and b (see Section 7.2.3 for the definition of nearest neighbours). Upon cooling below $T = 1$, n_{12} decreases continuously from 0.4 until a new plateau value of 0.3 is reached. In contrast, the fraction of nearest neighbour contacts between like particles, given by n_{11}

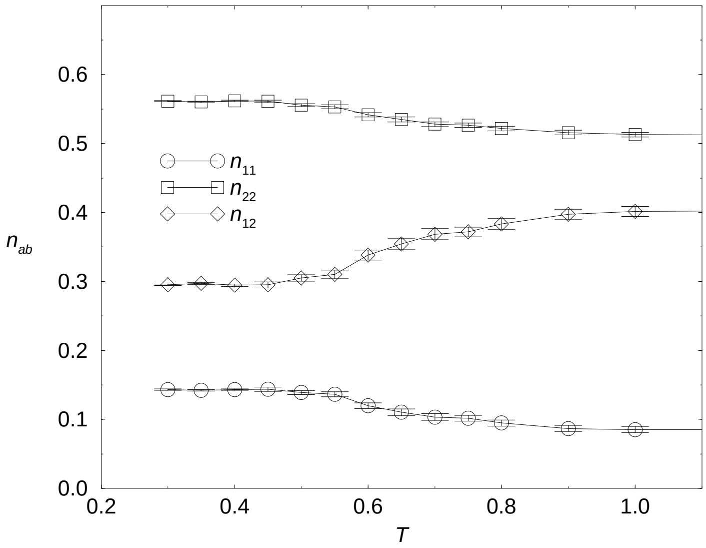

Figure 7.6: 'Bond' fractions as a function of temperature for $T \leq 1$. n_{ab} is the fraction of all nearest neighbours particle pairs that occur between particles of type a and b. Error bars represent one standard deviation.

and n_{22}, increases with cooling. This is a clear indication that the mixture undergoes phase separation as it is cooled. It does not, however, appear to be demixing into two single-component phases. n_{12} never decreases below a value of 0.3 and, although large fluctuations are observed in the instantaneous 'bond' fractions between $T =$ 0.55–0.4, we observe no systematic change during the extremely long production runs listed in Table C.18.

The distribution of local packing environments is plotted as a function of temperature in Figure 7.7. Only the most common environments are shown. From this data it is clear that the fraction of hexagonally packed large particles L06 increases dramatically below $T = 1$. At the same time the number of large particles with small particle neighbours decreases substantially (see L15, L24, L33 and L25). Both these results are consistent with the appearance of large particle domains at low temperature. The main change in the local environment around small particles is an increase in the number of small neighbours; S42 increases while S14 decreases. S60 also shows a small increase, but the fraction of small particles with six small neighbours remains quite small, i.e. the small particles do not substantially aggregate into a single-component phase.

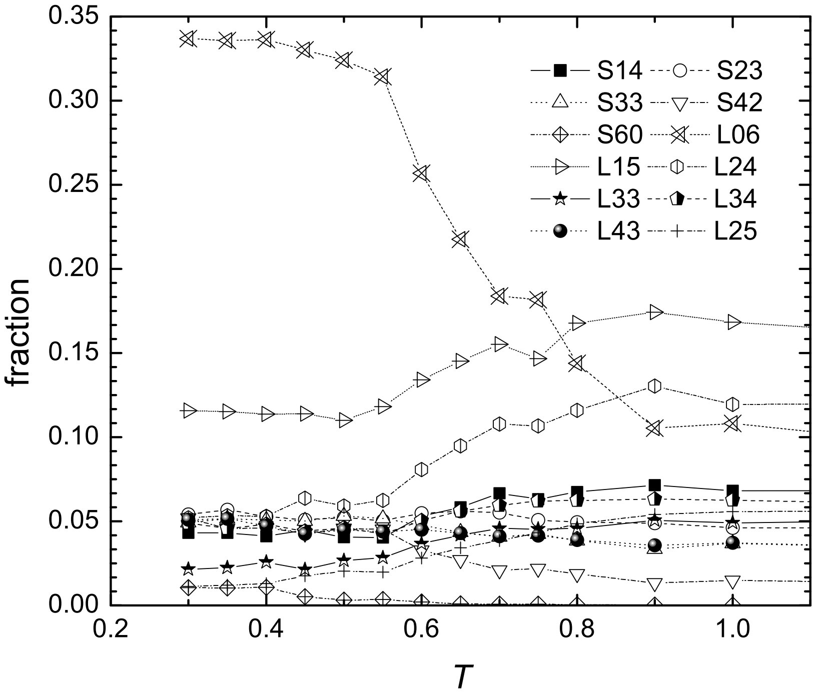

Figure 7.7: The distribution of local packing environments as a function of temperature. We have identified a particular neighbourhood with the following notation: A small particle with m small neighbours and n large neighbours is designated as Smn and the analogous large particle is indicated as Lmn.

Orientational Order Parameters

In order to quantify the orientational order throughout the system we have introduced the n-fold orientational order parameters (see Section 5.3.2 for their definitions). The bulk averaged n-fold order parameters Ψ_n, plotted in Figure 7.8, probe the local orientational order. The major change upon cooling is an increase in the hexagonal order about large particles $\Psi_{6,2}$, especially between $T = 0.65$ and $T = 0.55$. In contrast, $\Psi_{6,1}$ shows a smaller increase. What little 4-fold order was present at high temperatures decreases with cooling. The variation in 12-fold order can be explained by the presence of 6-fold order in the mixture.

We also tested for the presence of long-range orientational correlations between the local hexagonal domains. In Figure 7.9, we plot the partial 6-fold orientational correlation functions $G_{6,1}(r)$ and $G_{6,2}(r)$ over a range of temperatures. (These functions are defined in Section 5.3.2.) As the temperature is reduced, long-range orientational correlations develop between local hexagonal environments around large particles. This,

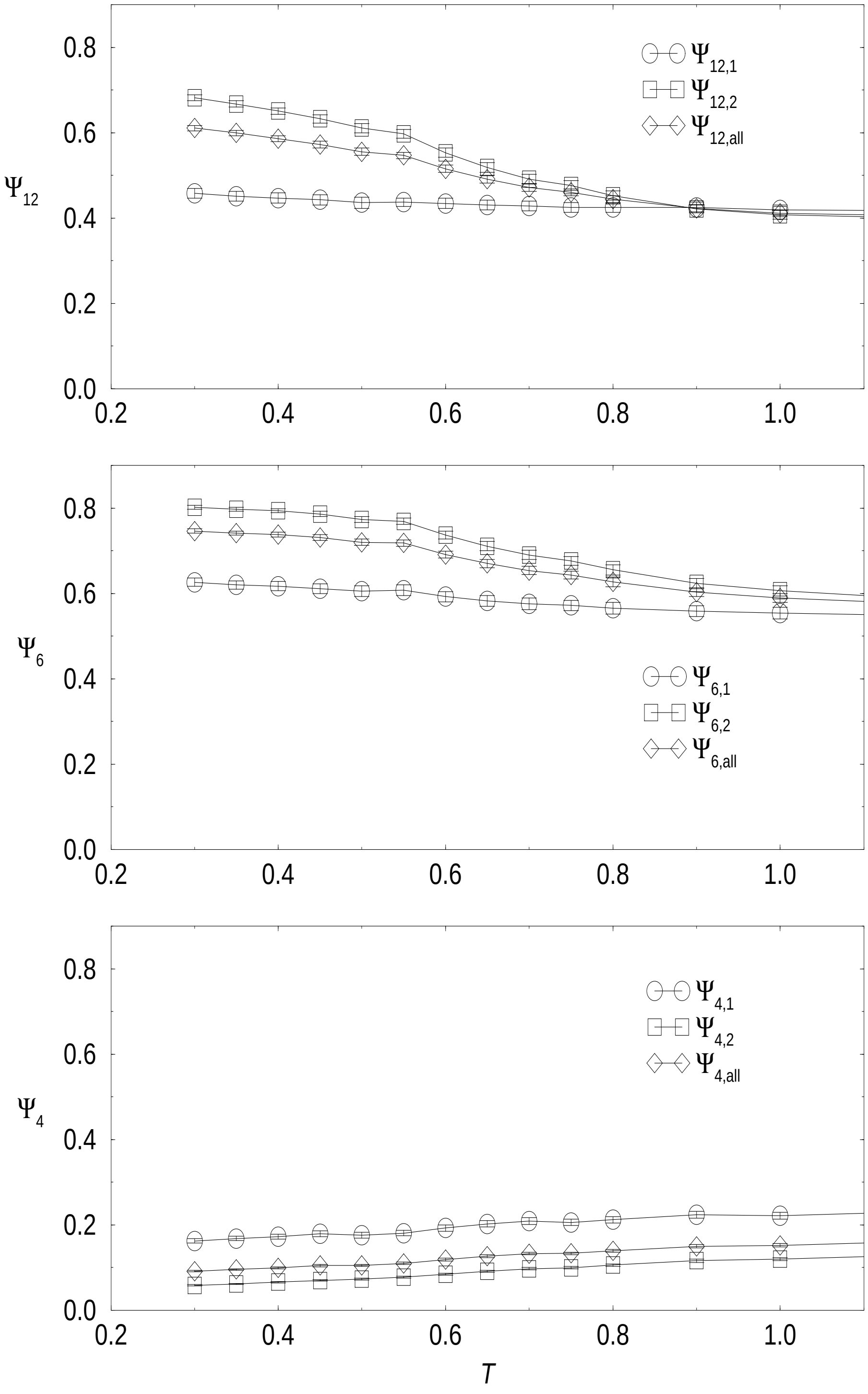

Figure 7.8: The temperature dependence of the bulk averaged n-fold order parameters Ψ_n, where $n = 4, 6, 12$, and their small ($\Psi_{n,1}$) and large ($\Psi_{n,2}$) particle contributions. The error bars represent one standard deviation about the average.

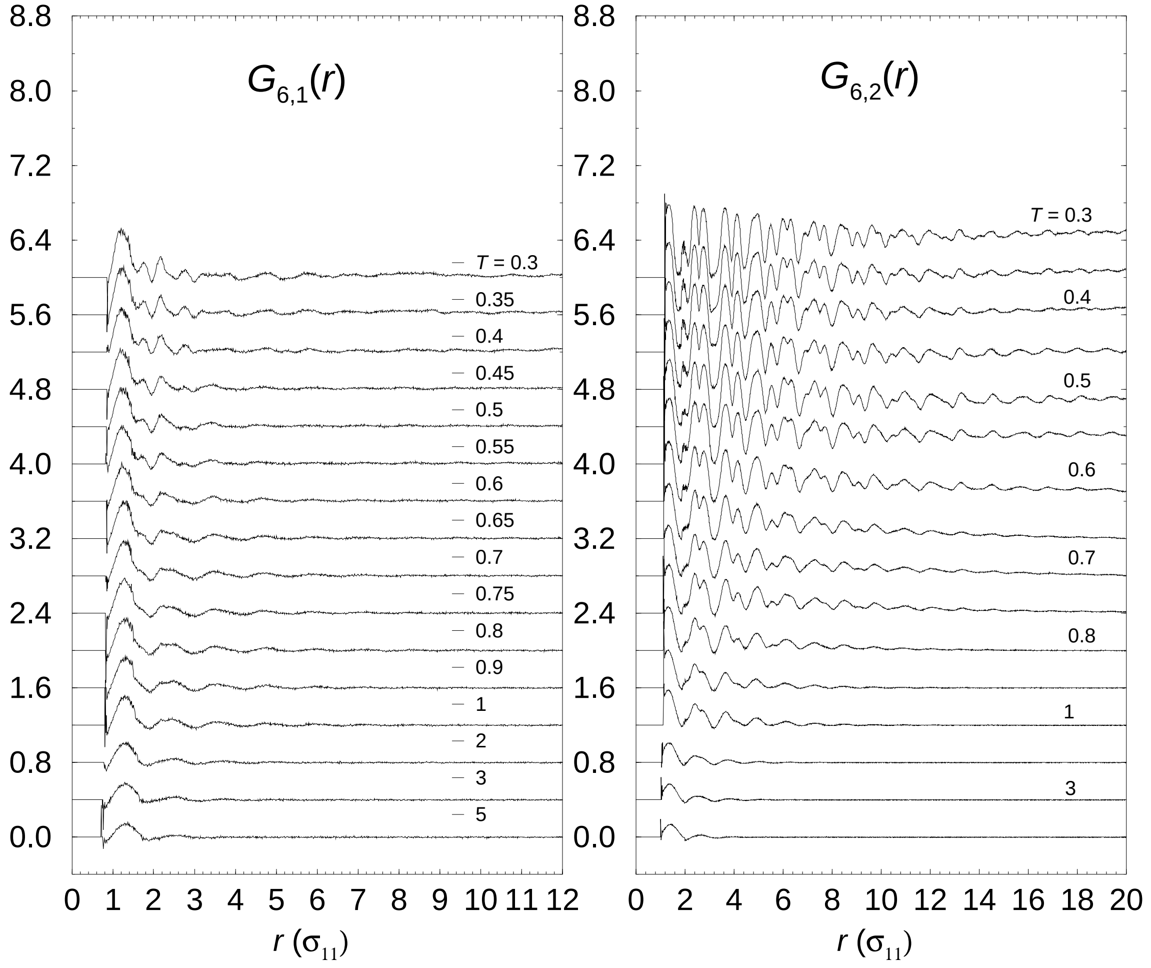

Figure 7.9: The partial 6-fold orientational correlation functions $G_{6,1}(r)$ and $G_{6,2}(r)$ for the small and large particles, respectively. For clarity, functions have been offset vertically by 0.4 units above the preceding curve. Note the different scales for the x-axes.

along with the local coordination analysis described above, provides clear evidence for the growth of extended crystalline clusters of large particles upon cooling. The presence of orientational correlation even at a distance of $r = 20\sigma_{11}$ (roughly half the system size) indicates that an extended crystalline domain of large particles spans the entire system for at least $T \leq 0.55$. In contrast, correlations between small-particle hexatic environments remain short-ranged over the entire temperature range studied. There is no orientational correlation between local 4-fold order in the system, and that the 12-fold orientational correlation functions mirror the trends observed in the 6-fold orientational correlation functions and therefore do not appear to contain any additional information. For this reason, we do not show these here.

7.2.4 Development of Heterogeneous Dynamics

We have already shown that the non-equimolar mixture undergoes partial phase separation into a crystalline large-particle phase and an amorphous two-component phase when it is cooled. In this section, we present an analysis of the changes in particle transport and structural relaxation that occur upon cooling.

Intermediate Scattering Functions and Arrhenius Plot

Log-linear plots of the self intermediate scattering functions are shown in Figure 7.10. $F_{s,1}(k,t)$ and $F_{s,2}(k,t)$ (defined in Section 5.3.3) have been measured at the positions of the first maxima in the static structure factors $S_{11}(k)$ and $S_{22}(k)$. The positions of these maxima are independent of temperature and are listed in the caption to Figure 7.10. The relaxation curves broaden with decreasing temperature until at $T = 0.5$ (for the large particles) and $T = 0.4$ (for the small particles) they are no longer able to decay to zero within the finite timescale of the simulations. The relaxation functions already span over five decades in time at these temperatures. At $T = 0.65$ (for the large particles) and $T = 0.55$ (for the small particles) a step appears in the relaxation curves at intermediate times. This step broadens into a plateau with an amplitude that increases with decreasing temperature. The height of the plateau also increases with decreasing temperature. Such two-step relaxation functions have been observed in a wide range of glass-forming systems as discussed in Section 1.2. Note that $F_{s,1}(k,t)$ decays substantially faster than $F_{s,2}(k,t)$.

Structural relaxation times $\tau_{e,1}$ and $\tau_{e,2}$ are defined as the time taken for the incoherent scattering functions $F_{s,1}(k,t)$ and $F_{s,2}(k,t)$, respectively, to decay to $1/e$ of their initial values. The temperature dependences of these relaxation times (shown in Figure 7.11) appear to be Arrhenius at high temperatures, but diverge strongly from Arrhenius dependence as the temperature drops below $T = 0.7$ and $T = 0.6$ for the large and small particles, respectively. The onset of non-Arrhenius temperature scaling occurs at the same temperature at which the step first appears in the relaxation curves. Diffusion constants were measured in the region where the mean-squared displacements (MSDs) have reached their long-time constant value (${R_a}^2(t) > \sigma_{11}^2$). They show a weaker deviation from Arrhenius temperature dependence than the structural relaxation times, with the onset of this deviation occurring around the same temperature. $D_1/D_2 \approx 1$ above $T = 1$, but increases steadily upon cooling below $T = 0.7$, i.e. the large particles move increasingly slow relative to the small

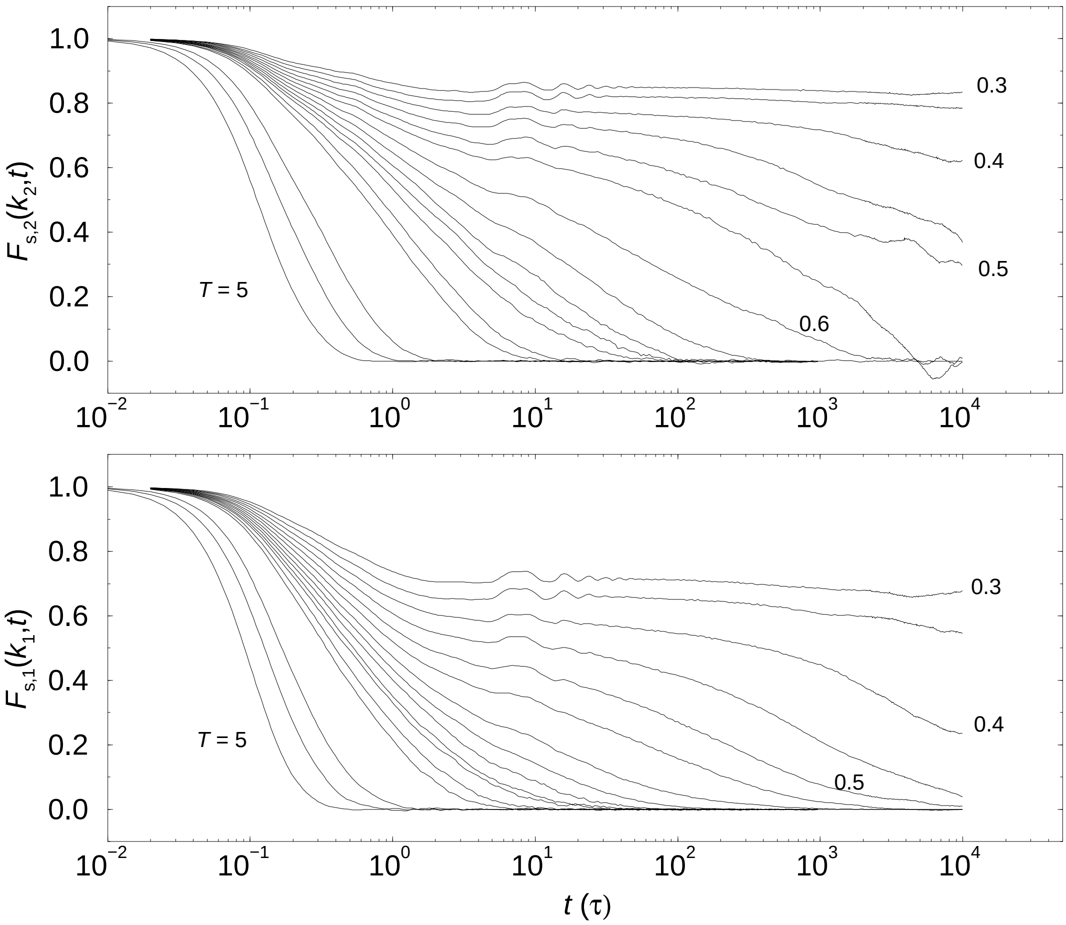

Figure 7.10: The incoherent scattering functions $F_{s,1}(k_1,t)$ and $F_{s,2}(k_2,t)$ for the small and large particles, respectively. The wave vectors $k_1 = 6.32\sigma_{11}^{-1}$ and $k_2 = 5.44\sigma_{11}^{-1}$ are the first peak positions in the respective partial structure factors. From left to right the temperatures of the curves are $T = 5$, 3, 2, 1, 0.9, 0.8, 0.75, 0.7, 0.65, 0.6, 0.55, 0.5, 0.45, 0.4, 0.35 and 0.3. Note the appearance of a two-step relaxation process in the intermediate scattering functions.

particles. For reference, the MSDs over all particles $R^2(t)$, and averaged over the two particle species ${R_2}^2(t)$ and ${R_1}^2(t)$, are plotted in Figure C.11 and the structural relaxation times and diffusion constants are listed in Table C.20. It is interesting to note that both the diffusion constants and relaxation times show behaviour that is typical of glass-forming systems despite the appearance of crystalline domains of large particles and a significant amount of phase separation in the system.

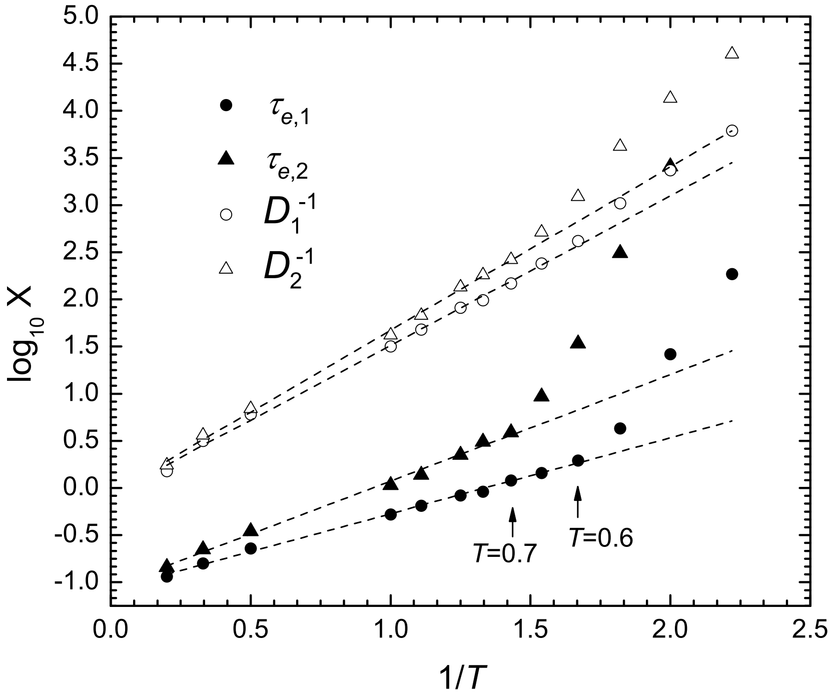

Figure 7.11: Arrhenius plot of the structural relaxation times $\tau_{e,1}$ and $\tau_{e,2}$ and the inverse diffusion constants D_1^{-1} and D_2^{-1}. The dashed lines are linear regressions through the data for $T \geq 0.7$. Note the divergence from Arrhenius behaviour at low temperatures.

Non-Gaussian Parameter

As explained in Section 5.3.3, the non-Gaussian parameters $A_a(t)$ can be used as a measure of the degree of dynamic heterogeneity in a sample. Large values at intermediate times can be attributed to a broad distribution of local mobilities. The non-Gaussian parameters for the present system are plotted in Figure 7.12. A rapid rise in non-Gaussian behaviour is observed at low temperature for both the large and small particle species. The maximum value of $A_2(t)$ increases rapidly below $T = 0.65$, while the maxima in $A_1(t)$ show a similar but smaller increase below $T = 0.55$. The trend is for the maxima to move to longer times as they increase in height; at the lowest temperatures the finite observation time of the simulations is too short to observe the maxima.

$A_2(t)$ and $A_1(t)$ are no longer able to decay to zero by $T = 0.65$ and $T = 0.45$, respectively. This suggests that the system falls out of equilibrium somewhere near $T = 0.65$. However, the average small and large particle is still able to travel $10\sigma_{11}$ within this observation time, indicating that much of the system is still highly mobile.

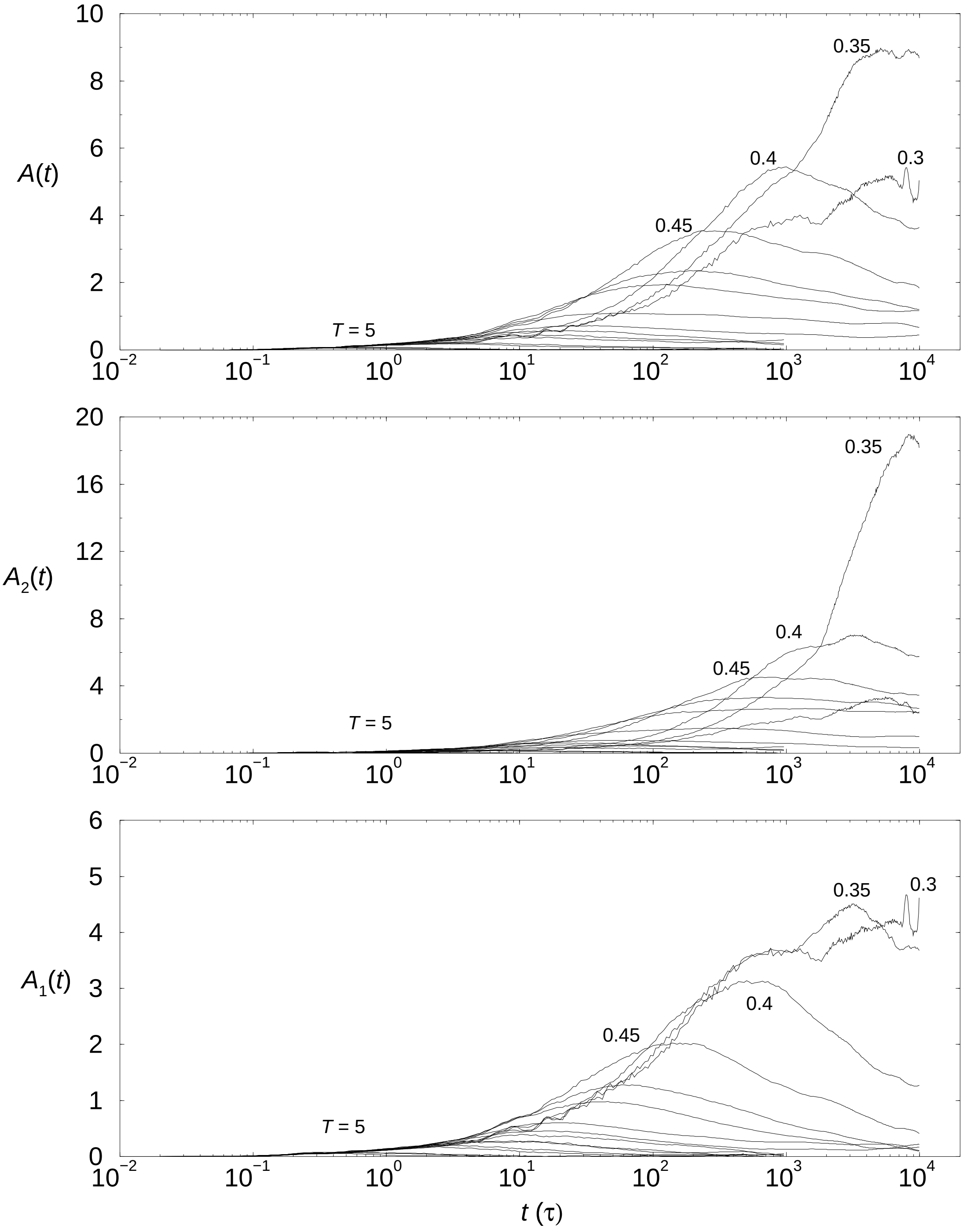

Figure 7.12: The non-Gaussian parameter averaged over all particles, $A(t)$, and averaged over small and large particles, $A_1(t)$ and $A_2(t)$, respectively. The temperatures of the curves are as listed in Figure 7.10. Observe the different y-axis scales and the rapid increase in the peak heights with decreasing temperature.

There must therefore be a broad distribution of mobilities among the large particles. We conclude that this is due to the distribution of large particles between crystalline and amorphous domains. While the average mobility of the large particles is still high at $T = 0.65$, some large particles must have low mobility (presumably those in the crystalline domains) and some must have very high mobility (presumably those in the amorphous domains). At $T = 0.45$ the average MSD for a large particle during equilibration is still greater than σ_{11}, yet the system no longer appears to be segregating (see Figure 7.6). This suggests that the crystal-amorphous composite structure is stable to further phase separation.

The dynamic properties clearly show that the equilibration run times were sufficiently long for the non-Gaussian parameters to decay to 0.2 or less for $T \geq 0.7$, and at least an order of magnitude longer than the structural relaxation times for $T \geq 0.55$. We therefore conclude that the non-equimolar mixture is very stable to complete phase separation, despite the presence of crystalline domains of large particles that span the simulation cell. Below $T = 0.7$ the non-equimolar mixture displays dynamic properties typical of supercooled liquids including: non-Gaussian dynamics; the appearance of a plateau in the MSD and scattering functions at intermediate times; and strong non-Arrhenius temperature dependence of the structural relaxation times, and to a lesser extent of the diffusion constants. We conclude that this behaviour is due to glass-formation in the substantial amorphous fraction of the system. The stronger non-Gaussian dynamics of the large particles is likely due to their distribution between the less mobile crystalline domains and the more mobile amorphous regions. We discuss this system further in Section 7.4.

7.3 Phase Separation in the Equimolar Mixture with $\sigma_{12} = 1.3$

Only a minimal set of cooling runs were studied for this system in order to identify the nature of the liquid to solid phase transition. Upon cooling, the liquid segregates into small and large particle fractions before freezing, initially of the large particle phase, and then of the small particle phase at a lower temperature. The freezing temperatures of both phases are substantially reduced relative to the freezing temperatures of the respective single component systems.

7.3.1 Model and Computational Details

We consider a 2D system consisting of a binary mixture of particles interacting via purely repulsive potentials of the form

$$u_{ab}(r) = \epsilon \left[\frac{\sigma_{ab}}{r}\right]^{12} \tag{7.2}$$

where $\sigma_{12} = 1.3 \times \sigma_{11}$ and $\sigma_{22} = 1.4 \times \sigma_{11}$. All units quoted have been reduced so that $\sigma_{11} = \epsilon = m = 1.0$ where m is the mass of both types of particle. Specifically, the reduced unit of time $\tau = \sigma_1 \sqrt{m/\epsilon}$. An equimolar mixture of $N = 1440$ particles were enclosed in a square box with periodic boundary conditions. The molecular dynamics simulations were carried out at constant number of particles, pressure ($P = 13.5$) and temperature using the Nosé-Poincaré-Andersen (NPA) algorithm as described in Appendix A. The 'masses' of the Anderson piston and Nosé thermostat were set to $Q_v = 0.0002$ and $Q_s = 1000$, respectively, at all temperatures.

The system was studied at 12 reduced temperatures: $T = 5$, 3, 2.5, 2, 1.8, 1.6, 1.4, 1.2, 1, 0.8, 0.6, and 0.4. The initial configuration at $T = 5$ was an equilibrated configuration at $T = 5$ for the equimolar system described in Chapter 6, i.e. with $\sigma_{12} = 1.1$. The starting configuration for each lower temperature run was the final configuration of the equilibration run at the preceding higher temperature. The length of the equilibration runs was 1000τ for $T \geq 2$ and 2000τ for $T \leq 1$. At all temperatures the equilibration runs were taken out until steady state was achieved, i.e. until the average thermodynamic properties remained constant in time. Except for at $T = 1.8$, this took less than one quarter of the total equilibration runtime. Densities were calculated using the latter part of the equilibration runs, i.e. after steady state had been achieved. No additional production runs were studied.

7.3.2 Changes in Configuration and Density

Representative configurations are plotted in Figure 7.13. At $T = 3$ [plot (a)] the liquid is more or less homogeneous, although small one-component domains are already present. By $T = 2$ [plot (b)] it is obvious that the liquid has begun to separate into separate small- and large-particle phases. The degree of phase separation gradually increases as the temperature is reduced until at $T = 1.2$ [plot (d)] the two phases are almost completely demixed. At this point the large-particle phase crystallises into a hexagonal lattice with some small particles imbedded, i.e. a substitutionally

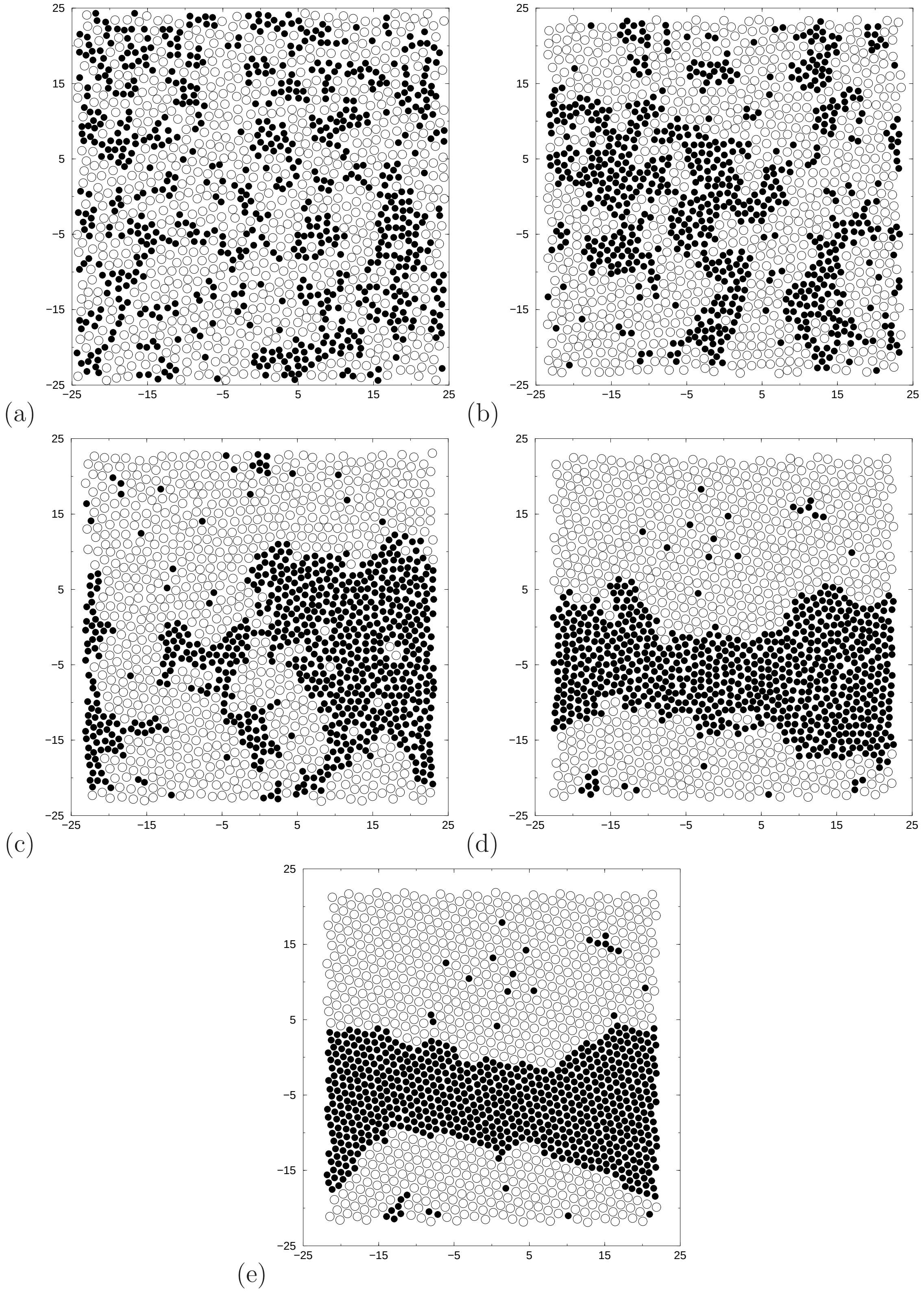

Figure 7.13: Representative particle configurations at (a) $T = 3$, (b) $T = 2$, (c) $T = 1.6$, (d) $T = 1.2$, and (e) $T = 0.4$. The small and large particles are represented by filled and open circles respectively.

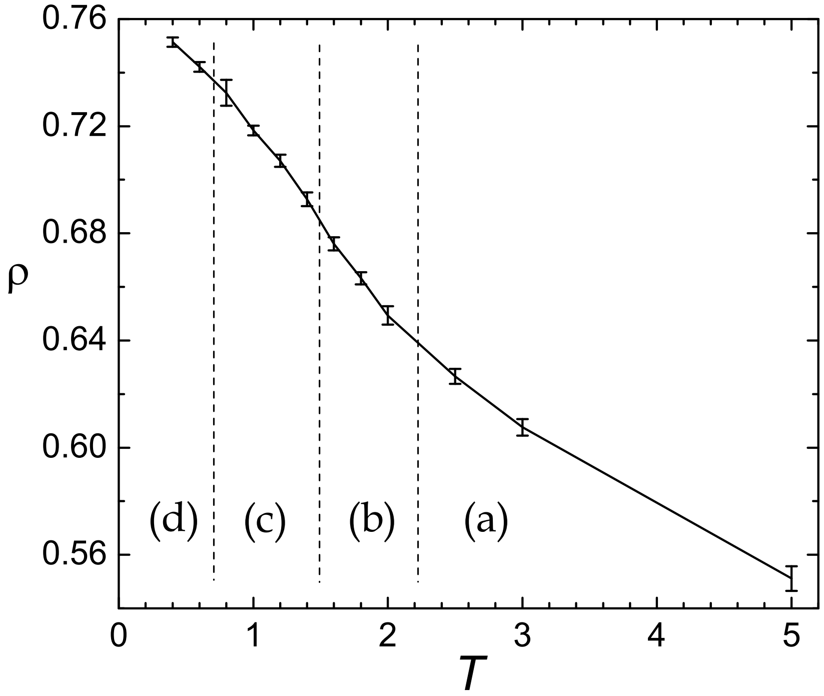

Figure 7.14: Isobaric ($P = 13.5$) phase diagram. The dashed vertical lines indicate approximate temperature ranges for the different structural regimes: (a) homogeneous liquid, (b) inhomogeneous liquid, (c) crystal-liquid coexistence, and (d) crystal-crystal coexistence. Errors bars represent one standard deviation.

disordered single-component crystal. The small particle phase remains fluid until $T = 0.4$ at which point it also freezes into a hexagonal lattice. Thus the liquid appears to demix before crystallisation, first of the large particle phase and then, at a lower temperature, of the small particle phase.

The different structural regimes are roughly indicated on the phase diagram shown in Figure 7.14. Within the different regions, the density variation can be well approximated by linear fits with different slopes. It is interesting to see that the freezing temperatures of the large- and small-particle liquid phases in this system ($T_{f,2} \approx 1.3$ and $T_{f,1} \approx 0.5$) are substantially reduced relative to the freezing temperatures obtained for the respectively one-component systems ($T_{f,2} = 1.7$ and $T_{f,1} = 0.95$) [67, 85, 171]. Some longer runs in the inhomogeneous liquid region would be useful in order to check whether further phase separation occurs given sufficient time for larger-scale compositional fluctuations to take place. This may affect $T_{f,2}$, but seems unlikely to affect $T_{f,1}$.

7.4 Discussion and Conclusions

The non-equimolar mixture undergoes partial phase separation into a crystalline large-particle phase and an amorphous two-component phase when it is cooled. The dynamic properties clearly show that the equilibration run times are sufficiently long for the non-Gaussian parameters to decay less than 0.2 above $T = 0.65$, and are at least an order of magnitude longer than the structural relaxation times above $T = 0.5$. We therefore conclude that the non-equimolar mixture is very stable to complete phase separation, despite the presence of crystalline domains of large particles that span the simulation cell. Below $T = 0.7$ the non-equimolar mixture displays dynamic properties typical of supercooled liquids, including non-Gaussian dynamics, non-Arrhenius temperature dependence of the diffusion constants and structural relaxation times, and the appearance of a plateau in the mean squared displacement and incoherent scattering functions at intermediate times. We conclude that this behaviour is due to glass-formation in the substantial amorphous fraction in the system. The stronger non-Gaussian dynamics of the large particles is likely due to their distribution between less mobile crystalline domains and more mobile amorphous regions.

One possible reason for the stability of the non-equimolar mixture to phase separation is that the use of a square simulation cell artificially stabilises the mixed structure with respect to the phase separated structure. The amorphous phase may act as filler between the crystalline domains which have the wrong dimensions to join up across the periodic boundaries. If the phase separated system does not pack efficiently into a square cell with periodic boundary conditions then it may not form despite being the thermodynamically more stable structure. The possibility of this occurring will be increased if the free energy difference between the mixed and separated structures is very small. One way to test this hypothesis would be to use a simulation cell with independent variation of the x and y dimensions to allow for a better fit of the cell dimensions to the preferred dimensions of the phase separated system. This artifical stabilisation of the mixed phase should also be system size dependent, becoming weaker with increasing size. In any case, the absence of greater phase separation in the non-equimolar mixture suggests that the free energy difference between the mixed and separated structures is not great. It may therefore still be a useful model in which to study the formation and properties of nanocrystalline materials.

We note that the mixture with $x_1 = 0.75$ has previously been investigated [237].

Despite the presence of large crystalline domains of small particles, the large particle fraction does not appear to cluster substantially and remains in the form of extended chain-like structures that separate crystalline domains of small particles. Thus structurally, this mixture appears similar to the mixture studied in this chapter with $x_1 = 0.3164$, except that the role of large and small particles is reversed.

Upon cooling, the equimolar mixture with $\sigma_{12} = 1.3$ separates almost completely into two single-component liquid phases. In terms of interparticle potential, this places the glass-forming alloy studied in Part I between the competing extremes of phase separation, on the one hand, and formation of a substitutionally ordered crystal, on the other. The latter, of course, refers to the H2 crystal characterised in Chapter 6. The large particle fraction in the phase separated system freezes around $T = 1.3$, but the small particle fraction remains fluid until about $T = 0.5$. Therefore the freezing temperatures of both phases are substantially reduced relative to their one-component systems ($T_{f,2} = 1.7$ and $T_{f,1} = 0.95$) [67, 85, 171].

Chapter 8

Final Discussion

In this thesis we have sought to provide a clearer picture of the relationship between structure and dynamics in supercooled liquids and glasses. We have developed new methods for investigating this relationship at a microscopic spatial level, and have applied these to the study of a two-dimensional glass-forming alloy. We have also characterised the phase behaviour, and structural and dynamic properties, of several related model alloys, thereby laying the foundations for a rich extension of the former work. Our results fimly portray the glass transition as a continuous transition from structure-independent dynamics to structure-dependent dynamics.

In Part I, we investigated the role of structure in the development of spatially heterogeneous dynamics in a supercooled random alloy. Specifically, a binary soft-disc mixture with additive interparticle potential was studied. New tools were conceived - the isoconfigurational ensemble, dynamic propensity, the single particle non-Gaussian function, and the single-particle Debye-Waller factor - and used to obtain the clearest picture yet of the relationship between structure and dynamics in a glass-forming liquid.

By considering the set of N-particle trajectories through a configuration, i.e. an isoconfigurational ensemble, we were able to study the effect of structure on dynamics at a microscopic level without the additional noise of momenta fluctuations. We found that over the isoconfigurational ensemble, some particles are on average more mobile than others, i.e. some particles have a higher susceptibility to motion than others. We studied this susceptibility on both the structural relaxation time - using the dynamic propensity, and on the timescale of the secondary β-relaxation - using the single particle Debye-Waller factor (DW factor).

As the random alloy is supercooled, structural variations become increasingly important for dynamics and ultimately cause relaxation times to vary by orders of magnitude from one region of the supercooled liquid to another. This was evidenced by the rapid increase in the variance and range of the propensity distribution upon supercooling, and the increasing clustering of particles with similar mobility. It also strongly suggests that the various properties of supercooled liquids that have been attributed to the appearance of spatially heterogeneous dynamics - such as the breakdown of scaling between translational and rotational diffusion, the appearance of non-Fickian transport, and the dependence of T_g on film thickness in polymer films - depend upon fluctuations in the structure of the liquid. If this is true, it places increased importance on understanding the structure of supercooled liquids and glasses, and in particular the spatial variation in structure, not just for understanding the stability of glass-formers to crystallisation, but also for understanding their macroscopic properties.

Upon supercooling, the variability of the individual particle motion also increases rapidly. Even the most susceptible regions become capable of 'sticking' in a given run, and when they do 'slip' the mobile particles move far from their initial positions. The individual particle displacements become increasingly non-Gaussian and the system dynamics becomes increasingly intermittent in character. This suggests a hierarchy of structural domains, from marginally jammed to overconstrained.

In Chapter 3 we demonstrated that the spatial heterogeneity of the single particle DW factor - a dynamic measure of structural 'looseness' - was able to predict the coarse-grained spatial variation in dynamic propensity. This provides a link - via the initial configuration - between dynamics occurring before and during the α-relaxation over timescales separated by two orders of magnitude. Given the subtlety of the collective mechanical constraints probed by the short-time dynamics, the DW factor should provide an upper bound on what one can hope to predict from any measure of the initial configuration.

While the present work has not looked at the effect of structure on dynamics below T_g, the results just described suggest that previous observations of spatial heterogeneity in vibrational motion below T_g are also likely to be due to spatial variations in structure. This therefore suggests a continuous relationship between spatial variations in structure and dynamics extending from below T_g up to the normal liquid regime.

We also found that the spatial distribution of DW factors changes substantially on the timescale of the β process. This implies that the susceptibility of the 'loosest' particles changes rapidly. It also makes the spatial correlation between the DW factor and the propensity all the more surprising. The answer is that although parts of the initial configuration change susceptibility very rapidly, other parts relax much slower and still influence the dynamics on much longer timescales. Thus, although the DW distribution changes rapidly the hot spots for short-time motion are mostly confined to the larger high propensity region(s) over much longer timescales. This appears to be supported by a comparison of the time series of DW maps with the propensity distribution for the configuration used as a starting point of the time series (in Chapter 3).

The local free volume, local potential energy and local coordination environment all fail to predict the spatial variation in dynamic propensity or the DW factor, even upon coarse-graining of the free volume and potential energy. This indicates that simple isotropic measures of structure are unable to capture the microscopic details of how structure affects dynamics. It appears that some more complicated - perhaps anisotropic - aspect of the particle packing is responsible for determining the dynamic susceptibility of different domains. The best defined regions - in terms of their effect on mobility - are the clusters of L06 environments which almost universally have low propensity and DW factors. We conclude that the heterogeneous effect of structure on dynamics, as characterised by the spatial variation in propensity, is due to a combination of overconstrained regions which consist mainly of distinct structural entities (large particle crystallites), and marginally constrained regions which have less well-defined structures. The latter are sufficiently constrained to prevent motion but are easily made mobile with an appropriate momenta fluctuation.

These results have a number of implications for various conceptual pictures of supercooled liquid dynamics. The failure of geometric free volume to predict the spatial variation in both the propensity and the DW factor, even after coarse-graining, casts doubt on the microscopic basis of theories of the glass transition based purely on free volume, and highlights the importance of testing whether correlations between macroscopic quantities persist at a microscopic level. The rapid changes that occur in the spatial distribution of the DW factor also demonstrate that a simple picture of defect diffusion is unable to account for the effect of structure on dynamics in this glass-former. Whatever property of the structure that causes one region of the sample to be more mobile than another is able to be transferred from one region to another with little movement of the intervening particles. Finally, we note that the spatial distribution of propensity is essentially the starting point for several models of glass relaxation such as the facilitated spin models and the cooperative lattice gas models. The failure of simple structural measures to predict the spatial distribution of propensity bears a mixed message for programs in which atomic models of glass-formers are mapped onto spin models through an appropriate spatial coarse-graining of the former. Our results suggest that finding this appropriate spatial averaging to capture the subtle nonlocal character of particle constraints is a highly nontrivial task. On the other hand, our results certainly support the proposition that the initial pattern of local facilitation, as measured be the short-time dynamics, governs much of the subsequent heterogeneous dynamics.

In Part II, we investigated the effect of varying the interparticle potential on the phase behaviour of this glass-former. The structural and dynamic properties of six new systems were characterised, thus substantially adding to previous knowledge of crystallisation and glass-formation in binary soft-disc mixtures. The results provide a sense of the generality of the picture described above, and have laid the foundations for a rich extension of the former work.

When the interparticle potential σ_{12} is made greater than additive, there is an effective repulsion between unlike particle species and phase separation occurs upon cooling. On the other hand, when σ_{12} is decreased from additive there is an effective attraction between unlike particle species and the asymmetric H2 and symmetric S1 substitutionally ordered crystals are stabilised at equimolar composition. Interestingly, at non-equimolar compositions amorphous solids are formed on cooling. Together with the mixture studied in Part I, these form a complete structural range of alloy glasses, from random alloy to chemically ordered. As the degree of chemical ordering increases, the number of dominant local environments decreases, the structure becomes more homogeneous, and the medium-range order becomes more defined. Thus, we find that small changes to the interparticle potential stabilise amorphous solids with substantially different structures. The structures of the glass-formers also differ with respect to the amount of crystalline order that they have. The random alloy has substantial regions of large particle crystallites (the X_L phase), while the glass-former with $\sigma_{12} = 1.1$ shows very little sign of X_L or H2 crystalline environments. The glass-former with $\sigma_{12} = 1.0$, studied in Chapter 5, is also intriguing,

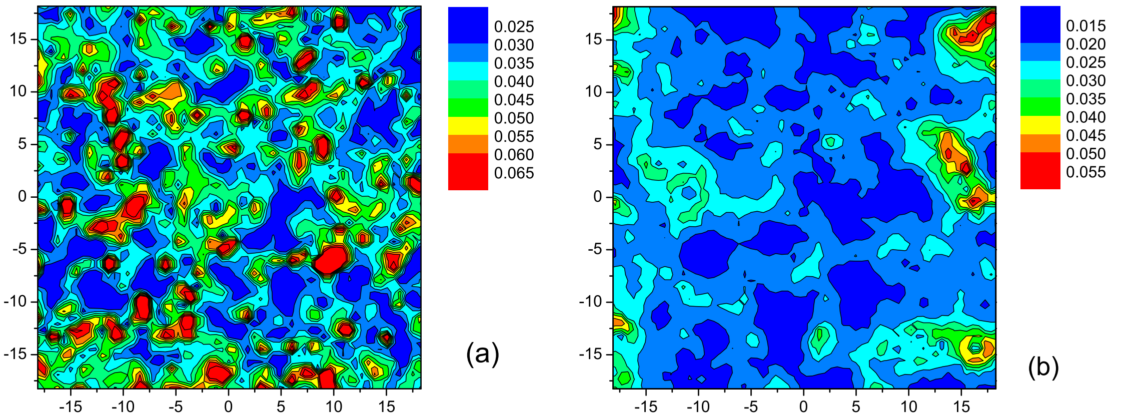

Figure 8.1: Contour plots of the spatial distribution of particle Debye-Waller factors for configurations at $T = 0.4$ for the system with (a) $\sigma_{12} = 1.1$, $x_1 = 0.3167$ and (b) $\sigma_{12} = 1.2$, $x_1 = 0.5$. The DW factors were calculated using 100 runs of 10τ duration each. Note the substantial difference in the spatial distribution of mobility. Different colour scales were used to enhance this difference.

because it appears to be as close to an ideal glass as one could hope to get. It is a particulate model, in which glass-formation arises naturally, without the need for ad-hoc model building; its low-temperature structure can be concisely described as a random tiling with defects, with most particles finding themselves in just five distinct environments; and videos of its low-temperature dynamics suggest that it is dominated by defect motion. (So perhaps defect diffusion models are appropriate for some glasses, namely those with strong chemical ordering.) The potentially soluble nature of the 1.0 glass-former also raises an interesting question: given a complete theoretical model of the glass transition, what next?

As we have already described, the presence of large particle crystallites in the random alloy glass-former has a significant impact on its dynamic properties. It should therefore be insightful to repeat the isoconfigurational analysis for these new glass-formers and compare the results to those obtained for the random alloy. As an example, in Figure 8.1 we compare the spatial distribution of structural 'looseness' for the non-additive system with $\sigma_{12} = 1.1$, and for the additive glass-former studied in Part I. Both plots are for configurations at $T = 0.4$, at which temperature the structural relaxation times for the two systems are similar. Note that the non-additive glass-former, which has the more homogeneous structure, also has a more homogeneous distribution of mobility, in the sense that particles with similar mobility are less clustered. The range between high and low mobility is roughly the same for both systems.

The results just described raise a number of questions. Does the effect of structure on particle motion vary significantly between different glass-formers, as the plots in Figure 8.1 suggest? To what extent does the type and quantity of higher-symmetry local and medium-range order affect the properties - such as strength, conductivity and stability to crystallisation - of the glass-former? And how does the relationship between structure and dynamics differ in strong liquids, in non-alloy glasses, and in 3D glass-formers?

In conclusion, our results describe the increasing influence of structure on dynamics during the glass transition. In particular, the development of heterogeneity in the spatial distribution of dynamic propensity for a fragile glass-former demonstrates that structural variations can have a significant impact on relaxation in supercooled liquids. The isoconfigurational ensemble method provides a real-space picture of this transition from structure-independent to structure-dependent dynamics, that is complementary to the configuration-space perspective of the energy landscape view of glass-formation. It also has the additional benefit of providing the means to test for the presence of spatial correlations between structural and dynamic quantities on a microscopic spatial level. As the work in this thesis has demonstrated, this is an important test for distinguishing between those correlations that exist only at the bulk level and those that also operate at the microscopic level. Only the latter can provide insight into the detailed structural dependence of material properties.

Appendix A

The Nosé-Poincaré-Andersen Molecular Dynamics Algorithm

The Nosé-Poincaré-Andersen (NPA) method [84] is a real-time Hamiltonian formulation of isothermal-isobaric molecular dynamics simulation based on a Poincaré time transformation of the Nosé-Andersen Hamiltonian (see below). It belongs to the so-called 'extended' Hamiltonians - in which extra degrees of freedom have been added to the system in order to ensure that the trajectory samples from the statistical distribution corresponding to the desired thermodynamic conditions. Unlike the Nosé-Hoover-Anderson method [238], the Hamiltonian structure of the NPA allows for the use of symplectic integrators, which have been shown to have superior stability over non-symplectic methods [239]. For integrating the equations of motion we use the generalised leapfrog algorithm (GLA), which is time-reversible, second-order, and symplectic.

The Nosé-Poincaré-Andersen (NPA) Hamiltonian is given by

$$\mathcal{H}_{NPA} = [\mathcal{H}_{NA} - \mathcal{H}_{NA}(t=0)]s, \tag{A.1}$$

where $\mathcal{H}_{NA}$ is the Nosé-Andersen Hamiltonian. For a d-dimensional system with uniform scaling (such as a square simulation cell) this is given by

$$\mathcal{H}_{NA} = V^{-2/d} \sum_i \frac{p_i^2}{2m_i s^2} + U(V^{1/d}\mathbf{q}) + \frac{\pi_V^2}{2Q_v} + \frac{\pi_s^2}{2Q_s} + gkT \ln s + P_{ext} V, \tag{A.2}$$

where p_i is the conjugate momentum of the scaled position $q_i = V^{-1/d} r_i$, P_{ext} is the external pressure and $g = N_f + 1$ where N_f is the number of degrees of freedom of the original system (note that in the NPA Hamiltonian the correct value of g is N_f). Q_v and Q_s are the masses of the Anderson 'piston' and the Nosé thermostat, respectively.

In order to properly sample the isothermal-isobaric distribution, these masses need to be chosen with some care [84]. If they are too large or too small, the natural vibrational frequency of the extended variables will lie outside the density of states of vibrational frequencies of the system, thus decoupling the extended variables from the motions of the system and destroying ergodicity. A useful method to monitor this is to examine the distribution of kinetic energy (for the thermostat mass) and density (for the pressure piston). For a decoupled system, the resulting distribution will be decidedly non-Gaussian. We found that masses near $Q_s = 1000$ and $Q_v = 0.0002$ worked well for most runs. The exceptions were at low temperatures (typically $T \leq 0.2$), when Q_s usually had to be reduced, and in the vicinity of melting transitions, when Q_v needed to be reduced.

The six equations of motion for the NPA algorithm of Laird et al. [84] are given by:

$$\dot{p}_i = -V^{-1/d} \nabla_i U(V^{1/d}\mathbf{q}), \tag{A.3}$$

$$\dot{q}_i = \frac{p_i}{s^2 m_i V^{2/d}}, \tag{A.4}$$

$$\dot{\pi}_V = \mathcal{P} - P_{ext}, \tag{A.5}$$

$$\dot{V} = \pi_V / Q_v, \tag{A.6}$$

$$\dot{\pi}_s = V^{-2/d} \sum_i \frac{p_i^2}{m_i s^2} - gkT - \Delta\mathcal{H}, \tag{A.7}$$

$$\dot{s} = \pi_s / Q_s, \tag{A.8}$$

where $\Delta\mathcal{H} \equiv \mathcal{H}_{NA} - \mathcal{H}_{NA}(t=0)$, and the instantaneous pressure $\mathcal{P}$ is given by

$$\mathcal{P} = \frac{2}{dV} \sum_i \frac{p_i^2}{2 m_i V^{2/d} s^2} - \frac{1}{dV} \sum_i \frac{\partial U}{\partial q_i} q_i. \tag{A.9}$$

It can be shown that the NPA dynamics generates trajectories that sample from an isothermal-isobaric (NPT) statistical distribution (assuming ergodicity), and that the NPA equations of motion for π_V, s, and V generate the appropriate virial relations for the NPT distribution.

For simulations using non-uniform scaling, such as a rectangular cell, the equations of motion must be modified slightly. Only the expressions for the particle kinetic and potential energies are dependent on non-uniform scaling. We define $m_x = x_0/V_0^{1/2}$ and $y_x = y_0/V_0^{1/2}$ where V_0 is the initial volume and x_0 and y_0 are the initial x and y dimensions. Then for a 2D system we have

$$\begin{aligned}\mathcal{H}_{NA} &= V^{-1}\sum_i \frac{1}{2m_i s^2}\left(\frac{p_{ix}^2}{m_x^2}+\frac{p_{iy}^2}{m_y^2}\right)+U(V^{1/2}\mathbf{q})+\frac{\pi_V^2}{2Q_V}+ \\ &\quad \frac{\pi_s^2}{2Q_s}+gkT\ln s+P_{ext}V, \qquad \text{(A.10)}\end{aligned}$$

where the scaled positions are now given by $q_{ix} = V^{-1/2}r_{ix}$ and $q_{iy} = V^{-1/2}y_{iy}$, and p_{ix} and p_{iy} are the conjugate momenta to these. The equations of motion need to be modified accordingly.

Appendix B

Supplementary Data for Part I

In this appendix we provide additional data on the spatial relationship between dynamics and structure. In particular, for each of the ten configurations studied at $T = 0.4$, we plot (in the order shown in Figure B.1) the spatial distribution of propensity, DW factors, local potential energy, local free volume and the inherent structure of each configuration. The potential energy and relative free volume were calculated for the inherent structures, and the propensity and DW factors were averaged over iso-configurational ensembles of 100 runs. The configurations have been listed in temporal sequence and each is separated from the previous one by $75\tau_e$.

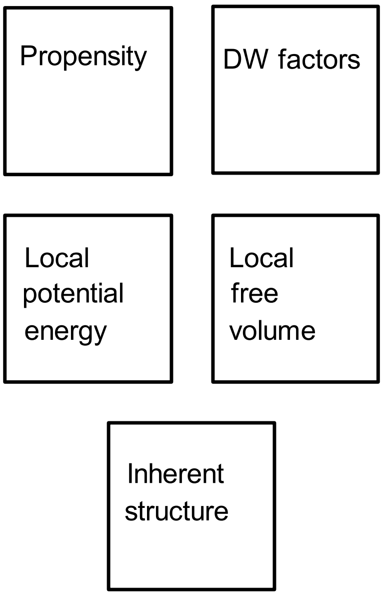

Figure B.1: Layout of plots.

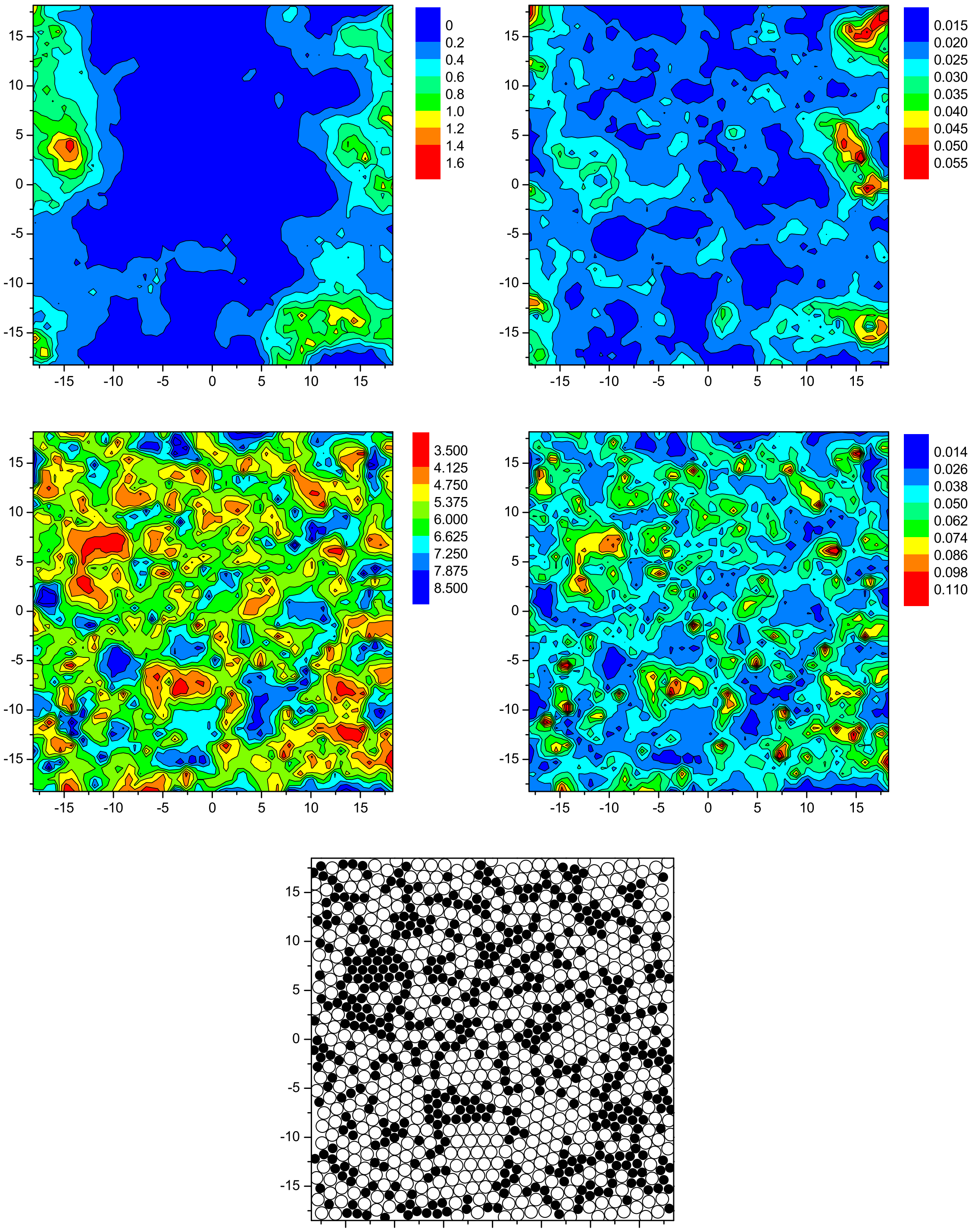

Figure B.2: Plots for configuration 1.

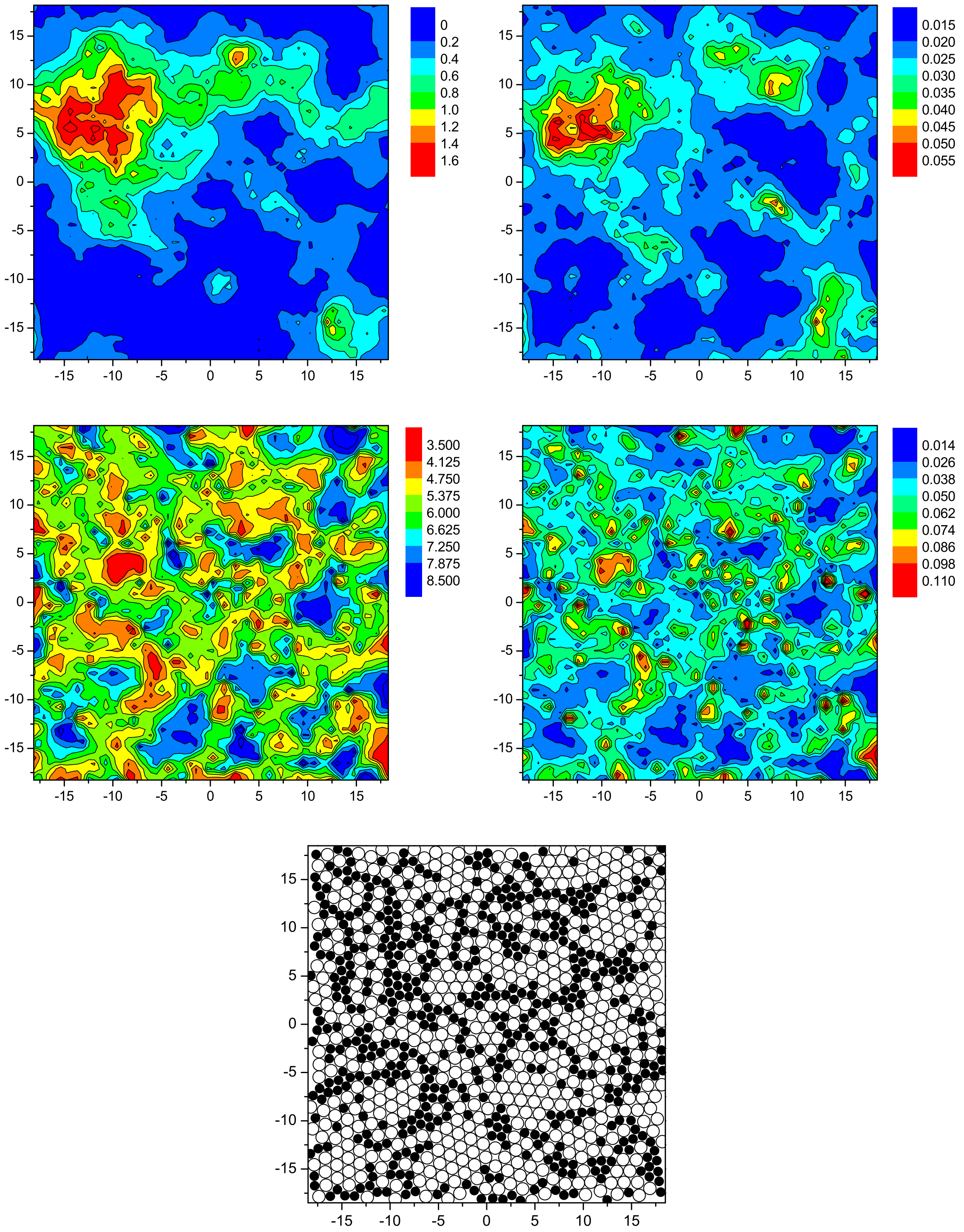

Figure B.3: Plots for configuration 2.

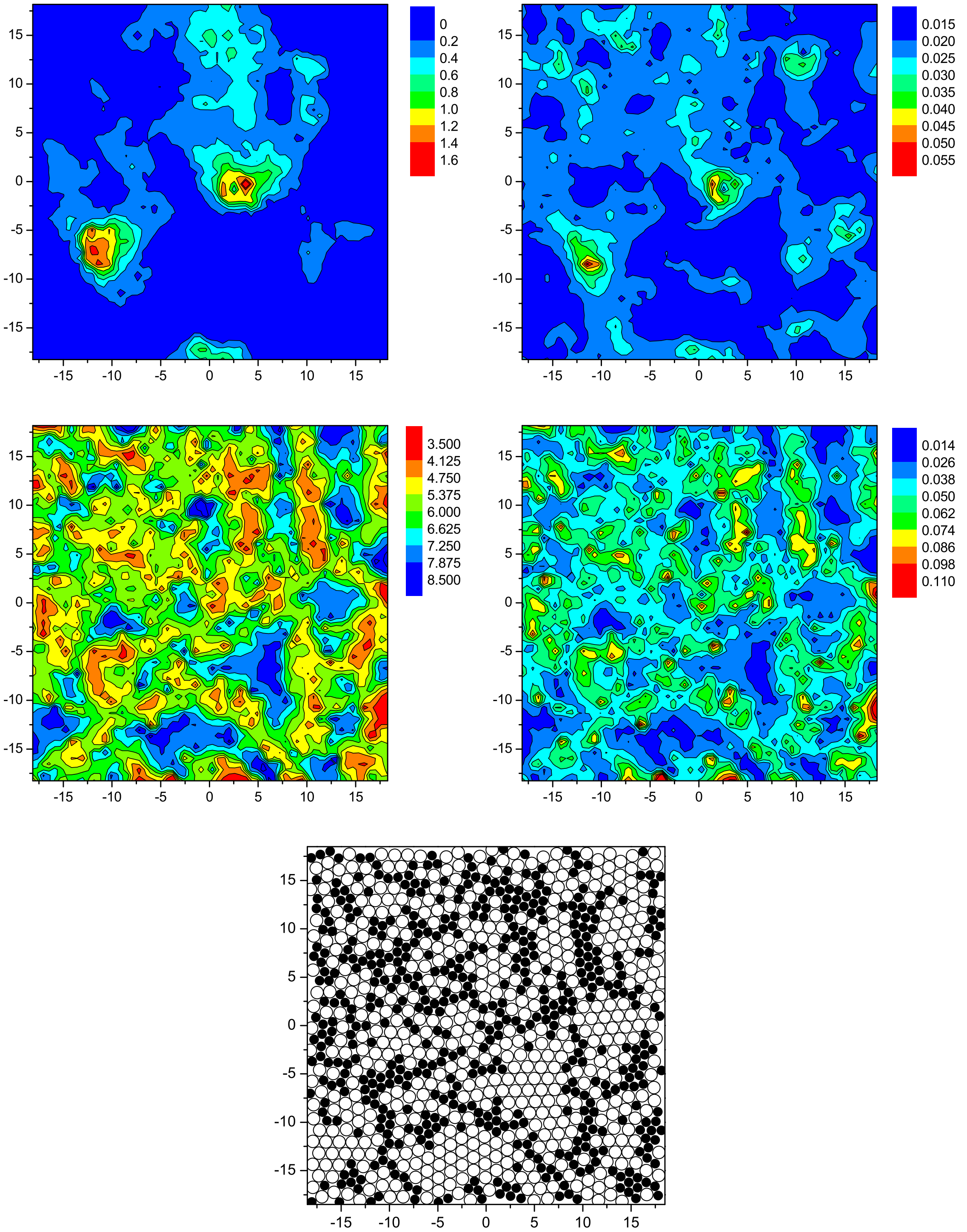

Figure B.4: Plots for configuration 3.

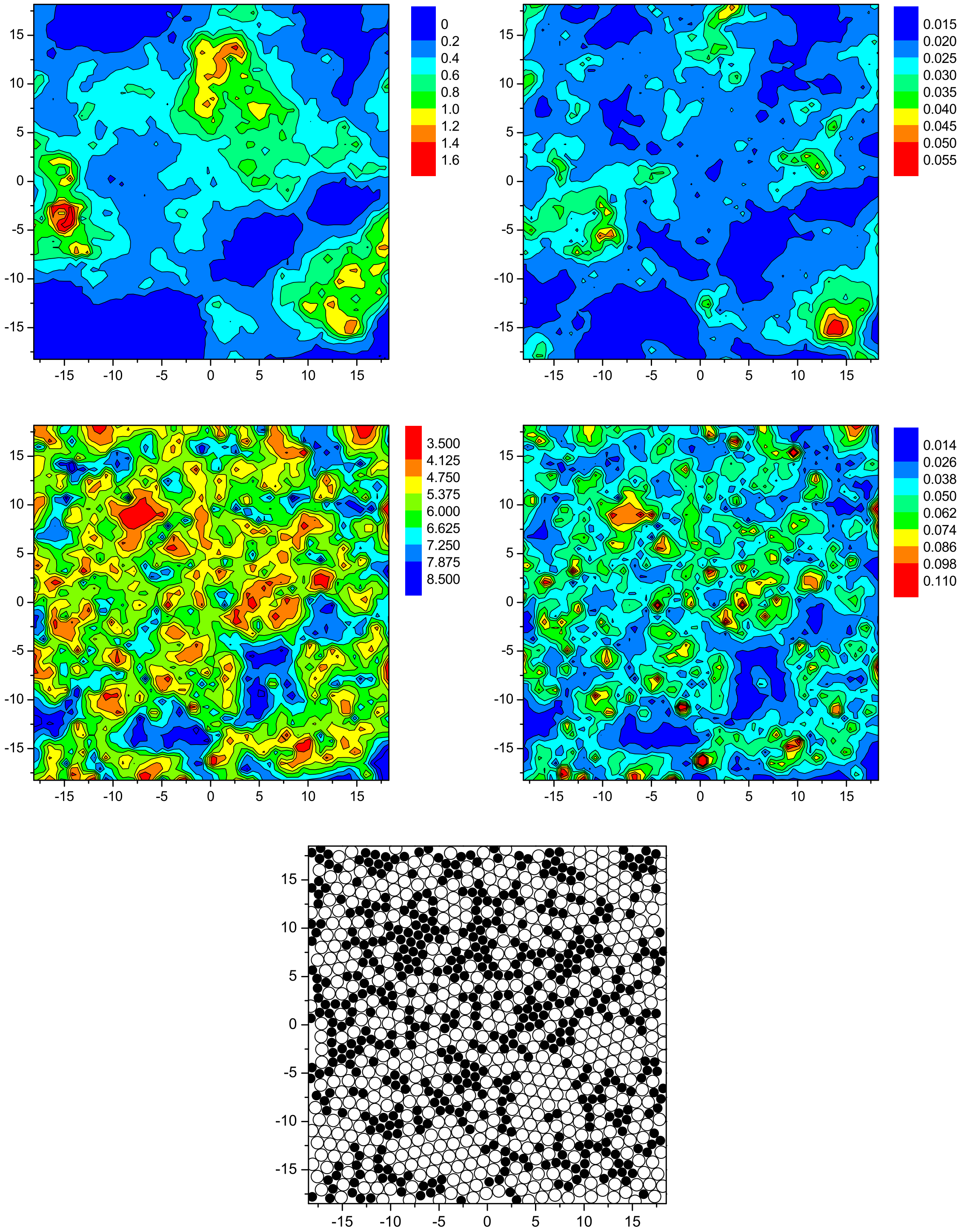

Figure B.5: Plots for configuration 4.

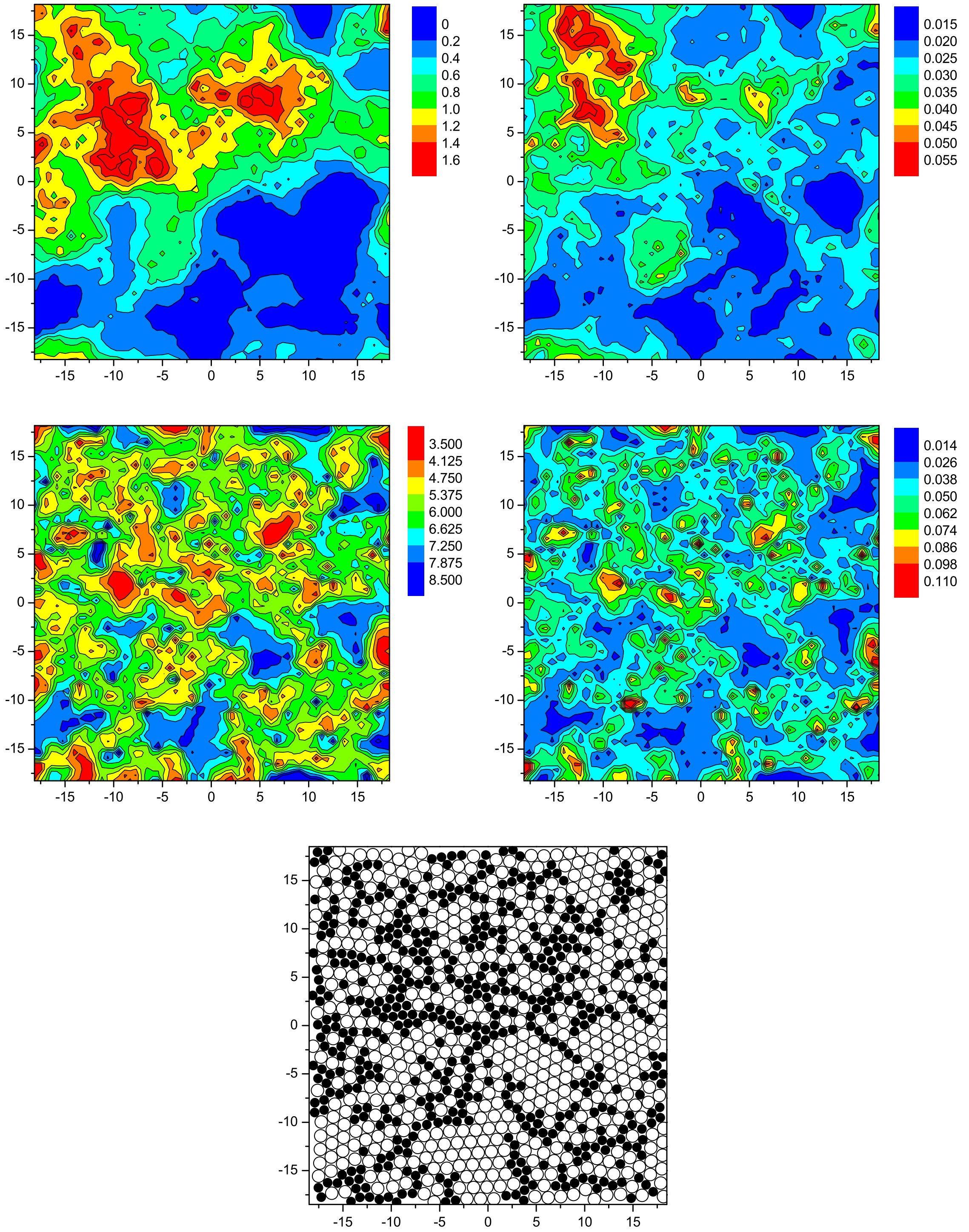

Figure B.6: Plots for configuration 5.

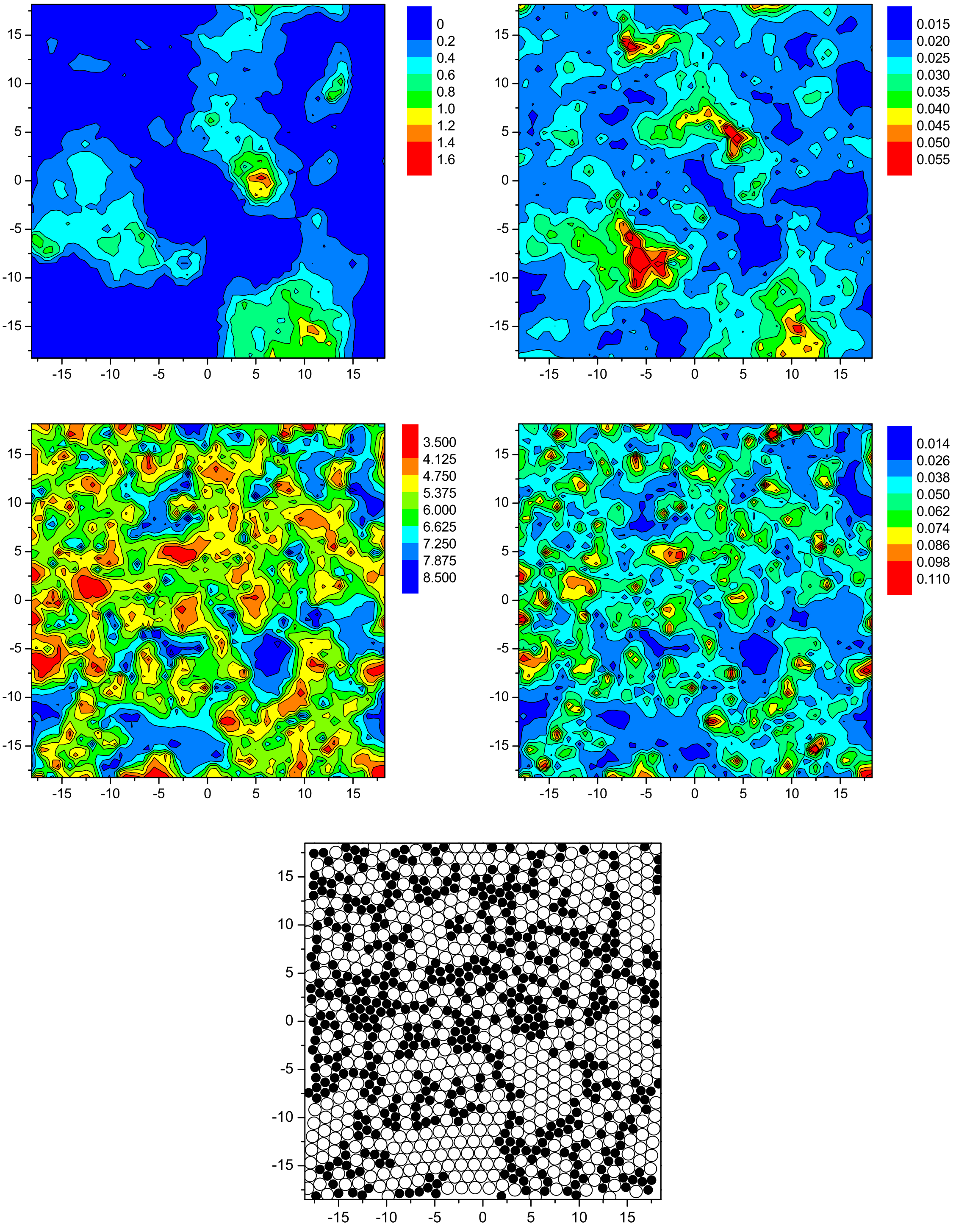

Figure B.7: Plots for configuration 6.

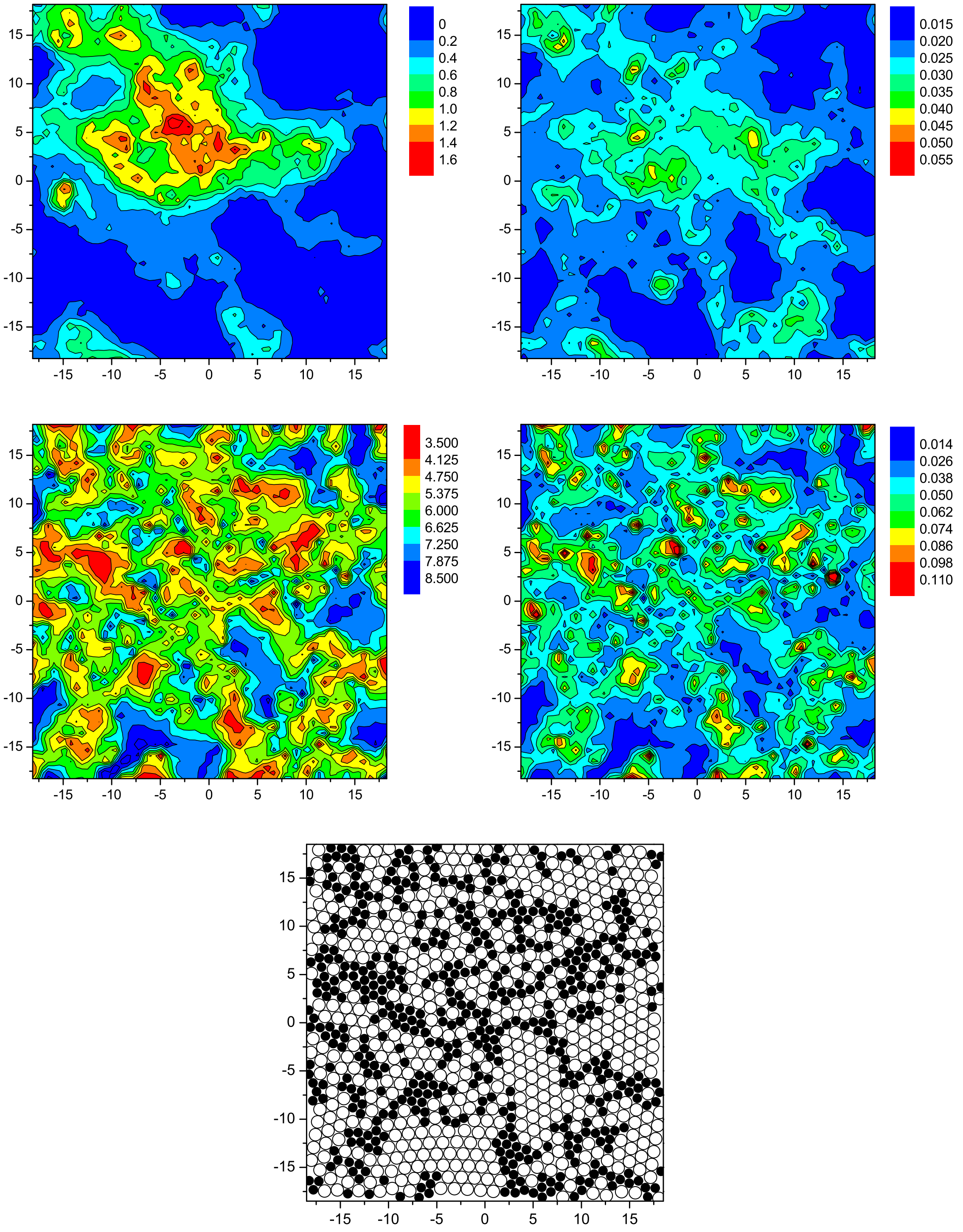

Figure B.8: Plots for configuration 7.

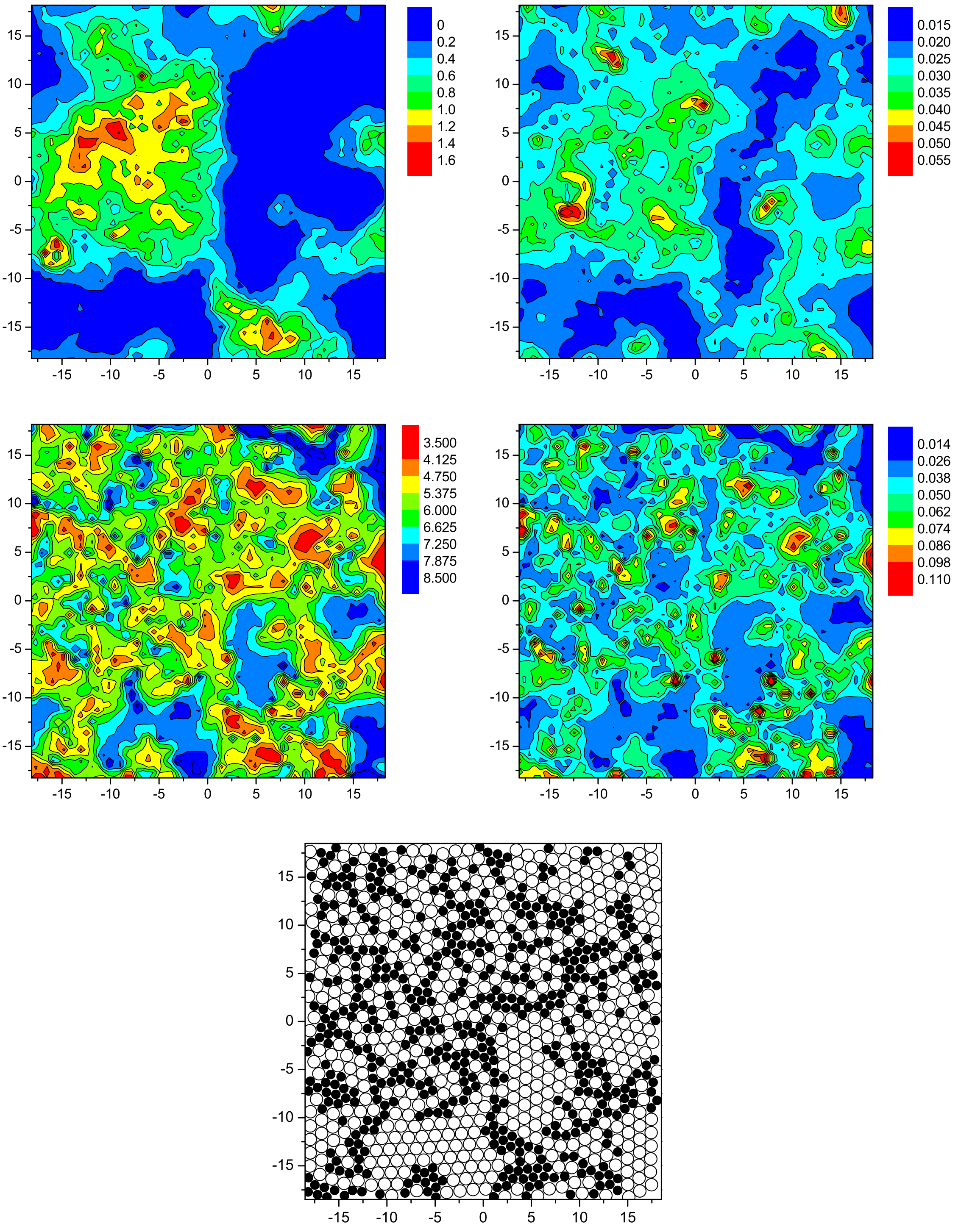

Figure B.9: Plots for configuration 8.

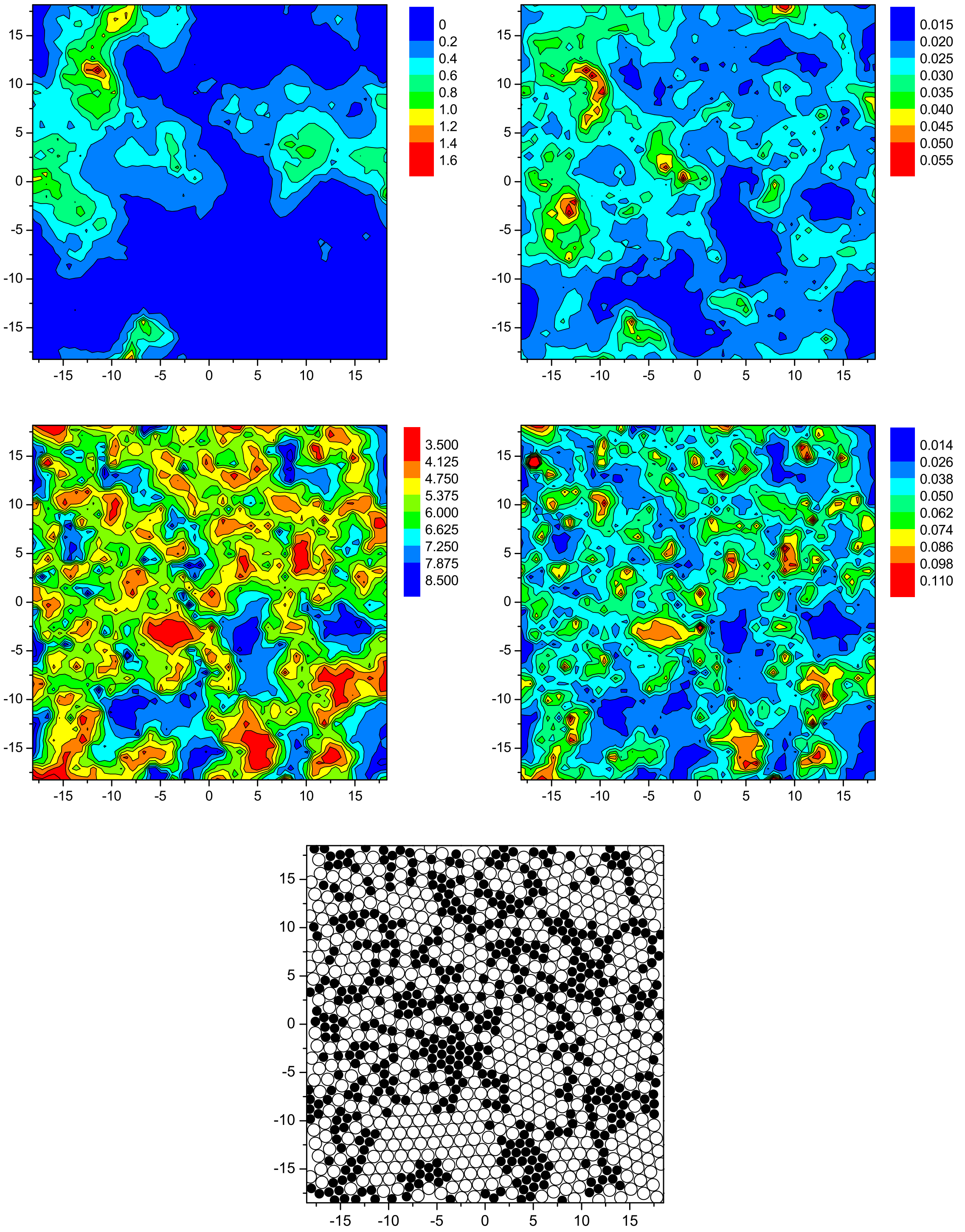

Figure B.10: Plots for configuration 9.

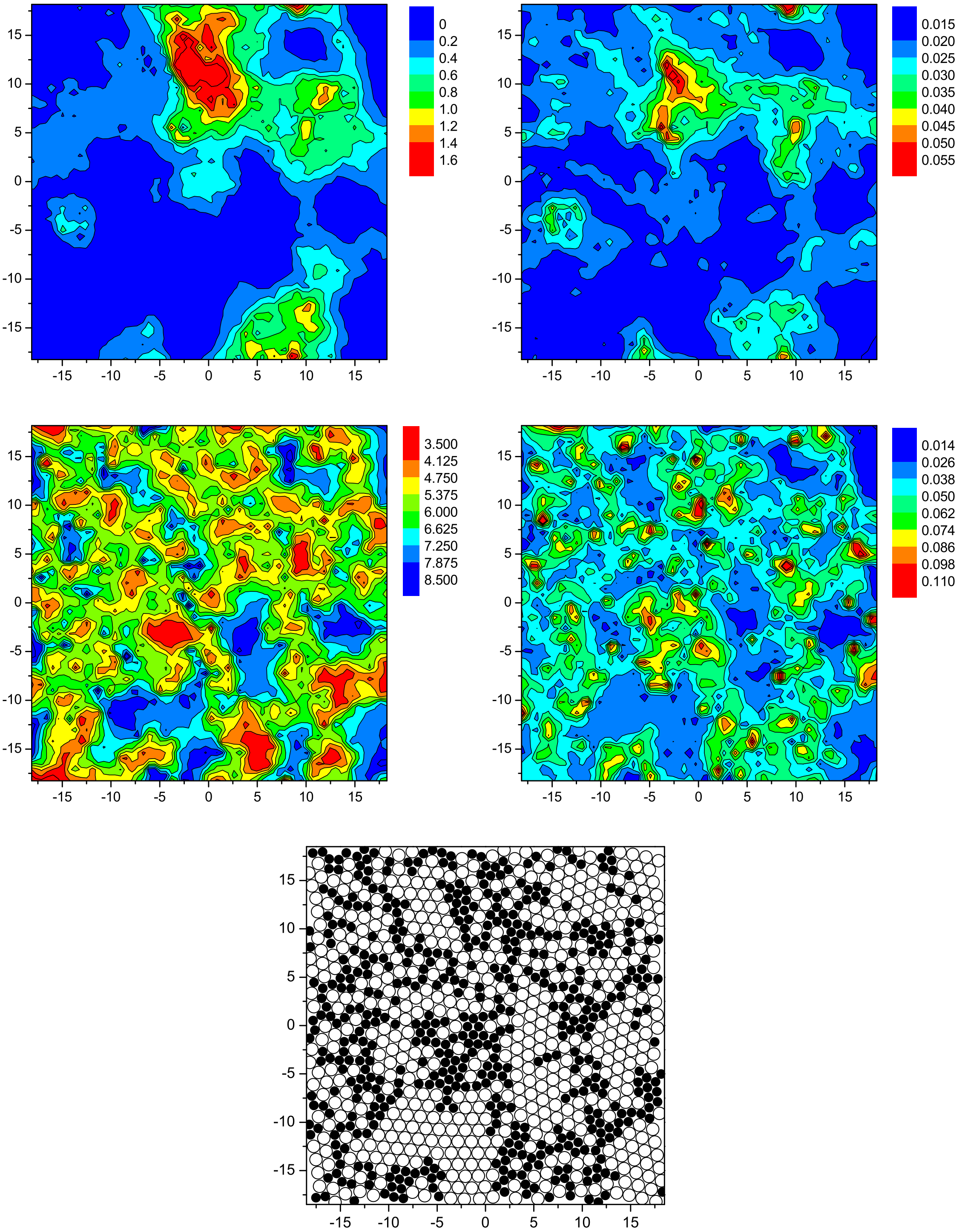

Figure B.11: Plots for configuration 10.

Appendix C

Supplementary Data for Part II

This appendix contains additional data for the soft-disc mixtures characterised in Part II.

C.1 $\sigma_{12} = 1.0,\ x_1 = 0.5$

Table C.1: The thermodynamic averages and their root mean square (rms) deviations for the cooling traverse for the equimolar binary mixture with $\sigma_{12} = 1.0$. Also shown are the effective coupling constant Γ, the compressibility factor Z, the equilibration time t_{eqlb}, and the production time t_{run} for each of these states.

T	t_{eqlb}/τ	t_{run}/τ	U	E	H	ρ
5	1000	1000	2.6122	7.5990	28.149	0.6529
3	1000	1000	2.5684	5.5637	24.019	0.7332
2	1000	1000	2.5261	4.5313	21.684	0.7867
1.5	2000	2000	2.4942	3.9711	20.372	0.8196
1.2	2000	2000	2.4674	3.6492	19.593	0.8433
1.15	2000	2000	2.4613	3.6073	19.525	0.8479
1.1	2000	2000	2.4543	3.5491	19.374	0.8528
1.08	2000	2000	2.4503	3.5222	19.293	0.8552
1.06	4000	2000	2.4459	3.5031	19.244	0.8577
1.04	10000	2000	2.4408	3.4768	19.154	0.8605
1.02	10000	20000	2.3689	3.3864	18.630	0.8860
1	10000	20000	2.3672	3.3620	18.558	0.8878
0.98	10000	20000	2.3654	3.3400	18.508	0.8896
0.96	10000	20000	2.3648	3.3223	18.471	0.8910
0.94	10000	20000	2.3630	3.2992	18.414	0.8928
0.92	10000	20000	2.3622	3.2776	18.356	0.8943
0.9	10000	20000	2.3607	3.2603	18.329	0.8960
0.8	10000	20000	2.3559	3.1514	18.080	0.9037
0.7	10000	20000	2.3528	3.0524	17.888	0.9110

continued on next page

Table C.1 continued

T	Γ	Z	rms(U)	rms(E)	rms(H)	rms(ρ)
5	0.4993	4.1355	0.0862	0.1626	0.7263	0.0051
3	0.6105	6.1379	0.0642	0.0794	0.3574	0.0042
2	0.7009	8.5800	0.0536	0.0665	0.3793	0.0040
1.5	0.7660	10.981	0.0460	0.0505	0.2736	0.0034
1.2	0.8181	13.340	0.0398	0.0439	0.2287	0.0027
1.15	0.8284	13.845	0.0400	0.0506	0.2862	0.0029
1.1	0.8394	14.391	0.0397	0.0474	0.2779	0.0030
1.08	0.8443	14.616	0.0369	0.0453	0.2611	0.0027
1.06	0.8494	14.849	0.0415	0.0484	0.2995	0.0034
1.04	0.8549	15.086	0.0386	0.0463	0.2792	0.0032
1.02	0.8831	14.938	0.0375	0.0465	0.2718	0.0028
1	0.8878	15.206	0.0360	0.0450	0.2610	0.0026
0.98	0.8926	15.486	0.0371	0.0425	0.2481	0.0028
0.96	0.8970	15.784	0.0371	0.0451	0.2625	0.0028
0.94	0.9020	16.087	0.0365	0.0411	0.2497	0.0027
0.92	0.9068	16.409	0.0360	0.0438	0.2579	0.0027
0.9	0.9119	16.741	0.0354	0.0405	0.2481	0.0026
0.8	0.9380	18.673	0.0337	0.0384	0.2313	0.0025
0.7	0.9668	21.171	0.0313	0.0371	0.2240	0.0023

Table C.2: The thermodynamic averages and their root mean square (rms) deviations for the heating traverse for the equimolar binary mixture with $\sigma_{12} = 1.0$. Also shown are the effective coupling constant Γ, the compressibility factor Z, the equilibration time t_{eqlb}, and the production time t_{run} for each of these states.

T	t_{eqlb}/τ	t_{run}/τ	U	E	H	ρ
0.1	2000	20000	2.3351	2.4336	16.538	0.9567
0.2	2000	20000	2.3358	2.5345	16.746	0.9497
0.3	2000	20000	2.3369	2.6360	16.957	0.9426
0.4	2000	20000	2.3385	2.7371	17.166	0.9354
0.5	2000	20000	2.3405	2.8386	17.383	0.9282
0.6	2000	20000	2.3429	2.9407	17.591	0.9209
0.7	2000	20000	2.3457	3.0432	17.816	0.9136
0.8	2000	20000	2.3489	3.1491	18.056	0.9063
0.9	2000	20000	2.3526	3.2501	18.269	0.8989
0.95	2000	20000	2.3564	3.3017	18.387	0.8945
1	2000	20000	2.3602	3.3552	18.507	0.8902
1.02	2000	20000	2.3611	3.3764	18.559	0.8887
1.04	6000	20000	2.3640	3.4007	18.626	0.8866
1.06	6000	20000	2.3651	3.4210	18.671	0.8850
1.08	12000	2000	2.4485	3.5236	19.292	0.8558
1.1	6000	2000	2.4543	3.5497	19.370	0.8528
1.12	2000	2000	2.4577	3.5732	19.419	0.8507
1.14	2000	2000	2.4600	3.5941	19.480	0.8488
1.16	2000	2000	2.4621	3.6158	19.531	0.8471
1.18	2000	2000	2.4651	3.6386	19.608	0.8451
1.2	2000	2000	2.4667	3.6605	19.662	0.8435

continued on next page

Table C.2 continued

T	Γ	Z	rms(U)	rms(E)	rms(H)	rms(ρ)
0.1	1.4042	141.11	0.0114	0.0192	0.0914	0.0013
0.2	1.2418	71.077	0.0168	0.0193	0.1193	0.0013
0.3	1.1520	47.741	0.0201	0.0218	0.1400	0.0014
0.4	1.0897	36.080	0.0253	0.0276	0.1768	0.0018
0.5	1.0419	29.089	0.0263	0.0296	0.1935	0.0019
0.6	1.0028	24.432	0.0277	0.0306	0.1955	0.0020
0.7	0.9696	21.109	0.0328	0.0391	0.2545	0.0023
0.8	0.9406	18.620	0.0350	0.0410	0.2508	0.0026
0.9	0.9148	16.687	0.0319	0.0370	0.2303	0.0022
0.95	0.9022	15.886	0.0356	0.0418	0.2528	0.0026
1	0.8902	15.165	0.0382	0.0440	0.2585	0.0028
1.02	0.8858	14.892	0.0392	0.0476	0.2790	0.0030
1.04	0.8808	14.642	0.0345	0.0408	0.2407	0.0027
1.06	0.8765	14.391	0.0408	0.0515	0.2965	0.0030
1.08	0.8449	14.607	0.0365	0.0417	0.2400	0.0031
1.1	0.8394	14.391	0.0371	0.0439	0.2518	0.0029
1.12	0.8347	14.170	0.0448	0.0579	0.3441	0.0032
1.14	0.8305	13.951	0.0398	0.0488	0.2784	0.0030
1.16	0.8264	13.739	0.0365	0.0322	0.2070	0.0028
1.18	0.8221	13.538	0.0381	0.0455	0.2785	0.0028
1.2	0.8182	13.338	0.0366	0.0411	0.2577	0.0028

Table C.3: Cutoff distances for the cooling traverse used to define nearest neighbour interactions for the calculation of local structural properties and the definition of 'bonds'. These correspond to the positions of the first minima in the respective pair distribution functions, except for cut_{11} at $T \leq 1.02$ where we have used the position of the first minimum in $g_{11}(r)$ at $T = 1.04$ for reasons that are explained in the text.

T	cut_{11}	cut_{12}	cut_{22}
5	1.53	1.72	1.75
3	1.53	1.67	1.75
2	1.5	1.66	1.75
1.5	1.48	1.64	1.76
1.2	1.34	1.62	1.76
1.15	1.32	1.62	1.78
1.08–1.1	1.3	1.62	1.8
0.7–1.06	1.28	1.62	1.8

Table C.4: The locations of the first peak positions k_1 and k_2 in the respective partial structure factors $S_{11}(k)$ and $S_{22}(k)$. These wave vectors have been used to calculate the incoherent scattering functions.

T	k_1	k_2
5	3.83	4.45
3	3.83	4.35
2	3.85	4.22
1.5	3.95	4.22
1.2	4.02	4.22
1.15	4.05	4.22
1.1	4.08	4.22
1.08	4.11	4.18
1.06	4.11	4.18
1.04	4.12	4.19

Table C.5: The temperature dependence of the structural relaxation times $\tau_{e,1}$ and $\tau_{e,2}$, and the self-diffusion coefficients of the small and large particles, D_1 and D_2, respectively, for the cooling traverse of the equimolar mixture. The diffusion constants with the subscript h were obtained for the heating traverse.

T	$\tau_{e,1}/\tau$	$\tau_{e,2}/\tau$	$D_1/\sigma_{11}^2\tau^{-1}$	$D_2/\sigma_{11}^2\tau^{-1}$	$D_{h,1}/\sigma_{11}^2\tau^{-1}$	$D_{h,2}/\sigma_{11}^2\tau^{-1}$
5	0.216	0.190	0.65597	0.55069		
3	0.338	0.327	0.33396	0.29077		
2	0.535	0.552	0.16490	0.14607		
1.5	0.757	0.826	0.08573	0.07474		
1.2	1.13	1.26	0.04544	0.04027	0.04102	0.03463
1.18					0.03992	0.03613
1.16					0.03489	0.03023
1.15	1.25	1.38	0.03661	0.03142		
1.14					0.03462	0.02954
1.12					0.03318	0.02981
1.1	1.42	1.62	0.02948	0.02665	0.02702	0.02309
1.08	1.47	1.77	0.02632	0.02286	0.02210	0.01902
1.06	1.57	1.86	0.02237	0.01871	0.00043	0.00005
1.04	1.71	2.07	0.01997	0.01742	0.00031	
1.02			0.00047	0.00018	0.00028	
1			0.00044	0.00017	0.00019	
0.98			0.00036	0.00015		
0.96			0.00024	0.00011		
0.95					0.00010	
0.94			0.00023	0.00013		
0.92			0.00019	0.00011		
0.9			0.00020	0.00010		
0.8			0.00018	0.00010		
0.7			0.00008	0.00004		

C.2 $\sigma_{12} = 1.0,\ x_1 = 0.3167$

Table C.6: The thermodynamic averages and their root mean square (rms) deviations for the binary mixture with $\sigma_{12} = 1.0$ and $x_1 = 0.3167$. Also shown are the effective coupling constant Γ, the compressibility factor Z, the equilibration time t_{eqlb}, and the production time t_{run} for each of these states.

T	t_{eqlb}/τ	t_{run}/τ	U	E	H	ρ
5	1000	1000	3.0312	8.0207	31.146	0.5821
4.5	1000	1000	3.0253	7.5201	30.158	0.5958
4	1000	1000	3.0187	7.0105	29.102	0.6104
3.5	1000	1000	3.0094	6.5015	28.057	0.6262
3	1000	1000	2.9982	5.9934	26.996	0.6431
2.8	1000	1000	2.9932	5.7883	26.545	0.6502
2.6	1000	1000	2.9874	5.5820	26.104	0.6577
2.4	1000	1000	2.9813	5.3783	25.646	0.6654
2.2	1000	1000	2.9745	5.1716	25.219	0.6734
2	1000	1000	2.9667	4.9586	24.740	0.6818
1.9	2000	2000	2.9627	4.8553	24.509	0.6858
1.8	2000	2000	2.9586	4.7461	24.257	0.6902
1.7	2000	2000	2.9538	4.6457	24.077	0.6948
1.6	2000	2000	2.9492	4.5392	23.803	0.6994
1.5	2000	2000	2.9441	4.4326	23.556	0.7042
1.4	2000	2000	2.9387	4.3297	23.346	0.7091
1.3	2000	2000	2.9334	4.2280	23.126	0.7141
1.2	2000	2000	2.9270	4.1223	22.871	0.7194
1.1	2000	2000	2.9211	4.0121	22.617	0.7246
1	2000	2000	2.9145	3.9024	22.337	0.7301
0.9	2000	2000	2.9078	3.8068	22.164	0.7357
0.8	2000	2000	2.9010	3.6986	21.898	0.7414
0.7	2000	2000	2.8936	3.5888	21.633	0.7473
0.6	2000	2000	2.8851	3.4850	21.400	0.7537
0.55	4000	20000	2.8800	3.4262	21.245	0.7571
0.5	10000	20000	2.8757	3.3730	21.115	0.7603
0.45	10000	20000	2.8700	3.3185	20.988	0.7639
0.4	10000	20000	2.8684	3.2647	20.861	0.7665
0.35	10000	20000	2.8656	3.2142	20.755	0.7695
0.3	10000	20000	2.8649	3.1638	20.653	0.7718
0.2	10000	20000	2.8639	3.0647	20.458	0.7766

continued on next page

Table C.6 continued

T	Γ	Z	rms(U)	rms(E)	rms(H)	rms(ρ)
5	0.4452	4.6383	0.0956	0.1664	0.7619	0.0042
4.5	0.4637	5.0350	0.0925	0.1529	0.6700	0.0043
4	0.4845	5.5288	0.0854	0.1434	0.6415	0.0036
3.5	0.5082	6.1599	0.0804	0.1299	0.6343	0.0036
3	0.5355	6.9975	0.0699	0.0991	0.4880	0.0033
2.8	0.5477	7.4155	0.0567	0.0560	0.3768	0.0029
2.6	0.5609	7.8949	0.0655	0.0840	0.4529	0.0031
2.4	0.5750	8.4541	0.0592	0.0760	0.4281	0.0028
2.2	0.5904	9.1131	0.0673	0.0945	0.4911	0.0031
2	0.6074	9.9009	0.0599	0.0752	0.4315	0.0029
1.9	0.6162	10.361	0.0581	0.0789	0.4299	0.0028
1.8	0.6258	10.866	0.0568	0.0745	0.4188	0.0027
1.7	0.6360	11.429	0.0561	0.0694	0.3998	0.0027
1.6	0.6467	12.063	0.0530	0.0678	0.3690	0.0026
1.5	0.6582	12.781	0.0512	0.0704	0.3716	0.0025
1.4	0.6705	13.598	0.0491	0.0616	0.3551	0.0024
1.3	0.6835	14.542	0.0484	0.0564	0.3299	0.0024
1.2	0.6978	15.639	0.0463	0.0543	0.3142	0.0023
1.1	0.7132	16.937	0.0441	0.0526	0.2958	0.0022
1	0.7301	18.491	0.0416	0.0521	0.3192	0.0020
0.9	0.7487	20.389	0.0399	0.0501	0.3058	0.0019
0.8	0.7695	22.761	0.0365	0.0379	0.2384	0.0018
0.7	0.7931	25.806	0.0353	0.0386	0.2318	0.0017
0.6	0.8206	29.854	0.0325	0.0384	0.2438	0.0016
0.55	0.8364	32.422	0.0309	0.0316	0.2014	0.0015
0.5	0.8534	35.511	0.0294	0.0322	0.2094	0.0014
0.45	0.8727	39.271	0.0278	0.0314	0.1993	0.0013
0.4	0.8930	44.029	0.0263	0.0281	0.1860	0.0013
0.35	0.9166	50.128	0.0247	0.0273	0.1803	0.0012
0.3	0.9434	58.302	0.0228	0.0236	0.1556	0.0011
0.2	1.0155	86.922	0.0203	0.0213	0.1464	0.0009

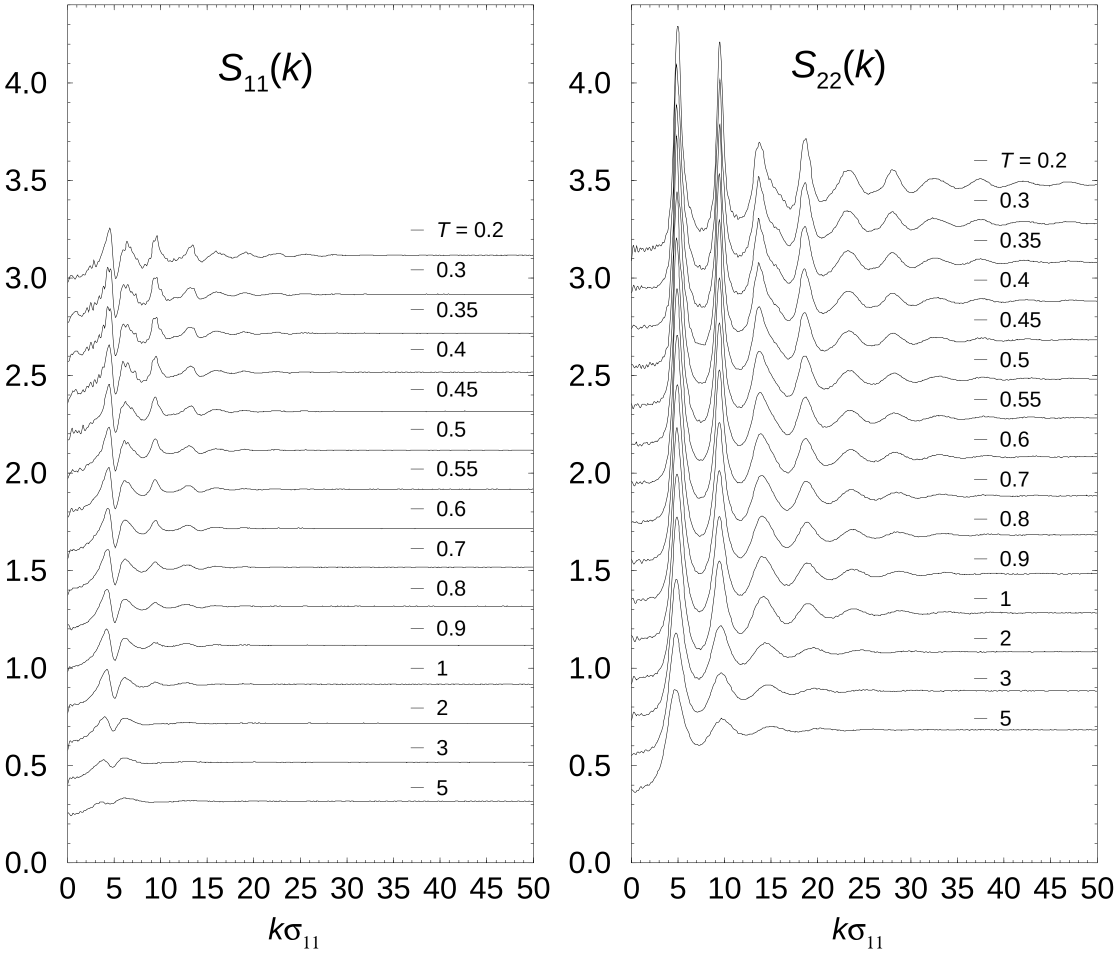

Figure C.1: The partial structure factors $S_{11}(k)$ and $S_{22}(k)$ for temperatures from $T = 5$ down to $T = 0.2$. For clarity, each curve below $T = 5$ has been shifted upwards by 0.2 units above the higher temperature curve directly preceding it.

Table C.7: The locations of the first peak positions k_1 and k_2 in the respective partial structure factors $S_{11}(k)$ and $S_{22}(k)$ for the non-equimolar mixture. These wave vectors were used to calculate the incoherent scattering functions.

T	k_1	k_2
5	3.76	4.91
4	3.92	4.91
3	4.07	4.91
0.2–2	4.34	4.91

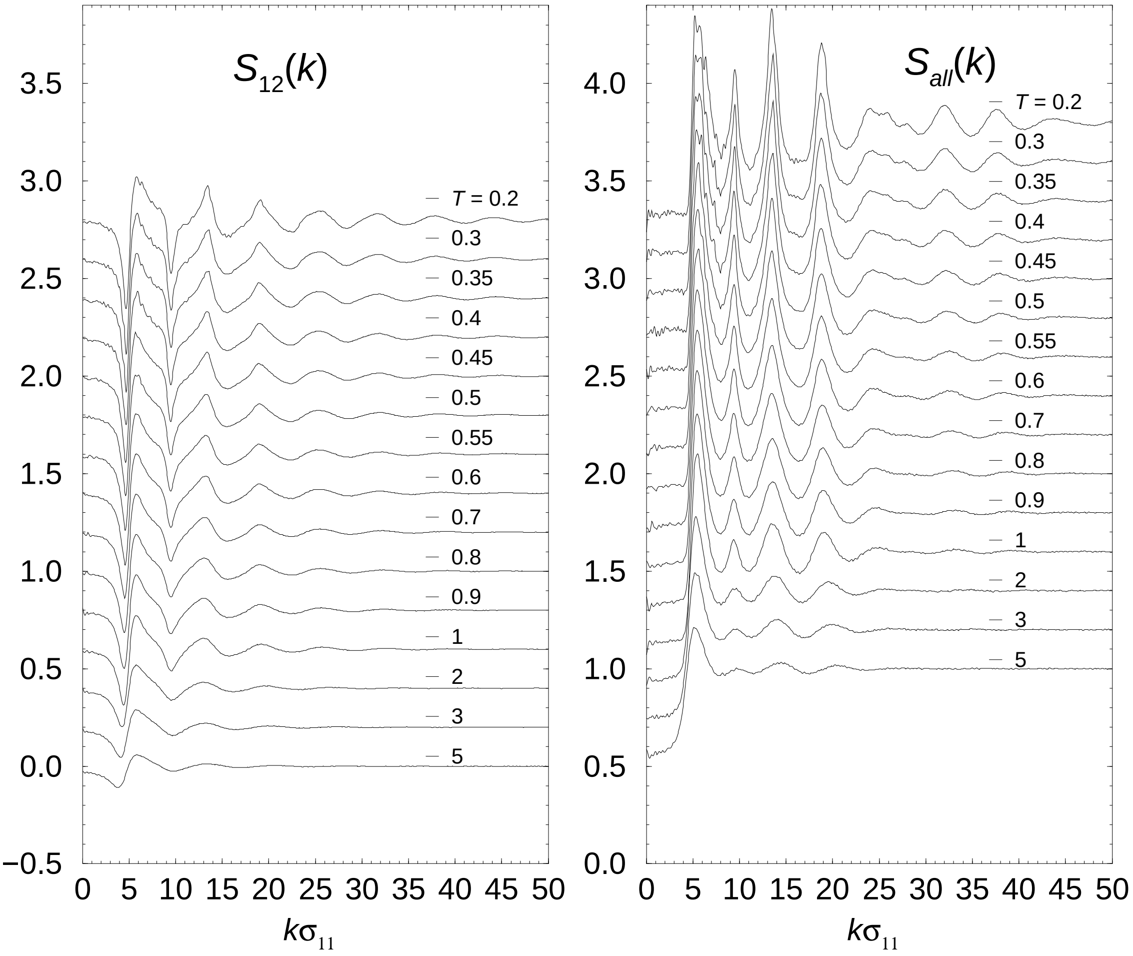

Figure C.2: The partial structure factor $S_{12}(k)$ and the total structure factor $S_{all}(k)$ as a function of wave vector from $T = 5$ down to $T = 0.2$. For clarity, each curve below $T = 5$ has been shifted upwards by 0.2 units above the higher temperature curve directly preceding it.

Table C.8: The temperature dependence of the structural relaxation times $\tau_{e,1}$ and $\tau_{e,2}$, and the self-diffusion coefficients of the small and large particles, D_1 and D_2, respectively.

T	$\tau_{e,1}/\tau$	$\tau_{e,2}/\tau$	$D_1/\sigma_{11}^2\tau^{-1}$	$D_2/\sigma_{11}^2\tau^{-1}$
5	0.214	0.167	0.69039	0.56054
3	0.293	0.267	0.34212	0.28468
2	0.391	0.419	0.18103	0.15102
1	1.23	1.28	0.03225	0.02704
0.9	1.61	1.64	0.02110	0.01668
0.8	2.3	2.3	0.01449	0.01187
0.7	3.85	3.76	0.00706	0.00589
0.6	14.8	14.1	0.00230	0.00156
0.55	47.3	47.3	0.00086	0.00055
0.5	202	207	0.00033	0.00018
0.45	2610	2790	0.00005	

C.3 $\sigma_{12} = 1.1,\ x_1 = 0.5$

Table C.9: The thermodynamic averages and their root mean square (rms) deviations for the cooling traverse for the equimolar binary mixture with $\sigma_{12} = 1.1$. Also shown are the effective coupling constant Γ, the compressibility factor Z, the equilibration time t_{eqlb}, and the production time t_{run} for each of these states. An asterisk (*) following the production runtime indicates that the thermodynamic averages at this temperature were calculated during the latter part of the equilibration run.

T	t_{eqlb}/τ	t_{run}/τ	U	E	H	ρ
5	2000	2500	2.8501	7.8350	29.911	0.6107
3	2000	2500	2.8200	5.8146	25.736	0.6777
2	2000	2500	2.7879	4.7828	23.501	0.7208
1	5000	5000	2.7283	3.7206	21.073	0.7770
0.9	5000	5000	2.7193	3.6162	20.833	0.7840
0.8	5000	5000	2.7094	3.5063	20.556	0.7913
0.7	5000	5000	2.6972	3.3940	20.280	0.7995
0.68	10000	5000	2.6947	3.3705	20.206	0.8011
0.66	10000	5000	2.6907	3.3459	20.142	0.8033
0.64	10000	5000	2.6859	3.3227	20.068	0.8056
0.62	10000	5000	2.6836	3.3009	20.019	0.8072
0.6	10000	5000	2.6774	3.2749	19.939	0.8100
0.58	10000	9000*	2.6740	3.2484	19.869	0.8121
0.56	10000	9000*	2.6701	3.2236	19.795	0.8143

T	Γ_e	Z	rms(U)	rms(E)	rms(H)	rms(ρ)
5	0.4670	4.4211	0.0919	0.1624	0.6991	0.0044
3	0.5643	6.6404	0.0808	0.1366	0.6336	0.0039
2	0.6422	9.3645	0.0579	0.0762	0.4149	0.0032
1	0.7770	17.374	0.0404	0.0478	0.2847	0.0023
0.9	0.7979	19.133	0.0390	0.0467	0.2768	0.0022
0.8	0.8213	21.325	0.0356	0.0418	0.2592	0.0021
0.7	0.8485	24.122	0.0329	0.0378	0.2367	0.0019
0.68	0.8543	24.781	0.0361	0.0413	0.2571	0.0021
0.66	0.8609	25.464	0.0373	0.0429	0.2653	0.0021
0.64	0.8678	26.184	0.0325	0.0365	0.2215	0.0019
0.62	0.8742	26.973	0.0328	0.0359	0.2278	0.0020
0.6	0.8819	27.779	0.0352	0.0380	0.2452	0.0021
0.58	0.8893	28.660	0.0315	0.0405	0.2176	0.0017
0.56	0.8969	29.606	0.0329	0.0416	0.2298	0.0018

Table C.10: The thermodynamic averages and their root mean square (rms) deviations for the heating traverse for the equimolar binary mixture with $\sigma_{12} = 1.1$. Also shown are the effective coupling constant Γ, the compressibility factor Z, the equilibration time t_{eqlb}, and the production time t_{run} for each of these states. An asterisk (*) following the production runtime indicates that the thermodynamic averages at this temperature were calculated during the latter part of the equilibration run.

T	t_{eqlb}/τ	t_{run}/τ	U	E	H	ρ
0.1	5000	5000	2.6220	2.7216	18.554	0.8527
0.2	5000	5000	2.6225	2.8213	18.754	0.8471
0.3	5000	5000	2.6234	2.9221	18.961	0.8416
0.4	5000	5000	2.6247	3.0228	19.169	0.8359
0.5	5000	5000	2.6264	3.1240	19.379	0.8302
0.6	10000	5000	2.6288	3.2259	19.593	0.8245
0.62	10000	5000	2.6290	3.2462	19.636	0.8233
0.64	10000	5000	2.6297	3.2659	19.673	0.8221
0.66	10000	5000	2.6308	3.2871	19.727	0.8208
0.68	10000	5000	2.6309	3.3082	19.770	0.8198
0.7	10000	5000	2.6321	3.3182	19.752	0.8184
0.72	10000	9000*	2.6328	3.3491	19.862	0.8173
0.74	10000	9000*	2.6327	3.3698	19.904	0.8162
0.76	10000	9000*	2.6351	3.3921	19.959	0.8146
0.78	10000	9000*	2.6352	3.4117	19.999	0.8135
0.8	10000	9000*	2.6361	3.4327	20.047	0.8123
0.82	10000	5000*	2.7168	3.5352	20.654	0.7900

T	Γ_e	Z	rms(U)	rms(E)	rms(H)	rms(ρ)
0.1	1.2516	158.32	0.0145	0.0147	0.1004	0.0008
0.2	1.1078	79.679	0.0181	0.0179	0.1207	0.0010
0.3	1.0286	53.472	0.0214	0.0228	0.1551	0.0012
0.4	0.9738	40.374	0.0260	0.0273	0.1817	0.0015
0.5	0.9319	32.521	0.0291	0.0323	0.2099	0.0017
0.6	0.8977	27.290	0.0337	0.0396	0.2443	0.0018
0.62	0.8916	26.448	0.0386	0.0405	0.2692	0.0024
0.64	0.8856	25.657	0.0325	0.0371	0.2312	0.0019
0.66	0.8797	24.920	0.0318	0.0355	0.2282	0.0018
0.68	0.8742	24.217	0.0334	0.0379	0.2336	0.0019
0.7	0.8685	23.565	0.0274	0.0274	0.1726	0.0017
0.72	0.8633	22.941	0.0267	0.0290	0.1824	0.0016
0.74	0.8582	22.350	0.0240	0.0249	0.1608	0.0015
0.76	0.8527	21.807	0.0395	0.0467	0.2824	0.0022
0.78	0.8479	21.275	0.0355	0.0409	0.2511	0.0021
0.8	0.8430	20.775	0.0225	0.0208	0.1386	0.0015
0.82	0.8165	20.841	0.0342	0.0375	0.2362	0.0020

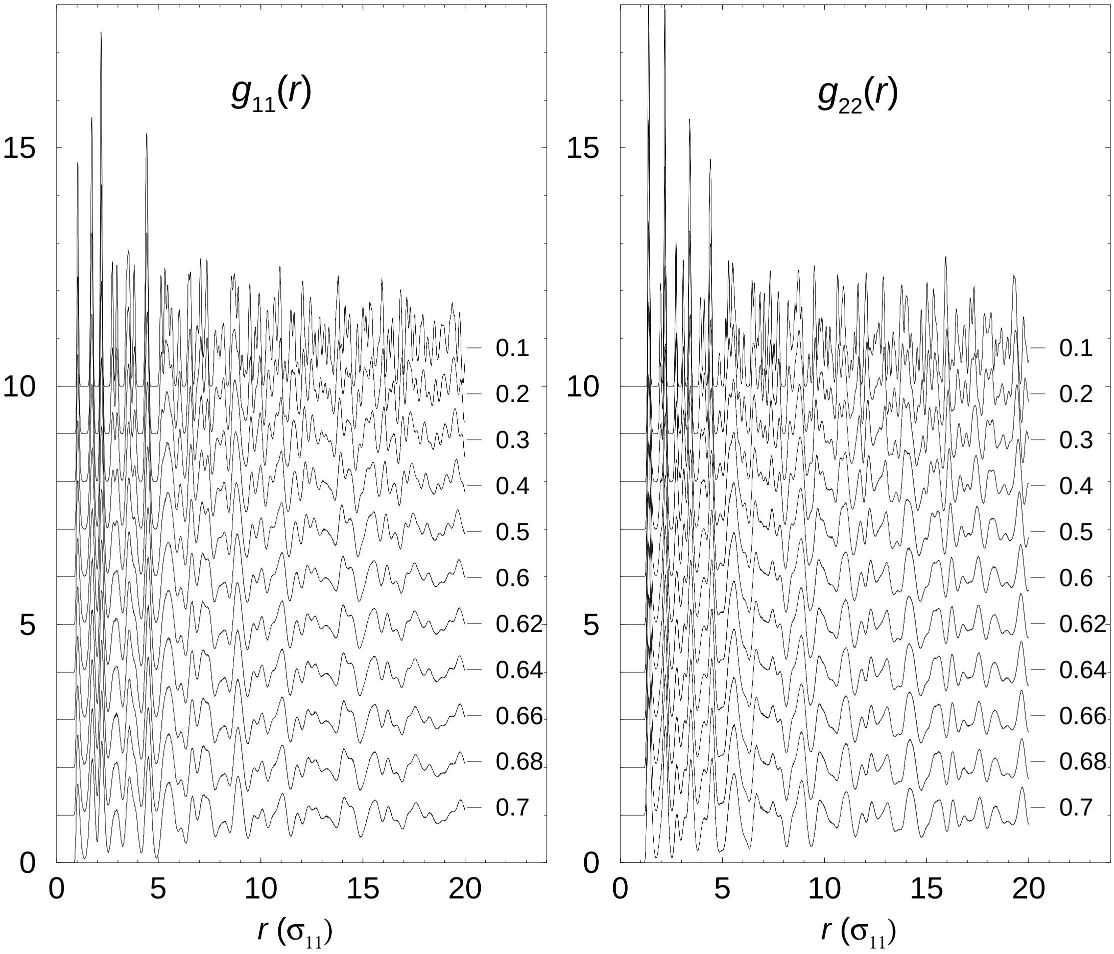

Figure C.3: The partial pair distribution functions $g_{11}(r)$ and $g_{22}(r)$ for the heating traverse as a function of distance from $T = 0.1$ up to $T = 0.7$. For $T \leq 0.7$, each curve has been shifted upwards by one unit from the lower temperature curve directly preceding it.

Table C.11: Cutoff distances for the cooling traverse used to define nearest neighbour interactions for the calculation of local structural properties. These correspond to the positions of the first minima in the respective pair distribution functions.

T	cut_{11}	cut_{12}	cut_{22}
0.6–0.7	1.41	1.64	1.77
0.8–1	1.44	1.66	1.79
2	1.54	1.69	1.84
3	1.60	1.74	1.84
5	1.64	1.77	1.92

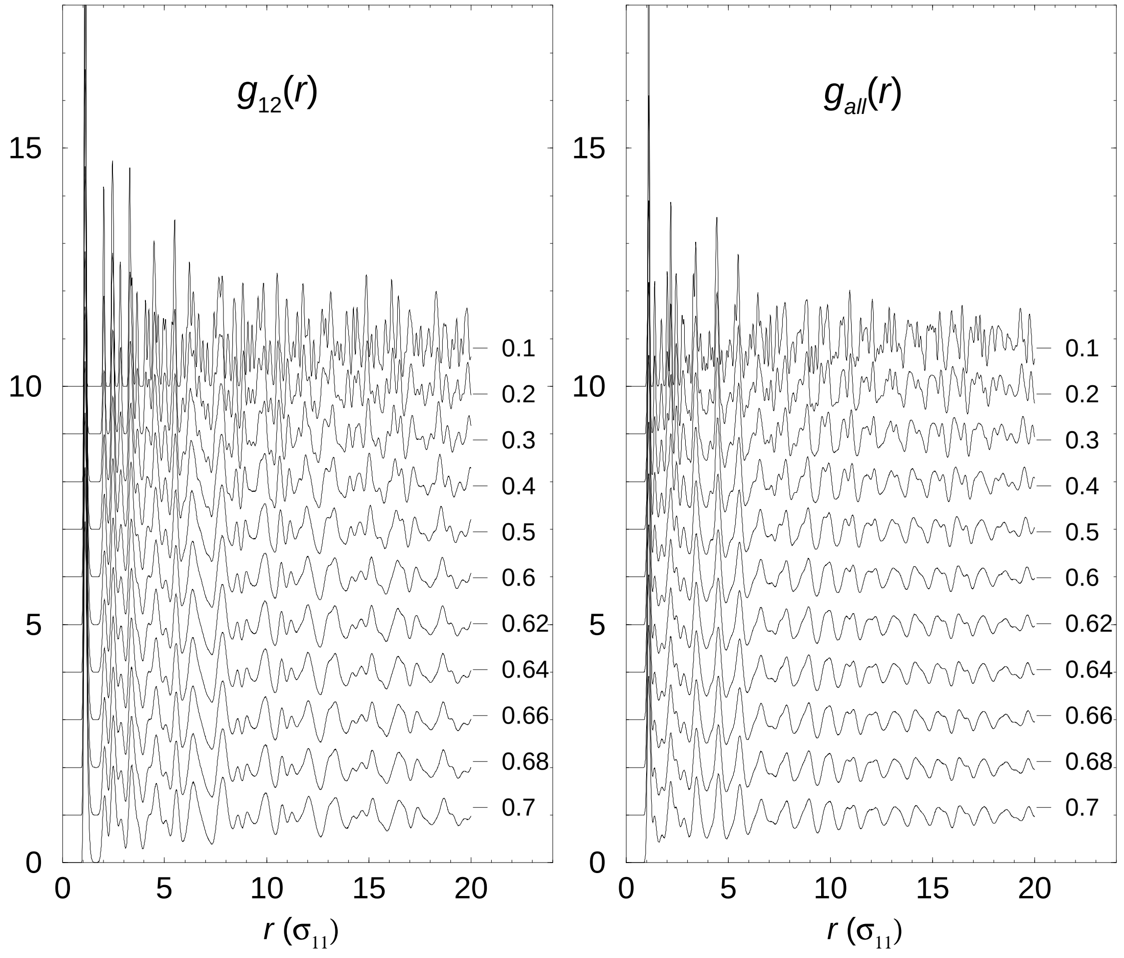

Figure C.4: The partial pair distribution function $g_{12}(r)$ and the total pair distribution function $g_{all}(r)$ for the heating traverse as a function of distance from $T = 0.1$ up to $T = 0.7$. For $T \leq 0.7$, each curve has been shifted upwards by one unit from the lower temperature curve directly preceding it.

Table C.12: Cutoff distances for the heating traverse used to define nearest neighbour interactions for the calculation of local structural properties. These correspond to the positions of the first minima in the respective pair distribution functions.

T	cut_{11}	cut_{12}	cut_{22}
5	1.53	1.72	1.75
0.7–1.06	1.28	1.62	1.8

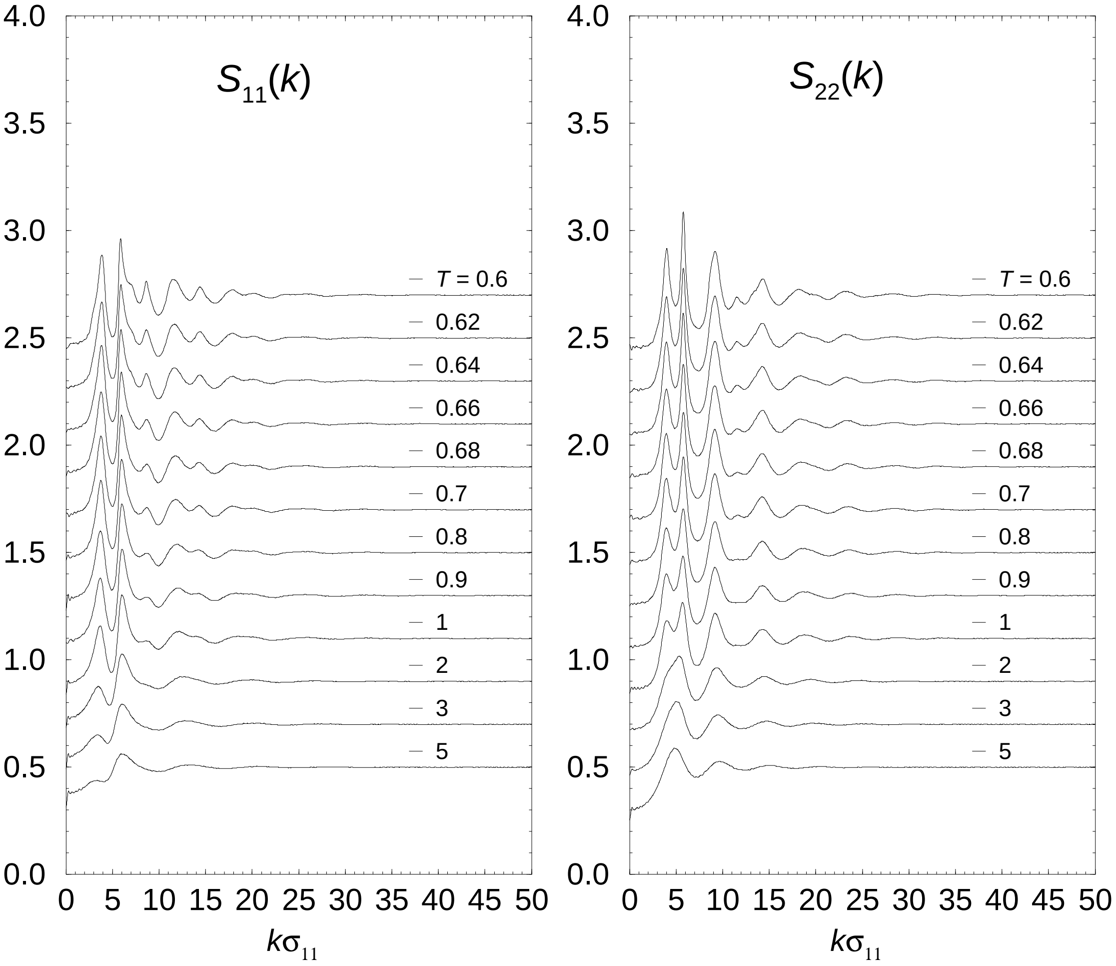

Figure C.5: The partial structure factors $S_{11}(k)$ and $S_{22}(k)$ for temperatures from $T = 5$ down to $T = 0.7$. For clarity, each curve below $T = 5$ has been shifted upwards by 0.2 units above the higher temperature curve directly preceding it.

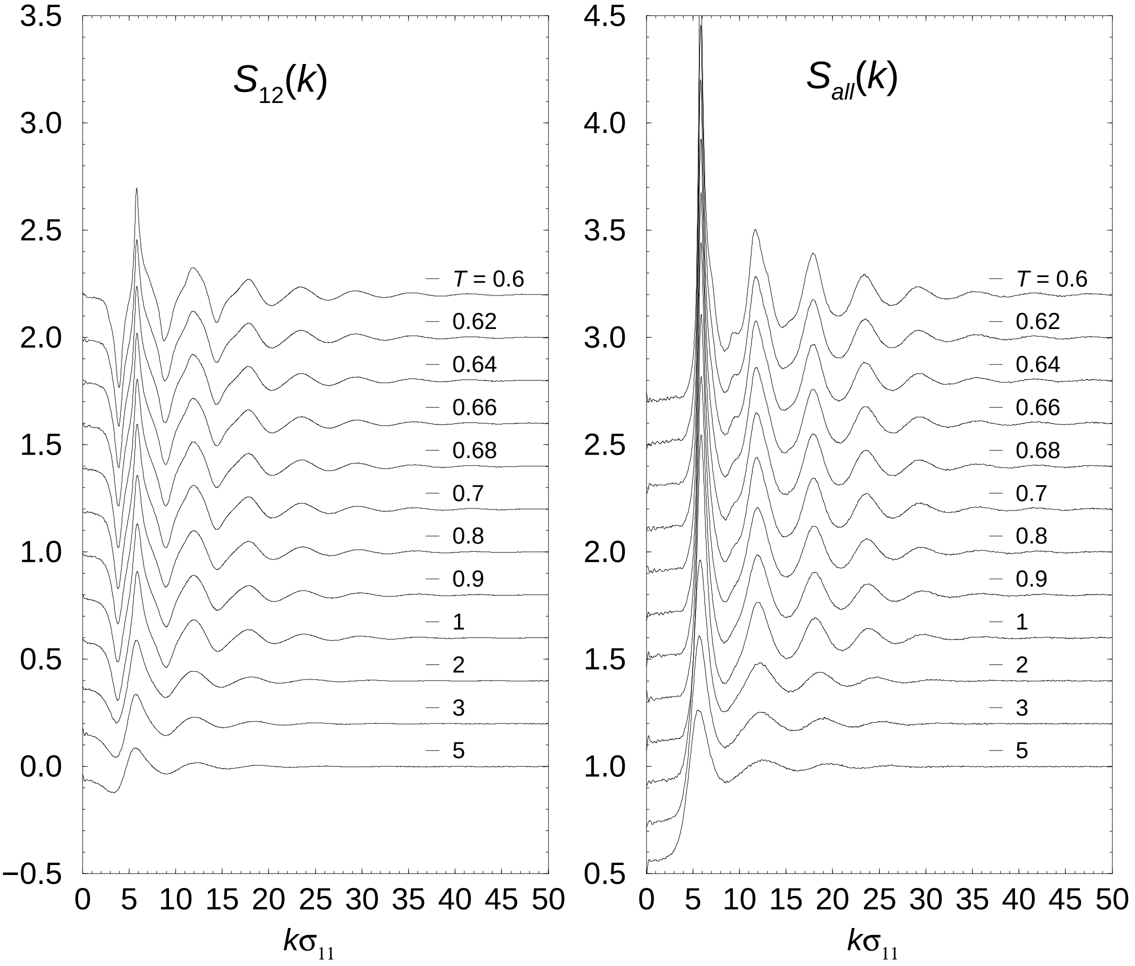

Figure C.6: The partial structure factor $S_{12}(k)$ and the total structure factor $S_{all}(k)$ as a function of wave vector from $T = 5$ down to $T = 0.7$. For clarity, each curve below $T = 5$ has been shifted upwards by 0.2 units above the higher temperature curve directly preceding it.

Table C.13: The locations of the first peak positions k_1 and k_2 in the respective partial structure factors $S_{11}(k)$ and $S_{22}(k)$. These wave vectors have been used to calculate the incoherent scattering functions.

T	k_1	k_2
0.6	5.87	5.80
0.62–0.64	5.93	5.80
0.66–0.7	5.99	5.80
0.8–0.9	6.04	5.75
1	6.04	5.71
2	6.04	5.34
3	6.10	5.06
5	6.10	4.92

Table C.14: The temperature dependence of the structural relaxation time $\tau_{e,1}$, and the self-diffusion coefficients of the small and large particles, D_1 and D_2, respectively.

T	$\tau_{e,1}/\tau$	$D_1/\sigma_{11}^2\tau^{-1}$	$D_2/\sigma_{11}^2\tau^{-1}$
5	0.118	0.65143	0.55817
3	0.170	0.33354	0.28988
2	0.243	0.17869	0.15712
1	0.603	0.03363	0.02966
0.9	0.733	0.02144	0.01906
0.8	0.945	0.01180	0.01045
0.7	1.45	0.00484	0.00413
0.68	1.64	0.00369	0.00349
0.66	1.88	0.00260	0.00207
0.64	2.51	0.00199	0.00166
0.62	2.77	0.00129	0.00102
0.6	5.02	0.00069	0.00054

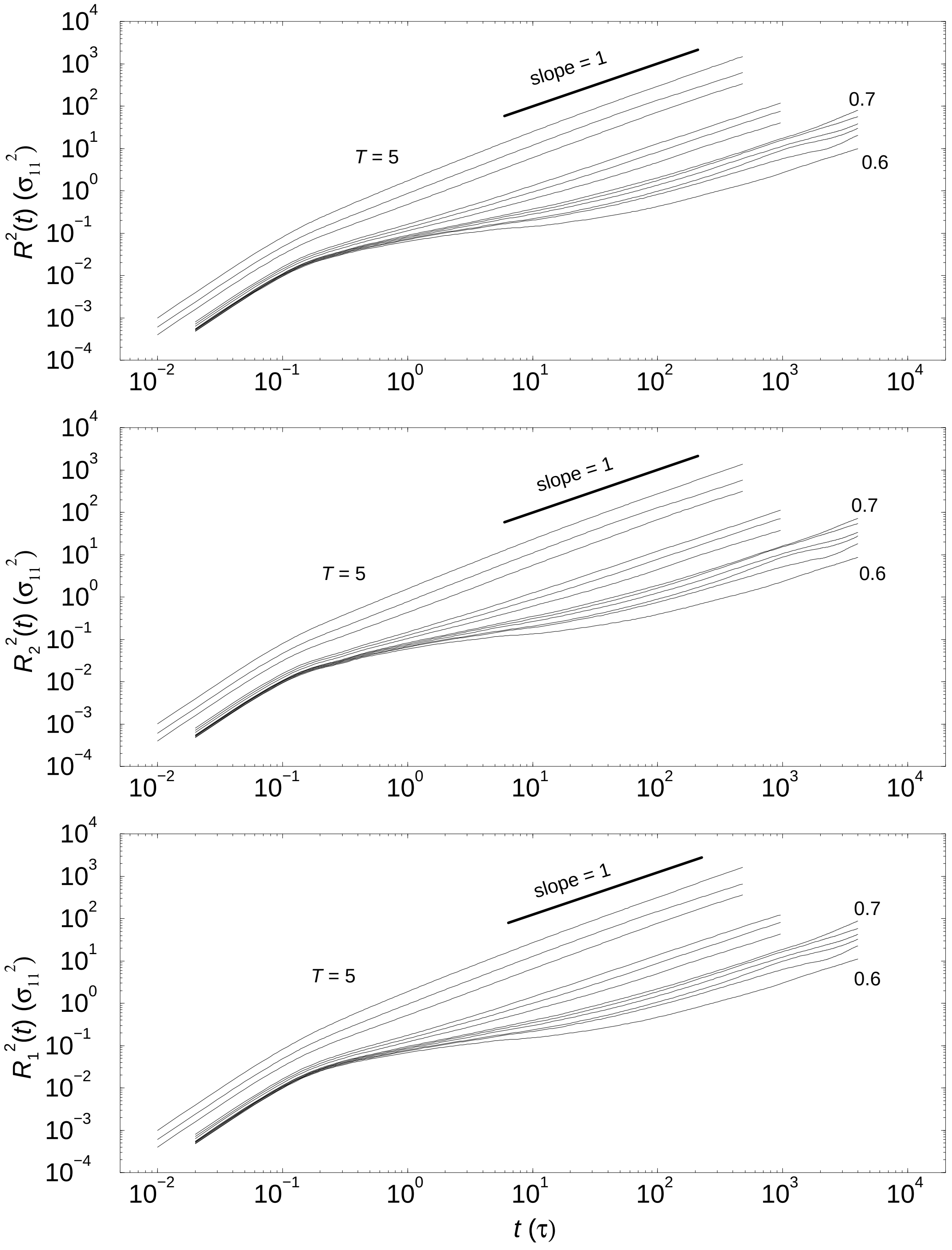

Figure C.7: The time dependence of the MSD averaged over all particles $R^2(t)$, and averaged over the two particle species, $R_2^2(t)$ and $R_1^2(t)$. The temperature of the curves from left to right is the same as in Figure 6.11.

C.4 $\sigma_{12} = 1.1,\ x_1 = 0.3167$

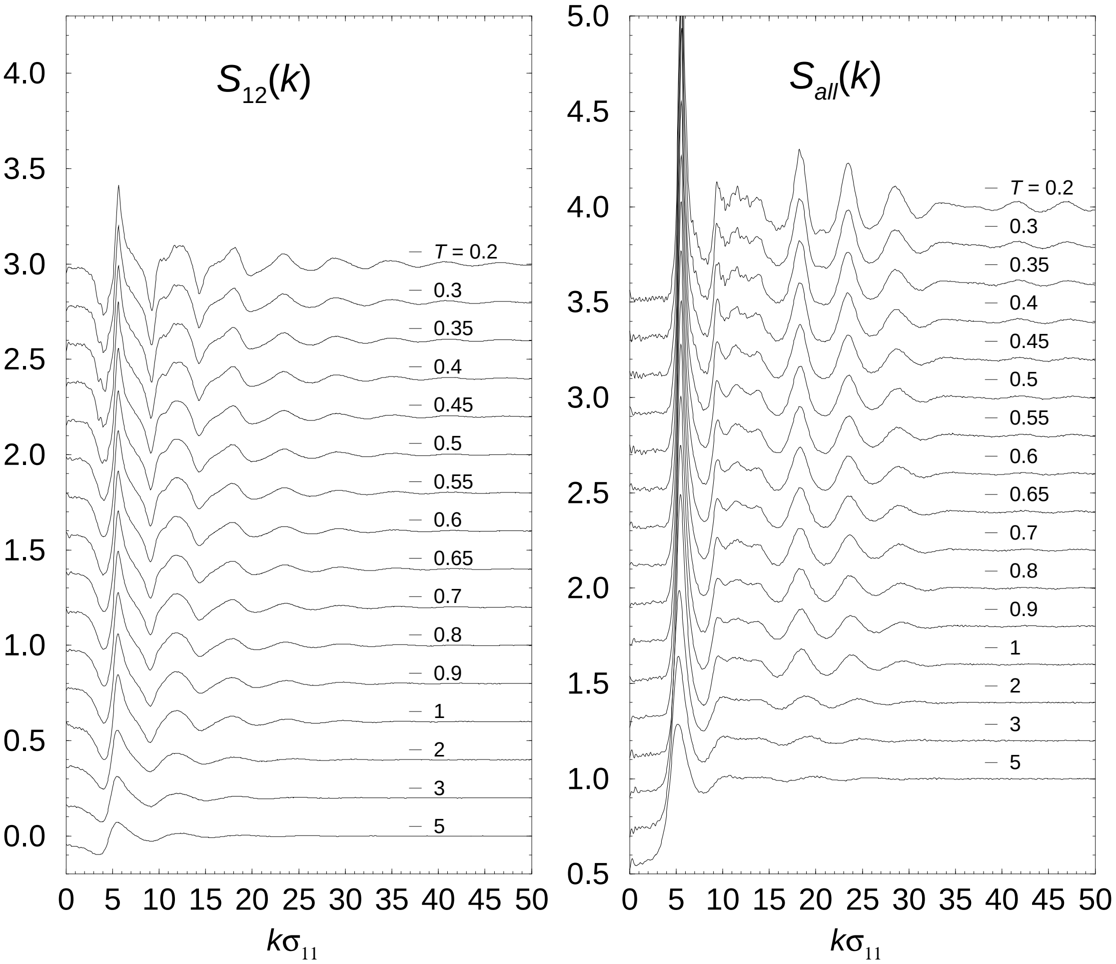

Figure C.8: The partial structure factor $S_{12}(k)$ and the total structure factor $S_{all}(k)$ as a function of wave vector from $T = 5$ down to $T = 0.2$. For clarity, each curve below $T = 5$ has been shifted upwards by 0.2 units above the higher temperature curve directly preceding it.

Table C.15: The thermodynamic averages and their root mean square (rms) deviations for the cooling traverse for the non-equimolar mixture with $\sigma_{12} = 1.1$. Also shown are the effective coupling constant Γ, the compressibility factor Z, the equilibration time t_{eqlb}, and the production time t_{run} for each of these states.

T	t_{eqlb}/τ	t_{run}/τ	U	E	H	ρ
5	500	1000	3.2077	8.1965	32.439	0.5567
3	500	1000	3.1764	6.1730	28.241	0.6120
2	500	1000	3.1455	5.1431	26.025	0.6467
1	500	2000	3.0932	4.0876	23.635	0.6901
0.9	1000	2000	3.0864	3.9868	23.425	0.6951
0.8	1000	2000	3.0790	3.8731	23.125	0.7003
0.7	1000	2000	3.0715	3.7664	22.881	0.7056
0.65	4000	2000	3.0678	3.7129	22.763	0.7083
0.6	4000	2000	3.0637	3.6589	22.624	0.7111
0.55	4000	2000	3.0599	3.6070	22.506	0.7138
0.5	6000	2000	3.0569	3.5574	22.408	0.7164
0.45	10000	20000	3.0535	3.5003	22.264	0.7191
0.4	10000	20000	3.0489	3.4487	22.148	0.7221
0.35	10000	20000	3.0479	3.3963	22.031	0.7243
0.3	10000	20000	3.0472	3.3476	21.938	0.7264
0.2	10000	20000	3.0463	3.2431	21.705	0.7306

T	Γ	Z	rms(U)	rms(E)	rms(H)	rms(ρ)
5	0.42573	4.8499	0.0971	0.1619	0.7132	0.0036
3	0.50960	7.3530	0.0782	0.1177	0.5780	0.0032
2	0.57612	10.438	0.0608	0.0770	0.4281	0.0027
1	0.69006	19.563	0.0433	0.0547	0.3094	0.0019
0.9	0.70740	21.580	0.0408	0.0493	0.3024	0.0018
0.8	0.72685	24.096	0.0396	0.0474	0.2858	0.0017
0.7	0.74887	27.331	0.0361	0.0391	0.2386	0.0015
0.65	0.76103	29.322	0.0358	0.0369	0.2414	0.0016
0.6	0.77431	31.641	0.0333	0.0363	0.2291	0.0014
0.55	0.78864	34.385	0.0328	0.0362	0.2395	0.0014
0.5	0.80418	37.686	0.0306	0.0323	0.2077	0.0013
0.45	0.82151	41.717	0.0294	0.0333	0.2177	0.0012
0.4	0.84127	46.737	0.0272	0.0287	0.1905	0.0011
0.35	0.86279	53.254	0.0255	0.0288	0.1881	0.0011
0.3	0.88785	61.947	0.0237	0.0239	0.1619	0.0010
0.2	0.95533	92.394	0.0191	0.0191	0.1297	0.0008

Table C.16: Cutoff distances for the cooling traverse used to define nearest neighbour interactions for the calculation of local structural properties and the definition of 'bonds'. These correspond to the positions of the first minima in the respective pair distribution functions.

T	cut_{11}	cut_{12}	cut_{22}
5	1.52	1.78	2.00
3	1.52	1.75	1.94
2	1.52	1.71	1.90
0.2–1	1.37	1.64	1.80

Table C.17: The temperature dependence of the structural relaxation times $\tau_{e,1}$ and $\tau_{e,2}$, and the self-diffusion coefficients of the small and large particles, D_1 and D_2, respectively.

T	$\tau_{e,1}/\tau$	$\tau_{e,2}/\tau$	$D_1/\sigma_{11}^2\tau^{-1}$	$D_2/\sigma_{11}^2\tau^{-1}$
5	0.234	0.143	0.67173	0.55700
3	0.374	0.219	0.33209	0.28625
2	0.613	0.342	0.17204	0.15034
1	2.01	0.959	0.03352	0.02753
0.9	2.75	1.2	0.02130	0.01746
0.8	4.02	1.61	0.01412	0.01208
0.7	6.89	2.46	0.00819	0.00666
0.65	10.8	3.29	0.00447	0.00368
0.6	20.2	5.03	0.00225	0.00184
0.55	48.4	12.1	0.00136	0.00109
0.5	130	37.8	0.00046	0.00036
0.45	665	237	0.00012	0.00009

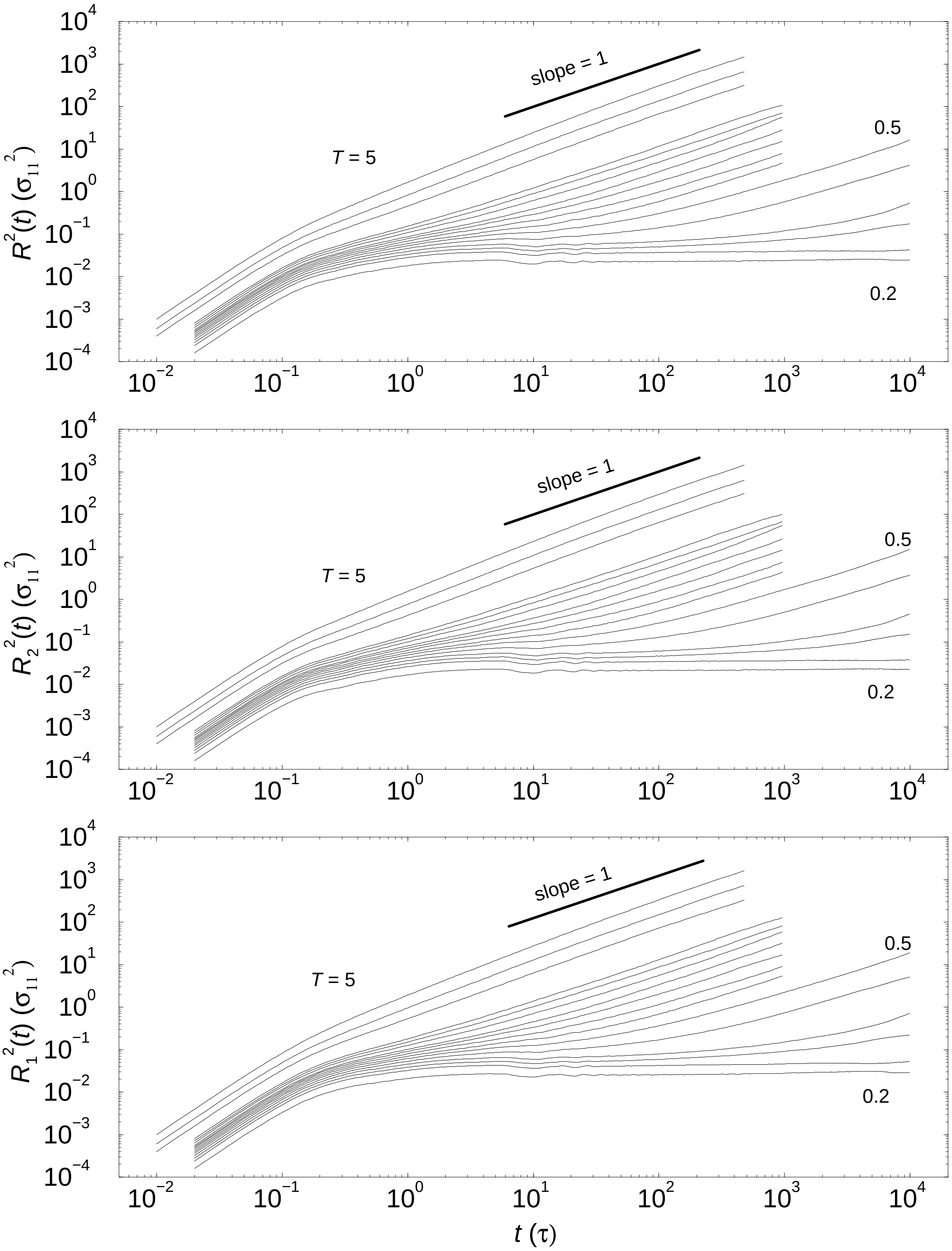

Figure C.9: The time dependence of the MSD averaged over all particles $R^2(t)$, and averaged over the two particle species, $R_2{}^2(t)$ and $R_1{}^2(t)$. The temperature of the curves from left to right is the same as in Figure 6.29.

C.5 $\sigma_{12} = 1.2,\ x_1 = 0.3164$

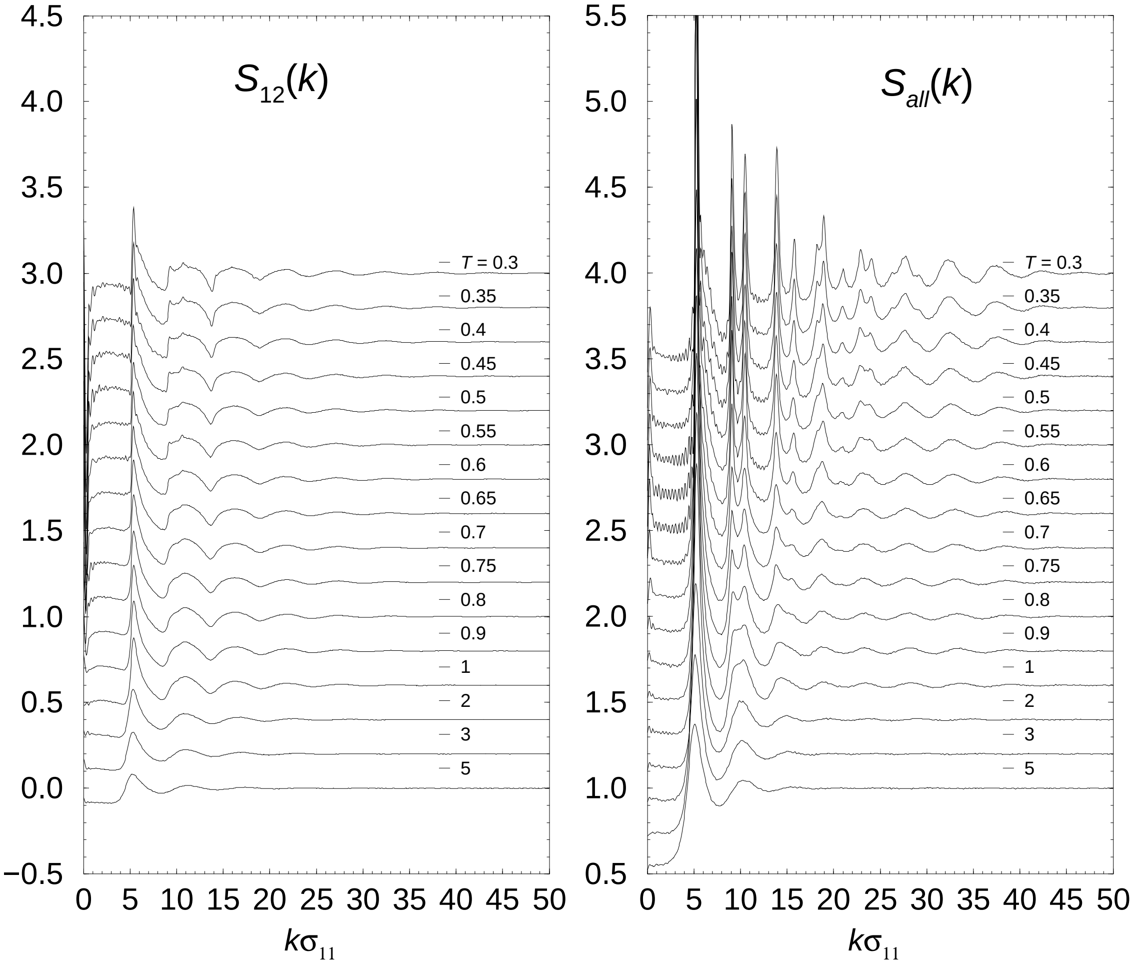

Figure C.10: The partial structure factor $S_{12}(k)$ and the total structure factor $S_{all}(k)$ as a function of wave vector from $T = 5$ down to $T = 0.3$. For clarity, each curve below $T = 5$ has been shifted upwards by 0.2 units above the higher temperature curve directly preceding it.

Table C.18: The thermodynamic averages and their root mean square (rms) deviations for the binary mixture with $\sigma_{12} = 1.2$ and $x_1 = 0.3164$. Also shown are the effective coupling constant Γ, the compressibility factor Z, the equilibration time $t_{\rm eqlb}$, and the production time $t_{\rm run}$ for each of these states.

T	$t_{\rm eqlb}/\tau$	$t_{\rm run}/\tau$	U	E	H	ρ
5	2000	2000	3.3864	8.3646	33.663	0.5331
3	2000	2000	3.3569	6.3560	29.552	0.5833
2	2000	2000	3.3280	5.3297	27.304	0.6146
1	2000	2000	3.2805	4.2768	24.969	0.6526
0.9	2000	4000	3.2742	4.1704	24.726	0.6570
0.8	4000	4000	3.2644	4.0605	24.434	0.6621
0.75	6000	4000	3.2587	4.0042	24.298	0.6649
0.7	8000	4000	3.2553	3.9510	24.173	0.6672
0.65	20000	20000	3.2491	3.8958	24.041	0.6701
0.6	50000	20000	3.2423	3.8370	23.879	0.6731
0.55	50000	20000	3.2346	3.7850	23.752	0.6764
0.5	50000	20000	3.2308	3.7287	23.616	0.6788
0.45	50000	20000	3.2283	3.6767	23.498	0.6811
0.4	50000	20000	3.2260	3.6242	23.375	0.6833
0.35	50000	20000	3.2244	3.5760	23.287	0.6854
0.3	50000	20000	3.2235	3.5210	23.153	0.6873

T	Γ	Z	rms(U)	rms(E)	rms(H)	rms(ρ)
5	0.4077	5.0648	0.1404	0.1922	0.9684	0.0060
3	0.4857	7.7143	0.0885	0.1297	0.6359	0.0030
2	0.5475	10.983	0.0650	0.0880	0.4614	0.0021
1	0.6526	20.686	0.0556	0.0615	0.3616	0.0021
0.9	0.6686	22.832	0.0489	0.0560	0.3417	0.0019
0.8	0.6872	25.487	0.0462	0.0519	0.3355	0.0018
0.75	0.6976	27.071	0.0696	0.0793	0.4829	0.0025
0.7	0.7081	28.905	0.0654	0.0755	0.4728	0.0024
0.65	0.7200	30.995	0.0433	0.0475	0.2996	0.0017
0.6	0.7329	33.427	0.0343	0.0367	0.2400	0.0013
0.55	0.7472	36.290	0.0363	0.0396	0.2580	0.0014
0.5	0.7620	39.773	0.0359	0.0396	0.2632	0.0014
0.45	0.7780	44.048	0.0339	0.0371	0.2440	0.0013
0.4	0.7960	49.393	0.0312	0.0325	0.2141	0.0012
0.35	0.8164	56.279	0.0288	0.0287	0.1922	0.0011
0.3	0.8400	65.475	0.0276	0.0285	0.1929	0.0010

Table C.19: Cutoff distances for the cooling traverse used to define nearest neighbour interactions for the calculation of local structural properties and the definition of 'bonds'. These correspond to the positions of the first minima in the respective pair distribution functions.

T	cut_{11}	cut_{12}	cut_{22}
5	1.71	1.85	2
3	1.65	1.8	1.98
2	1.61	1.77	1.96
1	1.54	1.74	1.92
0.75–0.9	1.5	1.72	1.9
0.5–0.7	1.46	1.7	1.88
0.3–0.45	1.43	1.68	1.86

Table C.20: The temperature dependence of the structural relaxation times $\tau_{e,1}$ and $\tau_{e,2}$, and the self-diffusion coefficients of the small and large particles, D_1 and D_2, respectively.

T	$\tau_{e,1}/\tau$	$\tau_{e,2}/\tau$	$D_1/\sigma_{11}^2\tau^{-1}$	$D_2/\sigma_{11}^2\tau^{-1}$
5	0.114	0.143	0.65793	0.57051
3	0.160	0.224	0.31750	0.27779
2	0.229	0.345	0.16750	0.14510
1	0.524	1.07	0.03136	0.02381
0.9	0.641	1.37	0.02106	0.01468
0.8	0.838	2.25	0.01242	0.00741
0.75	0.917	3.07	0.01022	0.00543
0.7	1.20	3.93	0.00683	0.00380
0.65	1.44	9.42	0.00418	0.00197
0.6	1.96	33.8	0.00241	0.00082
0.55	4.30	310	0.00096	0.00024
0.5	26.4	2550	0.00043	0.00007
0.45	185		0.00016	0.00003

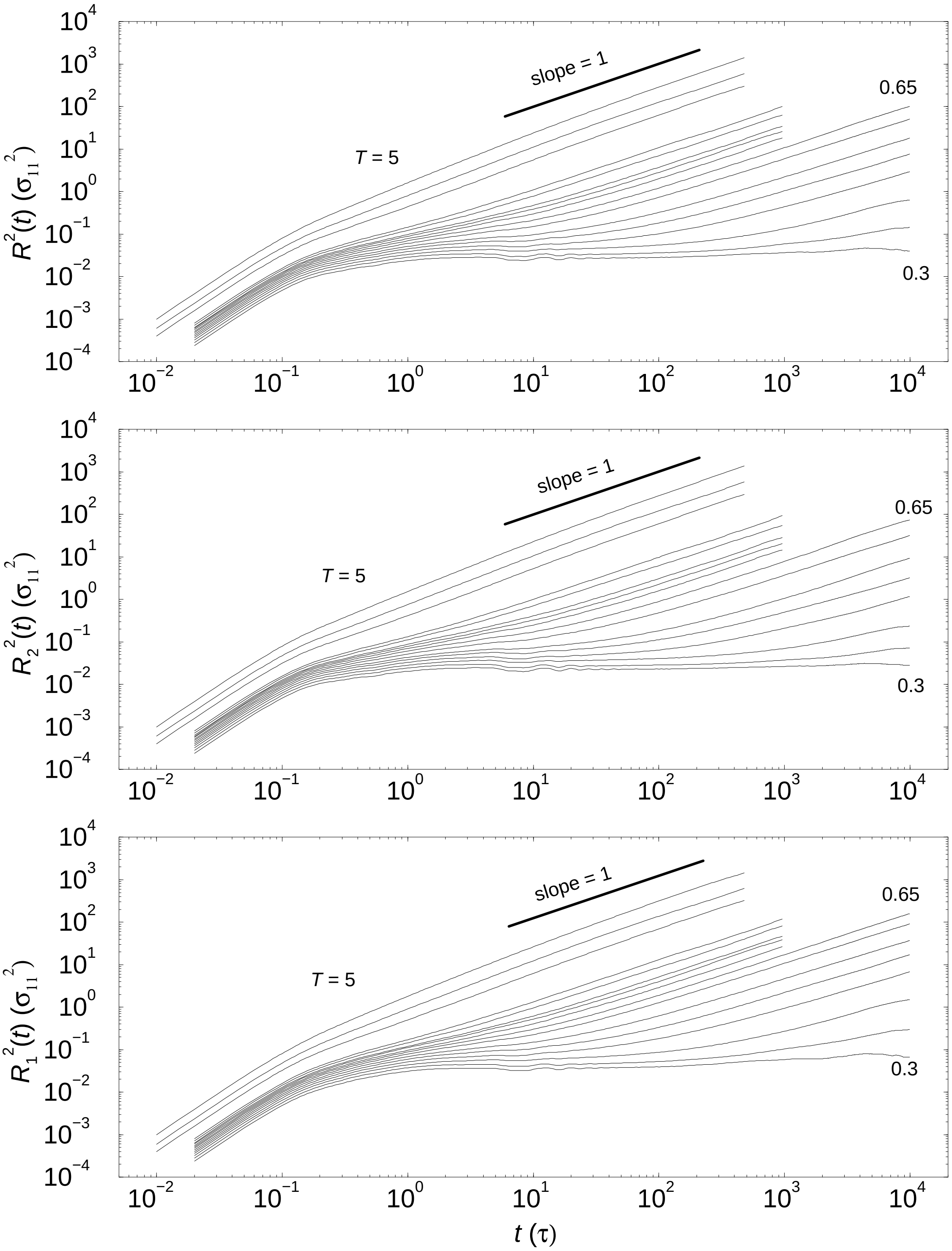

Figure C.11: The time dependence of the MSD averaged over all particles $R^2(t)$, and averaged over the two particle species, ${R_2}^2(t)$ and ${R_1}^2(t)$. The temperature of the curves from left to right is the same as in Figure 7.10.

References

[1] Anderson, P. W. *Science* **267**, 1615 (1995).

[2] Cahn, R. W. *The Coming of Materials Science*. Pergamon, Amsterdam (2001).

[3] Pusztai, L. & McGreevy, R. L. *Mol. Simul.* **1**, 359 (1988).

[4] McGreevy, R. L. *J. Phys. Cond. Matter* **13**, R877 (2001).

[5] Soper, A. K. *Chem. Phys.* **202**, 295 (1996).

[6] Biswas, P., Tafen, D. & Drabold, D. A. *Phys. Rev. B* **71**, 054204 (2005).

[7] Sheng, H. W., Luo, W. K., Alamgir, F. M., Bai, J. M. & Ma, E. *Nature* **439**, 419 (2006).

[8] Rawson, H. *Properties and Applications of Glass*. Elsevier, Amsterdam (1980).

[9] Zallen, R. *The Physics of Amorphous Solids*. John Wiley and Sons, New York (1983).

[10] Debenedetti, P. G. *Metastable Liquids*. Princeton University Press, New Jersey (1996).

[11] Ediger, M. D. *Ann. Rev. Phys. Chem.* **51**, 99 (2000).

[12] Angell, C. A., Ngai, K. L., McKenna, G. B., McMillan, P. F. & Martin, S. W. *J. App. Phys.* **88**, 3113 (2000).

[13] Debenedetti, P. G. & Stillinger, F. H. *Nature* **410**, 259 (2001).

[14] Andersen, H. C. *Proc. Natl. Acad. Sci. USA* **102**, 6686 (2005).

[15] Cipelletti, L. & Ramos, L. *J. Phys. Cond. Matter* **17**, R253 (2005).

[16] Angell, C. A. *Science* **267**, 1924 (1995).

[17] Fourkas, J. T. *Chem. Ind.* **16**, 644 (1998).

[18] Cicerone, M. T., Tellington, A., Trost, L. & Sokolov, A. *BioProcess Int.* **1**, 36 (2003).

[19] Böhmer, R., Ngai, K. L., Angell, C. A. & Plazek, D. J. *J. Chem. Phys.* **99**, 4201 (1993).

[20] Frick, B. & Richter, D. *Science* **267**, 1939 (1995).

[21] Bartsch, E. *et al.* *Ber. Bunsenges. Phys. Chem.* **95**, 1146 (1991).

[22] Kiebel, M. *et al.* *Phys. Rev. B* **45**, 10301 (1992).

[23] Fischer, E. W., Donth, E. & Steffen, W. *Phys. Rev. Lett.* **68**, 2344 (1992).

[24] Steffen, W., Patkowski, A., Meier, G. & Fischer, E. W. *J. Chem. Phys.* **96**, 4171 (1992).

[25] Steffen, W., Meier, G., Patkowski, A. & Fischer, E. W. *Physica A* **201**, 300 (1993).

[26] Schnauss, W., Fujara, F. & Sillescu, H. *J. Chem. Phys.* **97**, 1378 (1992).

[27] Lewis, L. J. & Wahnström, G. *Phys. Rev. E* **50**, 3865 (1994).

[28] Kob, W. & Andersen, H. C. *Phys. Rev. E* **52**, 4134 (1995).

[29] Segrè, P. N., Meeker, S. P., Pusey, P. N. & Poon, W. C. K. *Phys. Rev. Lett.* **75**, 958 (1995).

[30] Segrè, P. N., Behrend, O. P. & Pusey, P. N. *Phys. Rev. E* **52**, 5070 (1995).

[31] Mezei, F. *J. Non-Cryst. Solids* **131-133**, 317 (1991).

[32] Mezei, F., Knaak, W. & Farago, B. *Phys. Rev. Lett.* **58**, 571 (1987).

[33] Turnbull, D. & Fisher, J. C. *J. Chem. Phys.* **17**, 71 (1949).

[34] Cohen, M. & Turnbull, D. *J. Chem. Phys.* **31**, 1164 (1959).

[35] Turnbull, D. *Contemp. Phys.* **10**, 473 (1969).

[36] Uhlmann, D. R. *J. Non-Cryst. Solids* **7**, 337 (1972).

[37] Chang, S. S. & Bestul, A. B. *J. Chem. Phys.* **56**, 503 (1972).

[38] Brawer, S. *Relaxation in Viscous Liquids and Glasses.* Am. Ceram. Soc., Ohio (1985).

[39] Leheny, R. L. *et al.* *J. Chem. Phys.* **105**, 7783 (1996).

[40] Tolle, A., Schober, H., Wuttke, J. & Fujara, F. *Phys. Rev. E* **56**, 809 (1997).

[41] Tammann, G. *Der Glasszustand.* Leopold Voss, Leipzig (1933).

[42] Richert, R. *J. Phys. Cond. Matter* **14**, R703 (2002).

[43] Sillescu, H., Böhmer, R., Diezemann, G. & Hinze, G. *J. Phys. Cond. Matter* **16**, 307 (2002).

[44] Perera, D. N. & Harrowell, P. *J. Chem. Phys.* **11**, 5441 (1999).

[45] Foley, M. & Harrowell, P. *J. Chem. Phys.* **98**, 5069 (1993).

[46] Kob, W., Donati, C., Plimpton, S. J., Poole, P. H. & Glotzer, S. C. *Phys. Rev. Lett.* **79**, 2827 (1997).

[47] Doliwa, B. & Heuer, A. *J. Non-Cryst. Solids* **307-310**, 32 (2002).

[48] Doliwa, B. & Heuer, A. *Phys. Rev. E* **61**, 6898 (2002).

[49] Yamamoto, R. & Onuki, A. *Phys. Rev. E* **58**, 3515 (1998).

[50] Qian, J., Hentschke, R. & Heuer, A. *J. Chem. Phys.* **111**, 10177 (1999).

[51] Perera, D. & Harrowell, P. *Phys. Rev. E* **54**, 1652 (1996).

[52] Schmidt-Rohr, K. & Spiess, H. W. *Phys. Rev. Lett.* **66**, 3020 (1991).

[53] Yang, M. & Richert, R. *J. Chem. Phys.* **115**, 2676 (2001).

[54] Ediger, M. *J. Chem. Phys.* **103**, 752 (1995).

[55] Schiener, B., Böhmer, R., Loidl, A. & Chamberlin, R. V. *Science* **274**, 752 (1996).

[56] Chang, I. *et al.* *J. Non-Cryst. Solids* **172-4**, 248 (1994).

[57] Swallen, S. F., Bonvallet, P. A., McMahon, R. J. & Ediger, M. D. *Rev. Phys. Lett.* **90**, 015901 (2003).

[58] Forrest, J. A., Dalnoki-Veress, K. & Dutcher, J. R. *Phys. Rev. E* **56**, 5705 (1997).

[59] Tracht, U. *et al.* *Rev. Phys. Lett.* **81**, 2727 (1998).

[60] Reinsberg, S. A., Heuer, A., Doliwa, B., Zimmermann, H. & Spiess, H. W. *J. Non-Cryst. Solids* **307-310**, 208 (2002).

[61] Hansen, J. & Macdonald, I. *Theory of Simple Liquids.* Academic Press, New York (1986).

[62] Götze, W. *in Liquids, Freezing and the Glass Transition*, 287. North-Holland, Amsterdam (1991).

[63] Flyn, C. *Point Defects and Diffusion.* Clarendon Press, Oxford (1972).

[64] Szamel, G. *J. Chem. Phys.* **121**, 3355 (2004).

[65] Ritort, F. & Sollich, P. *Adv. Phys.* **52**, 219 (2003).

[66] Cates, M. *Preprint* , http://www.arxiv.org.abs/cond–mat/0211066 (2002).

[67] Perera, D. N. & Harrowell, P. *Phys. Rev. E* **59**, 5721 (1999).

[68] Donati, C. *et al.* *Phys. Rev. Lett.* **80**, 2338 (1998).

[69] Vogel, M., Doliwa, B., Heuer, A. & Glotzer, S. C. *J. Chem. Phys.* **120**, 4404 (2004).

[70] Delaye, J. M. & Limoge, Y. *J. Non-Cryst. Solids* **156-158**, 982 (1993).

[71] Fredrickson, G. H. & Andersen, H. C. *Phys. Rev. Lett.* **53**, 1244 (1984).

[72] Jäckle, J. & Eisinger, S. *Z. Phys. C* **84**, 115 (1991).

[73] Garraghan, J. & Chandler, D. *Proc. Natl. Acad. Sci. USA* **100**, 9710 (2003).

[74] Hurley, M. & Harrowell, P. *J. Chem. Phys.* **105**, 10521 (1996).

[75] Swallen, S., Urakawa, O., Mapes, M. & Ediger, M. D. *AIP Conf. Proc.* **708**, 491 (2004).

[76] Harrowell, P. & Oxtoby, D. W. *Ceramic Transactions* **30**, 35 (1993).

[77] Tarjus, G. & Kivelson, D. *J. Chem. Phys.* **103**, 3071 (1995).

[78] Perera, D. N. & Harrowell, P. *Phys. Rev. Lett.* **81**, 120 (1998).

[79] Donati, C., Glotzer, S. C., Poole, P. H., Kob, W. & Plimpton, S. J. *Phys. Rev. E* **60**, 3107 (1999).

[80] Starr, F. W., Sastry, S., Douglas, J. F. & Glotzer, S. C. *Phys. Rev. Lett.* **89**, 125501 (2002).

[81] Goldstein, M. *J. Chem. Phys.* **53**, 3728 (1969).

[82] Schrøder, T. B., Sastry, S., Dyre, J. C. & Glotzer, S. C. *J. Chem. Phys.* **112**, 9834 (2000).

[83] Bond, S. D., Leimkuhler, B. J. & Laird, B. B. *J. Comp. Phys.* **151**, 114 (1999).

[84] Sturgeon, J. B. & Laird, B. B. *J. Chem. Phys.* **112**, 3474 (2000).

[85] Broughton, J. Q., Gilmer, G. H. & Weeks, J. D. *J. Chem. Phys.* **75**, 5128 (1981).

[86] Doliwa, B. & Heuer, A. *Phys. Rev. Lett.* **91**, 235501 (2003).

[87] Fisher, N., Lewis, T. & Embleton, B. *Statistical Analysis of Spherical Data.* Cambridge University Press, Cambridge (1987).

[88] OriginLab. *Origin 7.5.* Northampton, MA (2005).

[89] Perera, D. N. *The Effect of Kinetic Inhomogeneities in Supercooled Glass-forming Liquids.* PhD thesis, University of Sydney, Australia, (1998).

[90] Kanji, G. K. *100 Statistical Tests.* SAGE Publications (1999).

[91] Chandrasekhar, S. *Rev. Mod. Phys.* **15**, 1 (1943).

[92] Odagaki, T. & Hiwatari, Y. *Phys. Rev. A* **A 43**, 1103 (1991).

[93] Odagaki, T. & Yoshimori, Y. *J. Phys. Cond. Matter* **12**, 6509 (2000).

[94] Chudley, C. T. & Elliott, R. J. *Proc. Phys. Soc.* **77**, 353 (1960).

[95] Vollmayr-Lee, K. *J. Chem. Phys.* **121**, 4781 (2004).

[96] Wahnström, G. *Phys. Rev. A* **44**, 3752 (1991).

[97] Miyagawa, H. & Hiwatari, Y. *Phys. Rev. A* **44**, 8278 (1991).

[98] Rose, C. & Smith, M. D. *Mathematical Statistics with Mathematica*, 256–259. Springer-Verlag, New York (2002).

[99] Zeldovich, Y. B., Ruzmaikin, A. A. & Sokoloff, D. D. *The Almighty Chance.* World Scientific, Singapore (1990).

[100] Batchelor, G. K. & Townsend, A. *Proc. R. Soc. A* **199**, 238 (1949).

[101] Buisson, L., Bellon, L. & Ciliberto, S. *J. Phys. Cond. Matter* **15**, S1163 (2003).

[102] Crisanti, A. & Ritort, F. *Europhys. Lett.* **66**, 253 (2004).

[103] Sastry, S. *Nature* **409**, 164 (2001).

[104] Kob, W. & Andersen, H. C. *Phys. Rev. E* **47**, 3281 (1993).

[105] Jäckle, J. & Krönig, A. *J. Phys. Cond. Matter* **6**, 7633 (1994).

[106] Biroli, G. & Mezard, M. *Phys. Rev. Lett.* **88**, 025501 (2002).

[107] Tsao, S. S. & Spaepen, F. *Acta Metall.* **33**, 881 (1985).

[108] Sastry, S., Debenedetti, P. G. & Stillinger, F. H. *Nature* **393**, 554 (1998).

[109] Büchner, S. & Heuer, A. *Phys. Rev. Lett.* **84**, 2168 (2000).

[110] Nave, E. L. & Sciortino, F. *J. Phys. Chem. B* **108**, 19663 (2004).

[111] Heggen, M., Spaepen, F. & Feuerbacher, M. *J. Appl. Phys.* **97**, 033506 (2005).

[112] Nagel, C., Ratzke, K., Schmidtke, E., Faupel, F. & Ulfert, W. *Phys. Rev. B* **60**, 9212 (1999).

[113] Falk, M. & Langer, J. S. *Phys. Rev. E* **57**, 7192 (1998).

[114] Cohen, M. H. & Grest, G. S. *Phys. Rev. B* **20**, 1077 (1979).

[115] Grest, G. S. & Cohen, M. H. *Adv. Chem. Phys.* **48**, 455 (1981).

[116] Bordat, P., Affouard, F., Descamps, M. & Ngai, K. L. *Phys. Rev. Lett.* **93**, 105502 (2004).

[117] Sastry, S., Corti, D. S., Debenedetti, P. G. & Stillinger, F. H. *Phys. Rev. E* **56**, 5524 (1997).

[118] Press, W. H., Flannery, B. P., Teukolsky, S. A. & Vetterling, W. T. *Numerical Recipies: The Art of Scientific Computing.* Cambridge University Press, Cambridge (2002).

[119] Butler, S. & Harrowell, P. *J. Chem. Phys.* **95**, 4466 (1991).

[120] Alcoutlabi, M. & McKenna, G. B. *J. Phys. Cond. Matter* **17**, R461 (2005).

[121] Scheidler, P., Kob, W. & Binder, K. *NATO Sci. Ser. II Math. Phys. Chem.* **114**, 297 (2003).

[122] Alexander, S. *Phys. Rep.* **296**, 65 (1998).

[123] Kustanovich, T., Rabin, Y. & Olami, Z. *Phys. Rev. B* **67**, 104206 (2003).

[124] Thorpe, M. F. *J. Non-Cryst. Solids* **57**, 355 (1983).

[125] Chubynsky, M. V. & Thorpe, M. F. *Curr. Opin. Solid State Mater. Sci.* **5**, 525 (2001).

[126] Maxwell, J. C. *Philos. Mag.* **27**, 294 (1864).

[127] Phillips, J. C. *J. Non-Cryst. Solids* **34**, 153 (1979).

[128] Brito, C. & Wyart, M. *Preprint* , cond–mat/0512197 (2005).

[129] Donev, A., Torquato, S., Stillinger, F. H. & Connelly, R. *J. Appl. Phys.* **95**, 989 (2004).

[130] Buchenau, U. & Zorn, R. *Europhys. Lett.* **18**, 523 (1992).

[131] Ngai, K. L. *Phil. Mag.* **84**, 1341 (2004).

[132] Ngai, K. L. *J. Non-Cryst. Solids* **275**, 7 (2000).

[133] Scopigno, T., Ruocco, G., Sette, F. & Monaco, G. *Science* **302**, 849 (2003).

[134] Roux, J. N., Barrat, J. L. & Hansen, J.-P. *J. Phys. Cond. Matter* **1**, 7171 (1989).

[135] Lindemann, F. A. *Z. Phys.* **11**, 609 (1910).

[136] Stillinger, F. H. *Science* **267**, 1935 (1995).

[137] Vollmayr-Lee, K., Kob, W., Binder, K. & Zippelius, A. *J. Chem. Phys.* **116**, 5158 (2002).

[138] Laird, B. B. & Schober, H. R. *Phys. Rev. Lett.* **66**, 636 (1991).

[139] Weeks, E. R., Crocker, J. C., Levitt, A. C., Schofield, A. & Weitz, D. *Science* **287**, 627 (2000).

[140] Glarum, S. H. *J. Chem. Phys.* **33**, 1371 (1960).

[141] Vlack, L. H. V. *Elements of Materials Science*. Addison-Wesley, London (1964).

[142] Wyart, M., Silbert, L. E., Nagel, S. R. & Witten, T. A. *Phys. Rev. E* **72**, 051306 (2005).

[143] Wolfram, S. *Nature* **311**, 419 (1984).

[144] Wolfram, S. *Phys. Rev. Lett.* **54**, 735 (1985).

[145] Israeli, N. & Goldenfeld, N. *Phys. Rev. Lett.* **92**, 74105 (2004).

[146] Bernal, J. D. *Proc. R. Soc. London, Ser. A* **280**, 299 (1964).

[147] Nelson, D. R. & Spaepen, F. *Solid State Phys.* **42**, 1 (1989).

[148] Tarjus, G., Kivelson, S. A., Nussinov, Z. & Viot, P. *J. Phys. Cond. Matter* **17**, 1143 (2005).

[149] Nelson, D. R., Rubenstein, M. & Spaepen, F. *Philos. Mag. A* **105**, 46 (1982).

[150] Novick, A. S. & Mader, S. R. *IBM J.* **Sept.-Nov.**, 358 (1965).

[151] Kob, W. & Andersen, H. C. *Phys. Rev. E* **51**, 4626 (1985).

[152] Sibug-Aga, R. & Laird, B. B. *Phys. Rev. B* **66**, 144106 (2002).

[153] Jalali, P. & Li, M. *Intermetallics* **12**, 1167 (2004).

[154] Wheatley, R. J. *Mol. Phys.* **93**, 965 (1998).

[155] Likos, C. N. & Henley, C. L. *Phil. Mag. B* **68**, 85 (1993).

[156] Rubenstein, M. & Nelson, D. R. *Phys. Rev. B* **26**, 6254 (1982).

[157] Sadr-Lahijany, M. R., Ray, P. & Stanley, H. E. *Phys. Rev. Lett.* **79**, 3206 (1997).

[158] Weber, T. A. & Stillinger, F. H. *Phys. Rev. E* **48**, 4351 (1993).

[159] Leung, P. W., Henley, C. L. & Chester, G. V. *Phys. Rev. B* **39**, 446 (1989).

[160] Widom, M., Strandburg, K. J. & Swendsen, R. H. *Phys. Rev. Lett.* **58**, 706 (1987).

[161] Lee, H. K., Swendsen, R. H. & Widom, M. *Phys. Rev. B* **64**, 224201 (2001).

[162] Speedy, R. J. *J. Chem. Phys.* **110**, 4559 (1999).

[163] Deng, D., Argon, A. S. & Yip, S. *Phil. Trans. R. Soc. Lond. A* **329**, 549 (1989).

[164] Deng, D., Argon, A. S. & Yip, S. *Phil. Trans. R. Soc. Lond. A* **329**, 575 (1989).

[165] Deng, D., Argon, A. S. & Yip, S. *Phil. Trans. R. Soc. Lond. A* **329**, 595 (1989).

[166] Deng, D., Argon, A. S. & Yip, S. *Phil. Trans. R. Soc. Lond. A* **329**, 613 (1989).

[167] Muranaka, T. & Hiwatari, Y. *Phys. Rev. E* **51**, R2735 (1995).

[168] Shintani, H. & Tanaka, H. *Nature Phys.* **2**, 200 (2006).

[169] Gray, J. J. & Bonnecaze, R. T. *Langmuir* **17**, 7935 (2001).

[170] Weis, J. J. *Mol. Phys.* **100**, 579 (2002).

[171] Broughton, J. Q., Gilmer, G. H. & Weeks, J. D. *Phys. Rev. B* **25**, 4651 (1982).

[172] Bocquet, L., Hansen, J.-P., Biben, T. & Madden, P. *J. Phys. Cond. Matter* **4**, 2375 (1992).

[173] Mountain, R. D. & Harvey, A. H. *J. Chem. Phys.* **94**, 2238 (1991).

[174] Naval Research Laboratory Center for Computational Materials Science. *The Crystal Structures of Intermetallic Alloy Phases*. Retrieved April 10, 2006 from: http://cst-www.nrl.navy.mil/lattice/alloys/index.html.

[175] (Hansen, M. & Anderko, K., eds). *Constitution of binary alloys*. McGraw-Hill, New York (1958).

[176] Shechtmann, D., Blech, I., Gratias, D. & Cahn, J. W. *Phys. Rev. Lett.* **53**, 1951 (1984).

[177] Klement, W., Willens, R. H. & Duwez, P. *Nature* **187**, 869 (1960).

[178] Inoue, A., Zhang, T., Nishlyama, N., Ohba, K. & Masumoto, T. *Mater. Trans. JIM* **34**, 1234 (1993).

[179] Peker, A. & Johnson, W. L. *App. Phys. Lett.* **93**, 2342 (1993).

[180] Liquidmetal Technologies. *Liquidmetal Technological Applications*. Retrieved April 10, 2006 from: http://www.liquidmetal.com/applications/.

[181] Chadwick, G. A. *Metallography of Phase Transformations*. Butterworths, London (1972).

[182] Johnson, W. L. *Curr. Opin. Solid State Mater. Sci.* **6**, 383 (1996).

[183] Inoue, A. & Takeuchi, A. *Mater. Sci. Eng. A* **375**, 16 (2004).

[184] Fecht, H.-J. & Johnson, W. L. *Mater. Sci. Eng. A* **375**, 2 (2004).

[185] Steurer, W. *Acta Cryst.* **A61**, 28 (2005).

[186] Bernal, J. D. *Nature* **185**, 68 (1960).

[187] Gaskell, P. H. *Nature* **276**, 484 (1978).

[188] Miracle, D. B. *Nature Mater.* **3**, 697 (2004).

[189] Yavari, A. R. *Nature Mater.* **4**, 1 (2005).

[190] Fernandez, J. R. & Harrowell, P. *to be published* (2006).

[191] Johnson, W. L. *JOM* **54**, 40 (2002).

[192] Egami, T. & Waseda, Y. *J. Non-Cryst. Solids* **64**, 113 (1984).

[193] Fernandez, J. R. & Harrowell, P. *Phys. Rev. E* **67**, 011403 (2003).

[194] Senkov, O. N., Miracle, D. B. & Mullens, H. M. *J. Appl. Phys.* **97**, 103502 (2005).

[195] Kawamura, H. *Prog. Theor. Phys.* **70**, 352 (1983).

[196] Frank, F. C. & Kasper, J. S. *Acta Crystallogr.* **11**, 184 (1958).

[197] Oxborrow, M. & Henley, C. L. *Phys. Rev. B* **48**, 6966 (1993).

[198] Rubenstein, B. & Ben-Abraham, S. I. *Mater. Sci. Eng. A* **294-296**, 418 (2000).

[199] Nissen, H.-U. & Beeli, C. *Int. J. Mod. Phys. B* **7**, 1387 (1993).

[200] Nienhuis, B. *Phys. Rep.* **301**, 271 (1998).

[201] Glaser, M. A. & Clark, N. A. *Phys. Rev. A* **41**, 4585 (1990).

[202] E. Abe, Y. F. & Pennycook, S. J. *Nature* **3**, 759 (2004).

[203] Grummelt, P. *Geometriae Dedicata* **62**, 1 (1996).

[204] Press, W. H., Flannery, B. P., Teukolsky, S. A. & Vetterling, W. T. *Numerical Recipies: The Art of Scientific Computing.* Cambridge University Press, Cambridge (1987).

[205] Landau, L. D. & Lifshitz, E. M. *Statistical Physics.* Addison-Wesley, Reading (1969).

[206] Rahman, A. *Phys. Rev.* **136**, A405 (1964).

[207] Grünbaum, B. & Shepard, G. C. *Tilings and Patterns.* Freeman, New York (1987).

[208] Dzugutov, M. *Phys. Rev. A* **46**, R2984 (1992).

[209] Ostwald, W. *Z. Phys. Chem.* **22**, 289 (1897).

[210] Woodruff, D. *The Solid-Liquid Interface.* Cambridge University Press, London (1973).

[211] Tiller, W. *The Science of Crystallisation: Microscopic Interfacial Phenomena.* Cambridge University Press, New York (1991).

[212] Howe, J. *Interfaces in Materials.* Wiley, New York (1997).

[213] Adamson, A. & Gast, A. *Physical Chemistry of Surfaces.* Wiley-Interscience, New York (1997).

[214] Laird, B. *in Encyclopedia of Computational Chemistry.* Wiley, New York (1998).

[215] Kyrlidis, A. & Brown, R. *Phys. Rev. E* **51**, 5832 (1995).

[216] Mori, A., Manabe, R. & Nishioka, K. *Phys. Rev. E* **51**, R3831 (1995).

[217] Davidchack, R. & Laird, B. *Phys. Rev. Lett.* **85**, 4751 (2000).

[218] Broughton, J. & Gilmer, G. *J. Chem. Phys.* **84**, 5759 (1986).

[219] Galejs, R., Raveche, H. & Lie, G. *Phys. Rev. A* **39**, 2574 (1989).

[220] Karim, O. & Haymet, A. *J. Chem. Phys.* **89**, 6889 (1988).

[221] Karim, O., Kay, P. & Haymet, A. *J. Chem. Phys.* **92**, 4634 (1990).

[222] Hayward, J. & Haymet, A. *J. Chem. Phys.* **114**, 3713 (2001).

[223] Abraham, F. & Broughton, J. *Phys. Rev. Lett.* **56**, 734 (1986).

[224] Landman, U. *et al. Phys. Rev. Lett.* **56**, 155 (1986).

[225] Jesson, B. & Madden, P. *J. Chem. Phys.* **113**, 5935 (2001).

[226] Hoyt, J., Asta, M. & Karma, A. *Phys. Rev. Lett.* **86**, 5530 (2001).

[227] Davidchack, R. & Laird, B. *Phys. Rev. E* **54**, R5905 (1996).

[228] Davidchack, R. & Laird, B. *Mol. Phys.* **97**, 833 (1999).

[229] Coura, P. Z., Mesquita, O. N. & Costa, B. V. *Phys. Rev. B* **59**, 3408 (1999).

[230] Gruhn, T. & Monson, P. A. *Phys. Rev. E* **64**, 061703 (2001).

[231] Sibug-Aga, R. & Laird, B. B. *J. Chem. Phys.* **116**, 3410 (2002).

[232] Valeriani, C., Sanz, E. & Frenkel, D. *J. Chem. Phys.* **122**, 194501 (2005).

[233] Melchionna, S., Ciccotti, G. & Holian, B. L. *Mol. Phys.* **78**, 533 (1993).

[234] Cahn, R. W. *Philos. Trans. R. Soc. Lond. A* **351**, 497 (1995).

[235] Verhoeven, J. D. *Sci. Am.* **284**, 74 (2001).

[236] Verhoeven, J. D. *Steel Res.* **73**, 347 (2002).

[237] Fernandez, J. & Harrowell, P. (2004).

[238] Hoover, W. G. *Phys. Rev. A* **31**, 1695 (1985).

[239] Sanz-Serna, J. M. & Calvo, M. P. *Numerical Hamiltonian Problems*. Chapman and Hall, New York (1995).